Experimental Investigation of the Phase Equilibria in the Mg-Mn-{Ce, Nd} and Ce-Mg-Zn Ternary Systems and Diffusivity Measurements of the Mg-{Ce, Nd, Zn} and Zn-{Ce, Nd} Binary Systems

Ahmad Omar Mostafa

A Thesis
In the Department
of
Mechanical and Industrial Engineering

Presented in Partial Fulfillment of the Requirements
For the Degree of Doctor in Philosophy (Mechanical Engineering) at
Concordia University
Montreal, Quebec, Canada

May 2014

CONCORDIA UNIVERSITY
School of Graduate Studies

This is to certify that the thesis prepared

By: Ahmad O. Mostafa

Entitled: Experimental Investigation of the Phase Equilibria in the Mg-Mn-{Ce, Nd} and Ce-Mg-Zn Ternary Systems and Diffusivity Measurements of the Mg-{Ce, Nd, Zn} and Zn-{Ce, Nd} Binary Systems

and submitted in partial fulfillment of the requirements for the degree of

DOCTOR OF PHILOSOPHY (Mechanical Engineering)

complies with the regulations of the University and meets the accepted standards with respect to originality and quality.

Signed by the final examining committee:

______________________ Chair
Dr. John Zhang

______________________ External Examiner
Dr. Vladimir Brailovski

______________________ External to Program
Dr. Michelle Nokken

______________________ Examiner
Dr. Suong V. Hoa

______________________ Examiner
Dr. Martin Pugh

______________________ Thesis Supervisor
Dr. Mamoun Medraj

Approved by ______________________
Chair of Department or Graduate Program Director

May, 2014

____
Dr. , Dean
Faculty of Engineering & Computer Science

ABSTRACT

Experimental Investigation of the Phase Equilibria in the Mg-Mn-{Ce, Nd} and Ce-Mg-Zn Ternary Systems and Diffusivity Measurements of the Mg-{Ce, Nd, Zn} and Zn-{Ce, Nd} Binary Systems

Ahmad O. Mostafa, Ph.D.
Concordia University, 2014

In this work, the 450°C Mg-Mn-{Ce, Nd} and 300°C Ce-Mg-Zn isothermal sections were established using diffusion couples and key alloys. The phase relationships were determined using XDR, EDS/WDS and metallography. Diffusion couples were also used to measure the interdiffusion coefficients of the Mg-{Ce, Nd, Zn} and Zn-{Ce, Nd} binary systems based on the experimental composition profiles and Boltzmann-Matano method.

No ternary compounds were found in the Mg-Mn-{Ce, Nd} isothermal sections at 450°C. Microstructures of the ternary diffusion couples showed stationary Mn grain morphology in most of the diffusion zones. This was attributed to the affinity of Ce and Nd to Mg atoms, which forming several Mg-{Ce, Nd} binary compounds during the diffusion process. However, some of these binary compounds dissolved Mn. The ternary solubility of $(\gamma\text{-Ce})^{Mg,Mn}$, (CeMg), ($CeMg_3$), ($CeMg_{12}$), $(\alpha\text{-Nd})^{Mg,Mn}$, (MgNd) and ($Mg_3Nd$) was measured at 450°C to be 3.0, 5.1, 3.2, 1.8, 3.0, 13.0 and 3.7 at.% Mn, respectively. In both systems, the phase boundary lines were pointing towards the Mn-rich corner, except for the $(\alpha\text{-Nd})^{Mg,Mn}+Mn_{17}Nd_2+$(MgNd) phase field.

Eight ternary compounds were observed in the Ce-Mg-Zn isothermal section at 300°C. These are: τ_1 ($Ce_6Mg_3Zn_{19}$), τ_2 ($CeMg_{29}Zn_{25}$), τ_3 ($Ce_2Mg_3Zn_3$), τ_4 ($CeMg_3Zn_5$), τ_5

($CeMg_7Zn_{12}$), τ_6 ($CeMg_{2.3-x}Zn_{12.8+x}$; $0 \leq x \leq 1.1$), τ_7 ($CeMgZn_4$) and τ_8 ($Ce(Mg_{1-y}Zn_y)_{11}$); $0.096 \leq y \leq 0.43$). The ternary solubility of Zn in Ce-Mg compounds was found to increase with the decrease in Mg concentration. Accordingly, the ternary solid solubility of Zn in ($CeMg_{12}$) and ($CeMg_3$) was measured as 5.6 and 28.4 at.% Zn, respectively.

Diffusion couples with Boltzmann-Matano analysis were used to calculate the interdiffusion coefficients of the Mg-{Ce, Nd, Zn} and Zn-{Ce, Nd} systems. A systematic annealing procedure was followed to obtain all expected phases in the studied systems. For the available literature data for some of the compounds in the Mg-{Ce, Nd, Zn} systems, the calculated interdiffusion coefficients are in good agreement. The activation energy and the pre-exponential factor for the growth of the Mg-{Ce, Nd, Zn} compounds were determined using Arrhenius equation. The activation energies of the growth of the Mg-Ce compounds showed relatively higher values than those of Mg-Nd and Mg-Zn compounds.

Dedication

To my parents for their love and support throughout my life

To my sister and brothers who have never left my side

To my beloved wife

To Prof. Adnan Kilani

Acknowledgements

First, I express my sincere gratitude to Professor Mamoun Medraj for his constant guidance, suggestions and cooperation in helping me to finish this work. Without his coherent and illuminating instructions, this thesis would not have reached its present form. I am especially grateful for the trust and the freedom he gave me to do this work.

I wish also to thank my committee members who were more than generous with their expertise and precious time and most of all patience throughout the entire program.

I like to express my profound thanks to Mr. Mazen Samara for his time and support throughout the entire doctorate program. I will always appreciate all he has done. Very warm thanks to my MSc supervisor, Prof. Adnan Kilani, for his continuous encouragement and parental feelings. Special thanks to Dr. Dmytro Kevorkov who built a very well-established research background, from where I could start. I sincerely thank former TMG members, especially Dr. Mohammad Shamekh for guiding me to use the lab equipment, Dr. Mezbahul-Islam for the excellent scientific collaboration, Guy-Joel Rocher for helping me to develop my language skills, Tian Wang for being a good teacher and A. Mert Kara for his sincere feelings. I extend my thanks to the current TMG members for their continuous support, especially Bolarinwa Komolafe, Madina Umairkhan and Hany Kirols. Special thanks to my friends in Palestine, Jordan, Canada, and other countries especially Hassan Salameh, Mohammad Al-sheikh, Khaled Younes, Dawood Yousef, Sandra Rodriguez, Alain Anctil, Dr. Simona Badilescu, Benjamin Wallace and Ibrahim for being my cheerleaders.

Last but not least, all thanks to my parents for being the reason behind my success in all life matters. All the support they have provided me over the years was the greatest gift anyone has ever given me, without them I may never have gotten to where I am today. I like to thank my sister, Asma'a, and her husband, Mohammad, and their kids, Osama, Zaid and Hala, for providing the family atmosphere that I needed during my settlement away from homeland. Special thanks to my brothers, Mohammad, Ehab and Baha'a, and their wives, Maram, Manar and Wala'a, and their kids, Omar, Hoor, Ahmad and Elyas, for their wonderful smiles and trustful feelings. They inspired me in an unbelievable way. I would like to extend my thanks to my wife, Diala. Her support, encouragement, quiet patience and unwavering love were undeniably the core upon which the work was accelerating.

Special thanks to the natural sciences and engineering research council (NSERC) for the financial support through magnesium network (MagNET) for excellence.

Contributions of the Authors

This thesis has been prepared in "Manuscript-based thesis" format. The entire contents represent results that have been published in the form of an unaltered original journal article and materials which are submitted for publication, or the clearly duplicated text of one or more published papers of which the student is the author or co-author. The complete citation for the published paper is provided below:

Chapter 2: Ahmad Mostafa and Mamoun Medraj, "Experimental investigation of the Ce-Mg-Mn isothermal section at 723 K (450°C) *via* diffusion couples technique", *Metallurgical and Materials Transactions A*; 45 (7), (2014), 3144-3160.

Chapter 3: Ahmad Mostafa and Mamoun Medraj, "Experimental investigation of the Mg-Mn-Nd isothermal section at 450°C", *Journal of Alloys and Compounds;* 608 (2014) 247-257.

Chapter 4: Ahmad Mostafa and Mamoun Medraj, "Phase equilibria of the Ce-Mg-Zn ternary system at 300°C", *Metals*; Accepted on May 15, 2014.

The next chapter is a paper that has been submitted for publication.

Chapter 5: Ahmad Mostafa and Mamoun Medraj, "On the atomic interdiffusion in Mg-{Ce, Nd, Zn} and Zn-{Ce, Nd} binary systems". Submitted to *Journal of Materials Research,* March (2014).

All the papers presented in this thesis were co-authored and reviewed prior to submission for publication by Prof. Mamoun Medraj, my supervisor. All of the remaining work and manuscript preparation were performed by the author of this thesis.

Table of Contents

List of Figures

List of Tables

Chapter 1 : Introduction

1.1. Magnesium Alloys

Magnesium is the lightest metal used as the basis of alloys used for structural applications. This has been a major factor in the widespread use of magnesium casting and wrought products, where weight savings are of great concern. Magnesium alloys are known for their high strength-to-weight ratio, castability and workability comparing to pure Mg [1, 2]. For these reasons, they are attractive to the automotive and aerospace industries, because the weight saving can reduce the fuel consumption. Thus, high reduction of CO_2 emissions can be achieved [2-5]. The two major disadvantages of magnesium alloys for the use in transportation applications are low creep resistance at elevated temperatures and relatively high susceptibility to corrosion [3]. The design of lightweight alloys with superior properties is one of the most challenging issues for the transportation industry. This requires the development of new magnesium alloys with enhanced microstructural stability and improved mechanical properties. At the same time, it is necessary to reduce the production cost of materials and processes to compete with other available materials [2, 3, 6].

Magnesium as a pure metal is limited to very few applications but its properties are improved by alloying. Alloying magnesium with other elements improves the mechanical properties by solid-solution strengthening or by precipitation hardening. Elements with high solid solubility in α-Mg are recommended for solid-solution strengthening, whereas those with limited solubility are suitable for precipitation hardening [2]. Table 1-1 lists the commonly used alloying elements and their effects on Mg-based alloys [7].

Table 1-1: Effect of major alloying elements on Mg-based alloys[7]

Element	Effect
Al	Increases hardness, strength and castability while only increasing density minimally.
Ca	Improves thermal and mechanical properties as well as assists in grain refinement and creep resistance. Also, reduces surface tension.
Cu	Assists in increasing both room and high temperature strength.
Mn	Increases saltwater corrosion resistance within some aluminum containing alloys.
Ni	Increases both yield and ultimate strength at room temperature. Negatively impacts ductility and corrosion resistance.
Sr	Used in conjunction with other elements to enhance creep performance.
Sn	When used with aluminum it improves ductility, and reduces tendency to crack during processing.
Y	Enhances high temperature strength and creep performance when combined with other rare earth metals
Zn	Increases the alloys fluidity in casting. When added to magnesium alloys with nickel and iron impurities, it can improve corrosion resistance. Additions of 2 wt.% or greater tend to be prone to hot cracking

Rare Earth (RE) additions are effective in improving the mechanical performance at elevated temperatures. This can be attributed to grain refinement, formation of secondary phase precipitates along the grain boundaries and formation of stable intermetallic compounds with high melting temperatures [8-10]. Besides enhancing the creep resistance of magnesium alloys at elevated temperatures, addition of RE can improve their strength, toughness, weldability, machinability and corrosion resistance compared to pure magnesium [11, 12]. Figure 1-1, redrawn after Mordike and Ebert [4], shows the development directions of magnesium alloys.

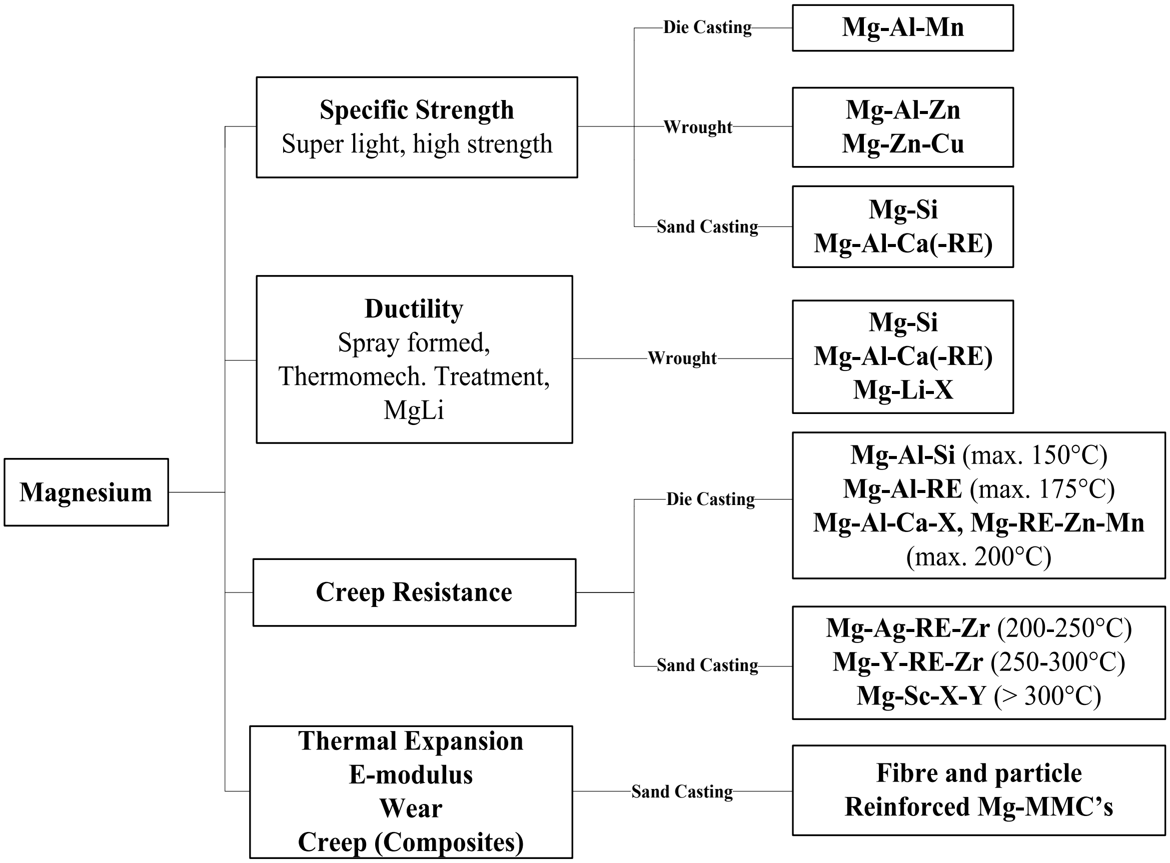

Figure 1-1: The development directions of magnesium alloys [4]

In this work, the three ternary systems Ce-Mg-Mn, Mg-Mn-Nd and Ce-Mg-Zn were experimentally investigated to provide better understanding of the phase relationships. Manganese and zinc are among the essential additives to enhance the corrosion resistance and specific strength of magnesium-based alloys. On the other hand, addition of RE elements, such as cerium and neodymium, improves their mechanical properties at elevated temperatures. In order to obtain the optimum properties of Mg alloys, knowledge of these ternary phase diagrams and the diffusivity measurements of their constituent binaries are essential.

1.2. Methods of phase diagram determination

1.2.1. Solid-Solid diffusion couples

The diffusion couple method is one of the important tools for phase diagram determination [13, 14]. Some advantages of using solid-solid diffusion couples are: (1) the phase formation takes place at the annealing temperature (without going through the melting and solidification), to avoid the problem of a high temperature phase decomposition when the liquid phase is present, (2) multiple phases may appear in a single diffusion couple, thus multiple tie-lines may be extracted representing the local equilibrium at the phase interfaces [15] and (3) It also eliminates the problems associated with alloy preparation especially when a low melting metal is added to systems with high melting temperatures [16].

Solid-state diffusion is relatively slow. Therefore, the appearance of all equilibrium phases is not guaranteed [17]. The solid-state diffusion couple is prepared when two bonded faces of the couple end-members are ground and polished flat, clamped together and annealed at a certain temperature. Various protective atmospheres can be used (e.g., vacuum or inert gas) depending on the initial materials. Quenching of the sample is desirable after the heat treatment, in order to maintain the high-temperature equilibrium structure [15]. The sequence of the phases for a multi-phase binary system, which form in a diffusion couple by the interdiffusion of species at a given temperature, corresponds directly to the binary phase diagram as illustrated in Figure 1-2. Figure 1-2 (a) gives an example of the compound layers formed in the Si-Ti binary diffusion couple annealed at 1150°C for 2000h [18]. Figure 1-2 (b) shows the presentation of the compounds formed in the Si-Ti diffusion couple (Figure 1-2 (a)) on the Si-Ti binary phase diagram [19].

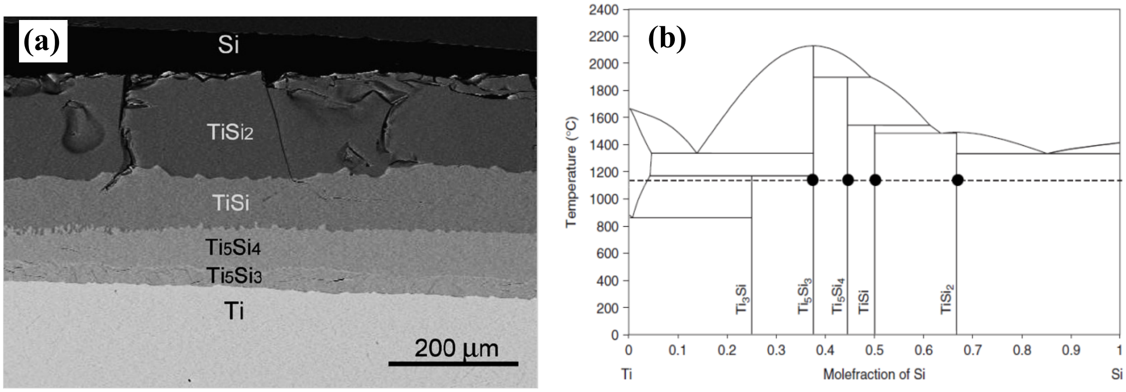

Figure 1-2: (a) Si-Ti diffusion couple annealed at 1100°C for 2000h [18]; (b) Si-Ti compounds representation on the Si-Ti phase diagram [19]

For a ternary system, however, the microstructure of the diffusion zones can be understood with the aid of the diffusion path, as shown in Figure 1-3, which is based on the law of mass conservation [20]. The law of mass conservation dictates that the diffusion path must cross the straight line between the end-members of the diffusion couple at least once, since no material is lost or created during the diffusion reaction [15, 20]. It is worth noting that the largest number of co-existing phases at zero number of degrees of freedom in a ternary system is four. According to the phase diagram rule, two-phase layers can be developed in a ternary diffusion couple, because of the extra degree of freedom, whereas three-phase layers are forbidden.

Figure 1-3 (a) represents the reaction zone structure in a hypothetical diffusion couple A/Z of the A-B-C system. The corresponding diffusion path determined from the couple A/Z is plotted on the isothermal section of the A-B-C system as shown in Figure 1-3 (b). The structures of diffusion zones in Figure 1-3 (a) are denoted by lower-case letters which correspond to the appropriate composition on the A-B-C isothermal section (Figure 1-3 (b)).

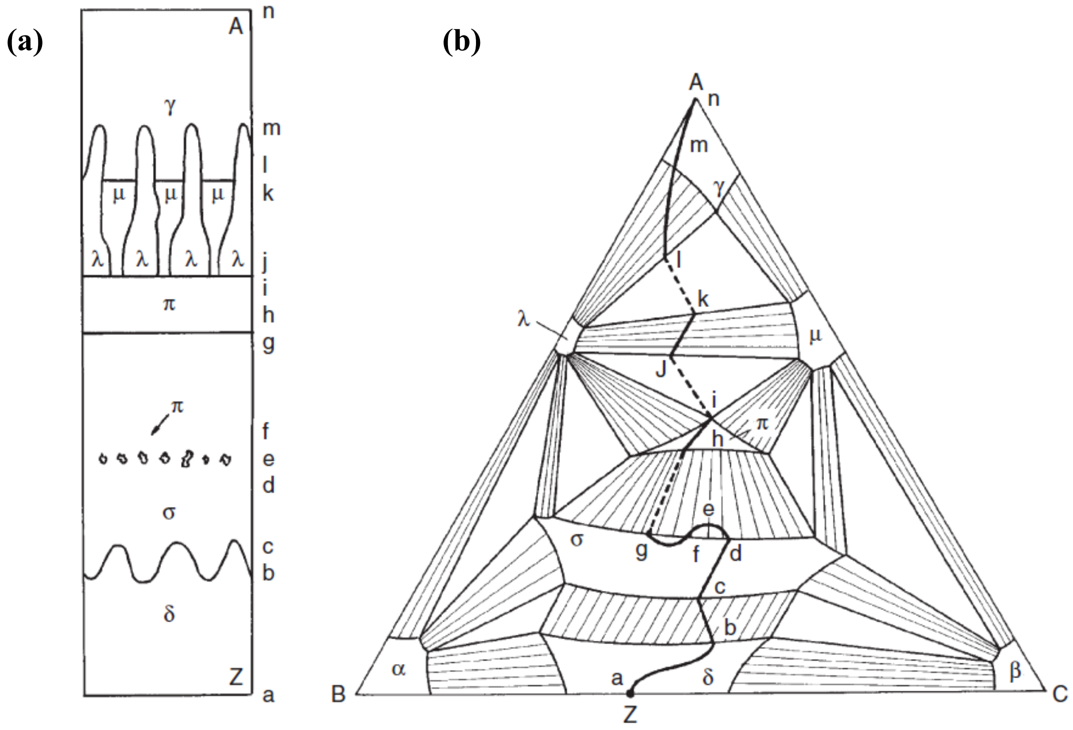

Figure 1-3: (a) The microstructure of diffusion zones in A/Z diffusion couple; (b) the diffusion path of a hypothetical couple A/Z of the ternary A-B-C system [20]

The main principle of diffusion couples is the formation of local equilibria in the diffusion zones, which is formed at a very slow rate. Diffusion zones usually consist of thin layers. Every thin layer is in thermodynamic equilibrium with the neighboring layers. In other words, the chemical potential of the diffusing species varies continuously through the layer and has the same value at both sides of the interface [21].

The composition-distance curves (composition profiles) of the elements are determined, perpendicular to the interface between every two adjacent phases in the diffusion couples, using different methods such as: energy dispersive X-ray spectroscopy (EDS), wavelength dispersive X-ray spectroscopy (WDS), electron probe micro-analysis (EPMA), spreading resistance profiling (SRP), Auger electron spectrometry (AES) and secondary ion mass spectrometry (SIMS) [22]. In this work, the composition profiles across various diffusion couples were obtained using EDS and/or WDS line-scans. The equilibrium composition of a phase can be obtained by extrapolating the composition profile of an element to the phase boundaries.

The experimental profiles of the binary diffusion couples were used to calculate the binary interdiffusion coefficients of the Mg-{Ce, Nd, Zn} and Zn-{Ce, Nd} systems using Boltzmann-Matano analysis [23, 24]. Interdiffusion coefficient is the proportional constant between the flux of components through the bulk of their growing layers, in the form of atoms or ions, and the gradient in their concentration. In the current work, the interdiffusion coefficient of the species at the metallic interfaces of the Mg-{Ce, Nd, Zn} and Zn-{Ce, Nd} systems is abbreviated as interdiffusion coefficient of the Mg-{Ce, Nd, Zn} and Zn-{Ce, Nd} systems. Discussion of the interdiffusion coefficients measurements will be covered in details in Chapter 5.

1.2.2. Equilibrated key alloys

In this work, the phase equilibria of the Mg-Mn-{Ce, Nd} and Ce-Mg-Zn systems were determined using diffusion couples and equilibrated key alloys. Equilibrated alloys of required constituents are used to verify the phase equilibria obtained from diffusion couple experiments and for the exact determination of the solid solubility in a particular phase. Key alloys are heat treated at a certain temperature to achieve equilibrium. The treated alloys are subjected to several characterization methods to identify the phases, so as to determine the liquidus and solidus temperatures, solidus lines and other phase transition lines. These methods include thermal analysis using differential scanning calorimeter (DSC), phase identification using X-ray diffractometer (XRD), measurements of phase composition using WDS/EDS, metallography using optical microscope (OM) and scanning electron microscope (SEM) and others. By obtaining all information regarding the temperature, composition and changes associated with phase transitions, the phase boundaries can be constructed according to the phase rule [15, 21].

Alloys are initially prepared from high purity constituent metals using arc melting and/or induction melting techniques under controlled atmosphere. Oxidation or evaporation of the prepared alloys can result in deviation from the global composition, resulting in inaccurate results. It is very important to prepare alloys with homogeneous composition, because inhomogeneous structures provide information only on the local equilibrium with these constituents and can be misleading. However, equilibrated key alloys are meant to achieve the global equilibrium state at certain compositions.

Non-equilibrium structures usually occur from solidification segregation, when alloys are cooled gradually through their liquidus and solidus. To overcome the non-equilibrium (as-cast) structures, alloys are subjected to homogenization heat treatment. The process involves heating the alloys at a temperature below their solidus for an extended period of time followed by quenching to room temperature. The quenching step is required to preserve the homogenized structure at room temperature for the analysis process. Selecting the proper annealing time and temperature has a great importance, because the homogenized structure is achieved through a diffusion process. Diffusion coefficients are highly dependent on temperature. Thus, annealing should be performed at relatively high temperature to accelerate the homogenization process [15].

Two methods are used for phase diagram determination using equilibrated alloys: (1) analysis of quenched samples to construct isotherms (static method) by means of XRD, EDS/WDS and metallography, and (2) analysis of samples by thermal analysis experiments to construct vertical sections and liquidus projections (dynamic method) [21]. The XRD, EDS/WDS and SEM methods used during this work are discussed below.

1.2.4. X-Ray Diffraction (XRD)

X-ray diffraction, as a method for phase diagram determination, is used to identify the available phases and their relative amounts in the key alloys. It is also important for providing information on the crystal structure of these phases; as well as it can provide valuable information about the solid solubility ranges of intermetallic compounds.

The X-ray beam is generated from a filtered CuKα radiation. When a high voltage is applied between the electrodes, high-speed electrons with sufficient kinetic energy, coming from the cathode, collide with the anode (metallic target). According to Bragg's law, Equation 1-1, when the X-ray beam impinges on a component, a portion of this beam will be scattered at a discrete angle based on the component's wavelength [25].

$$n\lambda=2d\,\sin\theta \qquad \text{Equation 1-1}$$

where, λ is the radiation wavelength, θ is the diffraction angle, d is the interplanar spacing as a function of the Miller indices and the lattice parameters and n is the order of reflection which equals to the number of wavelengths in the path. If Bragg's law is satisfied, diffraction can occur.

1.2.5 Scanning electron microscopy, Energy dispersive X-ray spectroscopy and Wavelength dispersive X-ray spectroscopy (SEM/EDS/WDS)

SEM is a very useful technique in phase diagram investigation. In SEM, a high energy electron beam bombards the surface of the specimen to generate backscattered electrons, secondary electrons, characteristic X-rays and other photons of various energy [26, 27].

Two imaging modes are possible in SEM, secondary and backscattered electron imaging. The secondary and backscattered electron images are characterized with three-dimensional appearance due to the large depth of field of the SEM and the shadow relief effect [27]. The contrast mechanism in the secondary electron imaging comes from the surface topology of the sample with small contribution from the backscattered electrons. The contrast of the backscattered images comes from the difference in the average atomic number at each point in the sample. Therefore, backscattered electrons provide some compositional information [15].

Characteristic X-rays are also emitted in the SEM as a result of electron impingement. The X-rays emitted from the samples can yield both qualitative identification and quantitative elemental information from an area of around 1 μm in diameter and 1 μm in depth under normal operating environments [27]. EDS makes use of the X-rays for the chemical microanalysis. In the EDS technique, a special detector collects the dispersed X-ray from the sample. The signal acquired by the detector represents the X-ray versus their energy in a form of peak; each peak corresponds to a certain element [28]. Figure 1-4 shows the EDS spectrum of glass containing heavy and light elements in an energy range up to 10 keV. Each individual element is identified straight from the EDS spectra, because each peak generated by a specific element exhibits a unique X-ray energy [29]. The EDS measurements can be performed with a high degree of confidence when measuring the major constituent of a sample. However, errors in peak assignment can arise if a minor or trace-level element is introduced. This poor accuracy of measurement can be attributed to the low signal to background ratio, which results in spectral interferences and artifacts [27, 28]. Thus, WDS is the preferred method for measuring low concentrations or trace-trace elements.

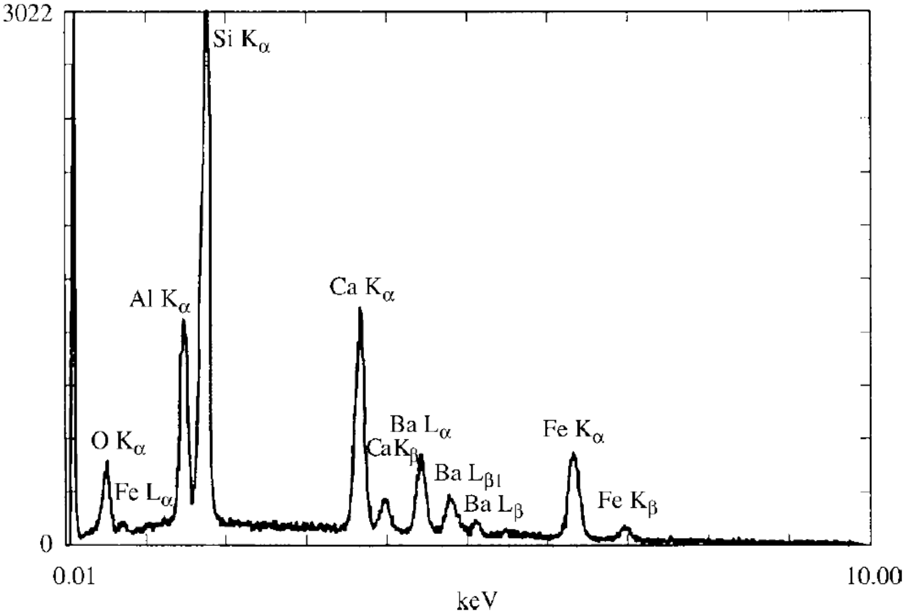

Figure 1-4: Schematic diagram for EDS spectrum of glass including (Si, O, Ca, Al, Fe and Ba) [29]

WDS is used for the quantitative determination of the composition of a phase. In WDS, characteristic X-rays are analyzed on the basis of their wavelength rather than their photon energy. The detection is accomplished when a small portion of the X-ray, reflected from the test specimen, impinges on an analyzing crystal. The crystal behaves as a three-dimensional diffraction gating and strongly diffracts X-ray photons. The X-ray intensity can be measured as a function of the photons' wavelengths [28].

Although WDS requires higher beam current than EDS and takes longer time than EDS to obtain multi-element quantitative information, it is superior to EDS in obtaining quantitative information. WDS is known for its high resolution of the crystal spectrometer, which results in higher peak-to-background ratios and in minimizing the possibility of peaks overlapping [27].

1.3. Objectives

The main objectives of this work are to study the phase equilibria in the Mg-{Ce, Nd}-Mn and Ce-Mg-Zn systems, by means of diffusion couples and equilibrated key alloys, and the binary interdiffusion coefficients of the Mg-{Ce, Nd, Zn} and Zn-{Ce, Nd} systems experimentally using diffusion couples and Boltzmann-Matano analysis. The microstructural characterization is carried out using XRD, EDS, WDS and SEM. EDS/WDS line-scans are performed to obtain the elemental profiles across diffusion zones of the diffusion couples. The interdiffusion coefficients of the binary systems are measured using composition profiles of the binary diffusion couples and Boltzmann-Matano analysis. Specific objectives include:

- Construction of the Mg-Mn-{Ce, Nd} isothermal sections at 450°C and the Ce-Mg-Zn isothermal section at 300°C by means of diffusion couples and equilibrated key alloys.

- Measuring the binary interdiffusion coefficients of the Mg-{Ce, Nd, Zn} and Zn-{Ce, Nd} systems by means of diffusion couple experiments and Boltzmann-Matano analysis.

- Measuring the activation energy and pre-exponential factor of the growth of the Mg-{Ce, Nd, Zn} binary compounds using Arrhenius equation.

1.4. Thesis layout

This section outlines the format of a manuscript-based thesis. This thesis consists of six chapters. Chapter 1 gives an introduction about the Mg-based alloys and their development through comprehensive understanding of phase diagrams. The experimental methods of phase diagram determination are discussed, and the objectives of this study are presented. Chapter 2 is dedicated to the study of the isothermal section of the Ce-Mg-Mn system at 450°C. The diffusion layer formation in the Ce-Mg-Mn system is discussed in detail and the equilibrium phase relations are established. In Chapter 3, the isothermal section of the Mg-Mn-Nd is determined at 450°C using solid-solid diffusion couples and key alloys. The effect of annealing time on the diffusion couples and key alloy microstructures is studied. Chapter 4 presents the experimental investigation of the Ce-Mg-Zn isothermal section at 300°C by means of diffusion couples and key alloys. The occurrence of eight ternary compounds is revealed. Interpolation of the two-phase field tie-lines is also demonstrated. In Chapter 5, the binary interdiffusion coefficients of the Mg-{Ce, Nd, Zn} and Zn-{Ce, Nd} systems are determined using diffusion couples and Boltzmann-Matano analysis. The interdiffusion coefficient, pre-exponential factor and activation energy of these binary systems are calculated. The anisotropic layer growth and diffusion sub-layer formation are discussed. Chapter 6 summarizes the conclusions, contributions and recommendations for future work. At the end of every manuscript, connecting texts that provide bridges between the chapters are added in order to ensure continuity of the thesis.

Chapter 2 : Experimental investigation of the Ce-Mg-Mn isothermal section at 723K (450°C) *via* diffusion couples technique

---

ABSTRACT

The isothermal section of the Ce-Mg-Mn phase diagram at 723 K (450°C) was established experimentally by means of diffusion couples and key alloys. The phase relationships in the complete composition range were determined based on six solid-solid diffusion couples and twelve annealed key alloys. No ternary compounds were found in the Ce-Mg-Mn system at 723 K (450°C). X-ray diffraction and energy dispersive X-ray spectroscopy spot analysis were used for phase identification. EDS line-scans, across the diffusion layers, were performed to determine the binary and ternary homogeneity ranges. Mn was observed in the diffusion couples and key alloys microstructures as either a solute element in the Ce-Mg compounds or as a pure element, because it has no tendency to form intermetallic compounds with either Ce or Mg. The fast atomic interdiffusion of Ce and Mg produces several binary compounds (Ce_xMg_y) during the diffusion process. Thus, the diffusion layers formed in the ternary diffusion couples were similar to those in the Ce-Mg binary diffusion couples, except that the ternary diffusion couples contain layers of Ce-Mg compounds that dissolve certain amount of Mn. Also, the ternary diffusion couples showed layers containing islands of pure Mn distributed in most diffusion zones. As a result, the phase boundary lines were pointing towards Mn-rich corner, which supports the tendency of Mn to be in equilibrium with all the phases in the system.

2.1. Introduction

Magnesium alloys are in increasing demand because of their unique properties. Some of the major advantages of magnesium alloys are: lowest density among all other metallic structural materials, high specific strength, good castability, suitability for high pressure die casting, high speed machinability, good weldability under controlled atmosphere, availability [4] and improved corrosion resistibility against salty water compared to pure Mg [30]. To obtain these advantages, attempts have been made to improve the mechanical properties of Mg by adding different alloying elements. For instance, addition of cerium leads to improved mechanical properties at elevated temperatures [31]. Furthermore, addition of manganese improves the corrosion resistance [1]. Ce-Mg-Mn alloys are considered promising for automotive and aerospace applications. They show excellent creep resistance at elevated temperatures [4]. Their light-weight, also, gives an opportunity for further structural weight reduction. Thus, it is essential to understand the phase relationships, resulting from addition of Ce and Mn to Mg, in the Ce-Mg-Mn system using different techniques.

The diffusion couple is a valuable experimental technique for phase diagram studies. It is subjected to the assumption of obtaining local equilibria in the diffusion zones [20]. Thin layers, in thermodynamic equilibrium, are formed adjacent to each other. The phase equilibria, then, can be determined via the composition profiles across these layers [17].

2.2. Literature data

2.2.1. The Ce-Mn system

The Ce-Mn phase diagram was studied experimentally by several investigators [32-36]. Rolla and Iandelli [32] and Iandelli [33] first suggested that a liquid miscibility gap exists at 1271 K (998°C) in the composition range of 45 to 64 wt.% Mn. Later, Thamer [34] investigated the Ce-Mn system in the Ce-rich side (below 20 at.% Mn). He [34] found that the eutectic occurs at 895 K (622°C), which is 10 K higher than the eutectic temperature proposed by Iandelli [33] at 885 K (612°C). Also, he [34] reported the solubility of Mn as 5 at.% in δ-Ce and 2 at.% in γ-Ce at 911 K (638°C). Palenzona and Cirafici [35] re-assessed the Ce-Mn phase diagram experimentally, taking into account all previous thermal analyses reported by Thamer [34]. They [35] corrected the allotropic transition temperatures of α→β Mn to 1000 K (727°C) instead of 983 K (710°C), β→γ to 1373 K (1100°C) instead of 1343 K (1070°C) and γ→δ to 1411 K (1138°C) instead of 1416 K (1143°C). The melting temperature of Mn remained the same as 1519K (1246°C). Because of the presence of the liquid miscibility gap in the Ce-Mn phase diagram, Tang *et al.* [36] re-assessed the system based on their own XRD and DTA measurements and the data from the literature [33, 34]. Furthermore, the Ce-Mn system was thermodynamically modeled by Tang *et al.* [37] and Kang *et al.* [38] considering all the experimental findings, except the liquid miscibility gap proposed by Iandelli [33].

2.2.2. The Mg-Mn system

Several experimental work [39-42] and thermodynamic modeling [38, 42, 43] concerning the binary Mg-Mn phase diagram were found in the literature. However, due to the high temperature of the liquid miscibility gap, experimental data is not available in this region. The temperature was estimated, using thermodynamic modeling, by many authors as 2175 K (1902°C) [38], 3475 K (3202°C) [42] and 3688 K (3415°C) [43]. The binary liquid miscibility gap, of the Mg-Mn binary system, was proposed to extend in the Ce-Mg-Mn ternary, based on the liquidus projection calculated by Zhang *et al.* [44].

2.2.3. The Ce-Mg system

Unlike the other two binaries, intermetallic compounds exist in the Ce-Mg system. The Ce-Mg phase diagram was experimentally studied by many authors [45-49]. Accordingly, Figure 2-1 was redrawn form Nayeb-Hashemi and Clark [50]. Recently, Zhang *et al.* [51] reported a shift in the compositions of Ce_5Mg_{41} and $CeMg_{12}$. Based on their [51] findings, some compounds were given different formulae such as Ce_5Mg_{39} instead of Ce_5Mg_{41} and $CeMg_{11}$ instead of $CeMg_{12}$. These compositional shifts were due to substitution of Mg sites with vacancies.

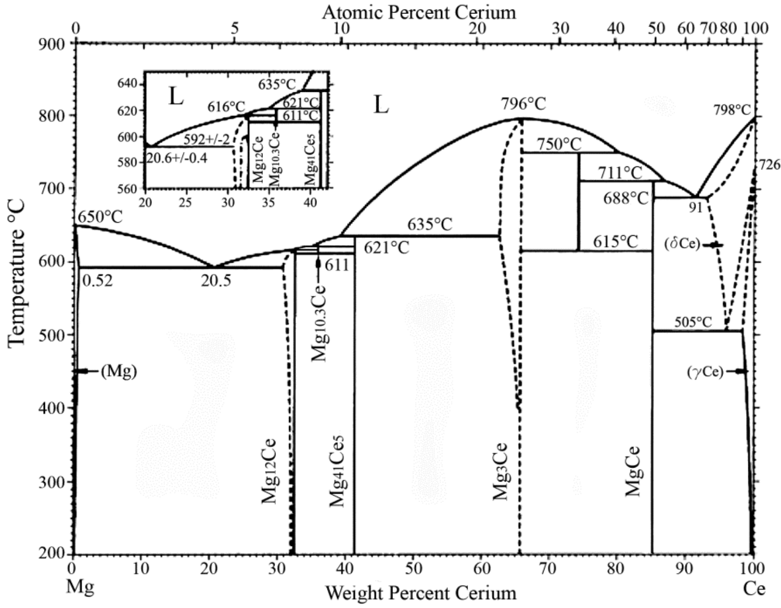

Figure 2-1: The Ce-Mg phase diagram redrawn from Nayeb-Hashemi and Clark [50]

More recently, Okamoto [52] re-evaluated the Ce-Mg phase diagram focusing on the modified phase diagram by Zhang *et al.* [51, 53, 54]. Based on the crystal structure data, Okamoto [52] changed Ce_5Mg_{39} and $CeMg_{11}$ to their former formulae Ce_5Mg_{41} and $CeMg_{12}$, respectively. Table 2-1 shows the crystal structure data and actual composition of Ce-Mg compounds [52, 55]. Also, he [52] suggested the re-examination of the $CeMg_3$ phase field; since the width of the two-phase region $CeMg_2$+$CeMg_3$ was shown to increase with temperature.

Table 2-1: Crystal structure data and actual composition of Ce-Mg compounds [52, 55]

Phase	Composition at.% Mg	Pearson's symbol	Space group	Structure type	Lattice parameters (Å)	
					a	c
(δCe)	0-30	*cI2*	*Im3m*	W	4.120	
(γCe)	0-8.2	*cF4*	*Fm3m*	Cu	5.160	
CeMg	50	*cP2*	*Pm3m*	CsCl	3.901	
$CeMg_2$	66.7	*cF24*	*Fd3m*	Cu_2Mg	8.733	
($CeMg_3$)	74.7-77	*cF16*	*Fm3m*	BiF_3	7.420	
Ce_5Mg_{41}	89.1	*tI92*	*I4/m*	Ce_5Mg_{41}	14.540	10.280
$CeMg_{10.3}$	91.2	*hP38*	$P6_3/mmc$	$Ni_{17}Th_2$	10.350	10.260
($CeMg_{12}$)	92.5-93	*tI26*	*I4/mmm*	$Mn_{12}Th$	10.330	5.960
Mg	100	*hP2*	$P6_3/mmc$	Mg	3.207	5.210

2.2.4. The Ce-Mg-Mn system

The Ce-Mg-Mn ternary system was first studied by Petrov *et al.* [31]. The samples were prepared initially from Mg-Mn master alloys containing 2.5 wt.% Mn. They [31] reported two vertical sections in the Mg-rich corner, at maximum 3 wt.% Mn with 0.3 and 1.6 wt.% Ce, respectively, by thermal and microscopic methods. No ternary compounds were observed in the two vertical sections. Based on the results of Petrov *et al.* [31], Raynor [56] concluded that addition of 1.5 wt.% Ce to Mg-Mn alloys reduces the solid solubility of Mn from 5 to 3.8 wt.% at 1123 K (850°C), while further additions will slightly affect the Mn solubility. Later, the Ce-Mg-Mn ternary system was studied by Pezat *et al.* [57]. They attempted partial substitution of Mg by M=(V, Cr, Mn, Fe and Co) in $CeMg_{12}$ to investigate the $CeMg_{11}M$ composition as a hydrogen storage compound. In their findings, $CeMg_{11}Mn$ was reported as a ternary compound. After further examination, they realized that $CeMg_{11}M$ was only a chemical composition in the $CeMg_{12}$+Mn two-phase field and not a ternary compound. Recently, Zhang *et al.* [44] studied the Mg-rich corner (up to 2.5 wt.% Mn and 25 wt.% Ce) of the Ce-Mg-Mn phase diagram experimentally with the aid of thermodynamic modeling. High purity starting materials were used in their [44] work and three isopleths at 0.6, 1.8 and 2.5 wt.% Mn and Ce up to 25 wt.% were selected. The system was investigated using two thermal analysis methods (cooling curve analysis (CCA) and DSC), SEM/EPMA and XRD techniques. A ternary eutectic reaction was observed at the composition of 1 wt.% Mn and 23 wt.% Ce and temperature of 865 K (592°C). In addition, the homogeneity range of $CeMg_{12}$ varies between 0.3 at.% and 0.6 at.% Mn, depending on alloy composition. Zhang *et al.* [44] also mentioned that $Ce(Mg,Mn)_{12}$ ternary solid solution has the same tetragonal structure as $CeMg_{12}$, indicating the substitution of Mg by Mn. No additional experimental data could be found on this system in the literature.

The main objective of this work is to establish the Ce-Mg-Mn isothermal section at 723 K (450°C) experimentally by means of diffusion couples and key alloys. This will give better understanding of the phase relationships in the system, which is necessary for alloy design and development.

2.3. Experimental procedure

In order to study the phase relationships in the Ce-Mg-Mn isothermal section at 723 K (450°C), six solid-solid diffusion couples along with twelve key alloys were prepared and analyzed using Hitachi S-3400 scanning electron microscope equipped with energy dispersive X-ray spectrometer (SEM/EDS). In most cases, the solubility ranges extended from the Ce-Mg binary compounds were below the detection limit of the EDS detector. Thus, the EDS results were used for qualitative analysis and the small solubilities were indicated as less than 2 at.%. X-ray diffraction was performed on powdered samples, in the range from 20 to 90 degree 2θ with 0.02° step size, to identify and confirm the phases obtained by EDS measurements. X-ray phase analysis was carried out using X'pert Highscore Plus software [58]. The standard intensity data were taken from Pearson's Crystal Data software [55]. Silicon was used in the powder samples as a calibration standard to correct for the zero shift and specimen displacement.

2.3.1. Key alloys preparation

Pure elements were used for alloy preparation and diffusion couple end-members. Ce ingots and Mn flakes with purity of 99.9% and 99.98%, respectively, were supplied by Alfa Aesar Co., and Mg ingots with purity of 99.8% were supplied by CANMET Materials Technology Laboratory (CANMET-MTL). The key alloys were prepared in an arc-melting furnace with water-cooled copper crucible and a non-consumable tungsten electrode under argon. The alloys were melted several times to ensure the composition homogeneity. Excess amount of Mg (around 15%) was added to compensate for Mg losses due to evaporation. The actual global composition was determined using an

Ultima2 inductively coupled plasma optical emission spectrometry (ICP-OES). The actual composition was determined by taking the average composition of three different portions from each sample.

2.3.2. Solid-solid diffusion couples

The end-members of the solid-solid diffusion couples were prepared from pure metals and/or alloys. Table 2-2 shows the compositions of the end-members and the annealing time periods of the diffusion couples annealed at 723 K (450°C). The contacting surfaces were ground gradually up to 1200 SiC paper using 99% pure ethanol as a lubricant and to prevent oxidation. High friction between the samples and the SiC papers was avoided to eliminate sparking during grinding due to Ce. After that, the ground surfaces were polished down to 1μm using alcohol diamond suspension. The end-members were strongly tightened together using stainless steel clamping rings to ensure good surface contact between the two members.

Table 2-2: Composition and annealing conditions of the diffusion couples

Couple	First end-member (at.%)			Second end-member (at.%)			Time (days)	Temperature K (°C)
	Ce	Mg	Mn	Ce	Mg	Mn		
#1	52.6	19.8	27.6	-	100	-	8	723 (450)
#2	34.7	38.1	27.2	-	100	-	8	723 (450)
#3	7.0	87.4	5.6	100	-	-	6	723 (450)
#4	60.0	40.0	-	-	-	100	10	723 (450)
#5	34.4	38.1	27.2	100	-	-	5	723 (450)
#6	52.6	19.8	27.6	14.5	82.7	2.8	4	723 (450)

For annealing purposes, alloys and diffusion couples were wrapped in tantalum foil and encapsulated inside an argon-purged quartz tube with the inside pressure of about 5×10^{-1} torr. To reach equilibrium at 723 K (450°C), alloys were heated up to 773 K (500°C) for 1hr, then the furnace temperature was brought down to 723 K (450°C) and kept for different annealing time. Therefore, annealing time was chosen as 8 days for some compositions, since no complete phase equilibrium was obtained from preliminary annealing attempts for 4 days. Other alloys were annealed for 35 days; especially those containing $CeMg_2$ phase. This was due to the slow kinetics of the eutectoidal decomposition of the $CeMg_2$ into (CeMg) and ($CeMg_3$). The diffusion couples were annealed at 723 K (450°C) for different periods of time, based on the composition of the chosen end-members. The annealing process was stopped when the tube was visually observed to be dark indicating significant evaporation. After annealing, the quartz tubes, containing alloys and diffusion couples, were rapidly quenched in cold water in order to maintain the high temperature structure. The equilibrated phases and the diffusion zones were analyzed using SEM/EDS spot analysis and line-scans. Based on the phase equilibrium data obtained from six solid-solid diffusion couples and 12 key alloys, the isothermal section of the Ce-Mg-Mn phase diagram at 723 K (450°C) was constructed.

2.4. Results and discussion

Diffusion couple technique combined with selected equilibrated alloys is used to achieve more reliable equilibrium phase relations in the Ce-Mg-Mn system. This combination guarantees the accuracy of the obtained data. In this work, six solid-solid diffusion couples were prepared and studied. Among these couples, only #1, #3, #4 and #6 will be presented in details. Diffusion couples #2 and #5 will not be discussed, because diffusion couple #2 showed similar results to diffusion couple #1 and diffusion couple #5 confirmed the results obtained from other diffusion couples.

In the following section, the binary solid solution of Mg in γCe is represented as $(\gamma\mathrm{Ce})^{\mathrm{Mg}}$, and the extended solid solubility of Mg and Mn in γCe is represented as $(\gamma\mathrm{Ce})^{\mathrm{Mg,Mn}}$. Also, the details of the equilibrium information obtained from the samples used in the diffusion couples end-members are covered in the key alloys part (Section 4.2).

2.4.1. Diffusion couples

The SEM micrograph of diffusion couple #1 is presented in Figure 2-2 (a), (b) and (c). The first end-member was made from pure Mg. The second end-member was made from sample #2, containing three phases, $(\gamma\mathrm{Ce})^{\mathrm{Mg,Mn}}$, (CeMg) and Mn, as shown in Figure 2-2 (d). Six diffusion zones were observed after annealing at 723 K (450°C) for 8 days. EDS spot analysis was carried out to measure the composition of each zone. The EDS line-scan, shown in Figure 2-3, was performed across the diffusion zones of diffusion couple #1 to measure the homogeneity ranges of the different phases. The EDS spot analysis and line-scan results of diffusion couple #1 are summarized in Table 2-3. It can be seen from the composition of the phases of diffusion couple #1 that Mn was associated with every diffusion zone as a pure element. Mn was originally provided from sample #2 (end-member). During the annealing process, adjacent layers representing the Ce-Mg binary compounds started to form, due to the fast atomic interdiffusion between Ce and Mg atoms. Mn was filtered from the end-member alloy, because it did not react with the diffusing components. This could be an indication that Mn is in equilibrium with these phases. Thus, four two-phase equilibria namely, (CeMg_{12})+Mn, $\mathrm{Ce}_5\mathrm{Mg}_{41}$+Mn, (CeMg_3)+Mn and (CeMg)+Mn were observed within the diffusion layers of couple #1; whereas, three three-phase equilibria were found at the interfaces. These three-phase equilibria are, $(CeMg_{12})$+Mn+Ce_5Mg_{41}, Ce_5Mg_{41}+Mn+$(CeMg_3)$ and $(CeMg_3)$+Mn+(CeMg). The Ce-Mg binary phase diagram [50] showed CeMg as a stoichiometric compound. However, the ternary results showed (CeMg) as a solid solution with 2.5 at.% Mn (Table 2-3). Thus, (CeMg) was used to describe this extended solid solution.

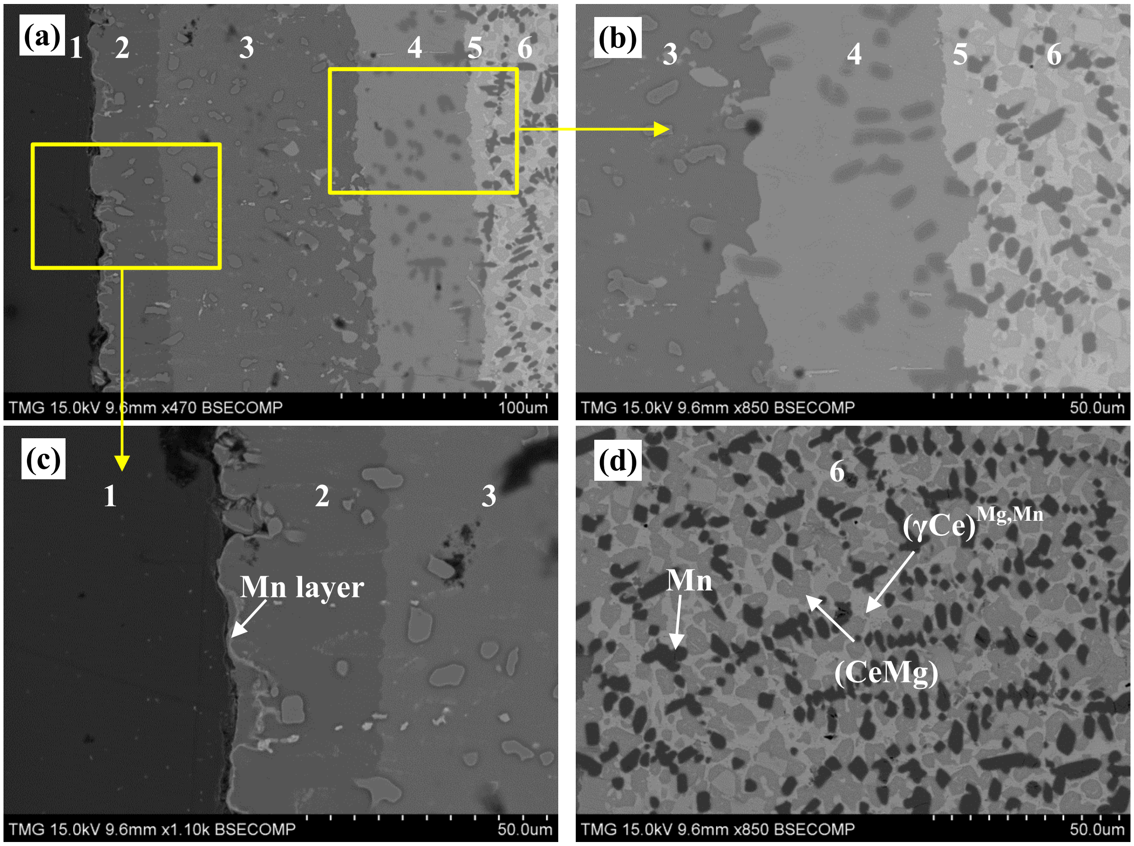

Figure 2-2: (a), (b) and (c) SEM micrographs of the diffusion zones of diffusion couple #1; (d) Microstructure of sample #2 (52.6Ce-19.8Mg-27.6Mn at.%). The numbers represent the diffusion zones and correspond to those in Figure 2-3 and Table 2-3

Table 2-3: Phases composition obtained by EDS spot analysis and line-scan of diffusion couple #1

Zone	Description	Composition (at.%)			Corresponding phase
		Ce	Mg	Mn	
1	Pure Mg (end-member)	0	100	0	Mg
2	Two-phase layer	8.5	91.5	0	$(CeMg_{12})$
		0	0	100	Mn
3	Three-phase layer	11.8	88.2	0	Ce_5Mg_{41}
		0	100	0	Mn
		24.6	74.7	< 2.0	$(CeMg_3)$
4	Two-phase layer	24.6-26.7	73.1-74.7	< 2.0	$(CeMg_3)$
		0	0	100	Mn
5	Two-phase layer	48.0	51.5	< 2.0	(CeMg)
		0	0	100	Mn
6	Three-phase alloy Sample #2 (end-member)	53.9	43.5	2.6	(CeMg)
		95.6	3.7	< 2.0	$(\gamma Ce)^{Mg,Mn}$
		0	0	100	Mn

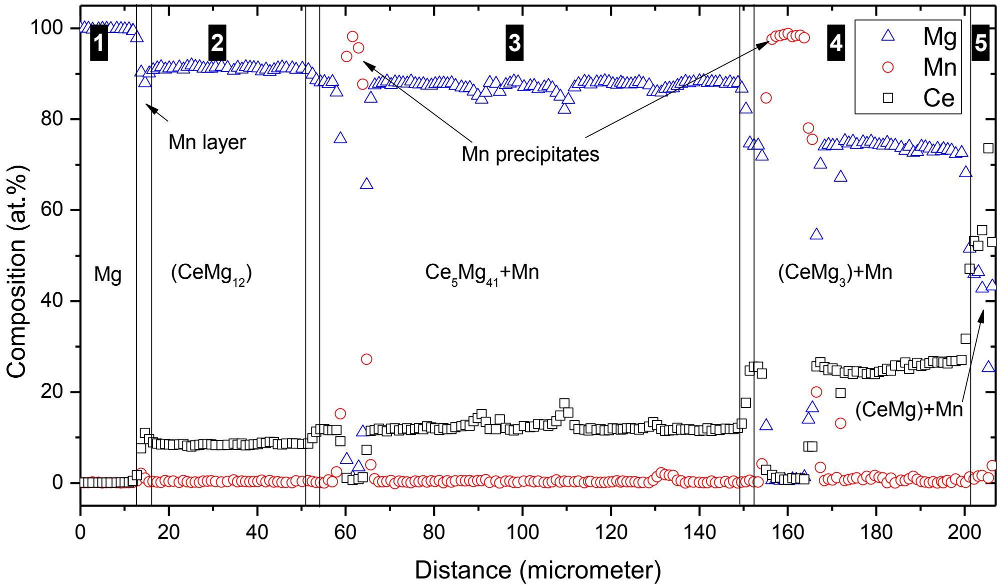

Figure 2-3: Composition profile obtained by EDS line-scan across diffusion zones of the diffusion couple #1

SEM micrographs of diffusion couple #1 showed that Mn was not contributing to the diffusion process, because Mn was localized in all diffusion zones as pure element.

Nevertheless, a continuous very thin layer of pure Mn was observed near the Mg end-member, as shown in Figure 2-2 (c). This layer indicates that Mn was also diffusing during the diffusion process. The diffusing Mn is in the form of small particles that most probably resulted from the dissolution of the $(\gamma Ce)^{Mg,Mn}$ solid solution present in the end-member. The existence of Mn layer between Mg and $(CeMg_{12})$+Mn two-phase field is necessary to fulfill the phase equilibrium. The Mn layer was not completely shown in the composition profile (Figure 2-3), because the layer thickness was much smaller than the spatial displacement of the point-to-point line-scan, which is ~1 µm in average.

Based on the microstructures of the diffusion zones and the composition profiles, the diffusion path can be depicted as follows: $(\gamma Ce)^{Mg,Mn}$+(CeMg)+Mn (end-member) → (CeMg)+Mn → $(CeMg_3)$+Mn+(CeMg) → $(CeMg_3)$+Mn → Ce_5Mg_{41}+Mn+$(CeMg_3)$ → Ce_5Mg_{41}+Mn → $(CeMg_{12})$+Mn+Ce_5Mg_{41}→ $(CeMg_{12})$+Mn → pure Mn → pure Mg (end-member). The arrows used here indicate the phase boundary lines and not a chemical reaction. The phase equilibria obtained from diffusion couple #1 are represented graphically in Figure 2-4. The two end-members of diffusion couple #1 are connected by a dashed line.

The shaded triangle in Figure 2-4 represents the three-phase equilibria of sample #2. Points 1, 3, 5 and 7 represent the two-phase equilibria between Mn and (CeMg), $(CeMg_3)$, Ce_5Mg_{41} and $(CeMg_{12})$, respectively; whereas points 2, 4 and 6 represent the three-phase equilibria (CeMg)+Mn+$(CeMg_3)$, $(CeMg_3)$+Mn+Ce_5Mg_{41} and Ce_5Mg_{41}+Mn+$(CeMg_{12})$, respectively.

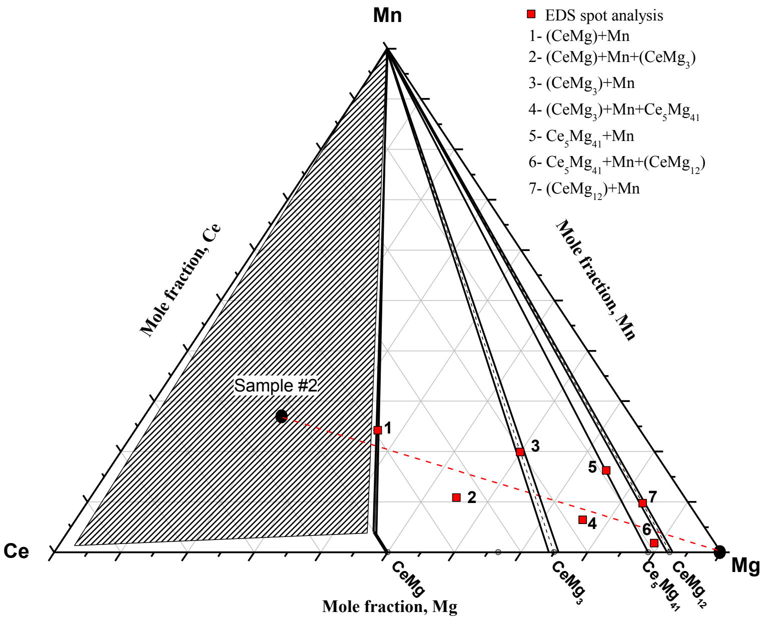

Figure 2-4: Phase equilibria depicted from diffusion couple #1

Diffusion couple #1 revealed the phase relationships from 0 to 50 at.% Ce in the Ce-Mg-Mn phase diagram at 723 K (450°C), which normally requires large number of key alloys to provide the same results. The results of diffusion couple #1 were confirmed by the results of diffusion couple #2, because the composition of their end-members is in close proximity.

The SEM micrograph of diffusion couple #3 is presented in Figure 2-5 (a). Figure 2-5 (b) shows the SEM micrograph of the end-member which was made from the ($CeMg_{12}$)+Mn two-phase alloy (sample #8). The other end-member was made from a block of pure Ce. After annealing and quenching, seven diffusion zones were observed. EDS line-scan was performed across the diffusion zones to determine the homogeneity ranges of the phases within the diffusion zones. The composition of the phases of each diffusion zone is given in Table 2-4.

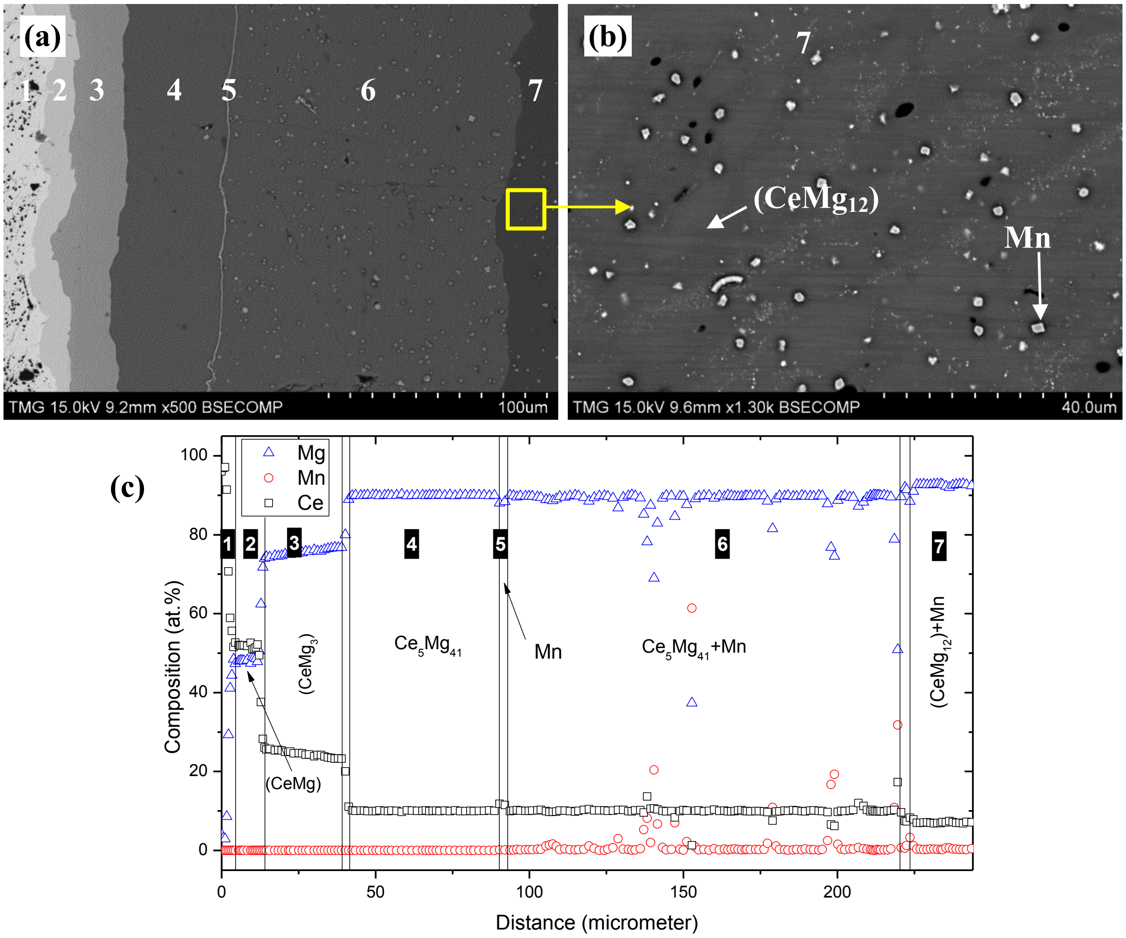

Figure 2-5: (a) SEM micrograph of diffusion couple #3; (b) SEM micrograph of sample #8; (c) EDS line-scan through the diffusion zones of diffusion couple #3. The numbers represent the diffusion zones and correspond to those in Table 2-4

Table 2-4: Phases composition obtained by EDS spot analysis and line-scan of diffusion couple #3

Zone	Description	Composition (at.%)			Corresponding phase
		Ce	Mg	Mn	
1	Pure Ce (end-member)	100	0	0	Ce
2	Single-phase layer	51.0-52.5	47.5-49.0	0	(CeMg)
3	Single-phase layer	23.3-25.6	74.4-76.7	0	($CeMg_3$)
4	Single-phase layer	10.9	89.1	0	Ce_5Mg_{41}
5	Single-phase layer	0	0	100	Mn
6	Two-phase layer	10.9 0	89.1 0	0 100	Ce_5Mg_{41} Mn
7	Two-phase alloy Sample #8 (end-member)	8.0 0	91.7 0	<1.0 100	($CeMg_{12}$) Mn

The ternary diffusion couple #3 behaved like Ce-Mg binary diffusion couple, where only binary phases formed until the end of zone #4. These phases, starting from Ce side, are: CeMg, $CeMg_3$ and Ce_5Mg_{41}. Ce_5Mg_{41} seems to be in equilibrium with Mn, since a continuous thin layer of pure Mn (zone #5), similar to that in diffusion couple #1, formed at the interface between zones #4 and #6 as shown in Figure 2-5 (a). Mn also appeared in larger quantity in zone #6 forming the Ce_5Mg_{41}+Mn two-phase region. The presence of Mn in equilibrium with ($CeMg_{12}$) solid solution, in zone #7, confirms the ($CeMg_{12}$)+Mn two-phase region in the ternary diagram in Figure 2-4.

Although Mn was detected as pure element in sample #8, traces of fine precipitates of Mn were observed in the ($CeMg_{12}$) solid solution matrix, as shown in Figure 2-5 (b). These precipitates might have resulted from the Mn-super saturated ($CeMg_{12}$) solid solution, where no more Mn could be dissolved. Thus, according to the phase equilibria in the diffusion couple #3, the diffusion path can be depicted as follows: Ce (end-member) → CeMg → $CeMg_3$ → Ce_5Mg_{41} → Mn → Ce_5Mg_{41}+Mn → ($CeMg_{12}$) +Mn (end-member).

The existence of the thin layer of pure Mn in diffusion couples #1 and 3 gives information about the location of the original interface between the two end-members. For instance, in diffusion couple #1, Mn atoms stopped diffusing at pure Mg end-member; also, no islands of pure Mn were seen on the left side of that thin layer. In diffusion couple #3, the pure Mn layer located in a position where Ce_5Mg_{41} formed on both sides. This leads to the conclusion that Ce_5Mg_{41} layer in zone #4 was formed due to the diffusion of Mg atoms from ($CeMg_{12}$)+Mn end-member towards Ce end-member.

Whereas, the Ce_5Mg_{41} layer in zone #6 was formed due to the diffusion of Ce from Ce end-member towards ($CeMg_{12}$)+Mn end-member.

In order to reveal the phase relations in the Ce-Mg-Mn phase diagram from 50 to 100 at.% Ce, diffusion couple #4, made from Ce-40 at.% Mg binary alloy and pure Mn end-members, was prepared. The 60Ce-40Mg (at.%) binary end-member contains two-phases, $(\gamma Ce)^{Mg}$ and CeMg. SEM micrograph of diffusion couple #4 is presented in Figure 2-6. After annealing at 723 K (450°C) for 10 days, five diffusion zones were observed. EDS spot analysis was carried out to measure the composition of each zone as listed in Table 2-5. EDS line-scan across the diffusion zones of diffusion couple #4, shown in Figure 2-7, was performed to reveal the homogeneity ranges of the binary and ternary solid solutions. According to the composition profile (Figure 2-7), diffusion zone #2 represents a MgCe layer that formed from the two-phase alloy ($(\gamma Ce)^{Mg}$ and MgCe in zone #1) due to the consumption of Ce, from the $(\gamma Ce)^{Mg}$, during the formation of zones #3 and 4. Diffusion zone #3 represents the $(\gamma Ce)^{Mg,Mn}$ solid solution with 3.8 at.% Mg and 5.1 at.% Mn. Diffusion zone #4 represents the $(\alpha\text{-}Mn)^{Ce}$ solid solution which contains 2.5 at.% Ce. Zone #5 represents the pure Mn end-member.

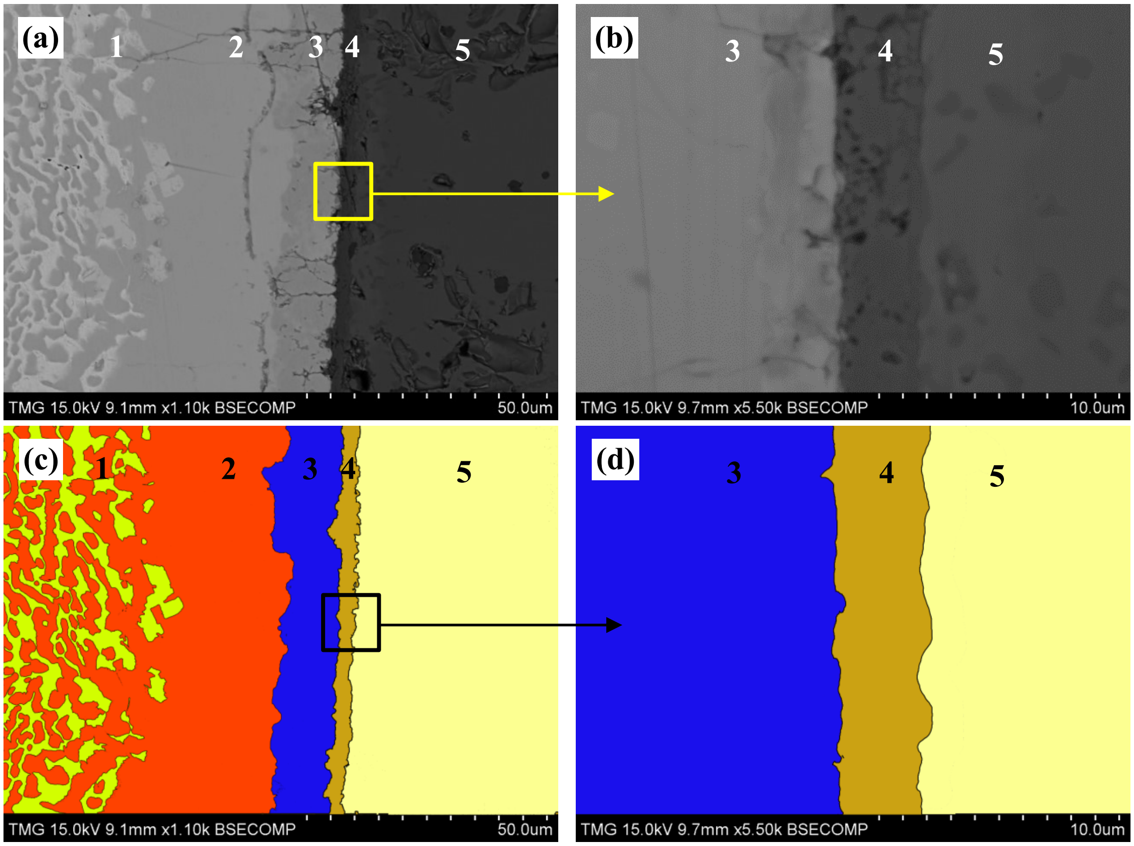

Figure 2-6: (a) and (b) SEM micrographs of diffusion couple #4; (c) and (d) their schematics. The numbers represent the diffusion zones and correspond to those in Figure 2-7 and Table 2-5. (For the color interpretation in this figure, it is recommended to refer to the web version of this article.)

Table 2-5: Phases composition obtained by EDS spot analysis and line-scan of diffusion couple #4

Zone	Description	Composition (at.%)			Corresponding phase
		Ce	Mg	Mn	
1	Two-phase alloy	51.5	48.5	0	CeMg
	(end-member)	94.0	6.0	0	$(\gamma\text{Ce})^{\text{Mg}}$
2	Single-phase layer	50.0-54.8	50.0-44.2	0	CeMg
3	Single-phase layer	95.3-98.7	<2.0-3.8	<2.0-5.1	$(\gamma\text{Ce})^{\text{Mg,Mn}}$
4	Single-phase layer	0-2.5	0	97.5-100	$(\alpha\text{Mn})^{\text{Ce}}$
5	Pure Mn (end-member)	0	0	100	Mn

Mn concentration was found to increase from <2.0 to 6.0 at.% towards the pure Mn end-member within diffusion zone #3. This increase was attributed to the exchange of Mn with the free Ce atoms released from the two-phase end-member. At the same time, the concentration of Mg dropped to <2.0 at.% at the interface with zone #4, and Ce was stabilized by dissolving small fractions of Mg and Mn to form $(\gamma\text{Ce})^{\text{Mg,Mn}}$. Some of the Ce diffused further into Mn end-member to form $(\alpha\text{Mn})^{\text{Ce}}$ binary solid solution with 2.5 at.% Ce. The amounts Ce and Mn in zones #3 and 4 were balanced by the formation of a wide CeMg diffusion layer in zone #2, which relatively contains higher Mg content. Hence, the rule of mass balance in diffusion couple #4 was fulfilled, because the diffusion path intersected the connecting line between the two end-members at least once as shown in Figure 2-8.

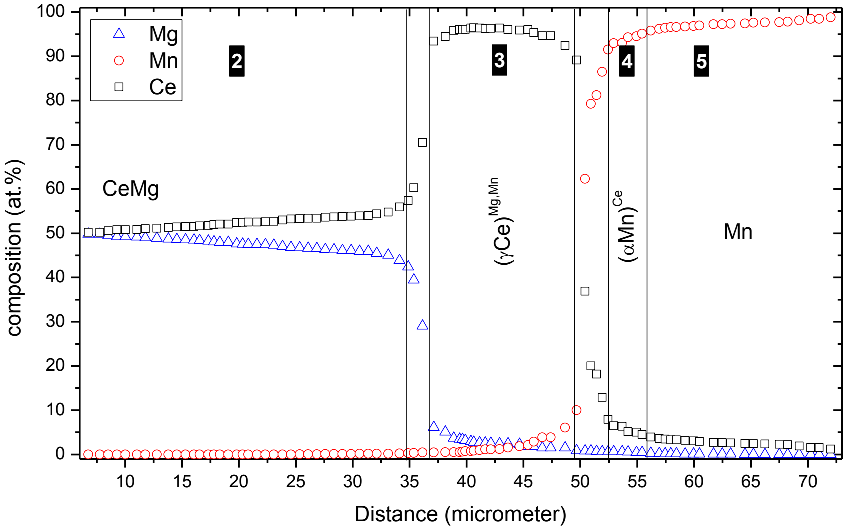

Figure 2-7: Composition profile across the diffusion couple #4

According to the EDS spot analysis and line-scan across the diffusion zones, the phase equilibria depicted from diffusion couple #4 are shown in Figure 2-8.

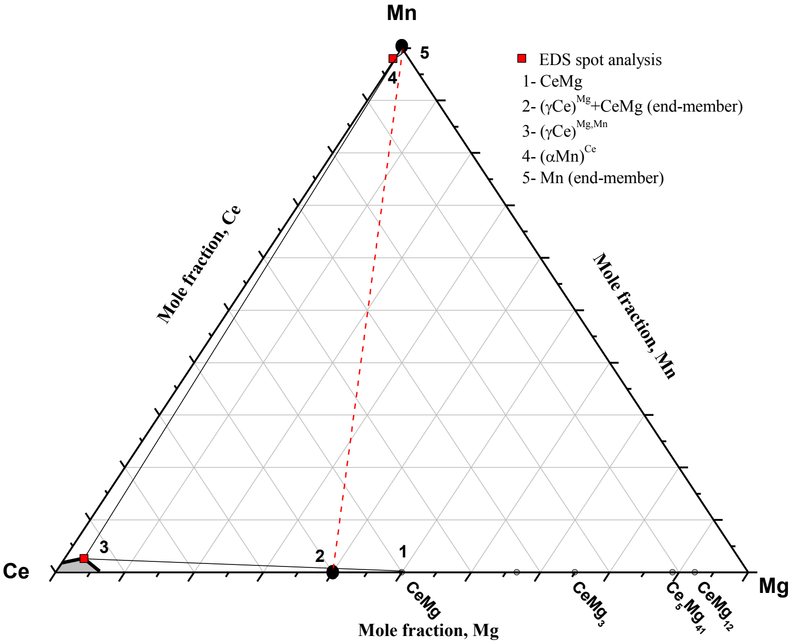

Figure 2-8: Phase equilibria depicted from diffusion couple #4

Diffusion couple #6 was prepared to investigate the phase relationships in the middle part of the Ce-Mg-Mn phase diagram. The first end-member was made from sample #10 ((CeMg)+Mn) and the second end-member was made from sample #9 ((CeMg$_3$)+Mn+Ce$_5$Mg$_{41}$), as shown in Figure 2-10. Diffusion couple #6 was annealed at 723 K (450°C) for 4 days. The SEM micrograph in Figure 2-9 (a) shows the three diffusion zones of diffusion couple #6. These zones are two end-members (zone #1 and zone #3) and one ~116μm thick diffusion layer (zone #2). EDS spot analysis was carried out to measure the phase composition of each zone as given in Table 2-6. EDS line-scan across the diffusion zones was performed to measure the composition profile shown in Figure 2-9 (b). The composition profile shows the Mg/Mn atomic exchange at constant composition of Ce in the (CeMg)+Mn phase field (zone #1). The maximum solubility of Mn was measured to be 4.8 at.% in (CeMg) solid solution.

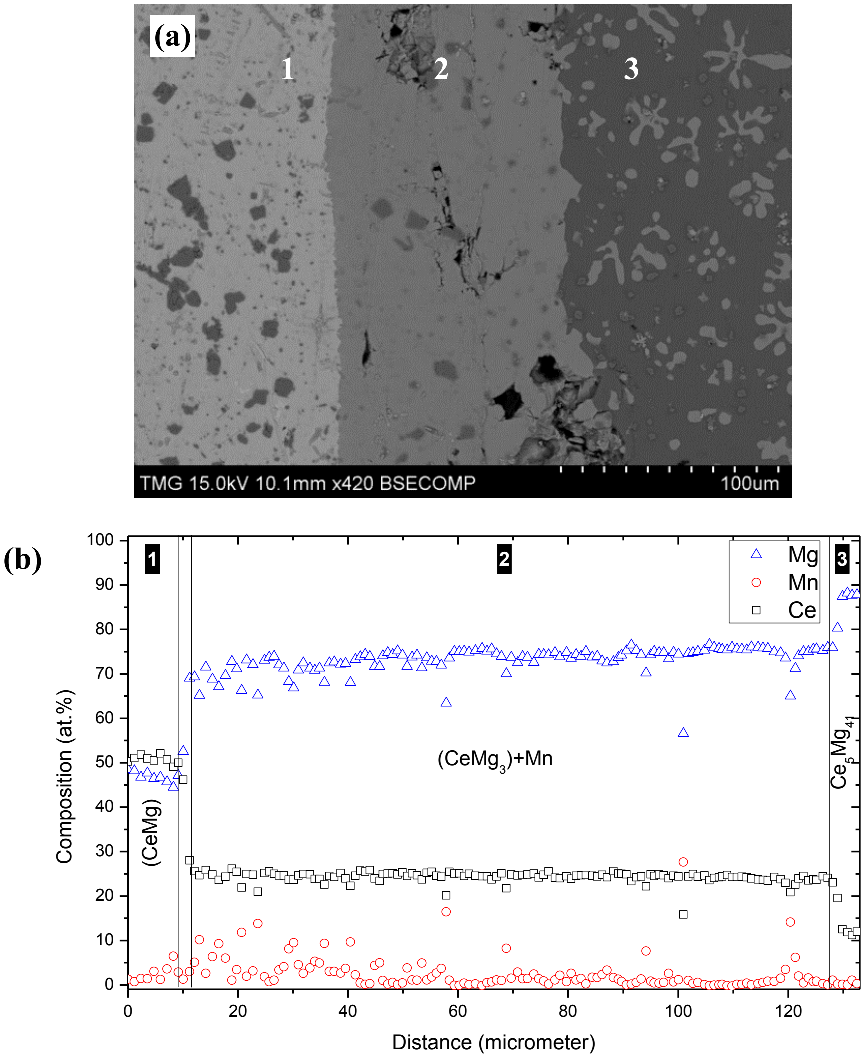

Figure 2-9: (a) SEM micrograph of diffusion couple #6; (b) composition profile across the diffusion couple #6. The numbers represent the diffusion zones and correspond to those in Table 2-6

Table 2-6: Phases composition obtained by EDS spot analysis and line-scan of diffusion couple #6

Zone	Description	Composition (at.%)			Corresponding phase
		Ce	Mg	Mn	
1	Two-phase alloy (end-member)	50.6 0	46.4 0	2.8 100	(CeMg) Mn
2	Two-phase layer	25 0	73.1-75 0	< 2.0 100	$(CeMg_3)$ Mn
3	Three-phase alloy (end-member)	24.0 11.6 0	75.7 88.4 0	0.3 0 100	$(CeMg_3)$ Ce_5Mg_{41} Mn

The line-scan was selected to cut across all possible features in the diffusion zones shown in the micrograph in Figure 2-9 (a). Therefore, the composition profile shows a general concentration trend of each element. The data obtained from the line-scan across zone #2 was noisy (Figure 2-9 (b)). The source of this noise was from the change of average composition measurements in the ($CeMg_3$) solid solution matrix, where the Mn particles exist. The diffusion path of couple #6 can be depicted as: (CeMg)+Mn (end-member) → ($CeMg_3$)+Mn → ($CeMg_3$)+Mn+Ce_5Mg_{41} (end-member). Figure 2-10 shows a graphical representation of the phase equilibria obtained from this diffusion couple.

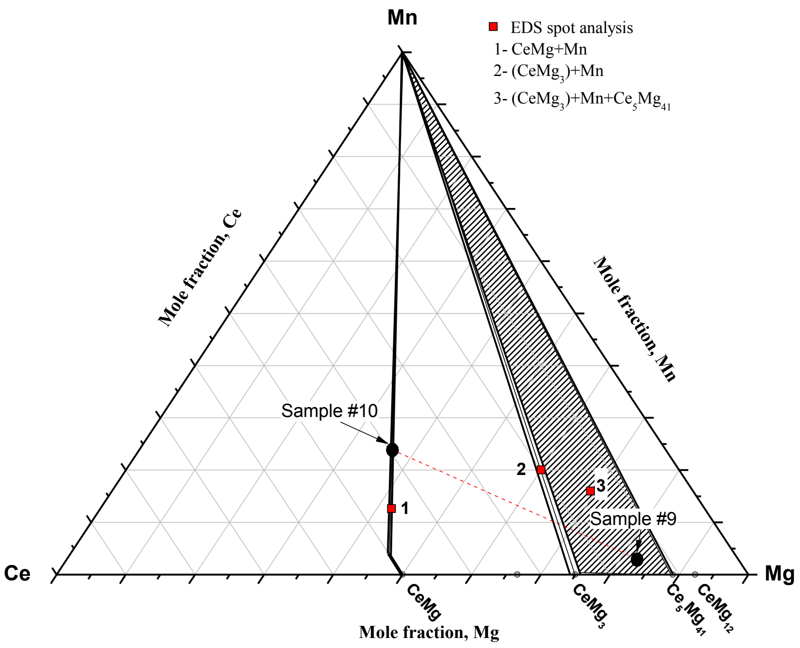

Figure 2-10: Phase equilibria depicted from diffusion couple #6

The phase relationships, concluded from the phase equilibria obtained from the diffusion couple experiments, are summarized in Figure 2-11. The numbers 1 to 11 in this figure are used to label the phase regions determined by diffusion couples. The ranges of different solid solutions will be determined more accurately by combining the diffusion couples with the key alloys results.

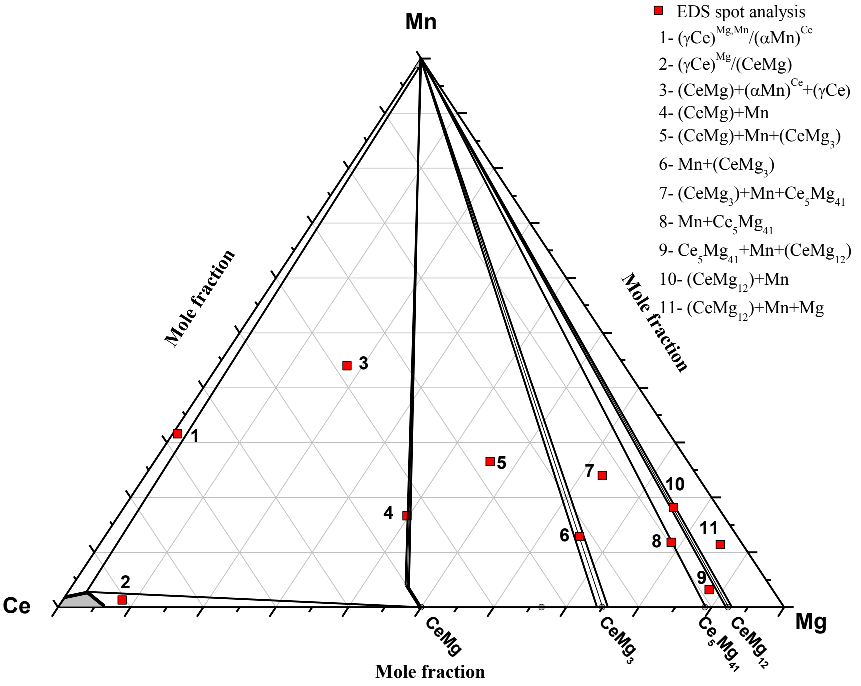

Figure 2-11: Phase equilibria determined from diffusion couple studies

2.4.2. Key alloys

Diffusion couple experiments are not always successful. It is possible to miss some phases due to the slow kinetics of solid-solid reactions [16, 20, 59]. Therefore, key alloy experiments are designed to verify the experimental results obtained from the diffusion couples. Twelve key alloys were prepared with different compositions to verify the phase relationships obtained by the diffusion couples study. Alloys were brought to equilibrium after annealing at 723 K (450°C) for different periods of time. The actual compositions of the alloys obtained from ICP along with the XRD and EDS results are listed in Table 2-7. EDS spot analysis was performed on the annealed samples to determine the composition of the observed phases. SEM micrographs for selected alloys are presented in Figure 2-12. XRD was performed to identify the equilibrated phases and to verify the phase relations obtained from EDS analysis. The XRD patterns of selected alloys in different regions of the Ce-Mg-Mn system (samples #1, 2, 3 and 9) are shown in Figure 2-13.

Table 2-7: Actual sample compositions and their XRD and EDS results

Sample	ICP results (at.%)			XRD	EDS	EDS analysis (at.%)		
number	Ce	Mg	Mn	results	results	Ce	Mg	Mn
1	54.7	1.8	43.5	Ce	$(\gamma Ce)^{Mg,Mn}$	96.2	2.6	< 2.0
				Mn	$(\alpha Mn)^{Ce}$	< 2.0	0	98.8
2	52.6	19.8	27.6	(CeMg)	(CeMg)	53.9	43.5	2.6
				Ce	$(\gamma Ce)^{Mg,Mn}$	95.6	3.7	< 2.0
				Mn	Mn	0	0	100.0
3*	34.7	38.1	27.2	Mn	Mn	0	0	100.0
4*	40.5	51.0	8.5	(CeMg)	(CeMg)	52.3	44.5	3.2
5*	32.2	53.4	15.4	$(CeMg_3)$	$(CeMg_3)$	25.8	71.3	3.9
6	23.6	72.4	4.0	-	Mn	< 1.0	< 1.0	98.52
				-	$(CeMg_3)$	23.5	72.8	3.7
7	9.8	82.6	7.6	-	Mn	0	0	100.0
				-	Ce_5Mg_{41}	11.5	88.3	< 1.0
8	7.0	87.4	5.6	Mn	Mn	0	0	100
				$CeMg_{12}$	$(CeMg_{12})$	8.0	92.0	0
9	14.5	82.7	2.8	Mn	Mn	0	0	100.0
				Ce_5Mg_{41}	Ce_5Mg_{41}	11.6	88.1	< 1.0
				$(CeMg_3)$	$(CeMg_3)$	23.8	75.8	< 1.0
10	40.6	35.2	24.2	-	Mn	0	0	100
				-	(CeMg)	50.6	46.4	2.8
11**	43.9	52.5	3.6	$(CeMg_3)$	$(CeMg_3)$	26.4	71.5	2.1
12**	41.2	57.2	1.6	(CeMg)	(CeMg)	52.0	47.2	< 1.0

* Samples #3, 4 and 5 fall in the same three-phase region

** Samples #11 and 12 fall in the same two-phase region

Figure 2-12 (a) shows the SEM micrograph of sample #1, which contains two-phase equilibrium between $(\gamma Ce)^{Mg,Mn}$ ternary solid solution (white phase) and $(\alpha Mn)^{Ce}$ binary solid solution (dark phase). Based on EDS spot analysis, the binary solid solubility of Ce in Mn was measured as <2.0 at.% Ce; whereas, the ternary solid solution in the Ce-rich corner contains 2.63 at.% Mg and 1.14 at.% Mn. Sample #2 was used as an end-member for diffusion couple #1 as shown in Figure 2-2 (d). The three-phase equilibrium was explained in section 4.1. Figure 2-12 (b) shows the three-phase equilibrium; Mn+(CeMg) +($CeMg_3$), of sample #3. The binary phase ($CeMg_2$) was not detected in any of the diffusion couples at 723 K (450°C). Nevertheless, it was observed as metastable phase in sample #3. Two additional alloys (samples #4 and #5) were prepared in the same triangulation to confirm the results obtained from sample #3. Figure 2-14 shows the two equilibrated phases of sample #12. It was concluded that $CeMg_2$ decomposed eutectoidally to form (CeMg) and ($CeMg_3$) phases. Figure 2-14 will be discussed in details below.

Figure 2-12 (c) shows the two-phase equilibrium between ($CeMg_3$) and Mn in sample #6. The matrix phase contains ($CeMg_3$) ternary solid solution with maximum Mn solubility of 2.5 at.%. Very fine Mn precipitates were observed in the ($CeMg_3$) matrix indicating Mn super-saturation. Samples #7 and #8 verified the two-phase equilibrium Ce_5Mg_{41}+Mn and ($CeMg_{12}$)+Mn, respectively. The microstructure of sample #8 is shown in Figure 2-5 (b). Three-phase equilibria of sample #9 are shown in Figure 2-12 (d). This alloy was used as an end-member for diffusion couple #6 and discussed in details in section 4.1. Sample #10, Figure 2-12 (e), was also used in diffusion couple #4, and the phase equilibria were clearly explained in section 4.1. Samples #11 and #12 were used to confirm the two-phase equilibrium of (CeMg) and ($CeMg_3$). Sample #11, Figure 2-12 (f), shows the eutectoid morphology of (CeMg)+($CeMg_3$) which resulted from the $CeMg_2$

phase decomposition. The morphologies observed in sample #11 were the same as those of sample #12.

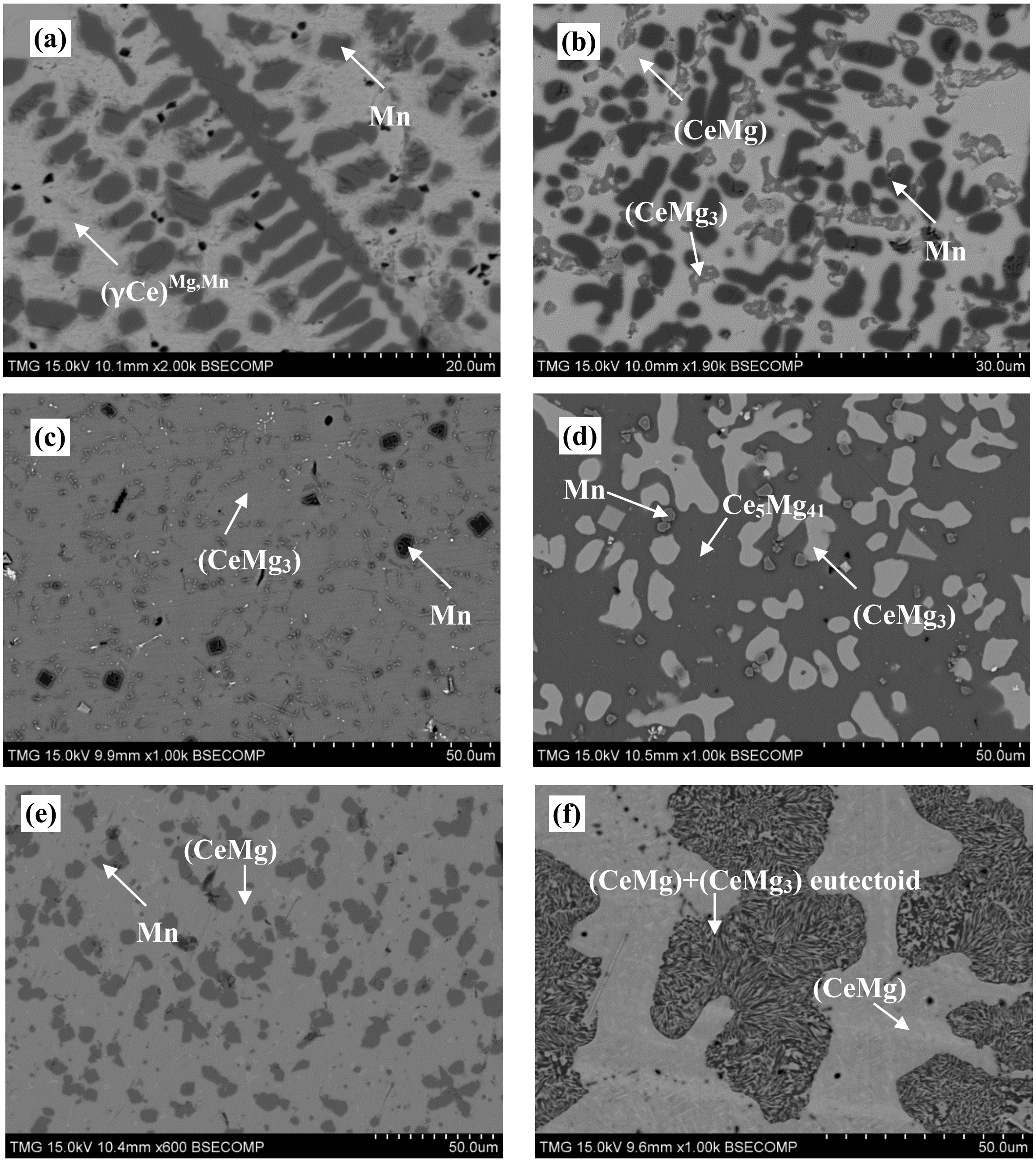

Figure 2-12: SEM micrograph of (a) sample #1; (b) sample #3; (c) sample #6; (d) sample #9; (e) sample #10; (f) sample #11

To confirm the results observed by EDS, XRD was used to identify the phases present in the key alloys. The diffusion couples and key alloys showed that Mn is in equilibrium with all phases in the system. This was also confirmed by XRD analysis, where Mn peaks appeared in the diffraction patterns of the analyzed samples, as shown in Figure 2-13.

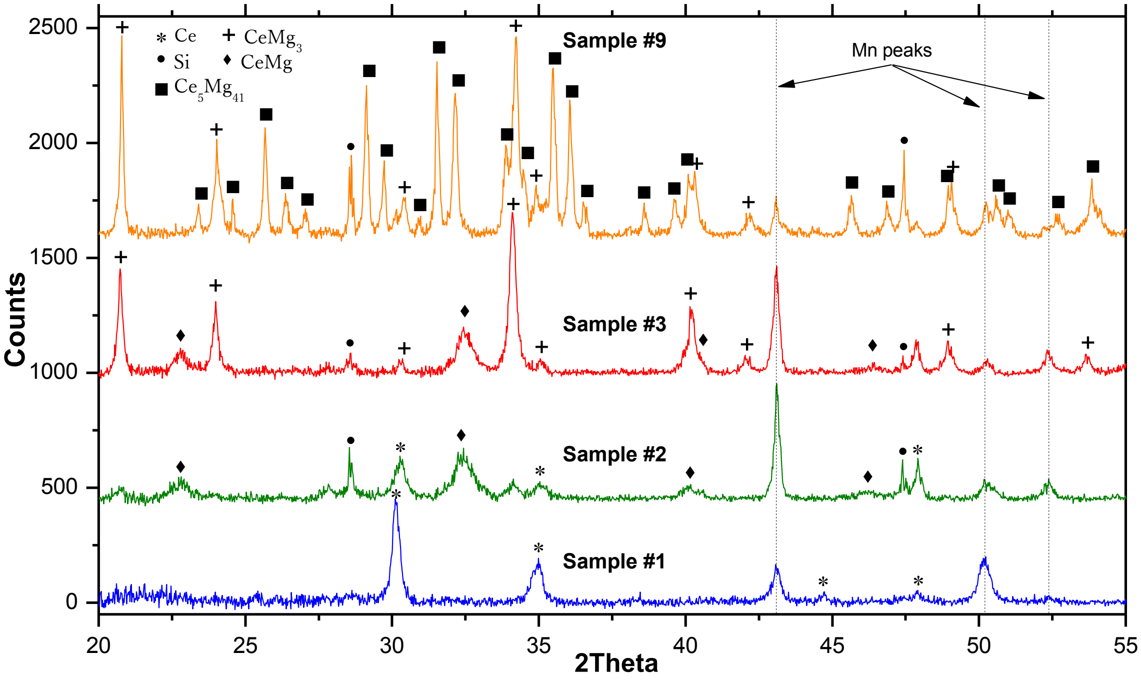

Figure 2-13: XRD patterns of samples #1, 2, 3 and 9 selected from different regions of the Ce-Mg-Mn system

As mentioned earlier, the eutectoidal decomposition of $CeMg_2$ into (CeMg)+(Mg_3Nd) was observed in the microstructures of samples #3, 4, 5, 11 and 12. The decomposition mechanism was inferred from Figure 2-14 (a) and (b). Figure 2-14 (a) shows the as-cast microstructure of sample #12. The EDS spot analysis gave the composition of the two phases as $CeMg_2$ and (CeMg). However, from the Ce-Mg binary phase diagram (Figure 2-1), it can be seen that the thermal stability range of $CeMg_2$ phase falls between 888 K (615°C) and 984 K (711°C), while the annealing was performed at

723 K (450°C). This means that $CeMg_2$ should not be observed in the equilibrated samples at 723 K (450°C). Therefore, further annealing was performed for sample #12. Figure 2-14 (b) shows the microstructure of sample #12 after annealing at 723 K (450°C) for 27 days having typical eutectoid structure. Based on the Ce-Mg binary phase diagram (Figure 2-1), besides the eutectoid structure, it is expected to have the primary solidified (CeMg). Figure 2-14 (b) proves that this is what happened after annealing at 723 K (450°C) for 27 days. However, due to the fine eutectoid structure, EDS was not accurate enough to obtain the phase composition of its microconstituents. Thus, XRD was carried out to identify the phases present in the as-cast and annealed conditions.

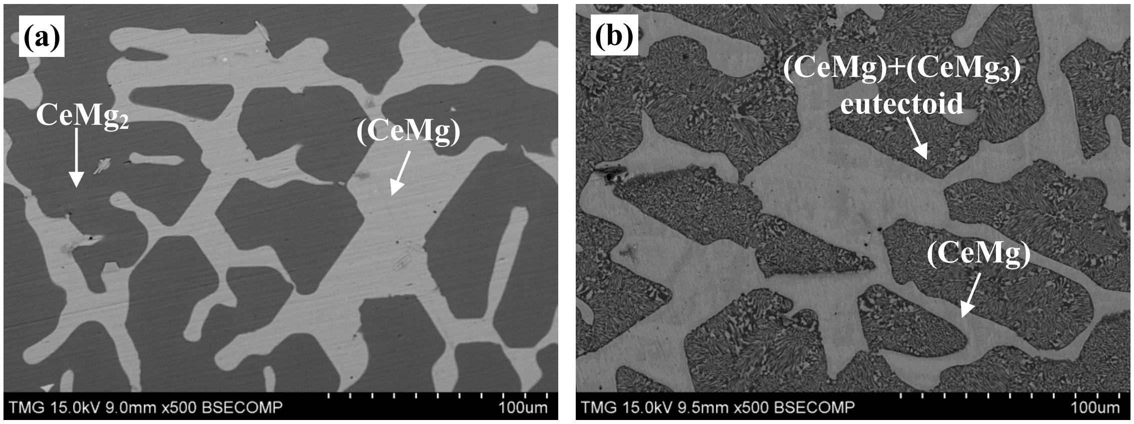

Figure 2-14: SEM micrographs of sample #12 (a) in the as-cast condition; (b) annealed for 27 days

The as-cast and annealed XRD patterns of sample #12 are shown in Figure 2-15. The XRD pattern of the as-cast sample #12 showed the presence of $CeMg_2$ along with (CeMg). After annealing for 27 days, the XRD pattern of the same sample showed (CeMg) and ($CeMg_3$) only. No peaks of $CeMg_2$ were detected. This ascertains that the eutectoidal decomposition of $CeMg_2$ led to the formation of (CeMg) and ($CeMg_3$). This also provides additional evidence of the presence of the (CeMg)+($CeMg_3$) phase equilibrium in the Ce-Mg-Mn isothermal section at 723 K (450°C).

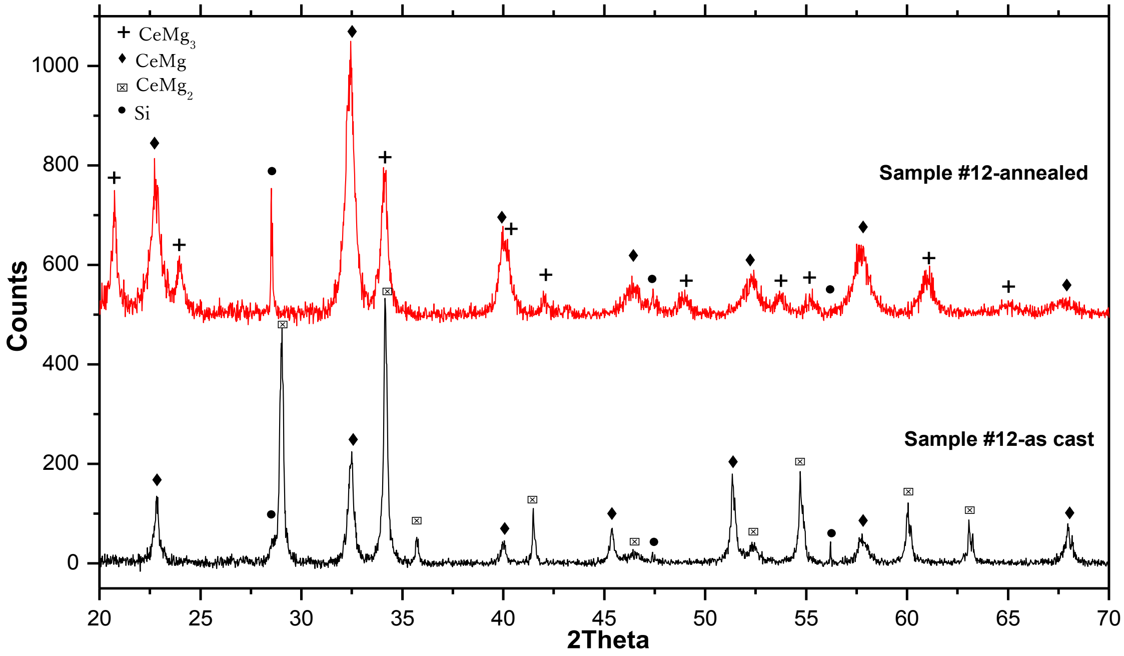

Figure 2-15: The as-cast and annealed XRD patterns of sample #12

The phase boundaries obtained from the studied key alloys are consistent with those obtained from the diffusion couples technique. These results were combined to establish the Ce-Mg-Mn isothermal section at 723 K (450°C) as described in the following section.

2.4.3. Ce-Mg-Mn isothermal section at 723 K (450°C)

The isothermal section of the Ce-Mg-Mn system at 723 K (450°C), constructed based on the results obtained from the diffusion couples and the equilibrated samples, is shown in Figure 2-16. The key alloys at the actual composition were shown as solid circles. The arrows indicate the phases obtained from XRD and EDS spot analysis for each alloy.

The (CeMg)+Mn two-phase field was constructed based on the EDS analysis, where Mn showed solid solubility in CeMg up to 5 at.%. The homogeneity range of the $CeMg_3$ binary solid solution was determined at 723 K (450°C), in the current work, using diffusion couple #3 as can be seen in Figure 2-5. The composition profile across the binary diffusion layers, shown in Figure 2-5 (b), showed that the composition of Mg changed from 74.5 to 76.7 at.% Mg. Accordingly, the binary homogeneity range of ($CeMg_3$) was determined. The ternary solubility of Mn in ($CeMg_3$) was determined as 3.2 at.% Mn by the diffusion couples and key alloys. Thus, the ($CeMg_3$)+Mn two-phase filed was confirmed. The homogeneity range of the ($CeMg_{12}$) binary compound at 450°C is taken from the Ce-Mg binary phase diagram [50] as 0.8 at.% Mg. This small solubility could not be accurately determined by the EDS in the current work due to the relatively high error limits of Ce (around ±1.5 at.%).

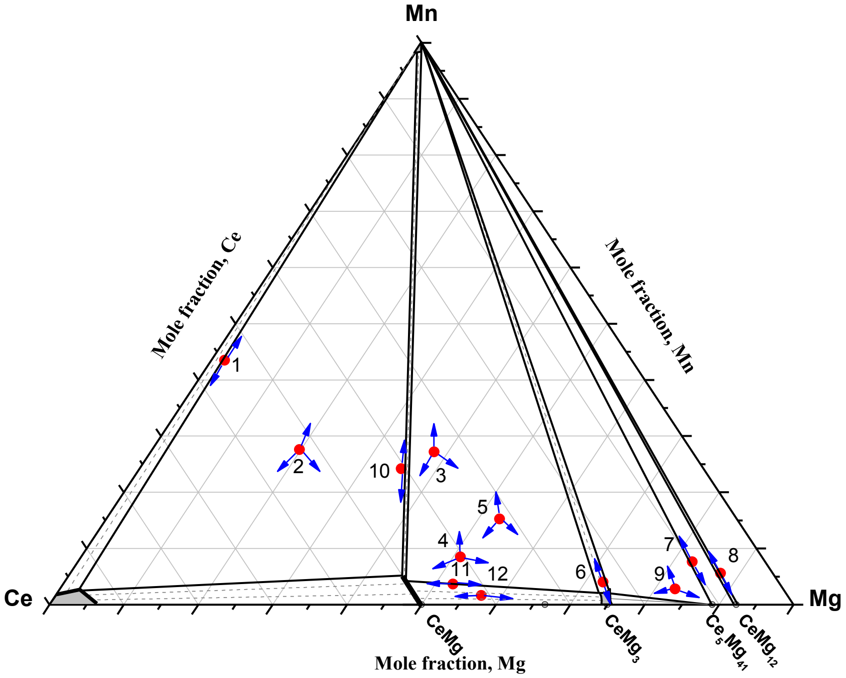

Figure 2-16: Phase relationships inferred from phase equilibria and diffusion paths analysis

The Ce-Mg-Mn system shows unique phase relationships, where Mn is in equilibrium with all phases in the system. Because Mn has no tendency to form intermetallic compounds with Ce and Mg, it was always observed as either dissolved in the Ce-Mg compounds or as pure element in all microstructures. Therefore, the phase boundary lines are pointing towards the Mn-rich corner.

2.5. Conclusions

The isothermal section of the Ce-Mg-Mn phase diagram at 723 K (450°C) was constructed for the full composition range. The phase relationships were determined using 6 solid-solid diffusion couples and 12 key alloys. No ternary compounds were detected in the studied system at 723 K (450°C). Diffusion couple experiments were instrumental in revealing the phase equilibria in this system. However, diffusion couples are not always successful due to the possible missing of some of the phases due their slow kinetics. Therefore, key alloys are essential to complement the diffusion couples. Key alloy experiments were designed to verify the results obtained from the diffusion couples and both results were found to be consistent.

Based on the accepted Ce-Mg binary phase diagram the thermal stability range of $CeMg_2$ phase is between 888 K (615°C) and 984 K (711°C), while annealing in this work was performed at 723 K (450°C). Thus, $CeMg_2$ is not a stable phase in the Ce-Mg-Mn isothermal section at 723 K (450°C). This was confirmed by SEM/EDS, XRD and metallographic studies.

Many two-phase regions, composed mainly of Mn and other phase, were observed in the microstructure of each zone. This confirms that Mn was not reacting, and the Mn source was from the ternary alloy end-members. However, the existence of a continuous thin layer of Mn in diffusion couples #1 and 3 indicates that Mn is diffusing.

2.6. Acknowledgement

This research was supported by funding from the Magnesium Strategic Research Network (MagNET). More information on the Network can be found at www.MagNET.ubc.ca. The authors would like to acknowledge Mr. Bolarinwa Komolafe from Concordia University for improving the English language.

2.7. Author's notes and significance of paper to thesis

In this chapter, the phase relationships of the Ce-Mg-Mn system were determined at 450°C by means of diffusion couples and equilibrated key alloys. The diffusion couple technique showed great efficiency in determining the phase equilibrium in this system from different perspectives. Firstly, the diffusion couple technique was used to overcome the problem associated with alloys preparation. These are: (a) significant evaporation of Mg when it is alloyed with Ce and Mn, both having relatively high melting temperature, and (b) the problem of inhomogeneous structures, which arises from the inability of Mn to form intermetallic compounds with Ce and Mg. Secondly, diffusion couples could cover large compositional ranges in the ternary isotherm by forming several diffusion zones. Thirdly, they can describe the diffusion behavior of the diffusing species. For instance, based on the microstructures of the diffusion zones, it was concluded that the affinity of Ce to Mg was higher than that of Ce and Mg to Mn. This can be referred to the ability of Ce and Mg to form intermetallic compounds; whereas, Mn is not able to form any with either Ce or Mg.

The formation of a continuous pure Mn thin layer and several ternary solid solutions are evidences of Mn diffusion. Nevertheless, the microstructures of diffusion zones and key alloys showed Mn as stationary phase islanding within matrices of Ce-Mg compounds. The formation of the Mn thin layer was essential to fulfill the phase equilibrium between Mg and Mn.

In order to study the effect of different RE additions on the Mg-Mn system, Ce was replaced by Nd. The next chapter presents the Mg-Mn-Nd isothermal section at 450°C. The knowledge gained through the study of the Ce-Mg-Mn system is essential for understanding the phase relationships in the Mg-Mn-Nd system.

Chapter 3 : Experimental investigation of the Mg-Mn-Nd isothermal section at 450°C

ABSTRACT

The Mg-Mn-Nd isothermal section at 450°C was constructed experimentally using solid-solid diffusion couples and key alloys. Diffusion couples and key alloys were annealed at the same temperature for different annealing time periods to understand the diffusion behavior of the system components, and to achieve the phase equilibrium in the system. The phase relations and solubility limits were determined using scanning electron microscope coupled with wave/energy dispersive X-ray spectrometers, X-ray diffraction and metallography. No ternary compounds could be observed in this system at 450°C. The microstructures of the diffusion zones showed Mn either as a pure element or as a solute atom. However, microstructures of the annealed key alloys near the Mn-rich side showed the formation of $Mn_{17}Nd_2$ at 450°C. Other Mn binary compounds, Mn_2Nd and $Mn_{23}Nd_6$, were observed only in the as-cast alloys, because they are not stable at 450°C. The experiments showed that Mn remained stationary in some diffusion zones forming Mn+(MgNd), Mn+(Mg_3Nd) and Mn+$Mg_{41}Nd_5$ two-phase regions. However, some of Mn atoms were diffusing in the system forming a continuous thin layer of pure Mn at the interface of pure Mg end-member, or to form $(\alpha\text{-Nd})^{Mg,Mn}$, (MgNd) and ($Mg_3Nd$) ternary solid solutions. The solubility of Mn in these solutions was estimated as 3.0, 13.0 and 3.5 at.% Mn, respectively. Since Mn is in equilibrium with most of the phases in the system, the phase boundary lines are pointing towards Mn-rich corner except that of $(\alpha\text{-Nd})^{Mg,Mn}$+(MgNd)+$Mn_{17}Nd_2$ three-phase field. This was confirmed based on the consistency of the results obtained from diffusion couples and key alloys.

3.1. Introduction

Magnesium and its alloys show an increasing commercial importance in automotive and electronic consumer products because of many advantages. Their light-weight, high specific toughness and rigidity, good machinability, castability and weldability using commonly known techniques, made them attractive for the use in industry [60]. In terms of structural properties, pure Mg is not suitable for direct commercial use. The liquid of pure Mg, however, is used to extract neodymium from solid FeNdB magnet scrap materials [61]. It was found that addition of Nd to Mg alloys improves their strength, ductility, toughness, weldability and machinability [11, 12, 30]. This is attributed to grain refinement and the formation of secondary phase precipitates at the grain boundary regions. On the other hand, addition of Mn improves the hot and cold strengths, resistance to corrosion and formability compared with the pure Mg [62]. This is due to high reactivity of Mn with other elements such as Fe [63], which leads to form a complex sequence of intermediate compounds [64]. Thus, it is necessary to understand the phase equilibria in the Mg-Mn-Nd system; which is essential for alloy design and development.

3.2. Literature review

3.2.1. The Mg-Mn binary system

The Mg-Mn system has been thoroughly studied [39-42]. According to these authors, no intermediate compound exists between Mg and Mn terminal sides. The maximum solubility of Mn in solid Mg was found to be 0.998 at.% Mn at the peritectic temperature, just below 650°C. Another invariant reaction of monotectic type $L_1 \rightarrow L_2+\delta$-Mn, takes place at 96 at.% Mn and 1198°C [41, 42]. Because of the difficulty of measuring the temperature of the liquid miscibility gap experimentally, attempts to estimate that temperature were carried out using thermodynamic calculations [38, 42, 43]. The calculated temperature of the liquid miscibility gap was reported as 3202°C [42], 1902°C [65] and 3415°C [43]. The temperature is significantly lower in the work of [65]. They adjusted the Mg-Mn binary model parameters to obtain consistency for the extrapolated Mg-Mn-Y ternary system.

3.2.2. The Mg-Nd binary system

According to Nayeb-Hashemi and Clark [66], who assessed the Mg-Nd phase diagram based on the literature data, five intermetallic compounds, MgNd, Mg_2Nd, Mg_3Nd, $Mg_{41}Nd_5$ and $Mg_{12}Nd$, along with the terminal solid solutions of Nd in Mg, Mg in α-Nd and Mg in β-Nd, were reported. The $Mg_{12}Nd$ compound was considered metastable, since it was observed in the samples quenched directly from liquid and not after annealing [67]. Three eutectic reactions were observed at 42.5 at.% Mg and 775°C, 64.5 at.% Mg and 750°C and 91 at.% Mg and 546°C. The terminal solubility of Mg in solid α-Nd was estimated as 8.2 at.% Mg [68] and in β-Nd as 34 at.% Mg [67] at 551°C and 775°C, respectively. Whereas, the terminal solubility of Nd in solid Mg was determined as 0.1 at.% Nd [69, 70]. Moreover, the two congruently melting compounds, MgNd and Mg_3Nd have solid solubility ranges. The solid solubility range of Mg_3Nd was estimated as 6 at.% extending towards the Mg-rich side [67]. The solid solubility range of MgNd was not determined quantitatively, its existence was proposed by Delfino *et al.*

[67] based on the change in the lattice parameters. Mg_2Nd phase was suggested to appear as a Laves phase with narrow stability range between ~660 and 755°C [71].

3.2.3. The Mn-Nd binary system

Many contradictory information on the Mn-Nd system were found in the literature [64, 72, 73]. Thus, three different versions of Mn-Nd phase diagram are available in the literature. To overcome these uncertainties, a self-consistent Mn-Nd phase diagram was reconstructed based on combination of experiments, CALPHAD methodology and first-principle calculations by our group [74]. A eutectic was found to occur at 27 at.% Mn and 685°C. Three incongruent intermetallic compounds, Mn_2Nd, $Mn_{23}Nd_6$ and $Mn_{17}Nd_2$, were reported at 850, 940 and 1025°C, respectively. The compounds Mn_2Nd and $Mn_{23}Nd_6$ were found to decompose eutectoidally in the temperature ranges of 550-650°C and 400-550°C, respectively. The maximum solid solubility of Mn in α-Nd at the eutectic temperature was estimated as 2.3 at.% Mn based on EPMA results. However, the solubility of Mn in β-Nd was determined as 5.0 at.% Mn by extrapolating the DSC points to 728°C. No solid solubility of Nd in Mn was detected.

3.2.4. The Mg-Mn-Nd ternary system

The system was first assessed by Drits *et al.* [75] using thermal analysis, microscopic investigation, and electrical resistivity measurements. The study was limited to the Mg-rich corner up to 4 wt.% Mn and 10 wt.% Nd to determine the boundaries of the solid solution region (by rapid quenching and annealing at 570°C, 600°C, and 630°C). Based on the resistivity measurements, they [75] reported a peritectic reaction $L+Mn \leftrightarrow \alpha+Mg_9Nd$ at 559.6°C. Also, they found that Mn and Mg_9Nd are in equilibrium with Mg solid solution. The compound Mg_9Nd was later given the formula $Mg_{41}Nd_5$ with *tI92*-Ce_5Mg_{41} type structure [67]. The results obtained by Drits *et al.* [75] were used later by Drits and Bochvar [76] to investigate the Mg-Mn-Nd-Ni quaternary alloys.

Very limited experimental information on the Mg-Mn-Nd ternary phase diagram could be found in the literature. The available study [75] covered the Mg-rich corner only and focused on finding the solid solubility ranges of Mn and Nd in Mg. The main objective of the present work is to construct the isothermal section of Mg-Mn-Nd phase diagram at 450°C experimentally for the whole composition range by means of solid-solid diffusion couples and key alloys using XRD, SEM/WDS and metallography.

3.3. Experimental procedure

The samples for diffusion couples and key alloys were prepared from pure metals. Mn-99.90 wt.% and Nd-99.95 wt.% purity were supplied by Alpha Aesar®, Johnson Matthey Company, Inc. Mg-99.8 wt.% purity was supplied by CANMET Materials Technology Laboratory (CANMET-MTL). Samples of 4-5g in weight were prepared in an arc-melting furnace with water-cooled copper crucible and non-consumable tungsten electrode under argon. Excess Mg (about 10%) was added to compensate for Mg losses due to evaporation, since Mg has to be alloyed with relatively high melting temperature elements (Mn and Nd). Samples were melted several times to ensure the composition homogeneity. The actual global composition was determined using Ultima2 inductively coupled plasma with optical emission spectrometer (ICP-OES). For each sample, three pieces from different locations were chosen. Average of the three corresponding compositions was considered as the actual composition. The difference between the three locations was found in the range ±2 at.%. Key alloys were subjected to a step annealing approach, which includes annealing for different time intervals. Then, the as-cast and annealed microstructures were compared in order to understand the phase equilibrium.

Solid-solid diffusion couples were prepared from two blocks of alloys and/or pure metals. The contacting surfaces were ground gradually up to 1200 grit SiC emery paper, then polished down to 1μm using alcohol-based diamond suspension and 99% ethanol as a lubricant. The blocks were attached together using stainless steel clamp rings. The samples and diffusion couples were wrapped in tantalum foil, encapsulated inside an argon-flushed quartz tube with inside pressure of (~8×10^{-1} torr) and annealed at 450°C for different time intervals to address the microstructural changes with time. Annealing time intervals were chosen systematically, based on the alloy composition, by performing annealing and quenching after different time increments. The microstructures, of the diffusion couples and/or alloys, were then compared to understand the phase equilibria and phase evolution.

Philips X'Pert pro X-ray diffractometer (XRD) was used. X-ray diffraction analysis was performed on powder-form samples in the range from 20 to 120 degree 2θ with 0.02° step size to identify the phases. Rietveld analysis was used to measure the relative amounts of these phases. The crystal structure of the compounds was characterized using X'Pert Highscore plus software [58]. The diffusion couples and equilibrated alloys were analyzed using Hitachi S-3400 scanning electron microscope (SEM) equipped with wavelength dispersive x-ray spectrometer (WDS) and energy dispersive X-ray spectrometer (EDS). WDS spot analysis was used to identify the phase composition of the diffusion zones and key alloys. WDS line-scans were performed across the diffusion zones to determine the solubility ranges of the various phases in the system. The WDS experimental error was estimated to be ~1 at.%, based on the actual difference between the readings. EDS elemental mapping was used to determine phase composition and distribution of elements within diffusion zones.

3.4. Results and discussion:

In the following section, the binary and ternary solid solutions are described using parentheses and superscripts. For example, (MgNd) indicates the ternary solid solubility of Mn in MgNd, the binary solid solution of Mg in α-Nd is represented as $(\alpha\text{-Nd})^{Mg}$, and the extended solid solubility of Mg and Mn in α-Nd is represented as $(\alpha\text{-Nd})^{Mg,Mn}$.

Solid-solid diffusion couples were annealed at 450°C to accelerate diffusion without causing melting, since the lowest liquidus temperature was estimated as 500°C based on the preliminary thermodynamic calculations of the system. Diffusion couples were annealed for different intervals to reveal the phase equilibrium between the formed layers and their constituents based on the microstructural changes of diffusion couples versus time. Different annealing time intervals were also essential to assure that all diffusion layers are present.

3.4.1. Solid-solid diffusion couples

The end-members of diffusion couple #1 were made from two binary alloys. The first end-member was made from an alloy containing 78Mn-22Nd at.%. The second end-member was made from an alloy containing 87Mg-13Nd at.%. Diffusion couple #1 was annealed at 450°C for 10 days. SEM micrographs of this diffusion couple are shown in

Figure 3-1. WDS spot analysis was carried out to identify the composition of the diffusion zones and their constituents. The results of WDS spot analysis are listed in Table 3-1. WDS line-scan performed across diffusion zones of diffusion couple #1 is shown in Figure 3-2.

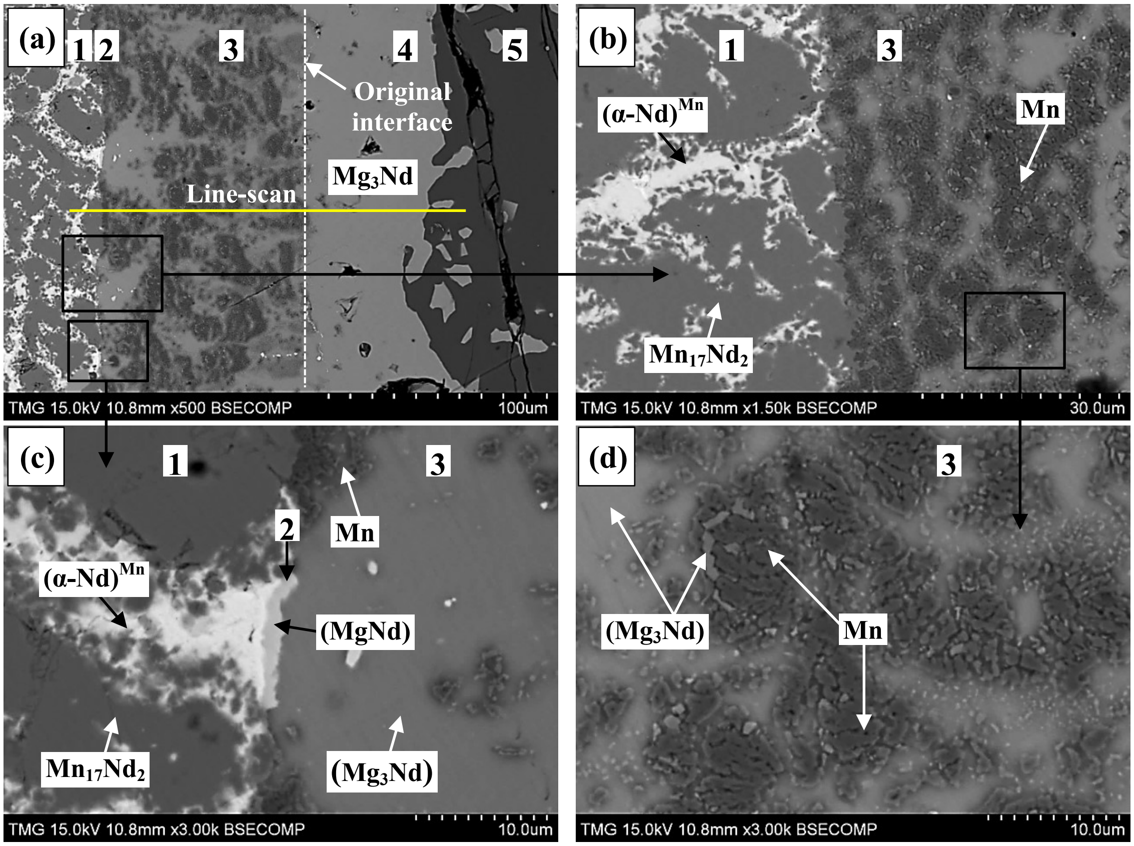

Figure 3-1: (a) SEM micrograph of the solid-solid diffusion couple #1 annealed at 450°C for 10 days; (b) magnified part showing diffusion zones #2; (c) microstructure of Mn17Nd2+(α-Nd)Mn end-member; (d) magnified part showing the phase morphology of diffusion zone #3. The numbers represent the diffusion zones and correspond to those in Table 3-1 and Figure 3-2

Initially, the as-cast composition of the first end-member (zone #1) contained (α-Nd)^{Mn}+$Mn_{23}Nd_6$. $Mn_{23}Nd_6$ is a peritectic compound forms at 930°C and decomposes eutectoidally at ~500°C [64, 74]. End-member (zone #1) was homogenized at 450°C for 15 days, before coupling with the second end-member (zone #5), in order to achieve the

$(\alpha\text{-Nd})^{Mn}$+$Mn_{17}Nd_2$ equilibrium structure. It is necessary to start with homogenized end-member to avoid forming diffusion layers amongst non-stable compounds. Although diffusion is a dynamic process and relies on the thermodynamic equilibrium between the adjacent layers and their constituents, it will take very long time to reach equilibrium if meta-stable compounds are presented.

Table 3-1: WDS spot analysis of diffusion couple #1

Zone #	Composition (at.%)			Corresponding phase
	Mg	Mn	Nd	
1 (end-member)	-	2.6	97.4	$(\alpha\text{-Nd})^{Mn}$
	-	89.1	10.9	$Mn_{17}Nd_2$
2	46.5	3.5	50.0	(MgNd)
3	21.3	3.7	25.0	(Mg_3Nd)
	-	100	-	Mn
4	75.0	-	25.0	Mg_3Nd
5 (end-member)	89.3	-	10.7	$Mg_{41}Nd_5$
	75.0	-	25.0	Mg_3Nd

Diffusion zone #2, shown in Figure 3-1 (c), represents the (MgNd) diffusion layer. The composition profile across this layer is shown in Figure 3-2 (a). The profile shows that Mn is substituting Mg with about 3.5 at.% at constant concentration of 50 at.% Nd. These points were obtained from a very thin layer (1.7 μm width). Thus, this solubility limit needs to be confirmed by key alloys. Nevertheless, the results obtained from the composition profile still important for the preliminary prediction of the phase relationships. It is worth noting that the elemental scan shown in Figure 3-2 (a) is done in a selective way by avoiding the secondary phases in the diffusion layers (i.e. Mn and $Mn_{17}Nd_2$), whereas a blind line-scan is shown in Figure 3-2 (b).

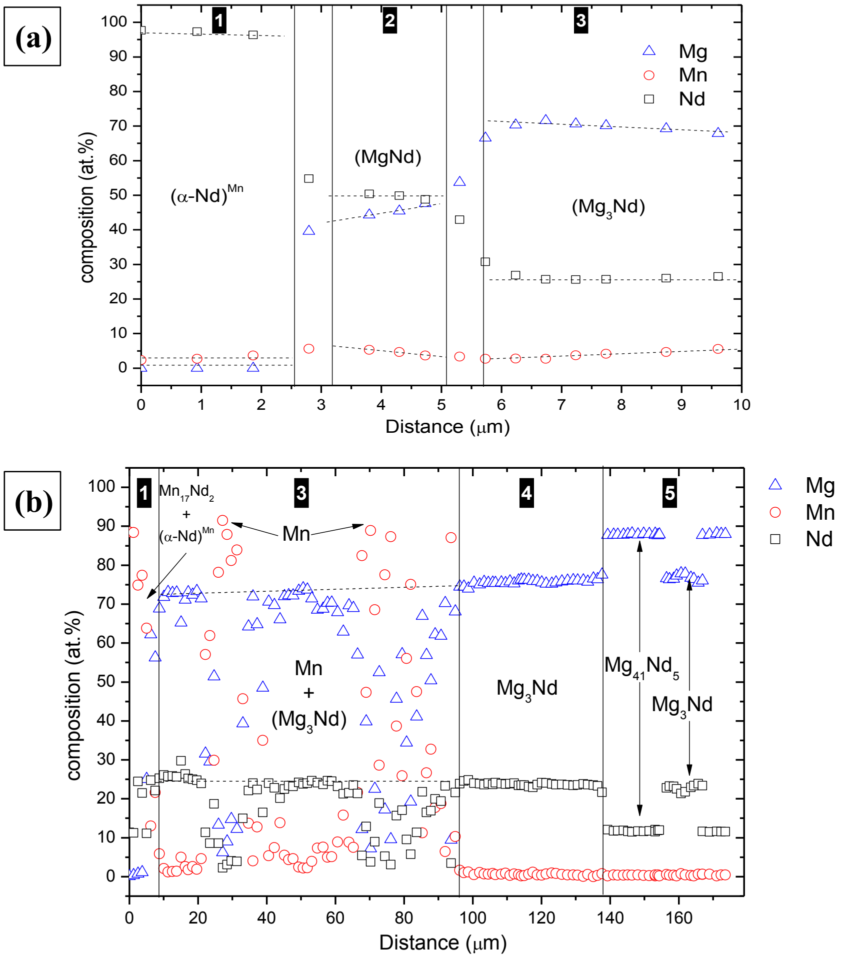

Figure 3-2: (a) Selective line-scan across zone #2 avoiding the secondary phases (Mn and $Mn_{17}Nd_2$); (b) blind line-scan across diffusion couple #1. The numbers represent the diffusion zones and correspond to those in Table 3-1 and Figure 3-1

(MgNd) layer seems to appear only when (α-Nd)^{Mn} has a large contact with (Mg_3Nd). Hence, it is not a continuous diffusion layer. Figure 3-1 (c) is redrawn to show the phase relations between the constituents of diffusion zones #1, 2 and 3 as illustrated in Figure 3-3. As can be seen from Figure 3-3, (MgNd) (zone #2) is in equilibrium with (α-Nd)^{Mn} and $Mn_{17}Nd_2$ from zone #1 and with (Mg_3Nd) from zone #3. Thus, the three-phase equilibrium (α-Nd)^{Mn}+$Mn_{17}Nd_2$+(MgNd) was determined at the interface between zone #1 and zone #2. Furthermore, the equilibrium between (MgNd) and (Mg_3Nd) was determined at the interface between zone #2 and zone # 3. The contact between zone #1 and zone #3 represents the phase equilibrium between $Mn_{17}Nd_2$ and pure Mn. These phase relations are shown on the Mg-Mn-Nd triangle below at the end of diffusion couple #1 discussion.

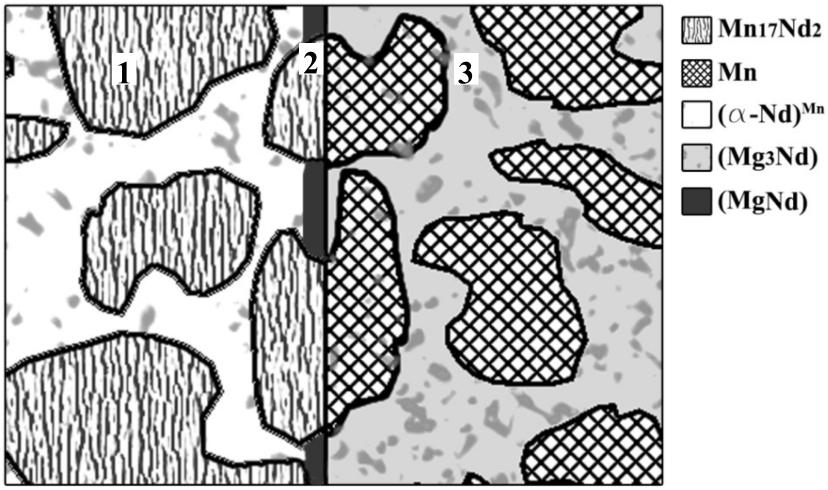

Figure 3-3: Schematic representation of the phase relations observed in Figure 3-1 (c) showing the phase equilibrium between (MgNd) (zone #2) and both $(\alpha\text{-Nd})^{Mn}$ ***from zone #1 and*** (Mg_3Nd) ***from zone #3. Also, it demonstrates the three-phase equilibria*** $(\alpha\text{-Nd})^{Mn}+Mn_{17}Nd_2+(MgNd)$ ***between zones #1 and #2***

Diffusion zone #3 appeared with a total thickness of ~100μm. This zone resulted mainly from the interatomic diffusion between Mg and Nd, when $(\alpha\text{-Nd})^{Mn}$ first reacted with diffusing Mg. Because of the high affinity of Mg to Nd, diffusing Mg continues to react with the Nd stemming from the decomposition of $Mn_{17}Nd_2$ that is originally present in the first end-member (zone #1). The decomposition of $Mn_{17}Nd_2$ liberates Mn particles due to Nd consumption. More Mn was liberated from the initial reaction between $(\alpha\text{-Nd})^{Mn}$ and the diffusing Mg. 3.7 at.% of the liberated Mn was dissolved in Mg_3Nd to form (Mg_3Nd) solid solution in zone #3, which is relatively wider than other zones. When the maximum solubility of Mn in (Mg_3Nd) was reached, no more Mn could be dissolved. Therefore, pure Mn regions remained stationary in zone #3 as shown in Figure 3-1 (b) and (d). WDS line-scan in Figure 3-2 (b) shows scattered data in this zone due to the random distribution of Mn in this layer. The phase morphology of $Mn_{17}Nd_2$ within zone #1 and later becoming Mn in zone #3 is shown in Figure 3-1 (b).

In terms of phase equilibrium, diffusion zone #3 represents the Mn+(Mg_3Nd) two-phase region in the Mg-Mn-Nd isothermal section at 450°C. It is worth noting that $Mn_{17}Nd_2$ (zone #1) is not in equilibrium with (Mg_3Nd) (zone #3). This is clear from the microstructure shown in Figure 3-1 (b) and Figure 3-3, where the extension of $Mn_{17}Nd_2$ morphology becomes pure Mn regions in zone #3. Because zone #1 contains two phases, two possible paths can be depicted from diffusion couple #1. The first possibility can be represented as follows: $Mn_{17}Nd_2 \rightarrow Mn \rightarrow Mn+(Mg_3Nd) \rightarrow Mg_3Nd \rightarrow Mg_3Nd+Mg_{41}Nd_5$. The second possibility can be as follows: $(\alpha\text{-}Nd)^{Mn}+Mn_{17}Nd_2 \rightarrow (\alpha\text{-}Nd)^{Mn}+Mn_{17}Nd_2+(MgNd) \rightarrow (MgNd) \rightarrow (Mg_3Nd) \rightarrow (Mg_3Nd)+Mn \rightarrow Mg_3Nd \rightarrow Mg_3Nd+Mg_{41}Nd_5$.

Zone #4 represents the Mg_3Nd binary compound, which resulted from the diffusion reaction of Nd and $Mn_{41}Nd_5$. The spot analysis in Table 3-1, line-scan in Figure 3-2 (b) and EDS elemental mapping in Figure 3-4 revealed that there is no Mn in zone #4. Accordingly, the original interface of diffusion couple #1 could be determined at the interface between zones #3 and #4 as demonstrated in Figure 3-1 (a).

EDS elemental mapping, shown in Figure 3-4, was performed to detect the distribution of the three elements among diffusion zones of diffusion couple #1. Figure 3-4 (a) represents the backscattered electron image of diffusion couple #1. Figure 3-4 (b-d) represents the elemental maps of Mg, Mn and Nd, respectively.

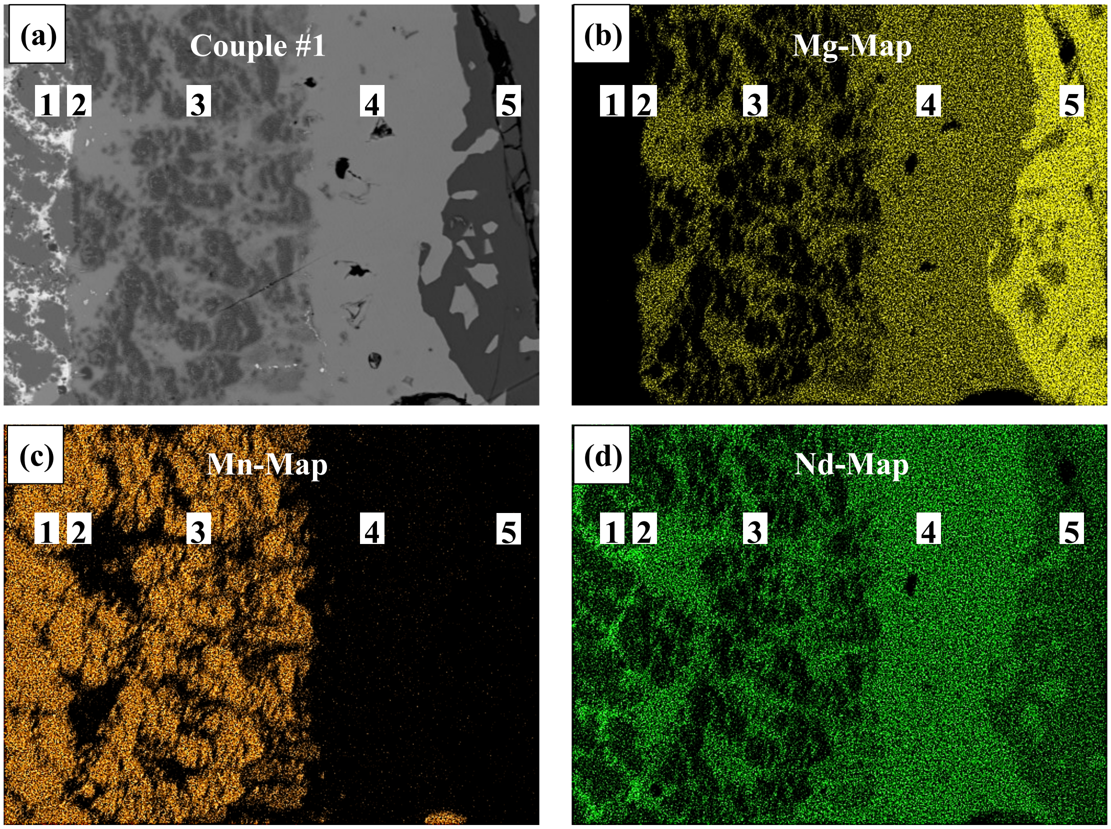

Figure 3-4: EDS elemental mapping of diffusion couple #1. Reader is encouraged to see the online version for the colored images

Mg map in Figure 3-4 (b) shows that Mg concentration decreases from 89.1 at.% (zone #5) to 46.5 at.% (zone #2). No Mg was detected in zone #1, which is the Mn-Nd binary alloy end-member. Because of the low magnification of the elemental mapping image, Mn was only observed in zones #1 and #3 as shown in Figure 3-4 (c). However, WDS line-scan (Figure 3-2 (b)) showed that zone #2 contains 3.5 at.% Mn as discussed earlier. Mn trace could be evidence of the original interface location, where the Mn liberated from $Mn_{17}Nd_2$ disappeared at the interface between zone #3 and zone #4 marking the original interface. On the other hand, Nd map (Figure 3-4 (d)) shows that Nd concentration decreases from 97.4 at.% in zone #1 to 10.7 at.% in zone #5.

According to the phase equilibrium analysis of diffusion couple #1 using WDS and EDS techniques, the phase relationships can be determined graphically on the Mg-Mn-Nd isothermal section at 450°C as shown in Figure 3-5. The two end-members (A-B) are connected by a dashed line. The width of the two-phase region Mn+(Mg_3Nd) is taken as 1.7 at.% Mg based on the binary solubility range of Mg_3Nd at 450°C [67]. The drawing in Figure 3-3 is used to describe the phase relationships on the Mg-Mn-Nd triangle at 450°C based on the microstructure of diffusion couple #1.

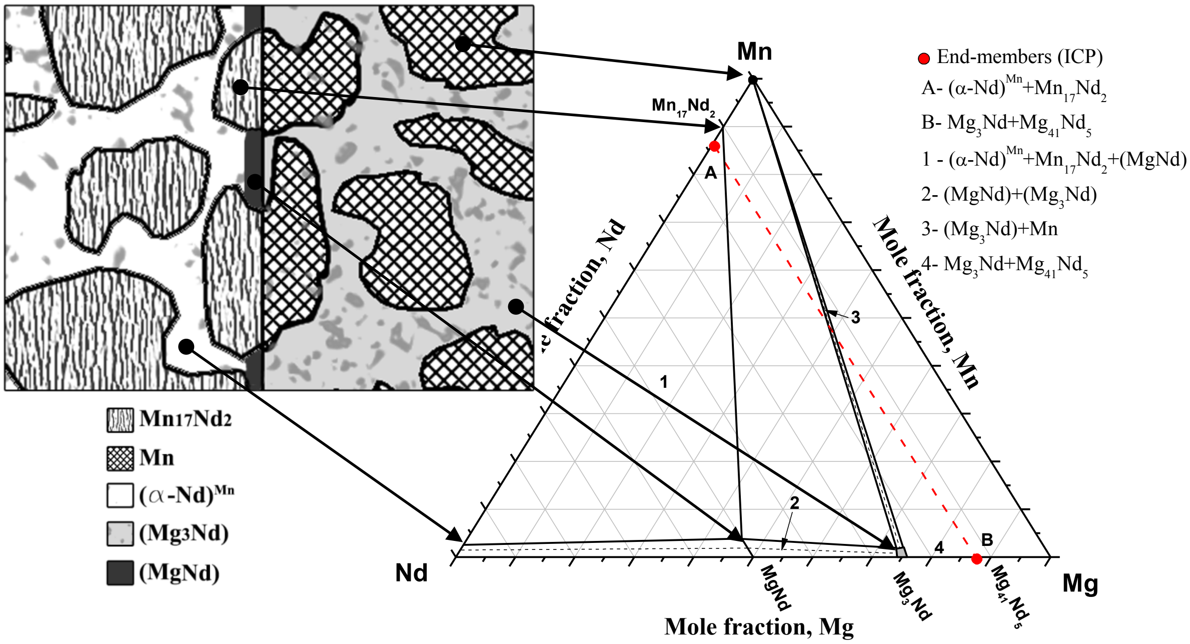

Figure 3-5: Phase equilibria obtained from diffusion couple #1 annealed at 450°C for 10 days. The numbers represent the corresponding phase field based on the obtained phase equilibrium. A and B represent the actual composition of the two end-members obtained by ICP

Diffusion couple #2, prepared from two ternary alloys whose details are listed in Table 2, was annealed at 450°C for 4 days. The annealing time here was shorter than that for couple #1, because the quartz tube was observed to be dark indicating significant evaporation of some of the elements. Longer annealing resulted in losing one of the end-members, which was experienced during the several attempts to obtain a successful diffusion between these two end-members.

The first end-member (zone #1) contains Mn, $Mn_{17}Nd_2$ and (MgNd). The second end-member (zone #4) contains Mn, $Mg_{41}Nd_5$ and (Mg_3Nd). WDS spot analysis was used to determine the composition of the diffusion zones and their constituents. The results of WDS spot analysis are listed in Table 3-2. The SEM micrograph of diffusion couple #2 is shown in Figure 3-6. Figure 3-6 (a) shows that diffusion couple #2 contains four diffusion zones. The original interface between the two end-members is marked by a dashed line in the same figure. Figure 3-6 (b) is a magnified part from diffusion zone # 2 showing the Mn particles resulting from the dissolution of $Mn_{17}Nd_2$ to provide Nd which reacts with the diffusing Mg to form (Mg_3Nd). The same figure shows that the Mn particles are dispersed in the (Mg_3Nd) solid solution matrix with 3.7 at.% Mn.

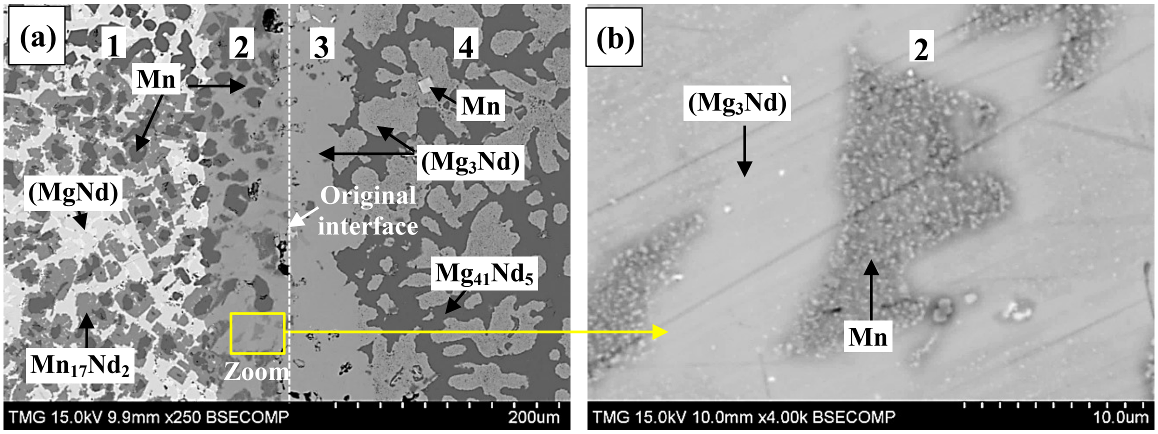

Figure 3-6: (a) SEM micrograph of the solid-solid diffusion couple #2 annealed at 450°C for 4 days; (b) magnified part of zone #2 showing the fine particles of Mn due to Nd consumption from $Mn_{17}Nd_2$. The numbers represent the diffusion zones and correspond to those in Table 3-2

Table 3-2: WDS spot analysis of diffusion couple #2

Zone	Composition (at.%)			Corresponding phase
	Mg	Mn	Nd	
1 (end-member)	-	100	-	Mn
	-	89.3	10.7	$Mn_{17}Nd_2$
	39.7	11.2	49.1	(MgNd)
2	74.0	3.7	22.3	(Mg_3Nd)
	-	100	-	Mn
3	75.8	<2.0	22.5	(Mg_3Nd)
4 (end-member)	-	100	-	Mn
	88.3	-	10.7	$Mg_{41}Nd_5$
	75.1	<2.0	23.6	(Mg_3Nd)

Besides the two three-phase equilibria $Mn_{17}Nd_2$+(MgNd)+Mn and Mn+(Mg_3Nd)+$Mg_{41}Nd_5$ inferred from the end-members of couple #2, the Mn+(MgNd)+(Mg_3Nd) three-phase equilibrium was observed at the interface between zones #1 and #2. The WDS results in Table 3-2 show that Mn concentration in zones #1 and 2 is relatively higher than that in zones #3 and 4. The relatively high Mn concentration can be as a result of $Mn_{17}Nd_2$ decomposition, which produced appreciable amount of free Mn atoms that have enough driving force to diffuse in a wide (Mg_3Nd) matrix (zone #2). However, most of the Mn in the second end-member alloy (zone #4) remained pure in the microstructure as can be seen in zone #4 of Figure 6 (a), because the composition of the end-member alloy lies in the Mn+$Mg_{41}Nd_5$+(Mg_3Nd) triangulation. Thus, only a little amount of Mn was dissolved by (Mg_3Nd) as indicated in Table 3-2

The solubility of Mn in (MgNd) was determined from the composition of the end-member alloy (zone #1) in diffusion couple #2. WDS spot analysis revealed that (MgNd) solid solution contains 11.2 at.% Mn. Whereas, the solubility of Mn in (Mg_3Nd) was measured as 3.7 at.% in both diffusion couples #1 and 2.

Based on the obtained results from diffusion couple #2, the phase relationships are represented in Figure 3-7. The two end-members (A-B) are connected by a dashed line. The shaded areas represent the triangles of the end-members' alloys used in diffusion couple #2.

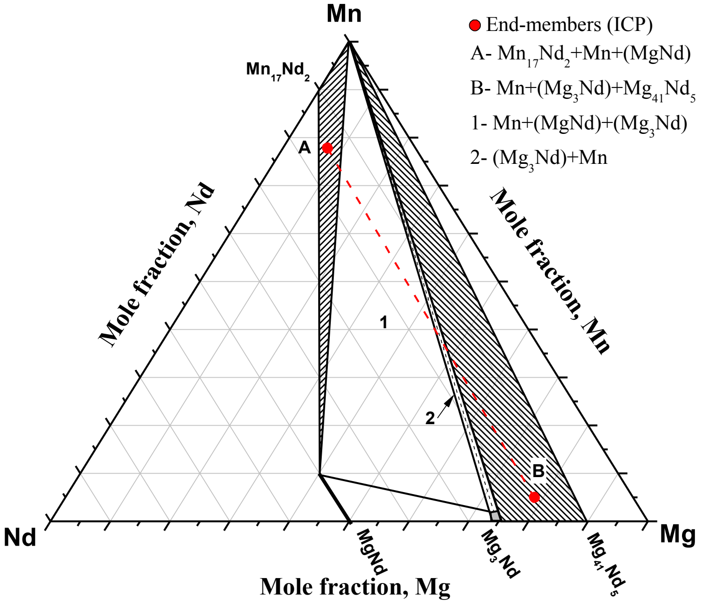

Figure 3-7: The phase relations determined from diffusion couple #2 annealed at 450°C for 4 days. The numbers represent the corresponding phase field based on the obtained phase equilibrium. A and B represent the actual composition of the two end-members obtained by ICP

The SEM micrograph of diffusion couple #3 is shown in Figure 3-8. The first end-member contains three phases, $Mn_{17}Nd_2$, (MgNd) and $(\alpha\text{-Nd})^{Mg,Mn}$. The second end-member is made from pure Mg (99.98 wt.% purity). During annealing, various phases formed due to the interdiffusion between Mg and Nd. The diffusion layers of this diffusion couple were similar to those of Mg-Nd binary system, i.e.: MgNd, Mg_3Nd and $Mg_{41}Nd_4$. The only difference is that the ternary diffusion couple contains pure Mn within these layers, forming two-phase region within each. The Mn content in all diffusion layers stemmed originally from $Mn_{17}Nd_2$ in the ternary alloy of the second end-member (zone #6). WDS spot analysis was used to identify the composition of the phases in each zone. The results of WDS spot analysis are summarized in Table 3-3.

Six diffusion zones were observed in diffusion couple #3 as shown in Figure 3-8 (a). Figure 3-8 (b) represents a magnified region from diffusion couple #3, showing that (Mg_3Nd) is in equilibrium, selectively, with (MgNd) (the grey phase). Figure 3-8 (c) shows the presence of pure Mn, resulting from the decomposition of $Mn_{17}Nd_2$, in diffusion zones #3 and 4.

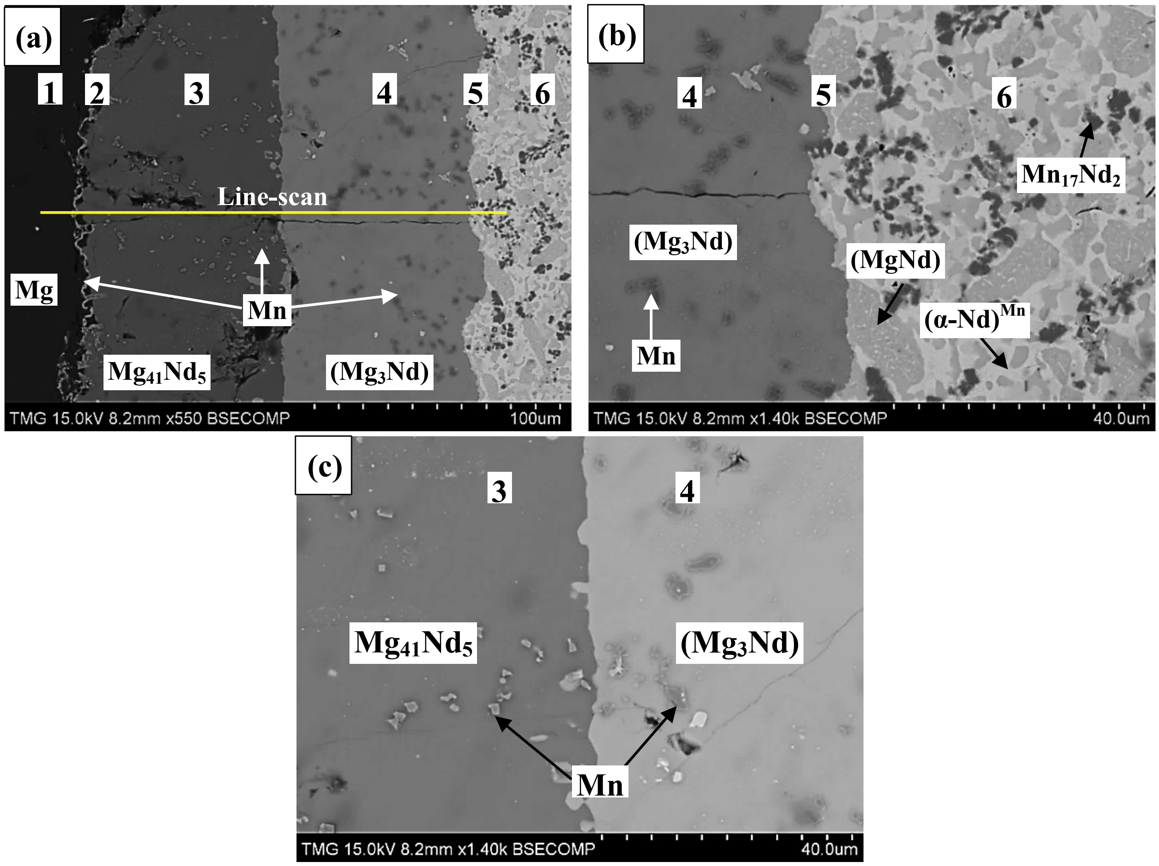

Figure 3-8: (a) SEM micrographs of the solid-solid diffusion couple #3 annealed at 450°C for 5 days; (b) magnified portion showing zones #4, 5 and 6; (c) magnified portion showing $Mg_{41}Nd_5$/Mg_3Nd interface (zones #3 and 4). The numbers represent the diffusion zones and correspond to those in Table 3-3 and Figure 3-9

Table 3-3: WDS spot analysis of diffusion couple #3

Zone	Composition (at.%)			Corresponding phase
	Mg	Mn	Nd	
1 (end-member)	100	-	-	Mg
2	-	100	-	Mn
3	88.4	-	11.6	$Mg_{41}Nd_5$
	-	100	-	Mn
4	72.6	2.6	24.8	(Mg_3Nd)
	-	100	-	Mn
5	44.8	5.2	50.0	(MgNd)
	-	100	-	Mn
6 (end-member)	44.6	6.1	49.3	(MgNd)
	6.0	2.0	92.0	$(\alpha\text{-Nd})^{Mg,Mn}$
	-	89.5	10.5	$Mn_{17}Nd_2$

Diffusion zone #1 represents the pure Mg end-member. Diffusion zone #2 represents a continuous thin layer of pure Mn whose exact composition was difficult to acquire using WDS spot analysis, because it is very thin. The composition profile in Figure 3-9, however, shows the drop in both Mg and Nd compositions with increase in Mn content in zone #2. This supports the presence of the observed Mn thin layer in zone #2. It is suggested that the pure Mn layer formed due to the diffusion of Mn atoms that were liberated from the Mn-containing phases. This suggestion was supported experimentally by diffusion couple #4, which will be discussed later. The formation of this thin layer is necessary to fulfill the equilibrium condition near the Mg-rich side, where Mg (zone #1) equilibrates with Mn (zone #2) and Mn equilibrates with $Mg_{41}Nd_5$ to form the $Mg_{41}Nd_5$+Mn two-phase region in zone #3. Diffusion zones #4 to 5 represent other two-phase layers, where Mn is in equilibrium with (Mg_3Nd) and (MgNd). Diffusion zone #6 represents the three-phase alloy end-member. Besides the three two-phase equilibria $Mg_{41}Nd_5$+Mn, (Mg_3Nd)+Mn and (MgNd)+Mn, two three-phase equilibria; namely: Mn+$Mg_{41}Nd_5$+(Mg_3Nd) and Mn+(Mg_3Nd) +(MgNd), could be obtained at the interface of zones #3 and 4 and zones #4 and 5, respectively.

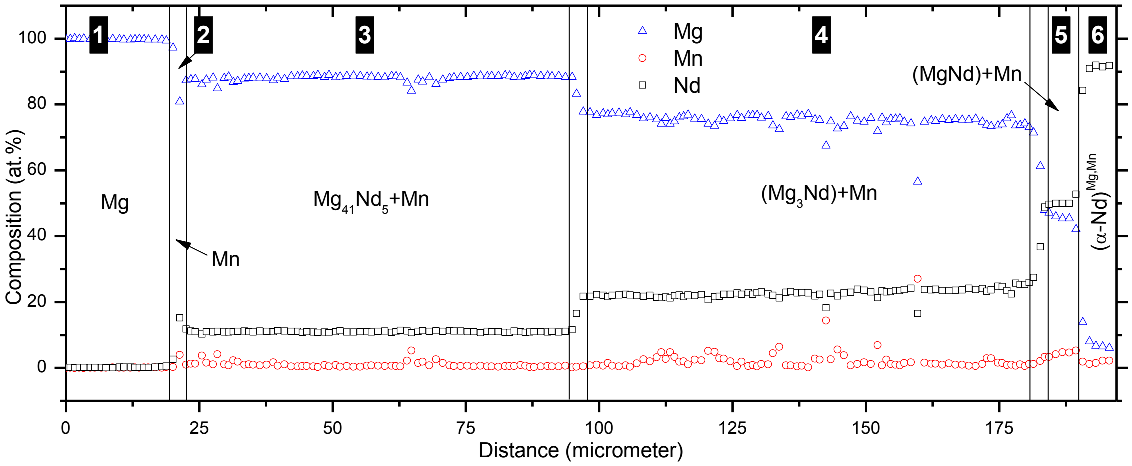

Figure 3-9: Measured composition profile across diffusion couple #3 using WDS line-scan with a spatial distance of ~1μm

Figure 3-9 shows the WDS line-scan that was performed with a step size of ~1μm across the diffusion zones of diffusion couple #3 as illustrated in Figure 3-8 (a). It is worth noting that zone #6 contains three phases. However, the WDS line-scan shows only one phase, because the line did not cross the other two phases.

The line-scan showed that no remarkable solubility of Nd and Mn in Mg end-member (zone #1). The composition profile through the $Mg_{41}Nd_5$+Mn diffusion layer (zone #3) showed constant composition of the three elements. The profile across (Mg_3Nd)+Mn (zone #4) shows an irregular distribution of the three elements at certain points. This was attributed to the presence of Mn in this diffusion zone. The composition profile across (MgNd)+Mn (zone #5) shows that up to 5.2 at.% Mg is substituted by Mn at constant concentration of Nd. This was also supported by the WDS spot analysis summarized in Table 3-3. According to these profiles, the solubility of Mn in both (Mg_3Nd) and (MgNd) was determined as 2.6 and 5.2 at.% Mn, respectively. This will be confirmed by key alloys in the next section.

The diffusion path was determined based on the local equilibria between the phases of diffusion couple #3 as follows: (MgNd)+$(\alpha\text{-Nd})^{Mg,Mn}$+$Mn_{17}Nd_2$ (end-member) → (MgNd)+Mn → (MgNd)+Mn+(Mg_3Nd) → (Mg_3Nd)+Mn → $Mg_{41}Nd_5$+(Mg_3Nd)+Mn → $Mg_{41}Nd_5$+Mn → Mn → Mg (end-member). The phase equilibria determined by diffusion couple #3 are shown in Figure 3-10. The two end-members (A-B) are connected by a dashed line. The shaded area represents the triangle of the three-phase end-member.

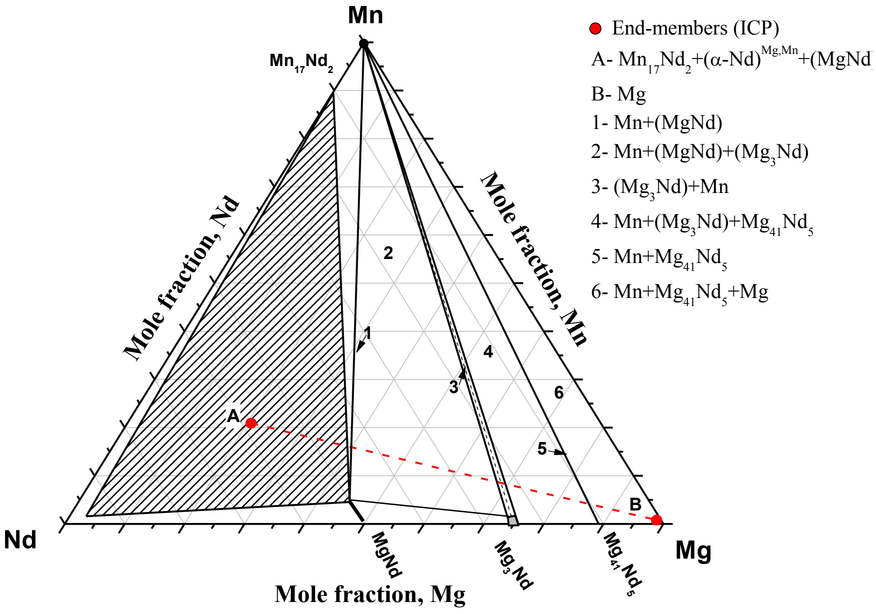

Figure 3-10: The phase equilibria determined by diffusion couple #3 annealed at 450°C for 5 days. The numbers represent the corresponding phase field based on the obtained phase equilibrium. A and B represent the actual composition of the two end-members obtained by ICP

Diffusion couple #4 was prepared to provide better understanding of the formation of pure Mn layer near the Mg end-member. The first end-member of this diffusion couple was made from pure Mg (zone #1). The second end-member was from a ternary alloys containing $Mn+Mn_{17}Nd_2+(MgNd)$ (zone #5). Diffusion couple #4 was annealed only for 2 days. Because the objective of this couple was to interrupt annealing at early stages of diffusion process to confirm the observations about Mn as pure metal and as solute atoms as discussed in previous diffusion couples #1-3. SEM micrograph of diffusion couple #4 is shown in Figure 3-11. Five diffusion zones were observed in this diffusion couple. The WDS results of the constituents of every diffusion zone are listed in Table 3-4.

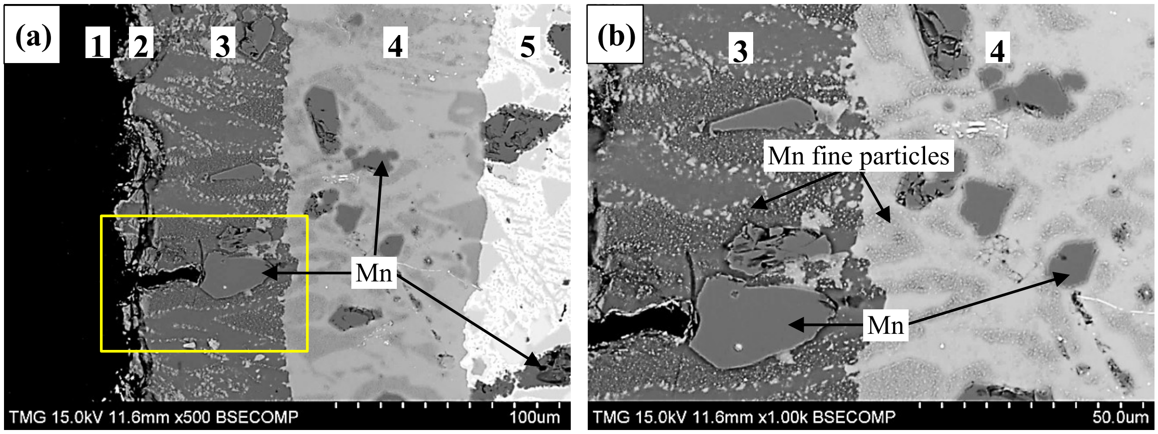

Figure 3-11: (a) SEM micrograph of the solid-solid diffusion couple #4 annealed at 450°C for 2days; (b) magnified portion showing different forms pure of Mn. The numbers represent the diffusion zones and correspond to those in Table 3-4

It is clear that diffusion couple #4 did not reach equilibrium, because three phases were observed in zone #3. This is not acceptable from thermodynamics point of view, since the maximum number of phases per diffusion layer in a ternary diffusion couple must be two, except at the interface. Nevertheless, this diffusion couple is discussed here to shed some light on the kinetics of diffusion in this system. The three phases seen in zone #3 are, (Mg_3Nd), $Mg_{41}Nd_5$ and Mn. Figure 3-11 shows that Mn grain morphology did not change from one diffusion zone to another, while Mg and Nd atoms are actively diffusing. Not only that, the pure Mn grain (in the rectangle in Figure 3-11 (a)) is also blocking the movement of the other diffusing atoms as shown clearly in Figure 3-11 (b), where a plate of non-diffusing Mg exists on the left-hand side of the Mn grain. Other parts of the pure Mg end-member were diffusing across the interface. On the other hand, Mn freed from $Mn_{17}Nd_2$ and (MgNd) in zone #5, is observed to be dispersed or dissolved by the growing (Mg_3Nd) ternary solid solution with time.

Table 3-4: WDS spot analysis of diffusion couple #4

Zone	Composition (at.%)			Corresponding phase
	Mg	Mn	Nd	
1 (end-member)	100	-	-	Mg
2	-	100	-	Mn
3	88.4	<2.0	10.5	$Mg_{41}Nd_5$
	-	100	-	Mn
	73.2	<2.0	25.3	(Mg_3Nd)
4	73.1	<2.0	24.1	(Mg_3Nd)
	-	100	-	Mn
	75.0	-	25.0	Mg_3Nd
5 (end-member)	44.6	6.1	49.3	(MgNd)
	-	89.1	10.9	$Mn_{17}Nd_2$
	-	100	-	Mn

According to the phase equilibria determined from diffusion couple experiments and alloys of the end-members, the phase relationships are shown in Figure 3-12. In the next section, key alloys are used to confirm the phase relations obtained by diffusion couples and to determine the solubility limits of the solid solutions extended in the ternary.

Different annealing time intervals were used to assure that no diffusion layer was missing. It is worth emphasizing that Dybkov [77] reported that diffusion layer formation is a sequential process, where the first formed layers are those adjacent to the end members. Other layers start to form in between when the initial layers reach their maximum thickness. Hence, some thin layers may be consumed by the reaction between the diffusing species and the constituents of the layer when they are over annealed. Thus, it was necessary to observe the microstructural changes after every annealing step.

As can be understood from the diffusion behavior of Mn, it has relatively lower diffusivity than that of Mg and Nd. Thus, pure Mn was observed stationary in some diffusion zones of the diffusion couples. However, the mobility of Mn atoms improves as they liberate from the Mn-rich compounds. These atoms can be dissolved by some of the stable Mg-Nd compounds to form extended ternary solubility.

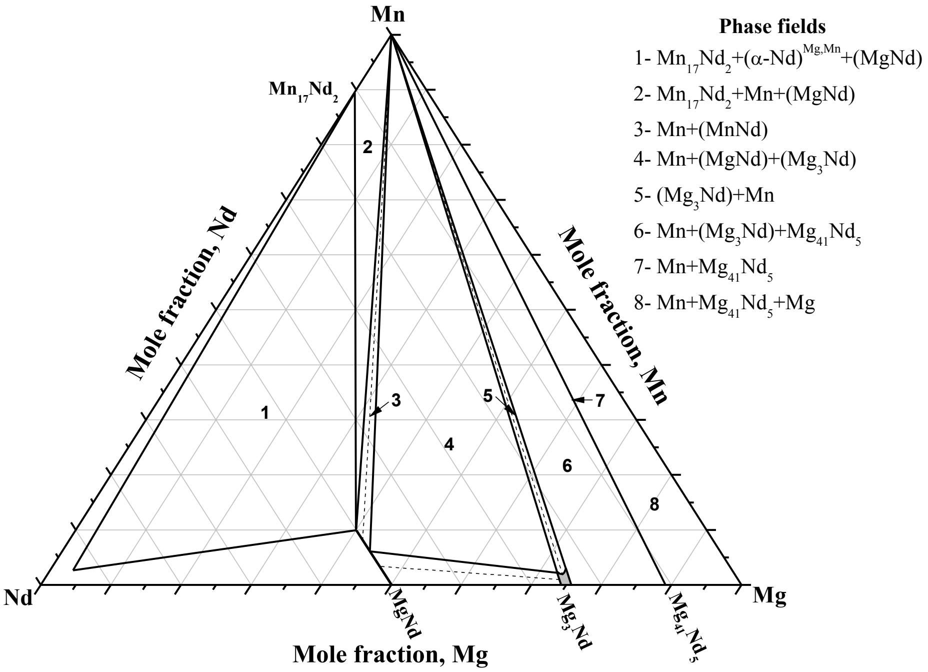

Figure 3-12: The phase equilibria inferred from the diffusion couple experiments

3.4.2. Key alloys experiments

Although diffusion couple studies are very useful to determine the phase relationships, they are not always successful. The possibility of missing a phase is a common phenomenon [78]. Sometimes the formation of some phases is too slow to form a detectable diffusion layer. Hence, key alloys experiments are designed to verify the experimental results obtained from the diffusion couples. Also, they are important to determine the maximum solid solubility of the binary and ternary components in the system.

The constituent phases and their compositions in the annealed alloys are listed in Table 3-5. XRD analysis was carried out to confirm the WDS findings. The XRD and WDS results of the annealed samples are consistent. Because of slow kinetics of the solid-solid phase transformation, step annealing approach was used and the key alloys were analyzed after each annealing step including the as-cast alloys. Accordingly, the phase equilibrium can be determined based on the microstructural and morphological changes that occur after each annealing step.

Some alloys showed significant difference between their as-cast and annealed microstructures. For instance, the as-cast microstructure of the sample #1 is shown in Figure 3-13 (a). Four phases (Nd, $Mg_{41}Nd_5$, $Mg_{12}Nd$ and Mn) were observed and labeled in the same figure indicating non-equilibrium condition. However, the microstructure of the same alloy after annealing for 14 days showed three phases ($Mg_{41}Nd_5$, $(Mg)^{Mn,Nd}$ and Mn) as shown in Figure 3-13 (b). $Mg_{12}Nd$ was observed in the as-cast alloy only, because it is a peritectic compound [7, 66] formed during the non-equilibrium cooling. $Mg_{12}Nd$ was reported as metastable phase [67, 71, 79] below 552°C. Thus, during annealing at 450°C, $Mg_{12}Nd$ decomposed to form $Mg_{41}Nd_5$ and $(Mg)^{Nd}$, because its composition falls between these two phases. The formation of $Mg_{41}Nd_5$ from $Mg_{12}Nd$ explains the significant increase in the amount of $Mg_{41}Nd_5$ in the annealed alloy as shown in Figure 3-13 (b).

Table 3-5: Selected key alloys and their experimental results

Sample	ICP (Actual composition at.%)			XRD Results	WDS Results	Phase composition (at.%) WDS		
	Mg	Mn	Nd			Mg	Mn	Nd
1	88.5	2.3	9.2	Mn	Mn	0.0	100	0.0
				Mg	$(Mg)^{Mn,Nd}$	99.0	<1.0	<0.1
				$Mg_{41}Nd_5$	$Mg_{41}Nd_5$	88.0	<1.0	11.0
2	52.2	16.5	31.3	Mn	Mn	-	100	-
				Mg_3Nd	(Mg_3Nd)	Small to be detected		
				(MgNd)	(MgNd)	41.7	9.1	49.2
3	24.7	19.1	56.2	α-Nd	$(\alpha\text{-Nd})^{Mg,Mn}$	6.0	3.0	91.0
				(MgNd)	(MgNd)	37.3	13.2	49.5
				$Mn_{17}Nd_2$	$Mn_{17}Nd_2$	<2.0	87.5	11.3
4	10.9	70.0	19.1	Mn	Mn	0.0	100	0.0
				$Mn_{17}Nd_2$	$Mn_{17}Nd_2$	<1.0	88.9	10.6
				(MgNd)	(MgNd)	38.3	12.0	49.7
5	91.1	6.5	2.4	Mn	Mn	0.0	100	0.0
				Mg	$(Mg)^{Mn,Nd}$	99.0	<1.0	<1.0
				$Mg_{41}Nd_5$	$Mg_{41}Nd_5$	88.8	<1.0	10.4
6	71.6	12.4	16.0	Mn	Mn	-	100	-
				$Mg_{41}Nd_5$	$Mg_{41}Nd_5$	88.0	<2.0	10.9
				(Mg_3Nd)	(Mg_3Nd)	75.0	2.7	22.3
7	70.8	5.8	23.4	Mn	Mn	-	100	-
				(Mg_3Nd)	(Mg_3Nd)	75.0	3.5	21.5
8	57.6	2.4	40.0	MgNd	(MgNd)	50.7	2.4	46.9
				Mg_3Nd	(Mg_3Nd)	Small to be detected		

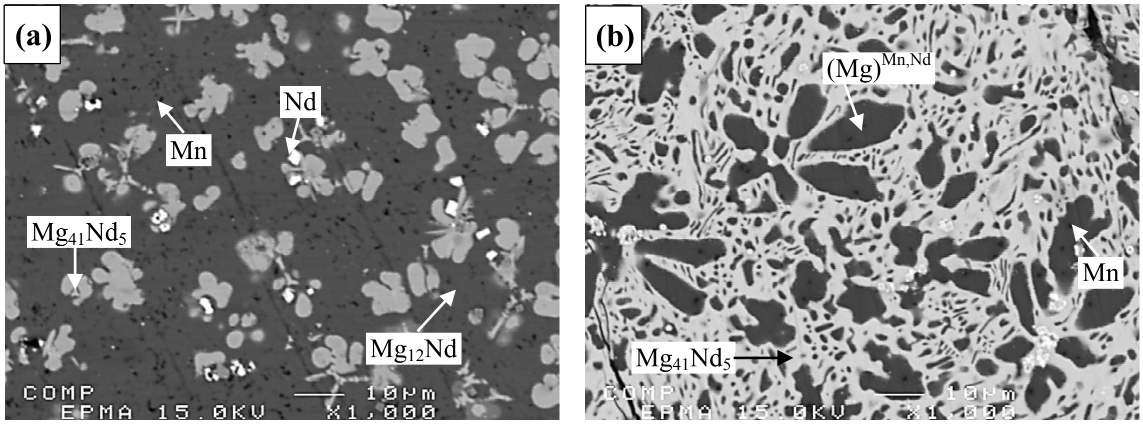

Figure 3-13: The microstructure of sample #1 (a) the as-cast condition; (b) annealed at 450°C for 14 days

The as-cast microstructure of sample #2, shown in Figure 3-14 (a), represents the three phases, Mn, (MgNd) and Mg_2Nd. Figure 3-14 (b) is for the microstructure of the same alloy after annealing at 450°C for 14 days. The annealed microstructure contains the three phases Mn, (MgNd) and Mg_3Nd. It is assumed that (Mg_3Nd) resulted from the eutectoidal decomposition of Mg_2Nd, which is known as a Laves phase with a narrow thermal stability range of 657-750°C [66, 67]. Thus, Mg_2Nd is not stable at 450°C. The phase morphology in Figure 3-14 (b) is evidence that Mg_2Nd decomposed eutectoidally as following $Mg_2Nd \leftrightarrow MgNd+Mg_3Nd$.

WDS spot analysis was not able to acquire the composition of the lamellae of the eutectoid phase individually, because they are very thin. However, the WDS area analysis of the eutectoid structure (Figure 3-14 (b)) revealed the following composition: 57.4Mg-9.2Mn-33.4Nd at.%, which falls in the (MgNd)+(Mg_3Nd) two-phase field. Therefore, X-ray powder diffraction was performed on the sample before and after annealing to identify the composition of the phases. The X-ray spectra of sample #8, before and after annealing, are shown in Figure 3-15. Silicon was used in the powder samples as a calibration standard to correct the zero shift and specimen displacement. XRD spectrum of sample #8 before annealing showed the presence of MgNd and Mg_2Nd, which is consistent with WDS results as can be seen in Table 3-5. The XRD spectrum of sample #8 after annealing showed Mg_3Nd peaks instead of Mg_2Nd. This elucidates the eutectoidal decomposition of Mg_2Nd.

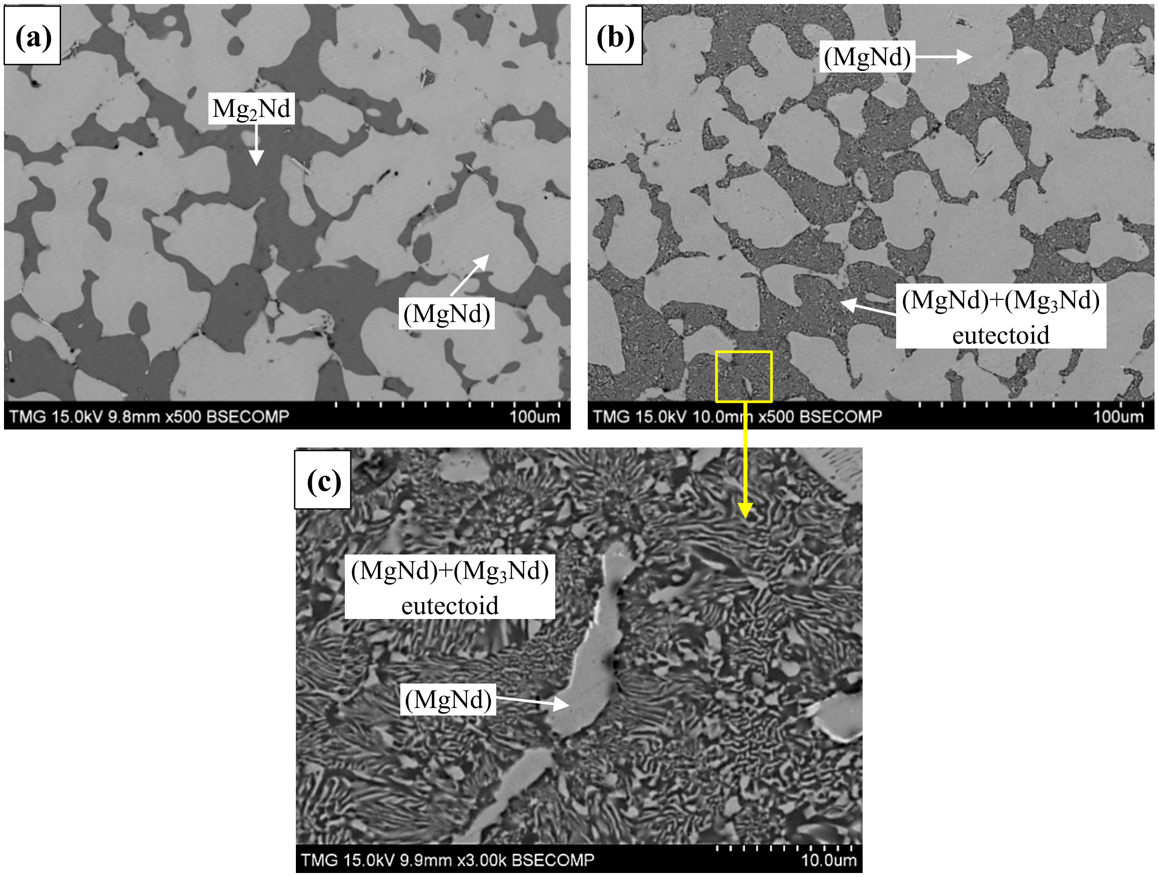

Figure 3-14: The microstructure of sample #8 (a) the as-cast condition; (b) annealed at 450°C for 5 days; (c) (MgNd)+(Mg_3Nd) eutectoid

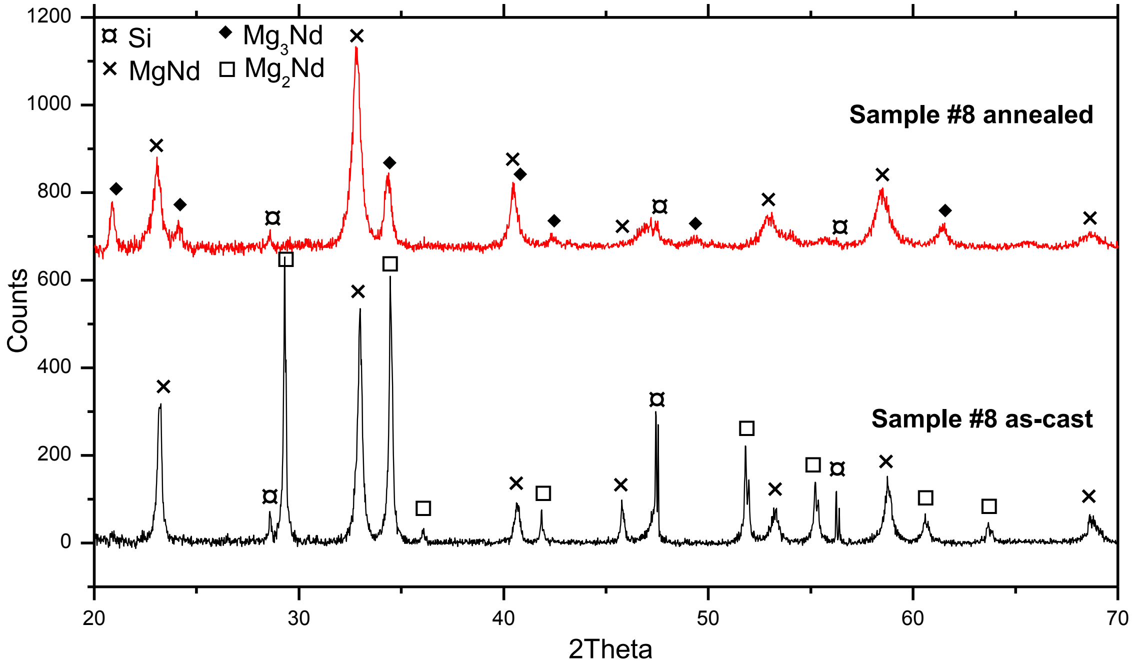

Figure 3-15: X-ray spectrum of sample #8 (a) before annealing; (b) annealed at 450°C for 5 days

Sample #3 was prepared to investigate the phase relationships near the Nd-rich corner. This can also provide valuable information on the maximum solid solubility of Mg and Mn in α-Nd at 450°C. The as-cast and annealed microstructures of sample #3 are shown in Figure 3-16 (a) and (b), respectively.

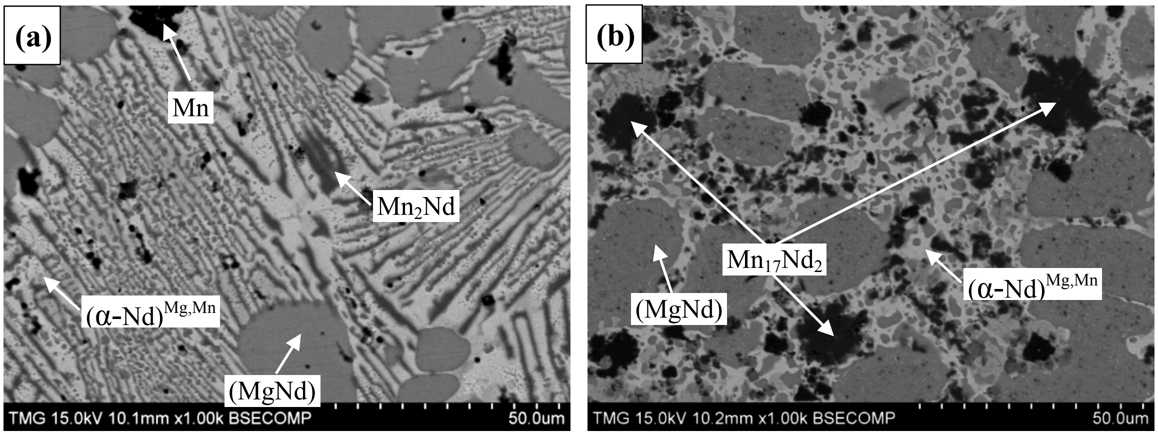

Figure 3-16: The microstructure of sample #3 (a) the as-cast condition; (b) annealed at 450°C for 14 days

The as-cast microstructure contains Mn, Mn_2Nd, (MgNd) and $(\alpha\text{-Nd})^{Mg,Mn}$. The annealed microstructure contains $Mn_{17}Nd_2$, (MgNd) and $(\alpha\text{-Nd})^{Mg,Mn}$. Mn_2Nd is another peritectic Laves phase in the system with a thermal stability range of ~600-830°C [64, 74]. It was observed with a lamellar morphology in the $Mn_2Nd+(\alpha\text{-Nd})^{Mg,Mn}$ eutectoid microstructure of the as-cast sample as shown in Figure 3-16 (a). The target annealing temperature in this study is 450°C, which is lower than the stability temperature of Mn_2Nd. According to the Mn-Nd phase diagram [64, 74], Mn_2Nd decomposes eutectoidally at ~570°C to form $Mn_{23}Nd_6$ and $(\alpha\text{-Nd})^{Mn}$, and $Mn_{23}Nd_6$ decomposes further at ~485°C to form $Mn_{17}Nd_2$ and $(\alpha\text{-Nd})^{Mn}$. From the microstructures of this alloy, $Mn_{17}Nd_2$ was obtained due to Mn_2Nd decomposition. Evidence is seen in Figure 3-16 (b) where $Mn_{17}Nd_2$ exists and the lamellar eutectoid microstructure changed to equiaxed grains.

Mn_2Nd was not the only source of $Mn_{17}Nd_2$ formation, pure Mn played additional role in the formation of $Mn_{17}Nd_2$. Based on the morphology of Mn grains, it seems that Mn reacted with Nd to form $Mn_{17}Nd_2$ as shown in Figure 3-16 (b). This can be an indication that the affinity of Mn to Nd atoms is higher than that of Mn to Mg; since Nd forms intermetallic compounds with Mn unlike Mg and Mn. The $Mn_{17}Nd_2$ formation reaction in this case is reversible to produce pure Mn due to $Mn_{17}Nd_2$ decomposition in the presence of Mg atoms as concluded from diffusion couples experiments.

It was also noticed that the available Mn was not completely transformed into $Mn_{17}Nd_2$. Part of Mn atoms were dissolved by (MgNd) and $(\alpha\text{-Nd})^{Mg,Mn}$ to form ternary solid solutions. It is evident from the WDS analysis that the solid solubility of Mn in

(MgNd) varied from 9 at.%, in the as-cast alloy, to 13 at.% Mn upon annealing. The solubility of Mn in (α-Nd)^{Mg,Mn} was determined as 3.0 at.% Mn.

3.4.3. The Mg-Mn-Nd isothermal section at 450°C

According to the diffusion couples and key alloys experiments, the Mg-Mn-Nd isothermal section at 450°C was constructed in the full concentration range as shown in Figure 3-17. The solubility of both Mn and Nd in Mg was relatively small; it was measured as <1.0 at.% Mn and <1.0 at.% Nd. These values fall within the WDS error of measurements, therefore, the solubility limits of both Mn and Nd in Mg at 450°C are taken from the work of Drits *et al.* [75] as 0.5 wt.% Mn and 1.3 wt.% Nd.

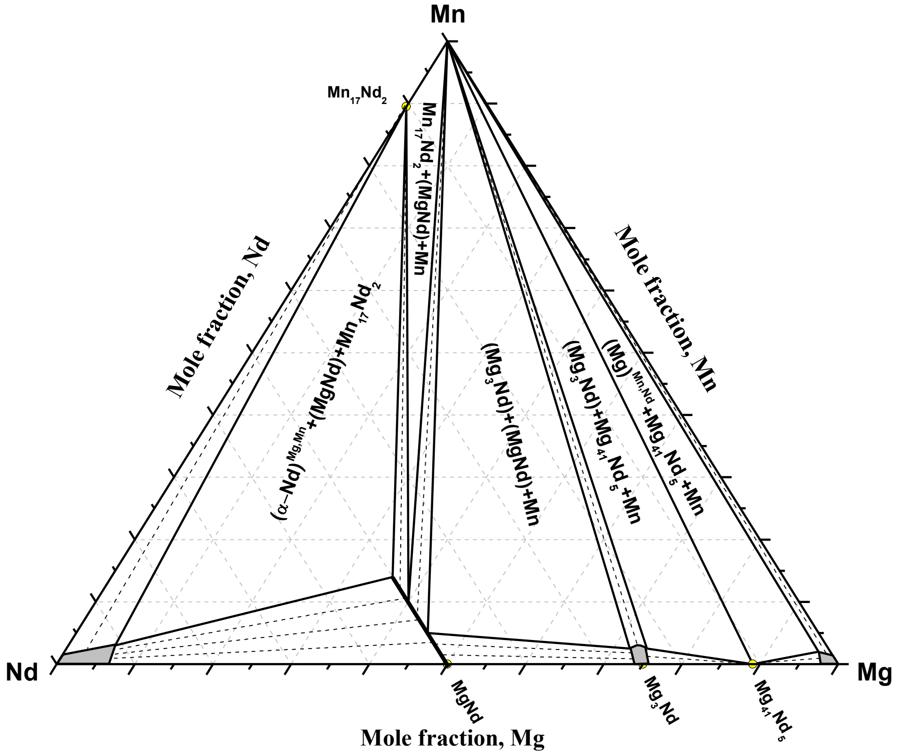

Figure 3-17: The Mg-Mn-Nd isothermal section at 450°C based on the phase equilibria of the diffusion couples and key alloys

Five three-phase regions were observed and confirmed by WDS and XRD analysis. The system showed unique phase relationships due to the presence of Mn. For instance, because Mn does not form intermetallic compounds with Mg, it was always seen as either solute in the Mg-Nd compounds or pure element in all microstructures. However, Mn forms a stable compound with Nd at 450°C, and this compound, $Mn_{17}Nd_2$, is in equilibrium with $(\alpha\text{-Nd})^{Mg,Mn}$, (MgNd) and pure Mn. Therefore, the phase boundary lines are pointing towards the Mn-rich corner, except for the $(\alpha\text{-Nd})^{Mg,Mn}$+(MgNd)+ $Mn_{17}Nd_2$ three-phase field, as shown in Figure 3-17.

3.5. Conclusions

The Mg-Mn-Nd isothermal section at 450°C was constructed in the full composition range using diffusion couples and key alloys, analyzed by XRD, SEM/EDS/WDS and metallography. No ternary compounds were observed in the system at 450°C. Key alloys were used to confirm the phase relations obtained from diffusion couples and to determine the solid solubility limits.

Diffusion couples revealed that Mn has relatively lower diffusivity than that of Mg and Nd. Thus, pure Mn was observed stationary in some diffusion zones forming Mn+(MgNd), Mn+(Mg_3Nd) and Mn+$Mg_{41}Nd_5$ two-phase regions. However, relatively small amount of Mn diffused towards the interface with Mg end-member forming a continuous thin layer of pure Mn. The remainder of Mn was dissolved in $(\alpha\text{-Nd})^{Mg,Mn}$, (MgNd) and ($Mg_3Nd$).

$(\alpha\text{-Nd})^{Mg,Mn}$ solid solution is considerably wider than the other single-phase regions, because of the wide binary solid solubility of Mg in α-Nd at 450°C, which is about 7.5 at.% Mg. The solubility of Mn in (MgNd) was characterized as a substitution of Mg by Mn atoms at constant Nd concentration with maximum solubility of 13 at.% Mn. Other extended solid solution, (Mg_3Nd), was found to have ~3.7 at.% Mn.

The microstructure of the studied alloys showed that Mn is in equilibrium with most of the phases in the system, since it appeared as individual particles within matrices of Mg-Nd phases. Accordingly, the phase boundary lines are pointing towards the pure-Mn corner, except for the $(\alpha\text{-Nd})^{Mg,Mn}$+$Mn_{17}Nd_2$+(MgNd) phase field.

3.6. Acknowledgement

The authors would like to acknowledge NSERC for the financial support of the project through MagNET network for excellence. Dr. Dmytro Kevorkov from Concordia University is also acknowledged for providing useful suggestions.

3.7. Author's notes and significance of paper to thesis

The phase relationships of the Mg-Mn-Nd isothermal section at 450°C were established in the full composition range using diffusion couples and key alloys. Diffusion couples and key alloys were annealed for different time intervals to reveal the phase equilibrium. Diffusion zones of diffusion couples showed grains containing pure Mn, resulting from $Mn_{12}Nd_2$ phase decomposition. These grains are spread within layers of Mg-Nd compounds. It was concluded that the phase decomposition occurred as a result of the high affinity of Mg to Nd during the diffusion reaction. Thus, Nd was consumed from $Mn_{17}Nd_2$ by the diffusing Mg atoms to form Mg-Nd compounds, leaving behind pure Mn. Although this work is not focusing on studying the solid phase formation and diffusion kinetics, the previous discussion is still necessary to understand the phase equilibrium resulted from diffusion reaction. In contrary, the key alloys microstructures revealed that $Mn_{17}Nd_2$ formed from the diffusion reaction of Mn and Nd upon annealing. This conclusion was achieved by comparing the microstructures and XRD patterns of the alloys before and after annealing.

The Mg-Mn-{Ce, Nd} isothermal sections at 450°C, established in Chapters 2 and 3, showed some similarity in terms of phase relationships, where most of the phase boundary lines were pointing towards the Mn-rich corner. The next chapter discusses the effect of Mn replacement by Zn in the Ce-Mg-Zn isothermal section at 300°C. It is important to note that unlike Mn, Zn forms compounds with both Ce and Mg. Therefore it would be interesting to see the type of equilibrium phase relationships that would occur in this case.

Chapter 4 : Phase equilibria of the Ce-Mg-Zn ternary system at 300°C

ABSTRACT

The isothermal section of the Ce-Mg-Zn system at 300 °C was experimentally established in the full composition range via diffusion multiple/couples and key alloys. Annealed key alloys were used to confirm the phase equilibria obtained by diffusion multiple/couples and to determine the solid solubility ranges. Spot analysis was carried out, using wavelength dispersive X-ray spectroscopy (WDS), to identify the composition of the observed phases. The composition profiles were obtained using WDS line-scans across the diffusion zones. X-ray diffraction (XRD) was performed to identify the phases in the annealed alloys and to confirm the WDS results. Eight ternary compounds, in the Ce-Mg-Zn isothermal section at 300 °C, were observed from 45–80 at.% Zn. These are: τ_1 ($Ce_6Mg_3Zn_{19}$), τ_2 ($CeMg_{29}Zn_{25}$), τ_3 ($Ce_2Mg_3Zn_3$), τ_4 ($CeMg_3Zn_5$), τ_5 ($CeMg_7Zn_{12}$), τ_6 ($CeMg_{2.3-x}Zn_{12.8+x}$; $0 \leq x \leq 1.1$), τ_7 ($CeMgZn_4$) and τ_8 ($Ce(Mg_{1-y}Zn_y)_{11}$; $0.096 \leq y \leq 0.43$). The ternary solubility of Zn in the Ce-Mg compounds was found to increase with a decrease in Mg concentration. Accordingly, the ternary solid solubility of Zn in $CeMg_{12}$ and $CeMg_3$ was measured as 5.6 and 28.4 at.% Zn, respectively. Furthermore, the CeMg and CeZn showed a complete solid solubility. The complete solubility was confirmed by a diffusion couple made from alloys containing CeMg and CeZn compounds.

4.1. Introduction

Casting magnesium alloys exhibit low mechanical strength and ductility, and Mg alloys, in general, are limited to certain applications, because of their poor plastic properties at room temperature and poor creep resistance at elevated temperatures [80]. Thus, the development of Mg alloys with high mechanical properties becomes essential for many applications. Zn is one of the potential alloying elements added to Mg to improve its mechanical properties and corrosion resistance [81]. The problem with the Mg-Zn binary alloys is the low melting point, deeming these alloys not suitable for elevated temperature applications. In order to improve the mechanical properties at elevated temperatures, rare earth (RE) elements are added to form precipitates by age hardening [82], on the one hand. On the other hand, the addition of rare earth elements can also refine the grains and form stable compounds with a high melting point [83]. Cerium, as a major component of the mischmetal, is considered one of the most important additives to modify the Mg-Zn binary alloys [84], because it forms a series of stable intermetallic compounds.

Diffusion couples are valuable experimental techniques for phase diagram studies. They are subjected to the assumption of the local equilibria in the diffusion zone, where the diffusion reaction takes place [20]. Thin layers in thermodynamic equilibrium are formed adjacent to one another. The phase equilibria, then, can be depicted via the diffusion paths across these layers [17]. In this work, diffusion couples and one diffusion multiple were used to understand the phase relationships in the Ce-Mg-Zn isothermal section at 300 °C. Key alloys, used to verify the phase relations obtained from diffusion paths and to study the regions that were not covered by the diffusion couples, were analyzed using X-ray powder diffraction (XRD), energy dispersive X-ray spectroscopy (EDS), wavelength dispersive X-ray spectroscopy (WDS) and scanning electron microscopy (SEM).

4.2. Literature review

The solubility of Ce and Zn in Mg in the Ce-Mg-Zn system was first studied by Korolkov and Sal`dau [85] using XRD, thermal and microstructural analysis. Thermal analysis results were used to construct six vertical sections with a mass ratio of Ce:Zn of 5:1, 2:1, 1:1, 1:2, 1:4.5 and 1:10, and to draw the liquidus surface near the Mg-rich corner. On the other hand, the microstructural studies were used to determine the combined solubility of Ce and Zn in Mg in the furnace cooled samples and those annealed at 200, 300 and 335°C. Korolkov and Sal'dau [85] reported an invariant reaction at 50 at.% Mg-47.5 at.% Zn-2.5 at.% Ce occurring between 341 and 343°C without giving further explanations on the reaction type. The partial phase diagram, shown in Figure 4-1 (a), was investigated by Melnik *et al.* [86] in the region Mg-$MgZn_2$-CeMg-CeZn at 300°C using XRD. Four ternary compounds were discovered τ_1 ($CeMg_7Zn_{12}$), τ_2 ($Ce(Mg,Zn)_{10.1}$), τ_3 ($CeMg_3Zn_5$) and τ_4 ($Ce(Mg,Zn)_3$). τ_2 and τ_4 showed extended solubility ranges from 9.1 to 45.5 at.% Zn and from 35 to 45 at.% Zn at 300°C, respectively. The crystal structures of τ_1 and τ_3 are unknown. They [86] suggested the existence of a wide two-phase region between the ternary solid solutions extending from $CeMg_{12}$ up to 40 at.% Zn, and Ce_3Mg up to 48 at.% Zn at 300°C. However, these findings have not been confirmed experimentally yet. Drits *et al.* [87], using XRD, differential thermal analysis (DTA), EPMA and microstructural analysis, constructed two vertical sections in the Mg-rich corner, at 24 wt.% Zn and 34 wt.% Zn, both from 0 to 20 wt.% Ce. Two ternary compounds were confirmed using X-ray analysis; these compounds are: $CeMg_7Zn_{12}$ and $Ce(Mg_{0.2\text{-}0.3}Zn_{0.1\text{-}0.3})_{10.1}$. In addition, two invariant reactions, $L+Ce(Mg_{0.2\text{-}0.3}Zn_{0.1\text{-}0.3})_{10.1}\leftrightarrow(\alpha\text{-}Mg)+CeMg_7Zn_{12}$ at 349±1°C and $L\leftrightarrow(\alpha\text{-}Mg)+CeMg_7Zn_{12}+Mg_{51}Zn_{20}$ at 341±1°C, were detected.

Later, Kolitsch *et al.* [88] re-evaluated the partial isothermal section constructed by Melnik *et al.* [86] at 300°C. In their review, the tie line between τ_1 and $Mg_{51}Zn_{20}$ was omitted, because $Mg_{51}Zn_{20}$ is not considered stable at 300°C [89]. Kevorkov and Pekguleryuz [90] studied the Ce-Mg-Zn phase diagram at 350°C, shown in Figure 4-1 (b), by means of diffusion couples and SEM/EDS analysis. As a starting point, they [90] used the isothermal section constructed by Kolitsch *et al.* [88] at 300°C. Two new ternary compounds, labeled as phase 2 ($Ce_{1.82}Mg_{53.14}Zn_{45.04}$) and phase 6 ($Ce_{6.21}Mg_{14.56}Zn_{79.23}$), were observed. In addition, solid solubilities of the ternary solid solutions were determined using EDS/EPMA techniques. Several tie-lines were not certainly recognized in the work of Kevorkov and Pekguleryuz [90]. These tie-lines were indicated as dashed-lines in the Ce-Mg-Zn isothermal section at 350°C. Also, the phase relationships with the Ce-Zn compounds were not well determined. Chiu *et al.*[91], using thermodynamic modeling and experimental investigation, studied the solubility ranges and the invariant reactions in the Mg-rich corner (34-85 at.% Mg) at 300°C. Their aim was to find the missing key data for their model using DSC, DTA, SEM/EDS techniques. They recalculated a ternary eutectic $L\rightarrow MgZn+Mg_7Zn_3+\tau_2$ (τ_2-$CeMg_{29.2}Zn_{24.8}$) at ~341°C with 2.5 at.% Ce in the liquid. The calculated eutectic temperature [91] was very close to the temperature reported by Korolkov and Sal`dau [85] at 342°C. Although

Kevorkov and Pekguleryuz [90] studied the system at 350°C. However, they [90] did not report any liquid at that temperature. Later, Huang *et al.* [80] studied the phase relationships in the Ce-Mg-Zn system, near the Mg-rich corner, at 350°C; using SEM/EPMA, XRD, selected area electron microscopy (SAED) and transmission electron microscopy (TEM). One linear ternary compound (*T*-phase), containing 7.7 at.% Ce and 19.3-43.6 at.% Zn, in equilibrium with (α-Mg) and (α-Mg)+$Ce_{1.8}Mg_{55}Zn_{43.2}$ was observed. The *T*-phase was designated as $Ce(Mg_{1-x}Zn_x)_{11}$; x=0.096-0.43 at.% which is different than the extended solid solution $Ce(Mg_{1-x}Zn_x)_{12}$; x=0-0.078 at.%. The crystal structure was reported as C-centered orthorhombic with lattice parameters of *a*=0.96-1.029nm, *b*=1.115-1.204nm and *c*=0.94-1.015nm. Recently, the crystal structures, compositions and phase relationships in the Ce-Mg-Zn system were identified at 400°C by Huang *et al.* [84]. The *T*-phase was found in equilibrium with the liquid phase at 400°C. Thus, the phase equilibria of (α-Mg)+($CeMg_{12}$), (α-Mg)+*T*-phase, (α-Mg)+*T*-phase+liquid and (α-Mg)+*T*-phase+($CeMg_{12}$) were identified. The maximum solubility of Zn in $CeMg_{12}$ was measured to be 7.8 at.% Zn. More recently, Pavlyuk *et al.* [92] established the Ce-Mg-Zn isothermal section at 197°C, shown in Figure 4-1 (c), using single crystal XRD and EPMA techniques. Seven ternary compounds; namely: τ_1 ($Ce(Mg_{0.137}Zn_{0.863})_{11}$), τ_2 ($CeMg_{29.2}Zn_{24.8}$), τ_3 ($CeMg_{1+x}Zn_{2-x}$; x=0.48), τ_4 ($CeMg_{2.5}Zn_{4.5}$), τ_5 ($Ce_3Mg_{13}Zn_{30}$), τ_6 ($CeMg_{2.3-x}Zn_{12.8+x}$; x=0.11) and τ_7 ($Ce_{20}Mg_{19}Zn_{81}$), were reported. The crystal structures and prototypes of the five ternary compounds were determined as τ_1-*Immm* and *La_3Al_{11}*, τ_3-*Fm-3m* and $MnCu_2Al$, τ_4-*P*6/*mmm* and $TbCu_7$, τ_5-*P*6$_3$/*mmc* and $Sm_3Mg_{13}Zn_{30}$, and τ_7-*F-43m* and $Ce_{20}Mg_{19}Zn_{81}$. The crystal structures of $CeMg_{1-x}Zn_x$ continuous solid solution and of $CeMg_{12-x}Zn_x$ and $CeMg_{3-x}Zn_x$ limited solid solutions were determined precisely. In the work of Pavlyuk *et al.* [92], $Mg_{51}Zn_{20}$ was shown to be a stable phase equilibrating with (α-Mg), τ_2, $Mg_{12}Zn_{13}$ and $Ce(Mg,Zn)_{10.1}$ at 197°C. However, $Mg_{51}Zn_{20}$ is only stable in the temperature range of 321-341°C [93], and was not detected by other authors [86, 90], who studied the system at higher temperatures. Table 4-1 summarizes the ternary phases in the Ce-Mg-Zn system at different temperatures as reported in the literature [80, 84, 86, 87, 90-92]. The ternary compounds observed in the current work will be given the same naming system as reported by Pavlyuk *et al.* [92].

The lowest temperature liquid in the Ce-Mg-Zn was reported around 340°C [88, 91]. In order to avoid liquid phase formation, the current work was performed at 300°C. The main objective of this work is to establish the Ce-Mg-Zn isothermal section in the full composition range at 300°C experimentally by means of diffusion couples and key alloys, using XRD, SEM/WDS and metallography. This will help in resolving the inconsistent data of the literature and will give better understanding of the phase relationships in the system, which is necessary for Mg-based alloys design and development.

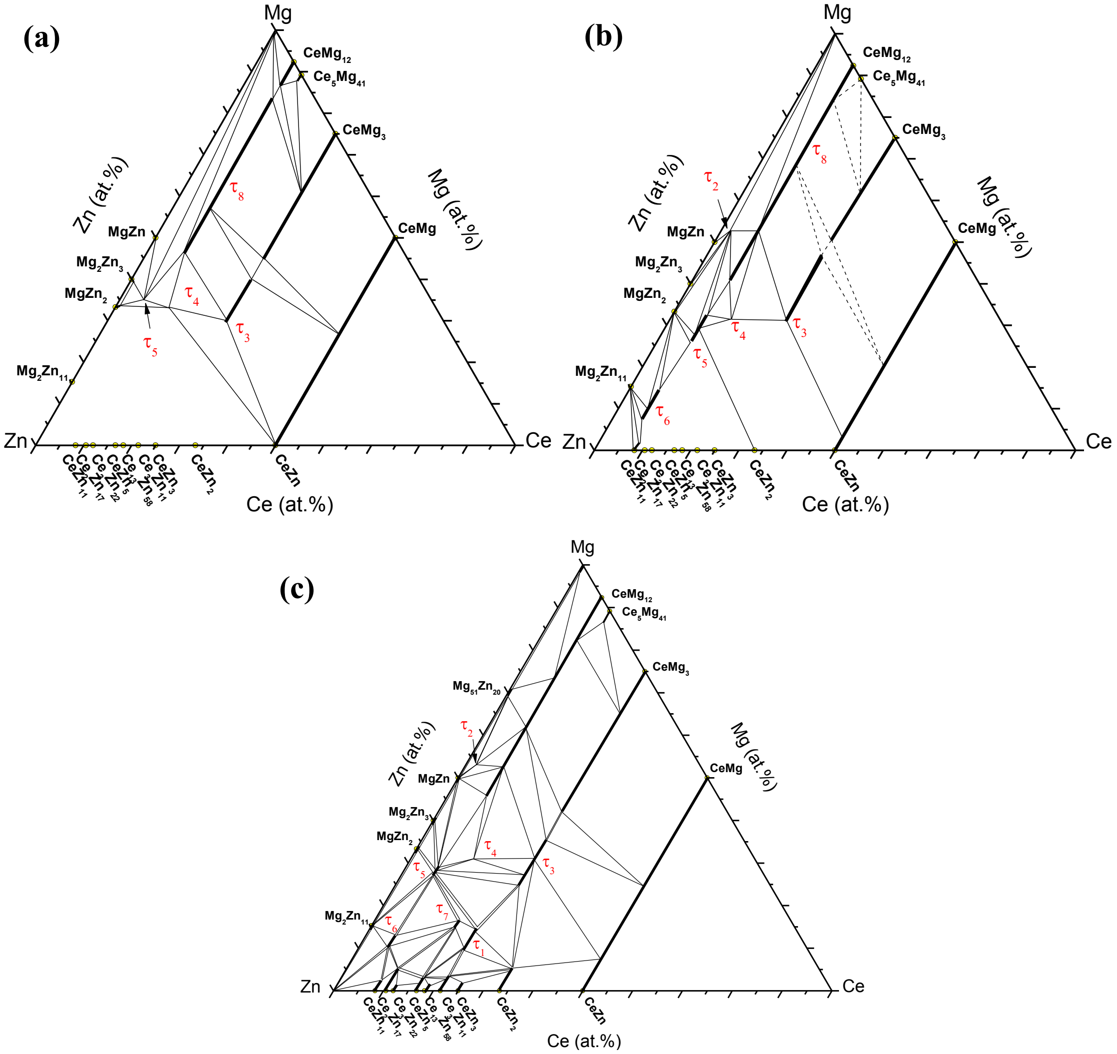

Figure 4-1: Experimental Ce-Mg-Zn isothermal section studied by (a) Melnik et al. [86] at 300°C; (b) Kevorkov and Pekguleryuz [90] at 350°C; (c) Pavlyuk et al. [92] at 197°C

Table 4-1: List of ternary phases in the Ce-Mg-Zn system reported in the literature

	Phase	Reference					
		[80]	[84]	[86]	[87]	[90]	[92]
		350°C	400°C	300°C		350°C	197°C
τ$_1$	$Ce_6Mg_3Zn_{19}$	-	-	-	-	-	$Ce_3(Zn_{0.863}Mg_{0.137})_{11}$
τ$_2$	$CeMg_{29}Zn_{25}$	-	-	-	-	Phase2	$CeMg_{29.2}Zn_{24.8}$
τ$_3$	$Ce_2Mg_3Zn_3$	-	-	$Ce_2Mg_3Zn_3$	-	Phase3	$CeMg_{1+x}Zn_{2-x}$ $0 \le x \le 0.48$
τ$_4$	$CeMg_{2.5}Zn_{4.5}$	-	-	$CeMg_3Zn_5$	-	Phase4	$CeMg_{2.5}Zn_{4.5}$
τ$_5$	$Ce_3Mg_{13}Zn_{30}$	-	-	$CeMg_7Zn_{12}$	$CeMg_7Zn_{12}$	Phase5	$Ce_3Mg_{13}Zn_{30}$
τ$_6$	$CeMg_{2.3-x}Zn_{12.8+x}$; $0 \le x \le 1.1$	-	-	-	-	Phase6	$CeMg_{2.3-1.2}Zn_{12.8-13.9}$
τ$_7$	$CeMgZn_4$	-	-	-	-	-	$Ce_{20}Mg_{19}Zn_{81}$
τ$_8$	$Ce(Mg_{1-y}Zn_y)_{11}$; $0.096 \le y \le 0.43$	$Ce(Mg_{1-y}Zn_y)_{11}$ $0.096 \le y \le 0.43$	$Ce(Mg_{1-y}Zn_y)_{11}$ $0.096 \le y \le 0.43$	$Ce(Mg,Zn)_{10.1}$	$Ce(Mg,Zn)_{10.1}$	Phase1	-

4.3. Results and discussion

Diffusion couple technique combined with selected equilibrated alloys was used to achieve more reliable information about the Ce-Mg-Zn isothermal section at 300°C. This combination guarantees the accuracy of the obtained phase equilibrium information. The phase equilibria were determined by means of solid-solid diffusion couples and a diffusion multiple. In this work, the diffusion multiple and three diffusion couples will be presented along with the results of the key alloys.

4.3.1. Diffusion multiple

The end-members of the diffusion multiple were prepared from three pure metals (Ce, Mg and Zn). Initially, the interface of the Mg and Zn end-members was polished using 1μm diamond suspension; then, the two members were screwed together using 4mm bolt and nut. After that, the assembled Mg and Zn pieces were treated as one-unit and polished in the same way as described earlier to be attached with pure Ce member, using a stainless-steel clamping ring. The idea was to obtain multiple diffusion, in the reaction zone, between the binaries and the ternary mixing at the triple point. The micrograph of diffusion multiple is presented in Figure 4-2 (a) and (b). Figure 4-2 (b) is the diffusion zone, magnified and rotated 90° counter clock wise, of Figure 4-2 (a).

From Figure 4-2, diffusion zones #1, 2, 3 and 4 represent the diffusion in the Mg-Zn binary system. These diffusion zones were recognized as Mg_2Zn_{11}, $MgZn_2$, Mg_2Zn_3 and $Mg_{12}Zn_{13}$, respectively. Zones #8 and 9 belong to the Ce-Mg binary system, and their composition represents the $CeMg_3$ and CeMg binary compounds. No diffusion occurred between pure-Ce and pure-Zn at 300°C after 21 days. Diffusion zones #5, 6 and 7 represent ternary diffusion zones occurred from the reaction at the triple point. WDS spot analysis was performed for each individual zone. The WDS spot results are listed in Table 4-2.

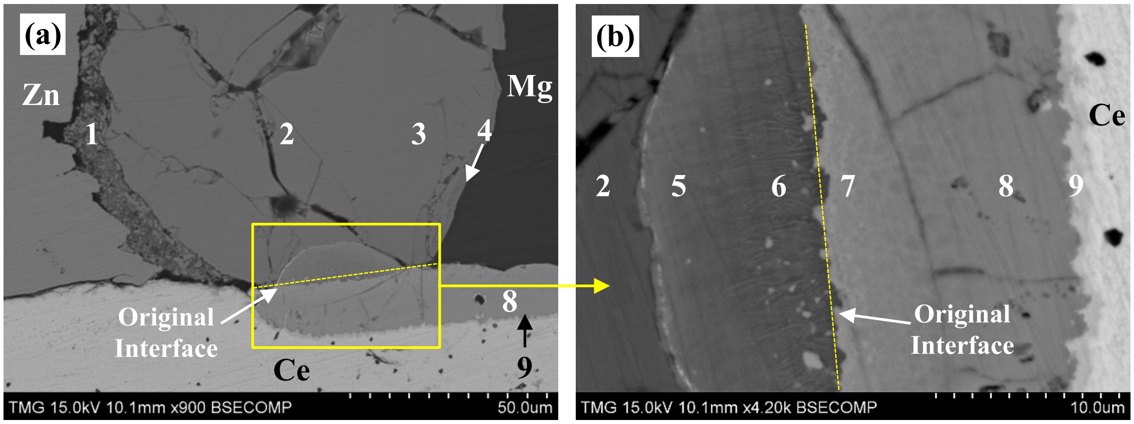

Figure 4-2: (a) and (b) SEM micrographs of the Ce-Mg-Zn diffusion multiple annealed at 300°C for 21 days. The end-members are given the chemical symbols and the diffusion layers are given numbers

WDS line-scan was performed across the microstructure shown in Figure 4-2 (b) (diffusion layers located between zones #2 and pure Ce end-members). Figure 4-3 demonstrates the composition profile of the three elements along the WDS line-scan.

Table 4-2: WDS spot analysis of different diffusion zones of the diffusion multiple

Zone	Composition (at.%)			Corresponding phase
	Ce	Mg	Zn	
Ce (end-member)	100	-	-	Ce
Mg (end-member)	-	100	-	Mg
Zn (end-member)	-	-	100	Zn
1	-	16.9	83.1	Mg_2Zn_{11}
2	-	32.9	67.1	$MgZn_2$
3	-	37.2	62.8	Mg_2Zn_3
4	-	43.5	56.5	$Mg_{12}Zn_{13}$
5	8.1	31.8	60.1	τ_5
6	9.5	55-67.1	35.5-23.3	τ_8
7	25	46.2-63.8	28.8-11.2	$Ce(Mg,Zn)_3$
8	25.5	74.5	-	$CeMg_3$
9	51.6	48.4	-	$CeMg$

According to the profile shown in Figure 4-3, the ternary compound in zone #6 and the solid solution in zone #7 were characterized based on the substitution of Mg with Zn atoms. The composition of the three elements in zone #6 matches with the composition of the ternary compound $Ce(Mg_{1-y}Zn_y)_{11}$ ($0.33 \leq y \leq 0.45$ at.%) which is denoted as τ_8 in this work. Zone #7 represents the $Ce(Mg,Zn)_3$ ternary solid solution with 25 at.% Ce and 46.2-75.0 at.% Mg. It is worthy to mention that the solubility limits of zones #6 and 7 are not accurate, since it was estimated from thin layers. However, the obtained data were enough to acquire the phase relations.

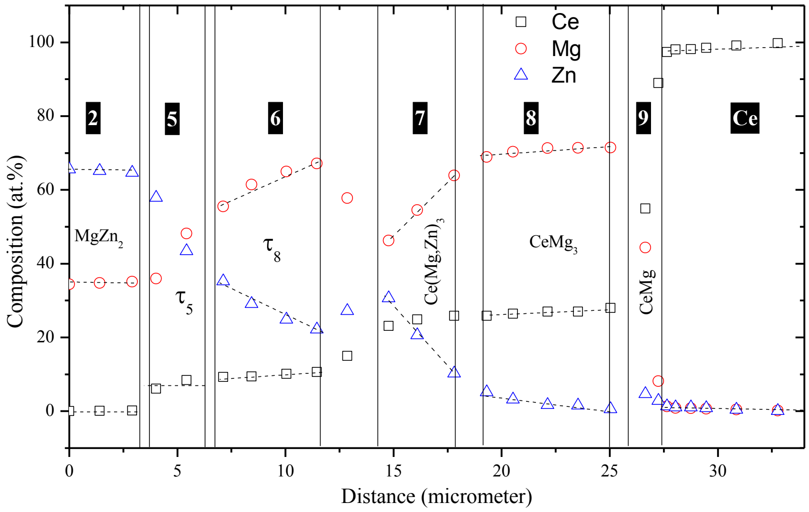

Figure 4-3: WDS line-scan across diffusion layers located between zone #2 and pure Ce end-member. The black-squared numbers given in the composition profile correspond to the number of diffusion zones indicated in Figure 4-2 and Table 4-2.

The composition of the ternary compound in zone #5 was detected by WDS spot analysis as 8.1 at.% Ce, 31.8 at.% Mg and 60.1 at.% Zn. This composition matches with the composition of $CeMg_7Zn_{12}$ ternary compound and given the symbol τ_5 in this work. The diffusion scenario between zone #8 and pure Ce end-member represents a binary diffusion behavior, because no Zn was detected beyond the interface between zones #8 and 9. This binary diffusion can be described as follows: $CeMg_3$ (zone #8) → CeMg (zone #9) → Ce (end-member).

Based on the microstructures of the diffusion zones and the WDS composition profile, the diffusion path was depicted as follows: $MgZn_2$ (zone #2) → $Ce_3Mg_{13}Zn_{30}$ → $Ce(Mg,Zn)_{10.1}$ → $CeMg_3Zn_5$ → $CeMg_3$ → CeMg (zone #9). The arrows used here represent the diffusion path and not a chemical reaction. The diffusion path depicted from diffusion multiple is represented graphically in Figure 4-4.

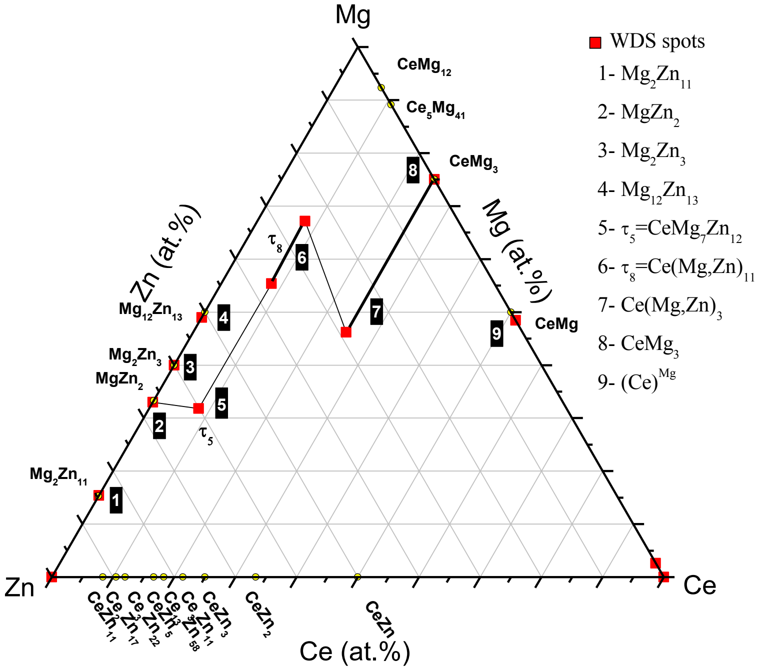

Figure 4-4: Diffusion path depicted from the diffusion multiple. Numbers in black boxes represent the diffusion zones indicated on the diffusion couple micrographs. Numbers on the right-hand side represent the phase equilibrium at every zone.

4.3.2. Diffusion couples

4.3.2.1. Diffusion couple #1: Zn/5.5Ce-94.5Mg at.%

SEM micrograph of the solid-solid diffusion couple #1 is presented in Figure 4-5 (a-c). The first end-member was made from pure Zn. The second end-member was made from an Mg and $CeMg_{12}$ two-phase binary alloy shown in Figure 4-5 (d). Diffusion couple #1 showed very peculiar phase morphologies between the two end-members, indicating the difficulty of extracting the phase relationships from this couple. These morphologies, however, are rich of information about the phase relationships, which normally requires large number of key alloys to be revealed. WDS spot analysis was carried out for every component of these diffusion zones. The WDS spot analysis results are listed in Table 4-3.

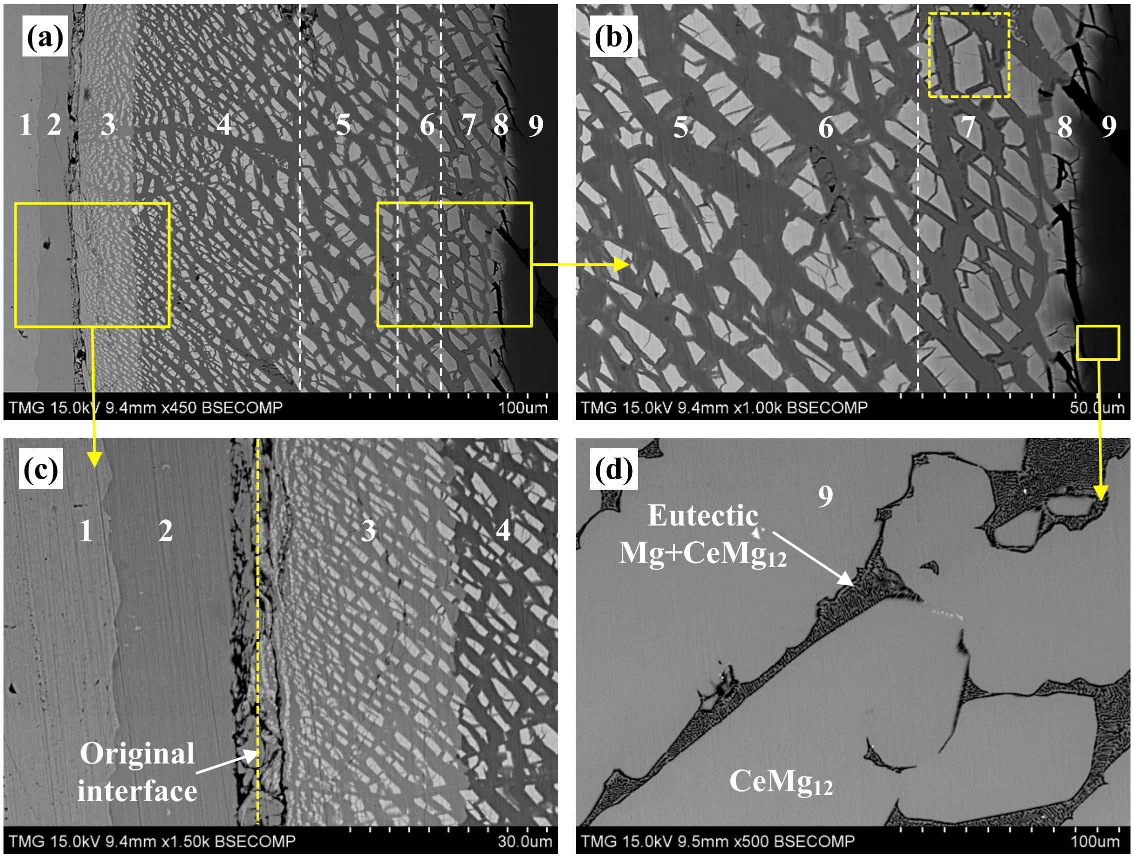

Figure 4-5: (a), (b) and (c) SEM micrographs of diffusion couple #1 annealed at 300°C for 21 days; (d) SEM micrograph of the Mg+$CeMg_{12}$ two phase alloy (end-member)

Upon annealing, nine diffusion zones formed. Diffusion zone #2 represents single phase with around 20μm in width. Diffusion zones #3-5 show layers with two-phase. Diffusion zones #6-8 show peritectic-like phase morphologies. Thus, zones #6-8 contain two two-phase equilibria, i.e.: solid A with solid B and solid B with solid C, as illustrated in zone #7 of Figure 4-5 (b) and Table 4-3.

Table 4-3: WDS spot analysis of different diffusion zones of diffusion couple #1

Zone	Composition (at.%)			Corresponding phase
	Ce	Mg	Zn	
1 (end-member)	-	-	100	Zn
2	-	15.6	84.4	Mg_2Zn_{11}
3	-	15.0	84.9	Mg_2Zn_{11} (grey)
	10.9	1.3	87.8	(Ce_2Zn_{17})
4	<1.0	32.8	67.1	$MgZn_2$ (grey)
	8.0	8.2	83.8	τ_6
5	-	33.4	66.6	$MgZn_2$ (grey)
	8.2	30.2	61.6	τ_5 (white)
6	7.9	36.0	56.1	τ_5 (white)
	0.1	32.8	67.1	$MgZn_2$(grey)
	0.1	32.8	67.1	$MgZn_2$(grey)
	2.3	49.0	48.7	τ_2
7	2.3	49.0	48.7	τ_2
	0.2	38.9	60.9	Mg_2Zn_3 (grey)
	8.6	42.4	49.0	τ_8 (white)
	2.3	49.0	48.7	τ_2
8	-	100	-	Mg
	2.3	49.0	48.7	τ_2
	8.1	53.2	38.7	τ_8 (white)
	-	100	-	Mg
9 (end-member)	8.66	91.34	-	$Ce(Mg,Zn)_{12}$
	-	100	-	Mg

The SEM micrograph of diffusion couple #1 in Figure 4-5 (a) showed a white phase, islanding within diffusion zones #3-8, and the grey phase is the matrix. WDS spots were performed across diffusion zones #3-8 to measure the composition of the white phase islands and the grey phase in the matrix. Figure 4-6 (a) and (b) show the composition profile of the white and grey phases across the diffusion couple. The x-axis does not represent a metric distance; hence it was labeled as step, because these readings were taken across the diffusion zone with no exact spatial measurements. One binary compound CeMg$_{12}$ and three linear ternary compounds τ_6 (CeMg$_{2.3-x}$Zn$_{12.8+x}$; $0 \leq x \leq 1.1$), τ_5 (CeMg$_7$Zn$_{12}$), and τ_8 (Ce(Mg$_{1-y}$Zny)$_{11}$; $0.096 \leq y \leq 0.43$) were detected from the white phase profile in Figure 4-6 (a), whereas, three binary compounds (Mg$_2$Zn$_{11}$, MgZn$_2$ and Mg$_2$Zn$_3$) were detected in the grey phase profile, Figure 4-6 (b). The concentration of Ce was almost constant within the ternary phases' profile in Figure 4-6 (a).

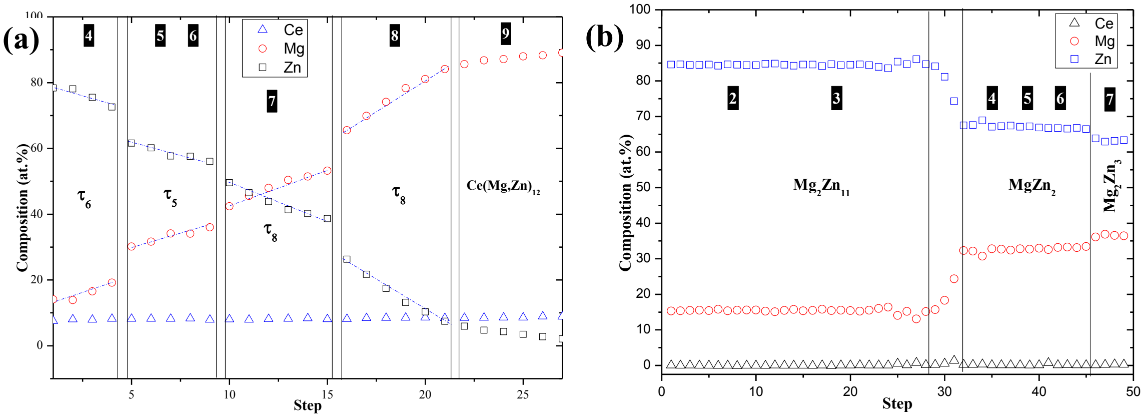

Figure 4-6: WDS composition profile of the (a) white phase islanding in the two-phase diffusion zones # 4-9; (b) grey phase in the matrix of the same diffusion zones including zone #2

The sequence of the phases in the grey phase matrix was similar to that of the Mg-Zn binary diffusion couple, annealed at 300°C and 21 days, shown in Figure 4-7 (a). WDS spot results of the Mg-Zn diffusion couple are listed in Table 4-4. The ternary diffusion couple #1 was compared with the Mg-Zn binary diffusion couple to give better understanding of the phase relations between the Mg-Zn binary compounds and the τ_5, τ_6 and τ_8 ternary compounds. In other words, the ternary compounds were distributed in a matrix of Mg-Zn compound layers as illustrated in Figure 4-7 (b).

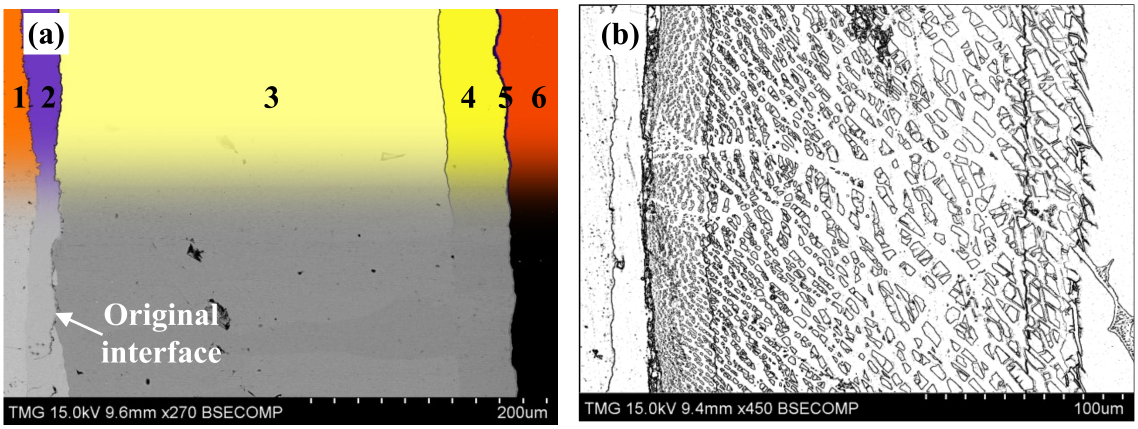

Figure 4-7: (a) SEM micrograph of the Mg-Zn binary diffusion couple annealed at 300°C for 21 days; (b) sketch of the ternary diffusion couple #1 showing three ternary compounds islanding in the Mg-Zn compound layers. Reader is encouraged to refer to the online version for the colored image

Table 4-4: WDS spot analysis of Mg-Zn binary diffusion couple

Zone	Composition (at.%)		Corresponding phase
	Mg	Zn	
1 (end-member)	-	100	Zn
2	15.3	84.7	Mg_2Zn_{11}
3	67.1	32.9	$MgZn_2$
4	61.8	39.2	Mg_2Zn_3
5	52.3	47.7	$Mg_{12}Zn_{13}$
6 (end-member)	100	-	Mg

EDS elemental mapping was used to define the composition of diffusion zones #5 to 9 shown in Figure 4-8 (a). The Ce, Mg and Zn elemental maps are shown in Figure 4-8 (b-d), respectively. The color contrast of the Mg element, Figure 4-8 (c), revealed that the dark phase at the interface between zones #8 and 9 is pure Mg, and not a crack as was suspected. The corresponding phase relationships determined from this part of diffusion couple will be discussed in combination with Figure 4-9.

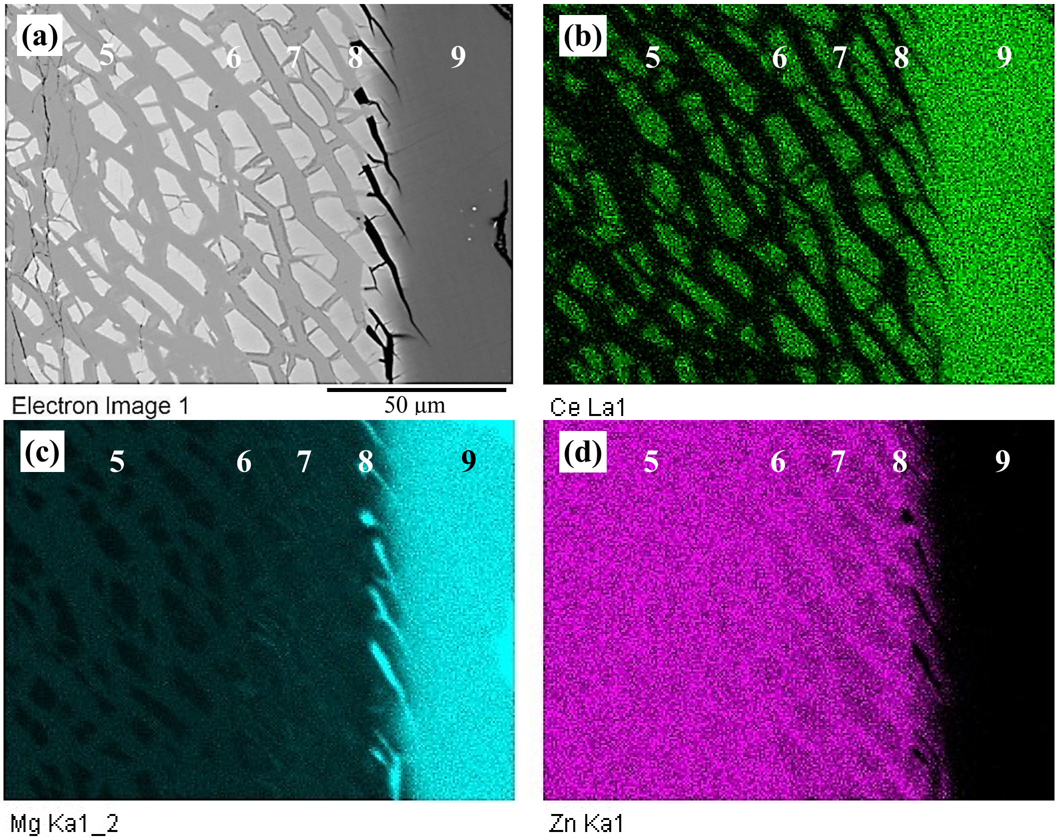

Figure 4-8: (a) SEM micrograph of zones #5-8 of diffusion couple #1; (b), (c) and (d) EDS elemental maps of Ce, Mg and Zn respectively. Reader is encouraged to refer to the online version to see the colored maps

The SEM micrograph shown in Figure 4-9 shows the formation of a dark phase falling between τ_8 and pure Mg phases. This phase is in equilibrium with τ_8, Mg_2Zn_3, $MgZn_2$, τ_5 and pure Mg. WDS spot analysis revealed that this phase is τ_2 ($CeMg_{29.2}Zn_{24.8}$) according to Table 4-1. Based on its chemical composition, τ_2 is located near the binary $Mg_{12}Zn_{13}$. However, the binary $Mg_{12}Zn_{13}$ appears as a thin layer in Figure 4-7 (zone #5). It is expected that the $Mg_{12}Zn_{13}$ layer was breaking into small parts upon the subsequent formation of the two ternary compounds τ_5 and τ_8, providing the 2.0 at.% Ce necessary to form τ_2.

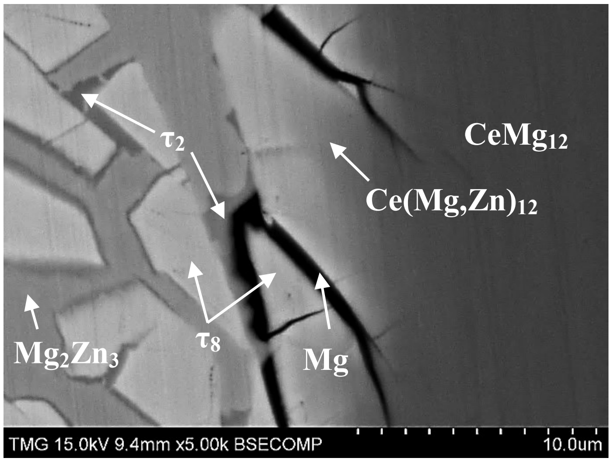

Figure 4-9: SEM micrograph of diffusion zones #7 and 8 of diffusion couple #1

One can raise an issue regarding the morphology of the scattered ternary compounds over a matrix of Mg-Zn compounds. It is presumed that the scattered formation of the ternary compounds was due to the preferential reaction of the diffusing species. Referring to the diffusion multiple in Figure 4-2 (a), Mg-Zn binary diffusion couple has thicker diffusion layers than those of Ce-Mg binary couple, as well as no diffusion occurred in the Ce-Zn binary diffusion couple at 300°C and 21 days. In conclusion, the mobility of the atoms in Mg-Zn system is higher than the atoms in both Ce-Mg and Ce-Zn systems. This conclusion will be discussed further below.

The composition of Ce was constant at 8.2 at.% in the profile of the $Ce(Mg,Zn)_{12}$ solid solution and the ternary compounds τ_8, τ_5 and τ_6 shown in Figure 4-6 (a). However, the Ce concentration must be 7.6 at.% Ce for $Ce(Mg,Zn)_{12}$. This difference could be due to the error of the WDS measurements, which was estimated as ±1 at.% for Ce. Thus, it is most likely that the ternary compounds were formed from the $Ce(Mg,Zn)_{12}$ due to the Mg/Zn atomic exchange. This can also be supported by monitoring the end of the white phase traces, which can indicate the original location of the interface between the two end-members. Figure 4-5 (c) shows clearly the location of the original interface where the crack exists and the Mg_2Zn_{11} forms on both sides. The $Ce(Mg,Zn)_{12}$ solid solution is characterized by the substitution of Mg with Zn atoms. However, Zn has smaller atomic radius (133pm) than Mg (160pm) [25]. Because of this difference in the atomic radii, distortion in the lattice structure might take place, and various ternary compounds with constant Ce concentration can be formed when Zn content reaches a threshold value. Evidence to this distortion, Figure 4-5 (a) shows that the size of the white grains near the Zn-rich side is smaller than those adjacent to the $Ce(Mg,Zn)_{12}$ solid solution; this was also illustrated in Figure 4-7 (b). The grains with more Zn, due to substitution, show smaller grain size. In addition, the substituted Mg atoms can be consumed by excess Zn atoms through the diffusion reaction to form Mg-Zn compounds. This can provide an explanation for the presence of pure-Mg (black phase in zones #8 and 9), which might be filtered from the solid solution due to the substitution mechanism.

In this system, the same phase morphology was observed in all diffusion couples containing Zn-rich end-members, specifically whenever a substitutional solid solution encountered within the diffusion path. Diffusion couple #2, for example, showed the same morphology due to the Mg/Zn substitution in the $Ce(Mg,Zn)_3$ solid solution. The results of diffusion couple #2 will be presented next.

According to the phase diagram rules, in a ternary system, the maximum number of phases in each diffusion layer is 2. However, in diffusion zones #6, 7 and 8, three phases were detected. These phases are $\tau_2+\tau_5+MgZn_2$ $\tau_5+Mg_2Zn_3+\tau_2$ and $\tau_8+Mg_2Zn_3+\tau_2$, respectively. This could be due to the anisotropic diffusion, which results sometimes during the sequential growth of the diffusion layers [77]. Such anisotropic growth might result in volumetric mismatch, at the interface between two dissimilar phases, which occurs due to the lattice distortion. This can give more chance to the phases in the diffusion layers to break a part into scattered islands equilibrating with the surrounding phases.

From the WDS spots and line-scans and the EDS elemental maps, the path of diffusion couple #1 is represented graphically in Figure 4-10. The two end-members of diffusion couple #1 are connected by a dashed line.

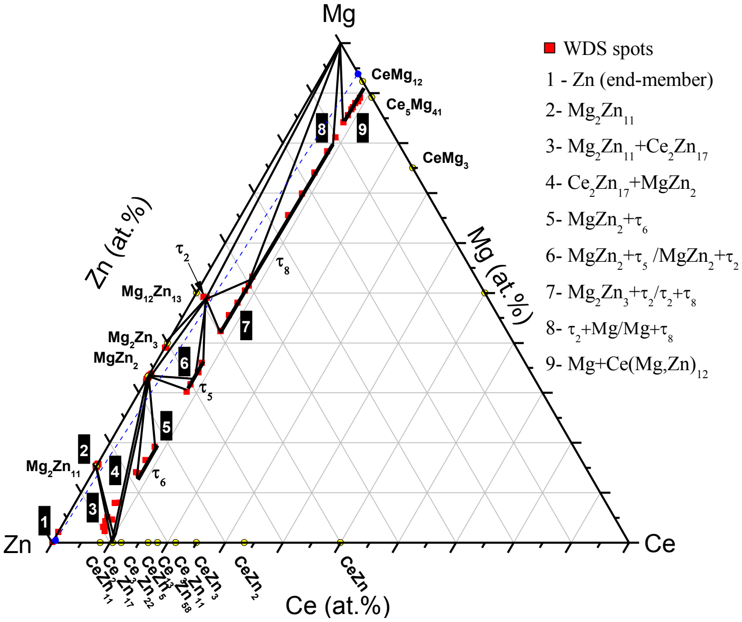

Figure 4-10: Phase equilibria depicted from the WDS spot analysis and line-scans across diffusion couple #1. Numbers in black boxes represent the diffusion zones indicated on the diffusion couple micrographs. Numbers on the right-hand side represent the phases in every zone.

5.4.2.2. Diffusion couple #2: Zn/27.0Ce-73.0Mg at.%

The SEM micrographs of the solid-solid diffusion couple #2 are represented in Figure 4-11. The first end-member was made from pure Zn. The second end-member was made from the CeMg and $CeMg_3$ two-phase binary alloy. Diffusion couple #2, similar to diffusion couple #1, showed dispersed ternary compounds within a matrix of Mg-Zn binary compounds. Also, the size of the white grains is decreasing with the increase in Zn concentration. The occurrence of this morphology was thoroughly discussed within the results of diffusion couple #1. In contrast to diffusion couple #1, the results of diffusion couple #2 showed that τ_3 is forming from the $Ce(Mg,Zn)_3$ solid solution due to further substitution of Mg by Zn, then τ_5 and τ_6 formed later, due to the increase in Zn concentration.

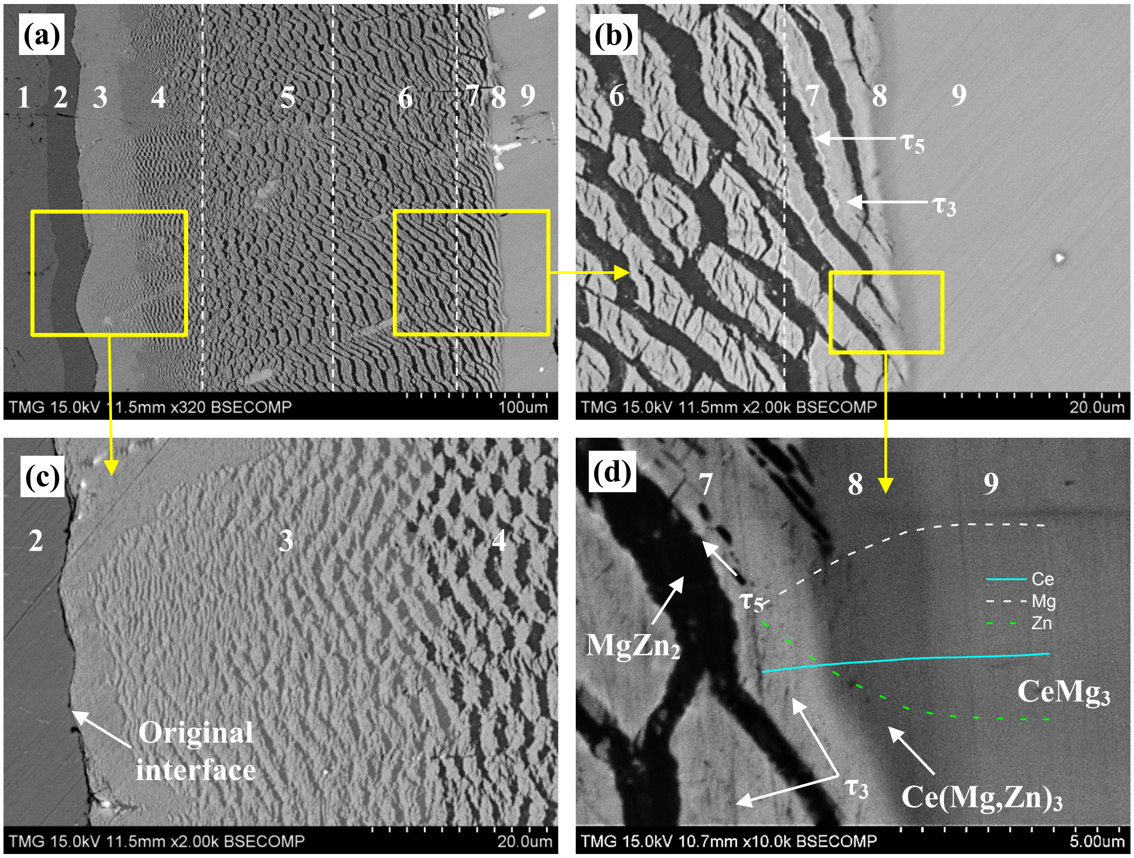

Figure 4-11: (a), (b), (c) and (d) SEM micrographs of diffusion couple #2 annealed at 300°C and 21 days

Nine diffusion zones were determined and analyzed using WDS spot analysis and line-scans. Diffusion zone #2 represents single phase of 10µm thickness. Figure 4-11 (c) is a magnified part from diffusion couple #2 showing diffusion zone #3; which represents a two-phase equilibrium between Mg_2Zn_{11} and Ce_2Zn_{17}. Diffusion zones #4, 5, 6 and 7 have two compounds. The results of WDS spot analysis of diffusion couple #2 are listed in Table 4-5. Figure 4-11 (b) shows a very thin bright phase surrounding τ_3 ($Ce_2Mg_3Zn_3$), the white dendrites of zone #7. Thus, the diffusion zone was magnified up to 10kX (Figure 4-11 (d)) to find out the composition of that phase using WDS spot analysis. The WDS spot analysis gave the following stoichiometry: 9.9 at.% Ce, 27.6 at.% Mg and 62.5 at.% Zn, which corresponding to τ_5 ($CeMg_7Zn_{12}$). This means that τ_5 is in equilibrium with $MgZn_2$ and τ_3. Also, the composition profile is represented in the same figure to show the concentration gradient within τ_3, Ce(Mg,Zn)$_3$ and $CeMg_3$.

Table 4-5: WDS spot analysis of different diffusion zones of diffusion couple #2

Zone	Composition (at.%)			Corresponding phase
	Ce	Mg	Zn	
1 (end-member)	0	100	0	Zn
2	0	15.9	84.1	Mg_2Zn_{11}
3	7.2 0	2.9 15.9	89.9 84.1	(Ce_2Zn_{17}) Mg_2Zn_{11}
4	7.5 0.7	5.2 31.6	87.3 67.7	(Ce_2Zn_{17}) $MgZn_2$ (dark)
5	5.9 0.7	10.8 31.6	83.3 67.7	τ_6 $MgZn_2$ (dark)
6	9.9 0.2	27.6 33.5	62.5 66.3	τ_5 (white) $MgZn_2$ (dark)
7	24.0 14.1	29.2 31.6	46.8 54.3	τ_3 τ_5
8	24.3	57.8	17.9	Ce(Mg,Zn)$_3$
9 (end-member)	25.0 50.0	75.0 50.0	0 0	$CeMg_3$ CeMg

Three ternary compounds, formed within the two-phase diffusion zones #5 to 7, were observed. These compounds are: τ_6, τ_5 and τ_3. The Three compounds were characterized by the Mg/Zn substitution at constant Ce concentration. The homogeneity ranges of these compounds were estimated, using WDS spot analysis, to be 6.0-12.4 at.%

Mg, 24.0-31.6 at.% Mg, and 25.0-29.0 at.% Mg, respectively. EDS elemental mapping was performed for diffusion zones #6 to 9, as shown in Figure 4-12. The elemental maps were used to recognize the composition of every phase in the targeted area; as well as, to determine the boundaries of every diffusion zone. Accordingly, the dark phase in the matrix of diffusion zones #6 and 7 (Figure 4-12 (a)) was recognized to be a binary compound containing Mg and Zn, since the trace of this phase in the Ce map is dark. In contrast, the traces of the bright dendrites, for the same diffusion zones, represent ternary compounds.

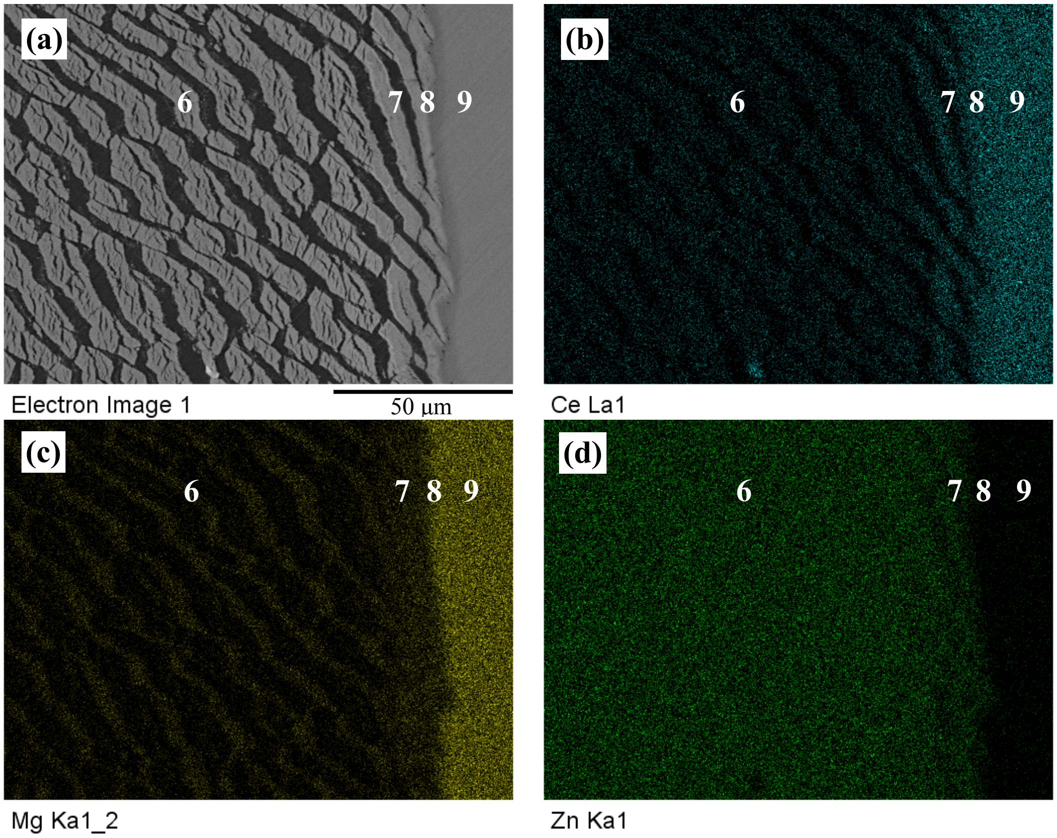

Figure 4-12: a) SEM micrograph of zones #6, 7, 8 and 9 of diffusion couple #2; (b), (c) and (d) EDS elemental maps of Ce, Mg and Zn respectively. Reader is encouraged to refer to the online version for the colored maps

Figure 4-12 (b), shows that the ternary dendrites of zone #7 contain higher Ce concentration in Zone #6, whereas, the proportion between Mg and Zn concentrations remains the same. However, these dendrites seem connected.

The phase equilibria depicted from diffusion couple #2 are represented graphically in Figure 4-13. The two end-members of diffusion couple #2 are connected by a dashed line.

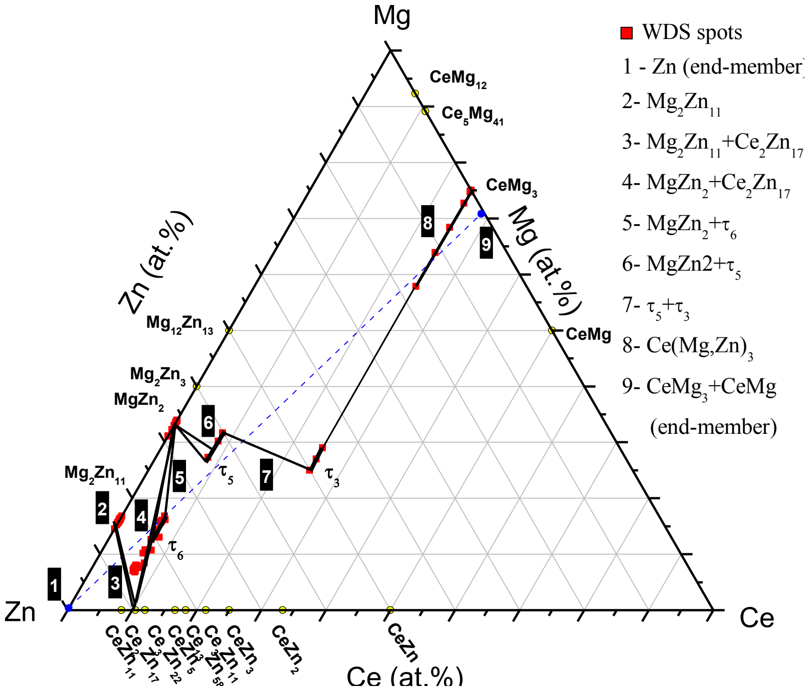

Figure 4-13: Phase equilibria depicted from the WDS spot analysis across diffusion couple #2

5.4.2.3. Diffusion couple #3: Ce/97.0Mg-3.0Zn at.%

Solid-solid diffusion couple #3, shown in Figure 4-14, was made from pure Ce and a binary alloy containing 83.0 at.% Mg and 17.0 at.% Zn, Figure 4-14 (b). Unlike other diffusion couples and the diffusion multiple, diffusion couple #3 was annealed for 40 days instead of 21 days, since no diffusion layers were observed after 21 days of annealing. 30 days was also tried and no diffusion layers could be observed either.

However, 6 diffusion layers with total thickness of ~12μm formed after 40 days of annealing. The WDS spot results of the diffusion zones are listed in Table 4-6.

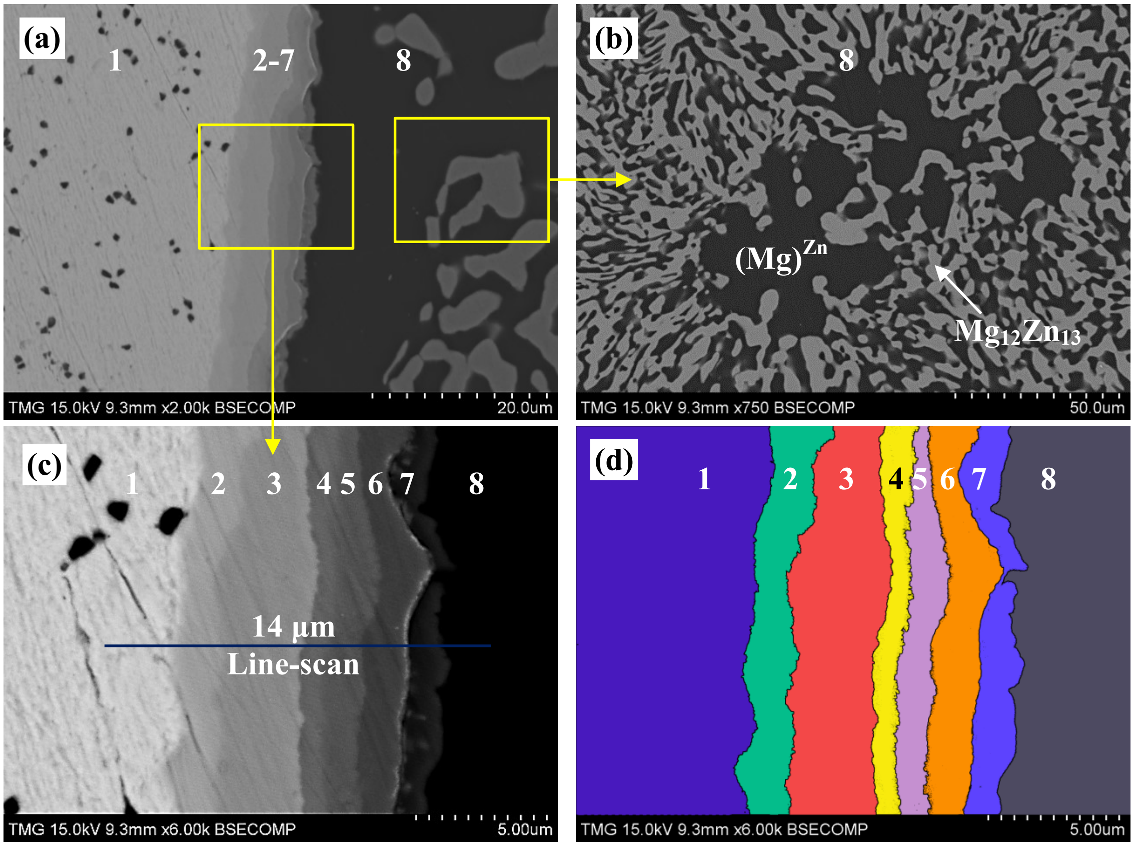

Figure 4-14: (a), (c) and (d) SEM micrographs of diffusion couple #3; (b) SEM micrograph of the 83Mg-17Zn (at.%) end-member

Table 4-6: WDS spot analysis of different diffusion zones of diffusion couple #3

Zone	Composition (at.%)			Corresponding phase
	Ce	Mg	Zn	
1 (end-member)	100	0	0	Ce
2	47.8	0	52.2	CeZn
3	32.1	0	67.9	$CeZn_2$
4	24.5	24.0	51.5	τ_3
5	16.7	20.4	62.9	τ_7
6	7.9	27.8	64.3	τ_5
7	2.0	53.7	44.3	τ_2
8 (end-member)	0	48.0	52.0	$Mg_{12}Zn_{13}$
	0	97.6	2.4	(Mg)^{Zn}

WDS line-scan was performed across the diffusion zones of diffusion couple #3. The composition of each layer was determined by, at least, two spots along the WDS line-scan as shown in Figure 4-15.

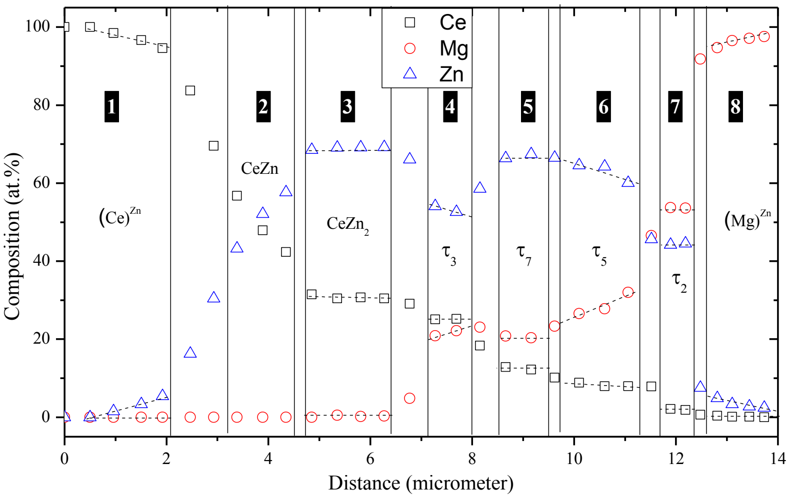

Figure 4-15: WDS line-scan across diffusion couple #3

Based on the WDS spot analysis and line-scan, the solubility of Zn in Ce, zone #1, was determined as 4.0 at.% Zn. As well as, the solid solubility of Zn in Mg, zone #8, was determined as 3.6 at.% Zn. Diffusion zones #2 and 3 represent the CeZn and $CeZn_2$ binary compounds, respectively. Diffusion zones #4 and 6 represent the ternary compounds τ_3 and τ_5, which is characterized by the Mg/Zn substitution at constant Ce composition. Diffusion zones #5 and 7 represent the stoichiometric ternary compounds τ_7 and τ_2, respectively.

According to WDS spot analysis and line-scans, the diffusion path of diffusion couple #3 can be represented as follows: Pure Ce (end-member) → $(Ce)^{Zn}$ → CeZn → $CeZn_2$ → τ_3 → τ_7 → τ_5 → τ_2 → $(Mg)^{Zn}$ → $(Mg)^{Zn}$+$Mg_{12}Zn_{13}$ (end-member). The diffusion path is represented graphically in Figure 4-16. The two end-members are connected by a dashed line.

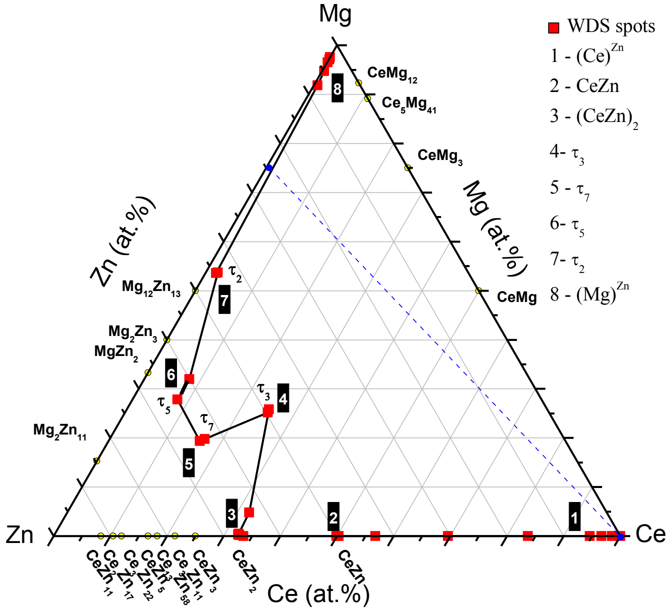

Figure 4-16: Diffusion path depicted from diffusion couple #3

The diffusion path of diffusion couple #3 (Figure 4-16) shows some of the phases, corresponding to the diffusion zones #2-6 (Figure 4-14), that form near the Zn-rich side. In order to understand the diffusion reaction, the mass balance principle must be taken into account. In this case, the diffusion reaction can be described as following: the pure Ce exists in the end-member of diffusion couple #3 was diffusing against Mg and Zn atoms, which were provided by the two-phase alloy of the other end-member. The atomic exchange took place, and the Ce concentration dropped gradually across the formed diffusion zones as shown in the WDS composition profile in Figure 4-15. Accordingly, several Zn-rich ternary compounds were formed to the left side of the line connecting the two end-members. In this case, the mass of the reacted Ce and Zn must to be compensated with more Mg. Thus, the diffusion reaction switched its path sharply towards the Mg-rich corner after zone #5, and the two-phase end-member contributed to this compensation by forming a considerably thick layer of Mg-rich solid solution,

$(Mg)^{Zn}$ in zone #8, to balance the mass. Therefore, the diffusion path fulfilled the mass balance condition by intersecting the line connecting the two end-members at least once.

Seven ternary compounds were detected in diffusion multiple and diffusion couples # 1, 2 and 3; these phases are: τ_2, τ_3, τ_4, τ_5, τ_6, τ_7 and τ_8. Obviously several of these compounds were observed in more than one couple, providing confirmation of their presence in the system at 300°C.

The three diffusion couples gave clear idea about the phase equilibria in the Zn-rich corner, up to 33 at.% Mg and 10 at.% Ce; since their results in that part were consistent. Other regions of the Ce-Mg-Zn isothermal section at 300°C were determined by the key alloys experiments and their results are discussed in the following section.

4.3.3. Key alloys analysis

Key alloys were used to verify the results obtained from diffusion couples experiments, and to cover the remaining parts of the Ce-Mg-Zn isothermal section at 300°C. Thus, twenty eight key alloys were prepared with different compositions. The actual composition was obtained by average of three EDS area-analysis. The actual composition of few samples (#1, 2, 4, 13 and 14), selected randomly, was measured using inductively coupled plasma-optical emission spectrometry (ICP-OEM) to confirm the EDS area measurements. Both EDS and ICP-OEM measurements were in good agreement. Figure 4-17 shows the actual composition obtained from the EDS and ICO-OEM methods.

Alloys were brought to equilibrium after annealing at 300°C for 30 days. WDS spot analysis was performed on the annealed samples to determine the composition of the observed phases. X-ray diffraction of the samples' was performed to identify the equilibrated phases and verify the phase relations obtained from WDS analysis.

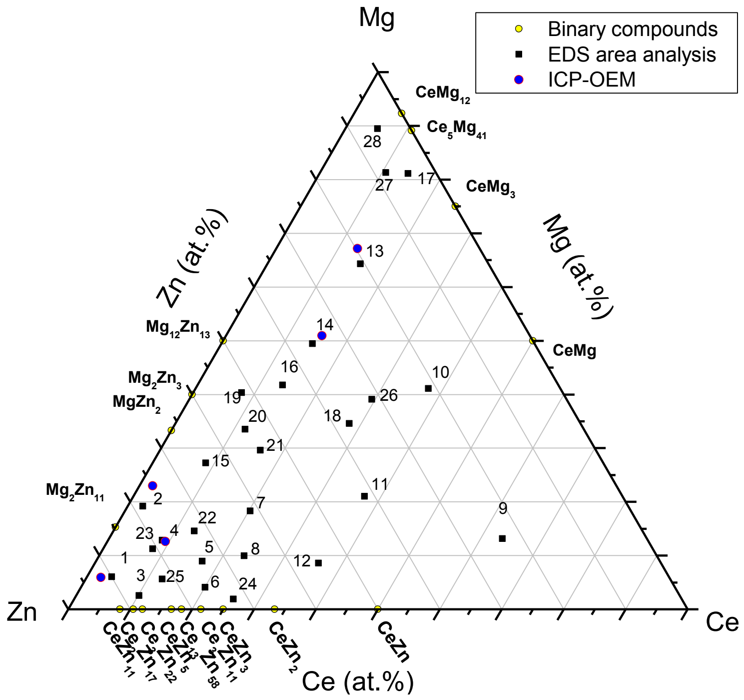

Figure 4-17: The actual composition of the key alloys obtained by EDS area analysis and ICP-OEM

5.4.3.1. Alloys with three-phase equilibria

Several three-phase regions in the Ce-Mg-Zn isothermal section at 300°C were determined by key alloys experiments. WDS spot analyses of samples with three-phase equilibria are listed in Table 4-7. Figure 4-18 shows the SEM micrographs of some selected alloys with three-phase equilibria with the labels of the detected phases. X-ray powder diffraction patterns of samples #1, 2 and 12, shown in Figure 4-19, are given as example of phase identification using X-ray diffraction analysis. However, XRD was performed on the all prepared samples. The results of WDS spot analysis and XRD were consistent for the phases of known crystal structures. More studies regarding the phases on the unknown crystal structures are still needed.

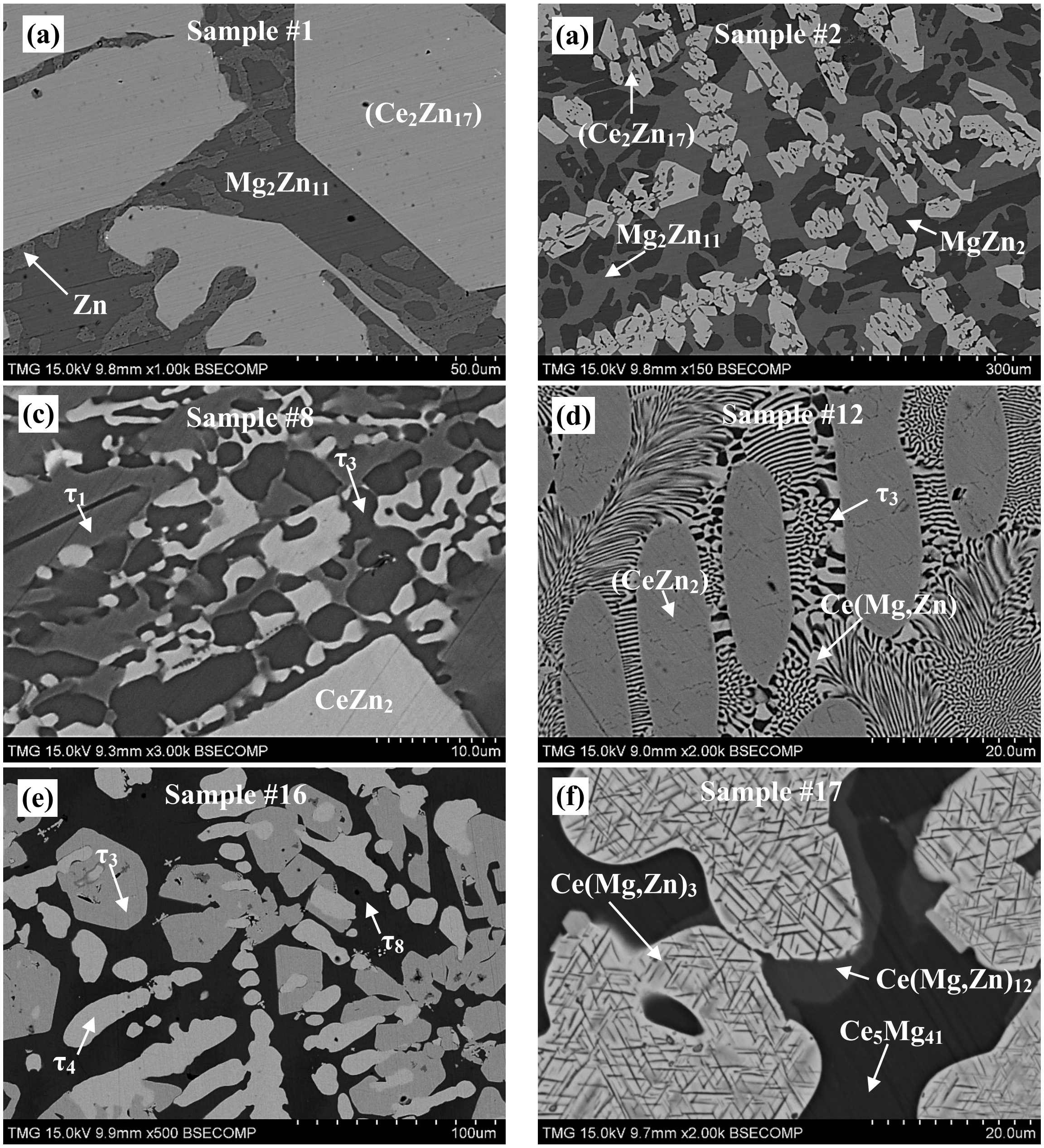

Figure 4-18: SEM micrographs of some samples of three-phase equilibria (a) sample #1; (b) sample #2; (c) sample #8; (d) sample #12; (e) sample #16; (f) sample #17

Table 4-7: WDS spot analysis of samples with three-phase equilibria

Sample number	Actual composition EDS (at.%)			WDS composition (at.%)			Corresponding phase
	Ce	Mg	Zn	Ce	Mg	Zn	
1	4.0	6.0	90.0	10.4	0.8	88.8	(Ce_2Zn_{17})
				0.0	15.8	84.2	Mg_2Zn_{11}
				0.0	1.0	99.0	$(Zn)^{Mg}$
2	2.5	19.2	78.3	10.4	1.2	88.4	(Ce_2Zn_{17})
				0.0	15.1	84.9	Mg_2Zn_{11}
				0.0	33.1	66.9	$MgZn_2$
5	17.2	8.9	73.8	16.4	16.6	67.0	τ_7
				16.5	4.1	79.4	($CeZn_5$)
				20.1	8.7	71.2	τ_1
7	20.2	18.3	61.5	16.3	16.7	67.0	τ_7
				24.5	23.3	52.2	τ_3
				20.6	8.6	70.8	τ_1
8	23.4	9.9	66.7	32.4	0.5	67.1	($CeZn_2$)
				20.8	7.2	72.0	τ_1
				25.0	22.0	53.0	$Ce_2Mg_3Zn_3$
12	36.1	8.6	55.3	50.0	8.5	41.5	Ce(Mg,Zn)
				33.3	1.9	64.8	($CeZn_2$)
				25.0	25.0	50.0	τ_3
16	13.7	41.7	44.6	25	25	50	τ_3
				14.3	28.9	56.8	τ_4
				8.5	56.8	34.7	τ_8
17	15.3	81.2	3.5	25.0	69.5	5.5	$Ce(Mg,Zn)_3$
				10.8	89.2	0	Ce_5Mg_{41}
				8.3	88.9	2.8	$Ce(Mg,Zn)_{12}$
24	25.7	1.6	72.7	32.0	0	68.0	$CeZn_2$
				20.5	2.6	76.9	(Ce_3Zn_{11})
				20.4	7.5	72.1	τ_1
25	12.3	5.6	82.1	16.3	4.5	79.2	$CeZn_5$
				11.2	2.2	86.6	(Ce_2Zn_{17})
				11.2	13.9	74.9	τ_6
28	5.2	89.5	5.3	8.6	79	12.4	τ_8
				8.6	85.3	6.1	$Ce(Mg,Zn)_{12}$
				1.0	97.5	1.5	$(Mg)^{Ce,Zn}$

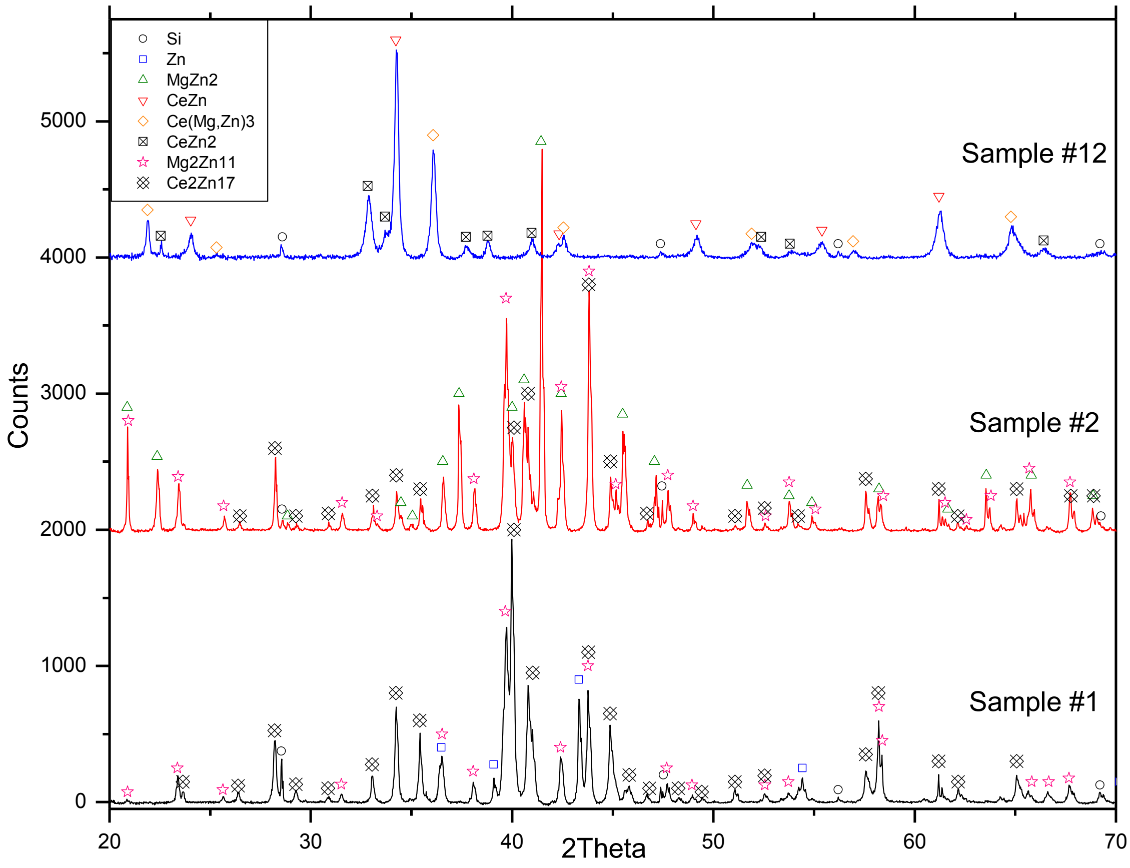

Figure 4-19: The X-ray powder diffraction of the annealed samples #1, 2 and 12 showing three phase equilibria. Silicon was used as a calibration standard to correct the zero shift and specimen displacement errors

It is worth noting that Figure 4-18 (f) exhibits a lamellar structure in the white grains. This structure has similarity to what so called Widmanstätten pattern, which forms due to lamellar growth of one phase in the crystal lattice of other phase. Because these phases are very small, it was difficult to determine their composition by WDS spot analysis. However, using XRD analysis, Ce(Mg,Zn)$_{12}$, Ce$_5$Mg$_{41}$ and Ce(Mg,Zn)$_3$ were positively determined in the diffraction pattern of sample #17. Since Ce(Mg,Zn)$_{12}$ and Ce$_5$Mg$_{41}$ are well identified according to WDS measurements, the white phase containing lamellar structure is assigned as Ce(Mg,Zn)$_3$. The maximum solubility of Zn in Ce(Mg,Zn)$_3$ was found to be 5.5 at.% Zn.

5.4.3.2. Alloys with two-phase equilibria

Many two-phase regions, in the Ce-Mg-Zn isothermal section at 300°C, were determined. In this section, selected alloys with two-phase equilibrium are presented in Figure 4-20. The WDS spot analyses of samples with two-phase equilibria are listed in Table 4-8. XRD patterns of samples #3, 10 and 23, shown in Figure 4-21, are given as example of phase identification using X-ray diffraction analysis.

SEM micrograph of sample #3, shown in Figure 4-20 (a), represents the two-phase equilibria between the two extended solid solutions from (Ce$_2$Zn$_{17}$) and (Ce$_3$Zn$_{22}$). Figure 4-20 (b) represents the two ternary solid solutions (Ce$_{13}$Zn$_{58}$) and (Ce$_3$Zn$_{11}$) occurring in sample #6. The maximum solubility of Mg in Ce-Zn binary compounds is listed in Table 4-8.

High magnification was required to observe the phase relationships of sample #9. Thus, SEM micrograph of sample #9 was magnified up to 5kX, as shown in Figure 4-20 (c). Fine eutectic-like structure, containing Ce+Ce(Mg,Zn), was in equilibrium with the Ce(Mg,Zn) ternary solid solution. Other micrographs correspond to the phase equilibrium that can be inferred from the labels.

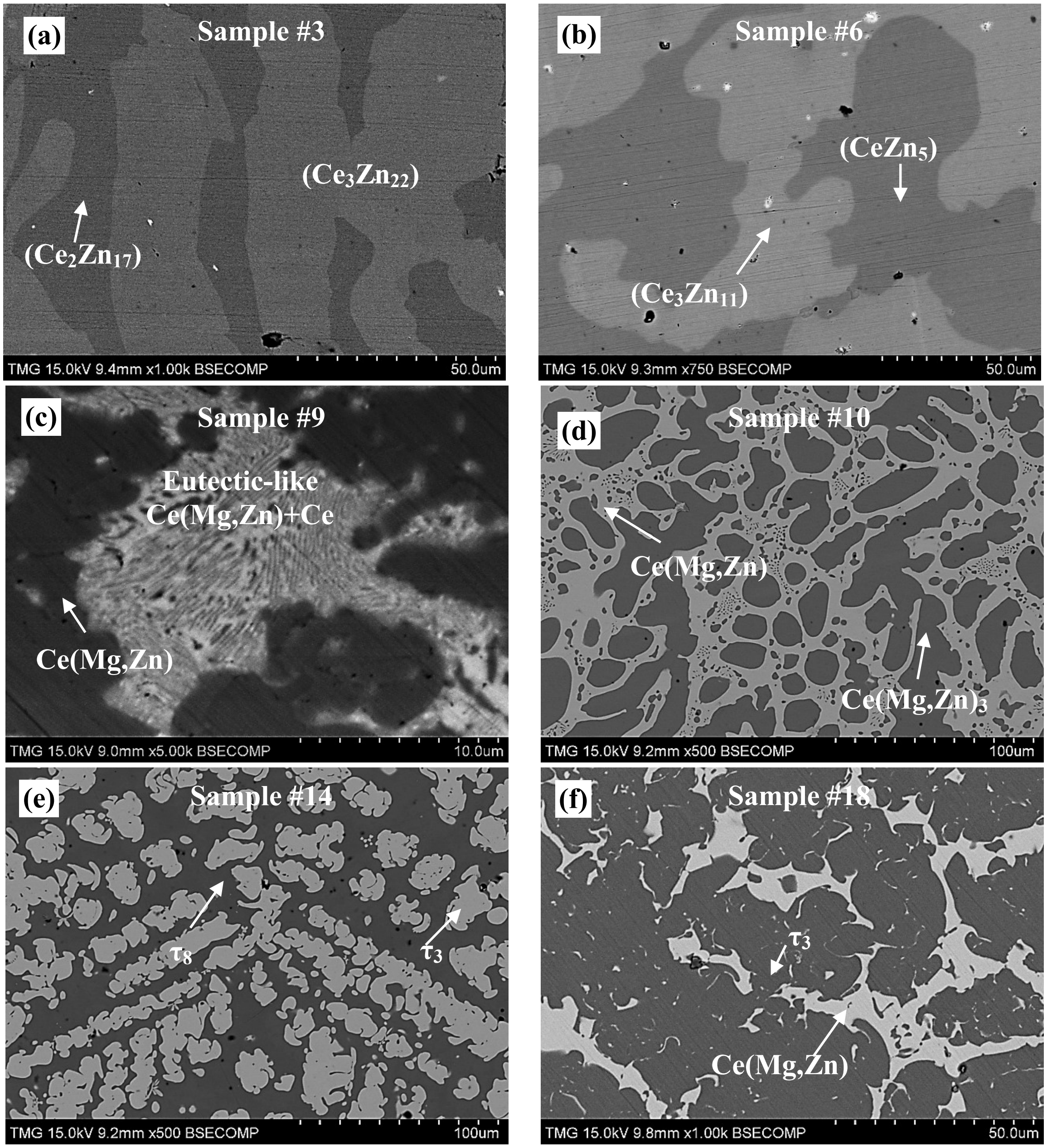

Figure 4-20: SEM micrographs of (a) sample #3; (b) sample #6; (c) sample #9; (d) sample #10; (e) sample #14; (f) sample #18

Table 4-8: WDS spot analysis of samples with two-phase equilibria

Sample number	Actual composition EDS (at.%)			WDS composition (at.%)			Corresponding phase
	Ce	Mg	Zn	Ce	Mg	Zn	
3	10.1	2.5	87.4	11.9	1.1	87.0	(Ce_3Zn_{22})
				10.5	1.3	88.2	(Ce_2Zn_{17})
4	9.8	12.8	77.4	10.7	7.2	82.1	τ_6
				8.6	31.4	60.0	τ_5
6	20.0	4.1	75.9	20.8	2.1	77.1	Ce_3Zn_{11}
				18.1	3.5	78.4	($CeZn_5$)
9	63.5	13.1	23.4	100.0	0	0	Ce
				50.0	21.0	29	Ce(Mg,Zn)
10	37.6	71.0	31.4	25	55	20	Ce(Mg,Zn)
				50	24	26	$Ce(Mg,Zn)_3$
11	37.4	21.0	41.6	50	9	41	τ_3
				25	35.2	39.8	Ce(Mg,Zn)
13	15.1	63.3	20.6	25	47	28	$Ce(Mg,Zn)_3$
				7.8	77.6	14.6	τ_8
14	14.7	49.5	35.8	25	29.5	45.5	τ_3
				8.2	65.5	26.3	τ_8
15	10.1	25.3	64.6	8.8	41.2	50.0	τ_5
				10.5	10.8	78.7	τ_6
18	28.1	34.5	37.4	50	10	40	Ce(Mg,Zn)
				25	38	37	τ_3
19	9.2	41.3	49.5	10.1	20.8	69.1	τ_6
				7.3	41.5	51.2	τ_5
20	12.8	33.5	53.7	14.3	28.9	56.8	τ_4
				8.1	44.8	47.1	τ_5
23	8.1	11.2	80.7	10.5	3.6	85.9	(Ce_2Zn_{17})
				0	33.4	66.6	$MgZn_2$

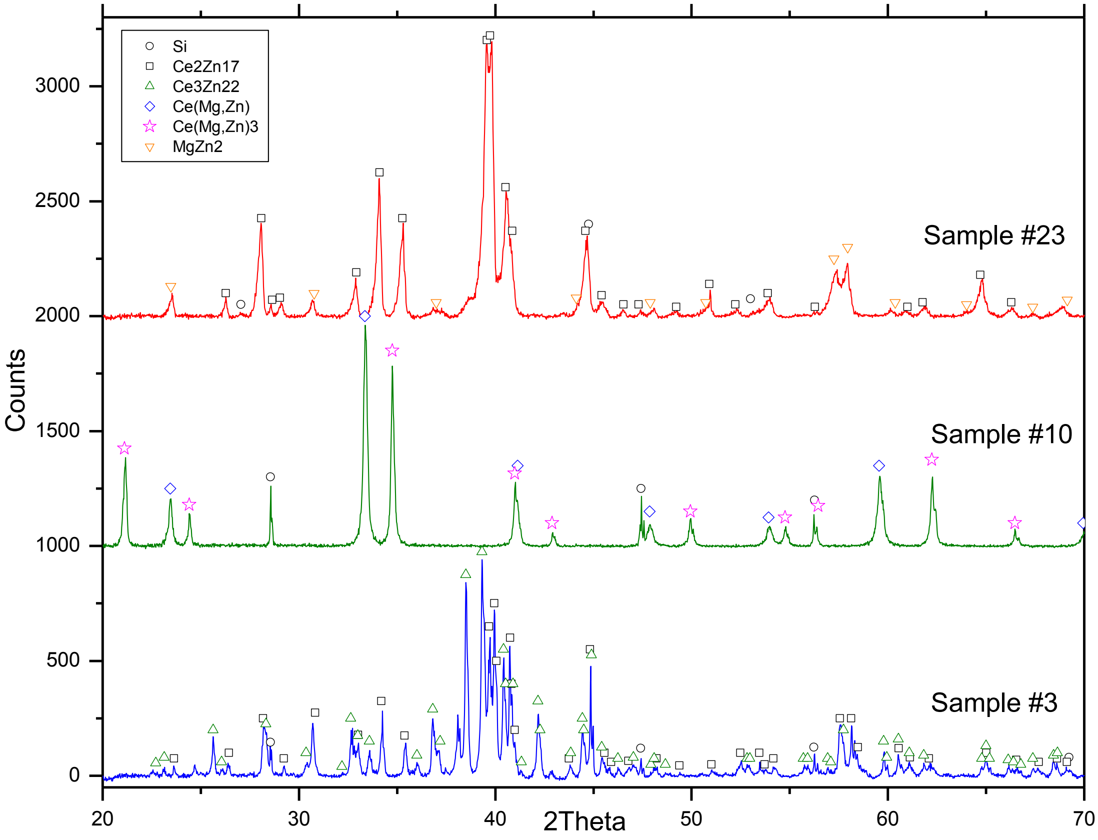

Figure 4-21: The X-ray powder diffraction of the annealed samples #3, 10 and 23. Silicon was used as a calibration standard to correct the zero shift and specimen displacement errors

Based on the WDS and XRD analyses, the determined phases from the equilibrated key alloys are shown graphically in Figure 4-22. The key alloys with the actual composition are shown as bold circles. The arrows indicate the phase equilibria determined from WDS and XRD studies of each alloy. In addition to the seven ternary compounds observed by diffusion couples experiments, one ternary compound was detected by the key alloys experiments. This compound is τ_1 ($Ce_6Mg_3Zn_{19}$).

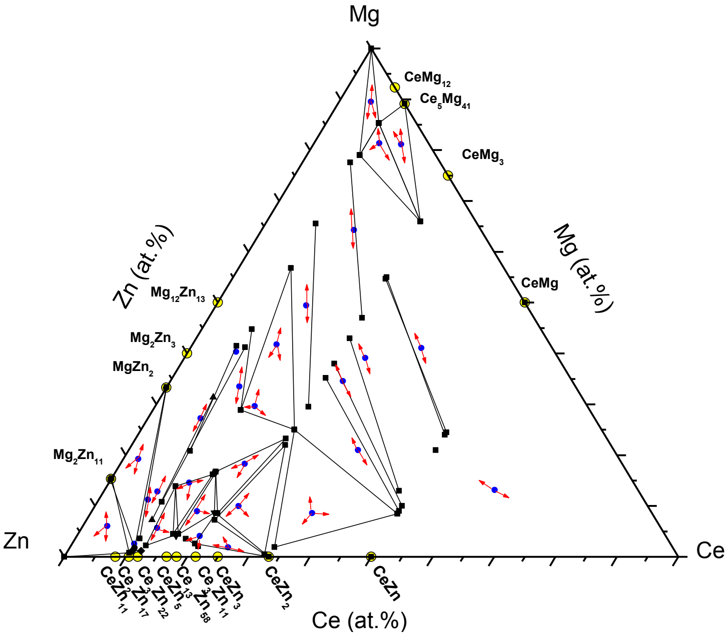

Figure 4-22: Phase relationships of the Ce-Mg-Zn isothermal section at 300°C obtained from key alloys experiments

4.3.4. Ce-Mg-Zn isothermal section at 300°C

The Ce-Mg-Zn isothermal section at 300°C, constructed based on diffusion multiple/couples and equilibrated key alloys studies, is shown in Figure 4-23. Eight ternary compounds were found and named from τ_1 to τ_8. The system shows the ternary compounds and the solid solutions with wide homogeneity ranges.

Because of many wide two-phase fields, the determination of the boundary tie-lines needs a lot of key alloys to verify the phase equilibrium. In this work, however, tie-lines were interpolated based on the mass balance principle [20]. In this method, at least three tie-lines must be determined experimentally for each two-phase field. Two lines, parallel to the boundary composition lines, are extended from the two ends of each experimental tie-line until they intersect. Three intersection points are determined. Matching these points gives the balance curve, which represents the amount of the equilibrated phases versus composition. Each point on the curve represents an intersection of any tie-line that occurs in that field. Once the curve is determined, the process can be reversed and additional tie-lines can be interpolated by extending two lines parallel to the phase boundary composition lines. Using the tie-line interpolation method, many regions in the Ce-Mg-Zn isothermal section could be determined, specifically the two three-phase regions, τ_8+τ_3+Ce(Mg,Zn)$_3$ and τ_3+Ce(Mg,Zn)$_3$+ Ce(Mg,Zn).

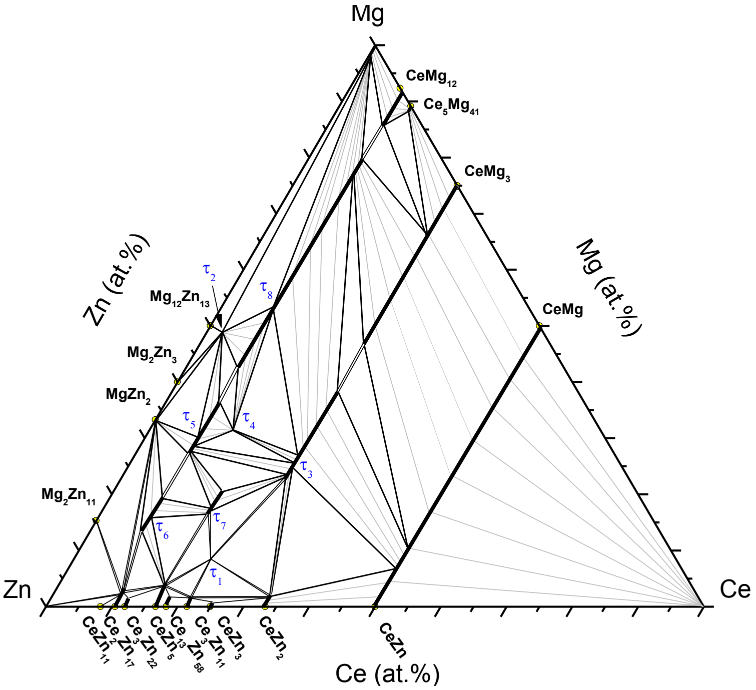

Figure 4-23: The Ce-Mg-Zn isothermal section at 300°C

The ternary solubility of Zn in the Ce-Mg compounds was found to increase with decreasing Mg concentration. The same was observed by [86], whereas no solubility trend was reported by [90] and [92]. In this work, the ternary solid solubility of Zn in $CeMg_{12}$ and $CeMg_3$ was measured at 300 °C as 5.6 and 28.4 at.% Zn, respectively. These are in good agreement with the solubilities reported by [86] at the same annealing temperature. Furthermore, a complete solubility between CeMg and CeZn compounds was reported by [86, 90, 92] at different annealing temperatures. In this work, the complete solid solubility was confirmed experimentally using a diffusion couple made from alloys of these compounds, as shown in Figure 4-24 (a). This diffusion couple was annealed at 300°C for 40 days. The composition profile obtained by the WDS line-scan is shown in Figure 4-24 (b). The composition profile shows the exchange of Mg and Zn around the interface (from left to right), whereas, the concentration of Ce is constant.

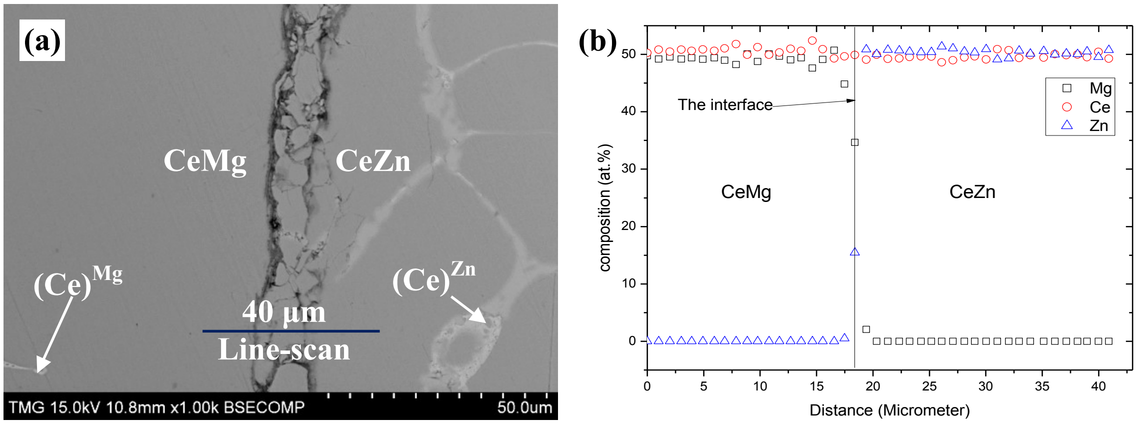

Figure 4-24: (a) SEM micrograph of the CeMg/CeZn diffusion couple annealed at 300°C for 40 days; (b) the composition profile obtained by the WDS line-scan

The Zn-rich side showed very complex phase relationships due to the existence of many ternary compounds. However, it was not possible to compare the current results with the available data of Melnik *et al.* [86] at 300 °C, because they did not establish the phase relations between all the compounds in this region. Furthermore, the phase relations in the same region were different than those in [90] and [92], due to the different annealing temperatures. Nevertheless, in the results obtained in the current work were verified using diffusion multiple/couples and equilibrated key alloys. The Mg-rich side showed relatively less complexity, since the $(Mg)^{Ce,Zn}$ ternary solid solution forms wide two-phase fields with τ_8 and $Ce(Mg,Zn)_{12}$. In this work, $Mg_{12}Zn_{13}$, τ_2, τ_8, $Ce(Mg,Zn)_{12}$ and $CeMg_{12}$ were found in equilibrium with $(Mg)^{Zn}$. This is similar to the results of Melnik *et al.* [86] to some extent, except that they reported equilibrium with τ_5 instead of

τ_2. The Ce-rich side shows the simplest phase relations, because Ce is equilibrating with the complete solid solution Ce(Mg,Zn).

4.4. Experimental procedure

In order to study the phase relationships in the Ce-Mg-Zn isothermal section at 300°C, solid-solid diffusion couples along with key alloys were prepared and analyzed using Hitachi (Tokyo, Japan) S-3400N SEM equipped with Oxford® (Abingdon, UK) EDS/WDS detectors and PANalytical (Almelo, The Netherlands) X-ray diffractometer (Cu K-α radiations). EDS and WDS analysis were used to determine the phases and to quantify their compositions. Pure metals (Ce, Mg and Zn) were used as standards for WDS calibration. X-ray scans were performed on powder-form samples, in the range from 20 to 120 degree 2θ with 0.02° step size, to identify and confirm the phases obtained by WDS measurements; since the stoichiometry of the Zn-rich compounds falls within the WDS error of measurements. X-ray phase analysis was carried out using X'pert Highscore Plus software [58]. The standard intensity data were taken from Pearson's Crystal Database [55]. Silicon was used in the powder samples as a calibration standard to correct the zero shift and specimen displacement.

4.4.1 Key alloys preparation

Pure elements were used for the preparation of key samples and diffusion couple end-members. Ce and Zn ingots with purity of 99.9% and 99.99%, respectively, were supplied by Alfa Aesar Co. (Haverhill, USA). Mg ingots with purity of 99.8% were supplied by CANMET Materials Technology Laboratory (Ottawa, Canada). The key alloys were prepared in an electric-induction furnace with a tantalum crucible and argon atmosphere. It was difficult to prepare the Zn-rich alloys (75-92 at.% Zn) by melting the three pure metals together. A severe exothermal reaction between liquid Zn and solid Ce took place, and the material evaporated as a result. Because of this difficulty, Pavlyuk *et al.* [92] prepared the Ce-rich (>50 at.%) samples by sintering the metal powders followed by arc-melting in argon atmosphere, whereas the Mg-rich and Zn-rich samples were prepared in a sealed Ta crucibles.

Alloys near the Zn-rich corner were prepared by adding pure Zn to Ce-Mg alloys; whereas, other compositions were prepared by melting the three pure metals. Excess amount of Mg and Zn (around 10%) were added to compensate for losses due to evaporation. The alloys were melted several times to ensure the composition homogeneity. The actual global composition was determined using Ultima (Longjumeau, France) optical emission spectrometer (OEM)-inductively coupled plasma (ICP). ICP standards of pure metals, 1000 mg/L in HNO_3, were supplied by Fischer Scientific Co. (Waltham, USA). Average of three readings, at least, was considered as the global composition of the alloy. EDS/SEM area analysis was also performed to obtain the actual composition prediction; because the samples structure was homogeneous. Both ICP and EDS results were in good agreement.

4.4.2 Solid-solid diffusion couples

The end-members of the solid-solid diffusion couples were prepared from pure metals and/or alloys. The contacting surfaces were ground gradually up to 1200 grit SiC paper using 99% pure ethanol as a lubricant and to prevent oxidation. High friction between samples and SiC papers was avoided to eliminate sparking during grinding due to Ce. After that, the ground surfaces were polished down to 1μm using alcohol diamond suspension. The end-members were strongly tightened together using stainless steel clamping rings.

For annealing purposes, samples and diffusion couples were wrapped in tantalum foil and encapsulated inside an argon-purged quartz tube with the inside pressure of about 8×10^{-1}torr. To reach equilibrium, diffusion couples and key alloys were heated up to 300°C for a predefined period of time. Annealing time was chosen as 21 days based on the composition of the selected end-members. Also, visual observation of the annealing tubes was used to stop the annealing process when the quartz tube becomes dark indicating significant evaporation. After annealing, the quartz tubes, containing samples and diffusion couples, were rapidly quenched in cold water in order to obtain the high temperature structure. The equilibrated phases and the diffusion zones were analyzed using SEM/WDS spot analysis and line-scans. WDS line-scans were performed across diffusion zones with a spatial distance of ~1 μm to obtain the concentration profile of the three elements. Based on the phase equilibrium data from the solid-solid diffusion couples and key alloys obtained by SEM/WDS analysis, the isothermal section of the Ce-Mg-Zn phase diagram at 300°C was constructed.

4.5. Conclusions

The Ce-Mg-Zn isothermal section at 300°C was constructed for the whole composition range using diffusion couples and key alloys experiments. Most of the ternary compounds and extended binary compounds have wide homogeneity ranges. The solid solutions in the system seem to occur due to the mutual substitution between Mg and Zn.

Diffusion couple studies coupled with key alloys experiments provide powerful tool in phase diagram determination. The diffusion couples of this system showed complex relationships due to the dispersed morphologies. However, their understanding provided very valuable information, which would be not possible without preparing large number of samples.

The fast interatomic diffusion between Mg and Zn atoms led to consume Mg from the $CeMg_{12}$ end-member by diffusion reaction to form Mg-Zn compounds in the matrix. As a result, pure Mg was freed from $Ce(Mg,Zn)_{12}$ solid solution, and a series of ternary compounds with constant Ce concentration, indicating the Mg/Zn substitution, were observed.

The ternary solubility of Zn in the Ce-Mg compounds was found to increase with decrease in Mg concentration. Accordingly, the ternary solid solubility of Zn in $CeMg_{12}$ and $CeMg_3$ was measured as 5.6 and 28.4 at.% Zn, respectively. Furthermore, the CeMg and CeZn showed a complete solid solubility. The complete solubility was confirmed by a diffusion couple made from CeMg and CeZn alloys.

4.6. Acknowledgement

This research was supported by funding from the Magnesium Strategic Research Network (MagNET) [94].

4.7. Author Contributions

Ahmad Mostafa, carried out the experiments and analysis of the results. Ahmad Mostafa and Mamoun Medraj prepared and revised the manuscript. Mamoun Medraj initiated and directed the project. He helped in the interpretation of the results and followed up on the progress step by step.

4.8. Conflicts of interest

The authors declare no conflict of interest.

4.9. Author's notes and significance of paper to thesis

The isothermal section of the Ce-Mg-Zn system at 300°C was constructed for the full composition range by means of diffusion couples and key alloys. Alloys of Ce-Mg-Zn system are known for their high strength and creep resistance at relatively high temperatures. This can be attributed to the formation of stable intermetallic compounds that have high melting temperatures. This is expected because the Ce-Zn binary phase diagram has nine intermetallic compounds.

Ternary diffusion couples of this system showed very complex phase morphologies. However, large amount of phase equilibrium data could be extracted. In this chapter, the phase equilibrium analysis of these complex morphologies was described thoroughly and the phase boundaries were established accordingly.

Equilibrated key alloys, used to confirm the obtained results from diffusion couple experiments, were analyzed using WDS and XRD techniques. XRD could not determine some of the new phases, because of the lack of the crystal structure data. Thus, more crystallographic studies are still needed to determine the crystal structure of the new phases.

Diffusion multiple, prepared from three pure elements Ce/Mg/Zn, was annealed at 300°C for 21 days. Based on the microstructural studies of the diffusion zones, it is concluded that the interdiffusivity between Mg and Zn is higher than that between Ce and Mg, which is evident from the wider diffusion zones in the case of Mg-Zn systems. No diffusion was detected between Ce and Zn at 300°C and 21 days. To understand the differences between diffusivity values of these systems, the study of binary diffusivity between the different components pertinent to the current work was carried out as detailed in Chapter 5.

In the next chapter, the binary interdiffusion coefficients of the Mg-{Ce, Nd, Zn} and Zn-{Ce, Nd} systems are calculated by means of diffusion couples and Boltzmann-Matano analysis. Arrhenius equation is used to calculate the activation energy and pre-exponential factor of the growth of the Mg-{Ce, Nd, Zn} binary compounds.

Chapter 5 : On the atomic interdiffusion in Mg-{Ce, Nd, Zn} and Zn-{Ce, Nd} binary systems

---

ABSTRACT

Binary interdiffusion data as function of composition in the Mg-{Ce, Nd, Zn} and Zn-{Ce, Nd} systems were obtained experimentally using solid-solid diffusion couples. For the studied systems, all intermetallic compounds formed based on the equilibrium phase diagrams, eliminating the problem of missing compounds in the diffusion couples found in the literature. The composition profiles were obtained using WDS line-scans across diffusion couples. The composition-dependent diffusion coefficient at each interface was determined using Boltzmann-Matano analysis. For the available literature data for some of the compounds in the Mg-{Ce, Nd, Zn} systems, the calculated interdiffusion coefficients were in good agreement. No diffusion data regarding Zn-{Ce, Nd} systems could be found in the literature. The activation energy and the pre-exponential factor of the growth of the Mg-{Ce, Nd, Zn} compounds were determined using Arrhenius equation. The activation energies of the growth of the Mg-Ce compounds showed relatively higher values than those of Mg-Nd and Mg-Zn compounds.

5.1. Introduction

Improving the mechanical and structural properties of Mg alloys is needed in order to increase their use in the automobile and aircraft industries. However, low formability and strength, especially at high temperature, can limit their use in certain applications. It was found that the problems of such poor mechanical properties could be improved by adding proper amounts of alloying elements. For instance, Zn is one of the alloying elements added to Mg to improve its room temperature strength and corrosion resistance [81]. Mg can dissolve small amount of Zn necessary for solution strengthening and precipitation hardening. Larger amounts of Zn result in the formation of Mg-Zn intermetallic compounds. Rare earth elements are also added to improve the mechanical properties of Mg-Zn alloys, because they form various intermetallic compounds with different crystal structures [47, 95]. These compounds usually show high thermal stability and distribute along the grain boundaries in the form of fine precipitates [96]. The existence of such precipitates leads to enhancing the mechanical properties by hindering the dislocations motion which thereby provides the strengthening effect.

Among the available rare earths, diffusion of Ce and Nd in Mg and Zn will be investigated in this work. Commercial sources of Nd are commonly extracted from Monazite ores, which normally contain high Ce content [97]. Recently, many studies were carried out to produce sheet metals out of Mg alloys containing rare earth elements [98]. Attempts were performed to replace Nd by Ce; since they show almost the same phase relationships with Mg and Zn. Furthermore, because Nd ores contain higher Ce content, using Ce could be the best economical choice on the industrial level.

Understanding the interatomic diffusion is very important to describe the solidification, crystal growth and precipitation processes of different metallic systems. The main goal of this work is to determine the interdiffusion coefficients of Zn in Mg and Ce and Nd in both Mg and Zn using diffusion couples and Boltzmann-Matano analysis [23, 24]. Different diffusion couples between pure elements were prepared and annealed at different temperatures, in which several phases in thermodynamic equilibrium formed by diffusion reaction. Once the interdiffusion coefficients are determined, the activation energies and pre-exponential factors can be obtained using Arrhenius equation [25].

5.2. Literature review

The diffusion coefficients of Ce and La in Mg were first determined by Lal and Levy [99] using diffusion couple technique. The diffusion couples were made from pure Mg and MgRE (RE=Ce and La) end-members annealed at several temperatures for different time periods. Table 5-1 gives the diffusion coefficients along with the activation energy (Q_d) and pre-exponential factor ($\widetilde{D}_0$) of Ce in Mg at different temperatures.

Table 5-1: Diffusion coefficients along with the activation energy and pre-exponential factor of Ce in Mg at different temperatures [99]

	Temperature (°C)	Diffusion coefficient ($cm^2.s^{-1}$)	Q_d (kJ/mole)	$\widetilde{D}_0$ ($cm^2.s^{-1}$)
Ce-Mg	550	2.9×10^{-9}	175.72	450
	565	5.4×10^{-9}		
	585	8.2×10^{-9}		
	598	1.3×10^{-8}		

Many studies were made to find an alternative commercial source for Nd metal. Extracting Nd from NdFeB magnet scrap was one of the suggested ideas. Xu *et al.* [61] developed a new approach to recycle magnets scrap. They [61] used liquid Mg to extract

Nd from NdFeB scrap relying on the capability of Nd to form several intermediate compounds with Mg. Since Fe and B are immiscible in liquid Mg, they will not be accepted by liquid Mg. In their [61] experiments, the molten Mg was held in a temperature range of 675-750°C for 2-8hr. Thickness of the formed diffusion layers was measured at 700, 725 and 750°C and 2-8hr as 280-600, 220-700 and 600-1200µm, respectively. To calculate the diffusion speed of Nd in Mg, Xu *et al.* [61] assumed that the flux of Nd out of the scrap equals to the flux into the liquid Mg. Based on that, the average diffusion coefficients of Nd in liquid Mg were reported and given in Table 5-2.

Table 5-2: Calculated values of average diffusion coefficients of Nd in liquid Mg [61]

Temperature (°C)	$\widetilde{D}$ ($cm^2.s^{-1}$)
675	$4.20\times10^{-10}\pm1.86\times10^{-10}$
700	$4.61\times10^{-8}\pm1.34\times10^{-8}$
725	$4.78\times10^{-8}\pm1.56\times10^{-8}$
750	$8.98\times10^{-8}\pm3.50\times10^{-8}$

Later, the binary interdiffusion coefficients of Dy, Nd, and Pr in Mg were measured by Xu *et al.* [100] using diffusion couple technique and Boltzmann-Matano analysis. The Nd/Mg diffusion couples were annealed at 500°C for 300, 100 and 300hr, respectively. The composition profiles across the diffusion zones were measured using SEM/EDS. The diffusion coefficients at each interface of the Mg/Nd diffusion couple, measured by Xu *et al.* [100] at 500°C, are mentioned in Table 5-3. In their [100] study, many compounds were missing; these compounds are: DyMg, $DyMg_2$, $Mg_{41}Nd_5$ and MgPr. They presumed that the proposed phase diagrams were incomplete and with large amount of uncertainty. Also, they related the absence of these phases to the difficulty of working with Mg. In contrast, $Mg_{41}Nd_5$, for example, was observed in the work of

Brennan *et al.* [101] who annealed three Mg/Nd diffusion couples at 400, 450 and 500°C for 504, 360 and 240hr, respectively. However, Brennan *et al.* [101] missed the MgNd compound from all the diffusion couples. They [101] calculated the activation energy and pre-exponential factor of the $Mg_{41}Nd_5$ and Mg_3Nd compounds as listed in Table 5-4. Resolving the difficulty of missing some of the compounds in the diffusion couples and explaining the possible reasons for this phenomenon will be attempted in this work.

Table 5-3: Diffusion coefficients of Mg-Nd system at 500°C [100]

Interface	$\widetilde{D}$ ($cm^2.s^{-1}$)
Nd/MgNd	9.75×10^{-13}
MgNd/Mg_3Nd	9.22×10^{-14}
Mg_3Nd/$Mg_{41}Nd_5$	missing
$Mg_{41}Nd_5$/Mg	missing

According to Kulkarni and Luo [102], two isothermal diffusion couple experiments at two different times are required to accurately determine the layer growth constant. Brennan *et al.* [101] determined the $Mg_{41}Nd_5$ and Mg_3Nd layer growth constants at three different temperatures and one annealing time only. Thus, similar experiments with different annealing time periods were carried out in this work in order to obtain more accurate results.

Table 5-4: Activation energy and pre-exponential factor for the growth of $Mg_{41}Nd_5$ and Mg_3Nd phases according to Brennan et al. [101]

Phase	$\widetilde{D}$ ($cm^2.s^{-1}$)			Q_d (kJ/mole)	$\widetilde{D}_0$ ($cm^2.s^{-1}$)
	400°C	450°C	500°C		
$Mg_{41}Nd_5$	8.3×10^{-11}	2.7×10^{-10}	5.1×10^{-10}	79.0	1.2×10^{-4}
Mg_3Nd	5.2×10^{-12}	1.7×10^{-11}	8.5×10^{-11}	120.0	9.6×10^{-3}

Sakakura and Sugino [103] calculated the growth constants and interdiffusion coefficients of Mg-Zn system using diffusion couples technique, considering the diffusion mechanism in the eutectic alloys. Diffusion couples were annealed at 250°C for 100 and 148hr and at 300°C for 72, 110 and 148hr. Two intermetallics were observed, $MgZn_2$ and Mg_2Zn_{11}, and their growth rates were evaluated. The interdiffusion coefficient, activation energy and pre-exponential factor of phase growth calculated by Sakakura and Sugino [103] are listed in Table 5-5.

Table 5-5: Interdiffusion coefficient, activation energy and pre-exponential factor for the growth of $MgZn_2$ and Mg_2Zn_3 phases according to Sakakura and Sugino [103]

Phase	$\tilde{D}$ (cm^2.s^{-1})	Q_d (kJ/mole)	$\tilde{D}_0$ (cm^2.s^{-1})
$MgZn_2$	4.4×10^{-9}	73.2	1.7×10^{-1}
Mg_2Zn_3	5.0×10^{-10}	61.9	3.2×10^{-3}

Recently, Brennan *et al.* [104] calculated the activation energy of growth of $MgZn_2$ and Mg_2Zn_3 phases using diffusion couples technique. Diffusion couples were annealed at 295, 315 and 325°C for 384, 168 and 120hr, respectively. In their [104] work, the MgZn phase was not observed in all diffusion couples. Also, the activation energy and pre-exponential factor of the layer growth was calculated for $MgZn_2$ and Mg_2Zn_3 only, as listed in Table 5-6. These will be obtained for all the stable Mg-Zn compounds in this work up to 300°C.

Table 5-6: Activation energies and pre-exponential factors for the growth of Mg_2Zn_3 and $MgZn_2$ phases according to Brennan et al. [104]

Phase	$\tilde{D}$ (cm^2.s^{-1})			Q_d (kJ/mole)	$\tilde{D}_0$ (cm^2.s^{-1})
	295°C	315°C	325°C		
Mg_2Zn_3	7.3×10^{-12}	1.1×10^{-11}	2.4×10^{-11}	105	1.2×10^{-2}
$MgZn_2$	9.0×10^{-11}	4.9×10^{-10}	7.7×10^{-10}	207	1.1×10^{-1}
Mg_2Zn_{11}	-	1.2×10^{-11}	1.5×10^{-11}	-	-
$Mg_{51}Zn_{20}$	-	-	1.6×10^{-12}	-	-

No data regarding the binary interdiffusion coefficients of the Zn-{Ce, Nd} systems could be found in the literature. Thus, it is essential to provide the diffusion information about these systems as well.

5.3. Analytical background

The Boltzmann-Matano analysis [23, 24] is widely used to measure the composition-dependent interdiffusion coefficients $\widetilde{D}(C^o)$ from experimental composition profiles. The composition profiles are usually obtained by elemental analysis techniques across the diffusion zones in the diffusion couples experiments. Once the composition profiles are measured, then, $\widetilde{D}$(C) can be obtained as [23, 24]:

$$\widetilde{D}(C') = \left(-\frac{1}{2t}\frac{dx}{dC}\right)|_{C'} \int_{C^-}^{C'} (x - x_o) dC \qquad \text{Equation 5-1}$$

where, C is the concentration and $C'$is the concentration at a specific location x_o, C^- is the concentration of the terminal component, x is the diffusion distance and t is the time. The position of Boltzmann-Matano plane, x_o, can be determined based on mass balance by the following equation [102, 105]:

$$\int_{x^-}^{x_o}(C' - C^-)dx = \int_{x_o}^{x^+}(C^+ - C')dx \qquad \text{Equation 5-2}$$

where, C^+ and C^- are the concentrations of the terminal components of the diffusion couple and x^+ and x^- are the left and right far distances from Boltzmann-Matano plane x_o. According to Mehrer [22], if the following boundary conditions are applied

$$\begin{aligned} C &= C^- \, for \, (x < 0, t = 0), \\ C &= C^+ \, for \, (x > 0, t = 0). \end{aligned} \qquad \text{Equation 5-3}$$

The following integrals balance across the Matano plane

$$\int_{C^+}^{C'} xdC + \int_{C'}^{C^-} xdC = 0 \qquad \text{Equation 5-4}$$

This method is applicable for both single and multi-phase systems since the assumption is valid even when there is a discontinuity at the phase boundary in the concentration profiles [106].

In order to measure the activation energy (Q_d) and pre-exponential factor (D_o) at any interface in a diffusion couple, diffusion couple experiments are carried out at different temperatures. After obtaining $\widetilde{D}(C^o)$ for each temperature, Arrhenius equation [25] can be applied as following:

$$\widetilde{D} = \widetilde{D}_o \, exp\left(-\frac{Q_d}{RT}\right) \qquad \text{Equation 5-5}$$

where, Q_d and $\widetilde{D}_o$ are the activation energy and the pre-exponential factor for interdiffusion, respectively, R is the gas constant and T is the absolute temperature. Equation 5-5 suggests that the Q_d and $\widetilde{D}_o$ for interdiffusion can be determined by plotting log $\widetilde{D}$ versus $1/T$ [102]; in which the slope of the linear segment is equal to $-Q_d/2.3R$ and the intercept at $1/T=0$ is the value of $log\, \widetilde{D}_o$ [25].

5.4. Experimental procedure

Diffusion couples were prepared from pure Mg (99.8%), Ce (99.96%), Nd (99.98%) and Zn (99.99%) metals. The contacting surfaces were ground gradually up to 1200 SiC paper using 99% pure ethanol as a lubricant and to protect metals from oxidation. After that, the ground surfaces were metallographically polished to 1µm using alcohol-based alumina suspension. The end-members were ultrasonically cleaned in pure ethanol and then clamped together using stainless steel clamping rings. The clamped end-members were then wrapped in tantalum foils, to eliminate direct contact with the tube walls, and encapsulated inside an argon-flushed quartz tube with a vacuum of around 1×10^{-2} torr. The diffusion couples were then annealed at the target temperature in a box furnace with a temperature control of ± 3°C. The annealing time periods of the Mg-Nd diffusion couples were chosen carefully based on our systematic annealing and quenching studies and benefiting from the literature data [100, 101]. For instance, Xu *et al.* [100] annealed the Mg/Nd diffusion couple at 500°C for 100hr, but their micrographs showed the formation of MgNd and Mg_3Nd layers only. On the other hand, Brennan *et al.* [101] annealed the Mg/Nd diffusion couples at 400, 450 and 500°C for 504, 15 and 24hr, respectively. Their [101] micrographs showed the formation of $Mg_{41}Nd_5$ and Mg_3Nd layers only. The MgNd phase was not observed. This could be due to over-annealing which makes other phases dominate the MgNd layer. Hence, in this work, different annealing temperatures and times were tried to obtain all the compounds in all the studied systems. After the diffusion annealing, the diffusion couples were quenched from the annealing temperature into cold water in order to obtain the high temperature structure.

The composition profiles were obtained using Hitachi S-3400 scanning electron microscope (SEM) equipped with wavelength dispersive spectroscopy (WDS) and energy dispersive X-ray spectroscopy (EDS) detectors. The WDS error of measurements was estimated to be ± 1.0 at.% for Mg, Nd and Zn, whereas Ce oxidation resulted in higher error of about ± 2.0 at.%, in the worst case, because Ce end-member was used as calibration standard for WDS measurements. It is worth noting that in some layers the error was significantly lower than this limit, e.g. CeMg layer, as will be discussed later.

Besides, this is not expected to give significant errors in the diffusion coefficients calculations because composition gradient is more critical for interdiffusion coefficients calculation than the absolute composition values.

5.5. Results and discussion

The diffusion couples of five binary systems studied in this work were evaluated, and the diffusion layers, representing intermetallic compounds, were compared with the equilibrium diagram of each system to gain confidence about the reliability of the results. For each system, composition profiles were measured using EDS/WDS line-scans across the diffusion zones. Accordingly, position of Matano plane [24] was identified at the interface between each two diffusion layers. Composition-dependence diffusion coefficients were measured from the concentration profiles using Boltzmann-Matano analysis. The activation energies and pre-exponential factors of the intermetallic phases were calculated using Arrhenius equation.

In this section, the results of the diffusion couples are presented in two groups. The first group contains Mg-{Ce, Nd, Zn} diffusion couples annealed at three different temperatures for different time intervals. Thus, the activation energies and pre-exponential factors along with composition dependent diffusion coefficients are provided. The second group contains Zn-{Ce, Nd} diffusion couples annealed at 400°C for 240hr. For this group, only the composition dependent diffusion coefficients are presented. It is highly challenging to obtain all the expected phases for such systems at every annealing temperature, because they have large number of intermetallic compounds. The detection of these compounds is also difficult, since there is no big difference in their composition, specifically in the Zn-rich side. Thus, there would be higher chance for experimental errors than for the first group. The experimental data of the first group diffusion couples are summarized in Table 5-7, and the results of the second group are in Table 5-8.

Table 5-7: Annealing conditions of the Mg-Ce, Mg-Nd and Mg-Zn diffusion couples and the layers thickness of intermetallics

System		Thickness (µm)		
	Temperature (°C)	400	450	490
	Time (hr)	120	96	48
Mg-Ce	MgCe	3.5	5.9	8.7
	Mg_3Ce	5.8	8.6	16.7
	$Mg_{41}Ce_5$	39.7	71.5	101.4
	$Mg_{12}Ce$	21.6	31.2	19.6
Mg-Nd	MgNd	1.5	1.9	2.1
	Mg_3Nd	47.5	40.5	40.5
	$Mg_{41}Nd_5$	62.5	62.4	33.5
	Temperature (°C)	250	275	300
	Time (hr)	552	408	504
Mg-Zn	$Mg_{12}Zn_{13}$	~1	~1	2.5
	Mg_2Zn_3	30.5	34.8	50.9
	$MgZn_2$	227.6	245.3	327.2
	Mg_2Zn_{11}	25.4	37.2	36.4

Table 5-8: The layers thickness of intermetallics in Ce-Zn and Nd-Zn diffusion couples annealed at 400°C for 240hr

System	Compounds	Thickness (µm)	System	Compounds	Thickness (µm)
Ce-Zn	CeZn	4.4	Nd-Zn	NdZn	~1
	$CeZn_2$	19.5		$NdZn_2$	17.8
	$CeZn_3$	14.7		$NdZn_3$	9.7
	Ce_3Zn_{11}	16.5		Nd_3Zn_{11}	24.3
	$Ce_{13}Zn_{58}$	266.4		$Nd_{13}Zn_{58}$	414.2
	$CeZn_5$	Missing*		Nd_3Zn_{22}	13.4
	Ce_3Zn_{22}	Missing*		Nd_2Zn_{17}	84.1
	Ce_2Zn_{17}	37.9		$NdZn_{11}$	26.9
	$CeZn_{11}$	57.4			

*** These compounds were observed in the diffusion couple annealed at 400°C**

5.5.1. Mg-{Ce, Nd, Zn} binary systems

Backscattered electron images of the Mg-Ce diffusion couples, annealed at 400, 450 and 490°C for 120, 96 and 48hr, respectively, are shown in Figure 5-1 (a-c). Four diffusion layers were observed in all the diffusion couples. EDS spot-analysis confirmed the presence of four compounds; namely, MgCe, Mg_3Ce, $Mg_{41}Ce_5$ and $Mg_{12}Ce$. This is consistent with the Mg-Ce phase diagram [52], shown in Figure 5-1 (d), in the temperature range between 400°C and 490°C. The interface between diffusion layers indicates the local equilibria between the corresponding compounds. The occurrence of the correct number of layers and associated compounds is necessary for sound interdiffusion analysis using diffusion couples.

WDS line-scans were performed across the diffusion zones between the end-members. The composition profile of Mg-Ce diffusion couple, annealed at 490°C and 48hr, is presented in Figure 5-2. The composition profiles within the $Mg_{12}Ce$ and $Mg_{41}Ce_5$ layers show constant compositions of 92 and 88.6 at.% Mg, respectively. This means that these compounds are stoichiometric. The diffusion layers of MgCe and Mg_3Ce show deviation from constant composition. Thus, Mg_3Ce is a solid solution with a homogeneity range of 1.0, 1.3 and 2.3 at.% at 400, 450 and 490°C, respectively. Although the Mg and Ce terminal far ends of the diffusion couples were used as standard metals for WDS calibration, the stoichiometry in the MgCe phase was not 1:1 in the three diffusion couples. However, this deviation is not expected to give significant errors in the diffusion coefficients calculations.

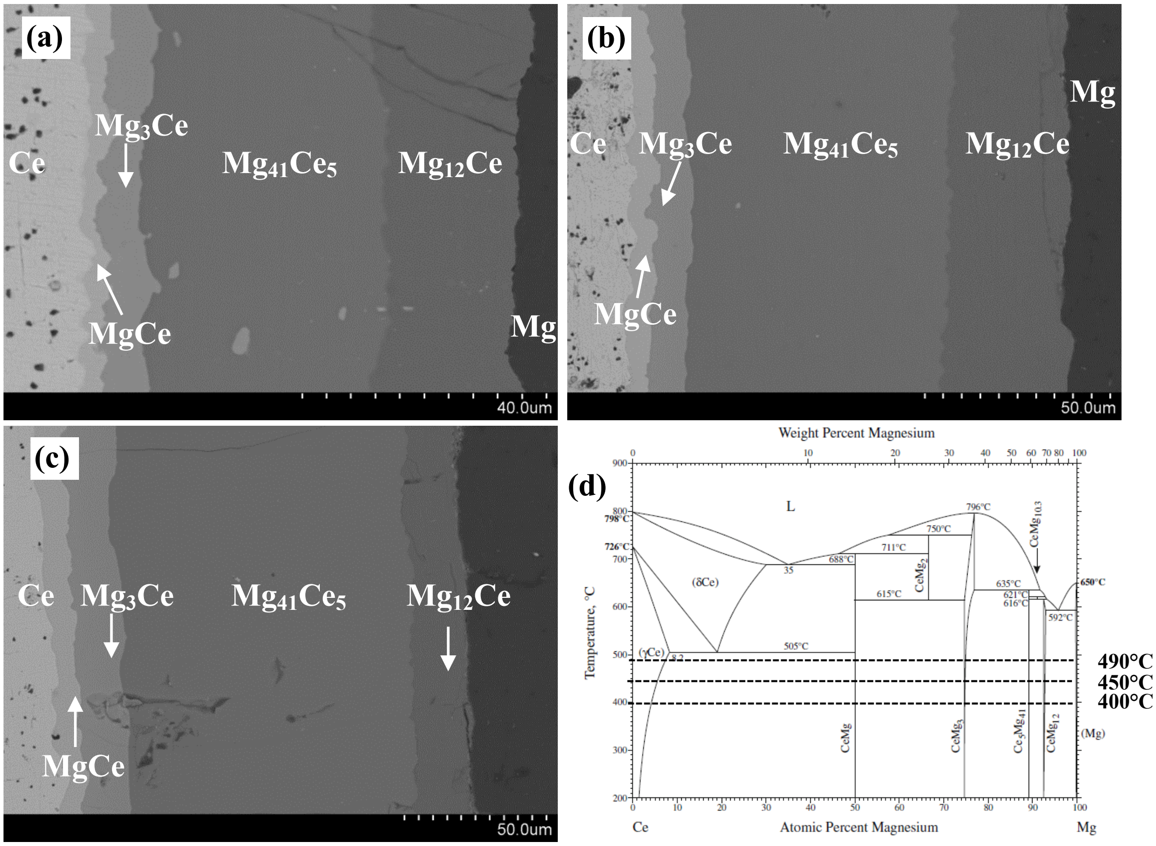

Figure 5-1: Backscattered electron images of Mg-Ce diffusion couples annealed at (a) 400°C for 120hr; (b) 450°C for 96hr; (c) 490°C for 48hr; (d) Ce-Mg binary phase diagram [52] with the annealing temperatures marked as dashed lines

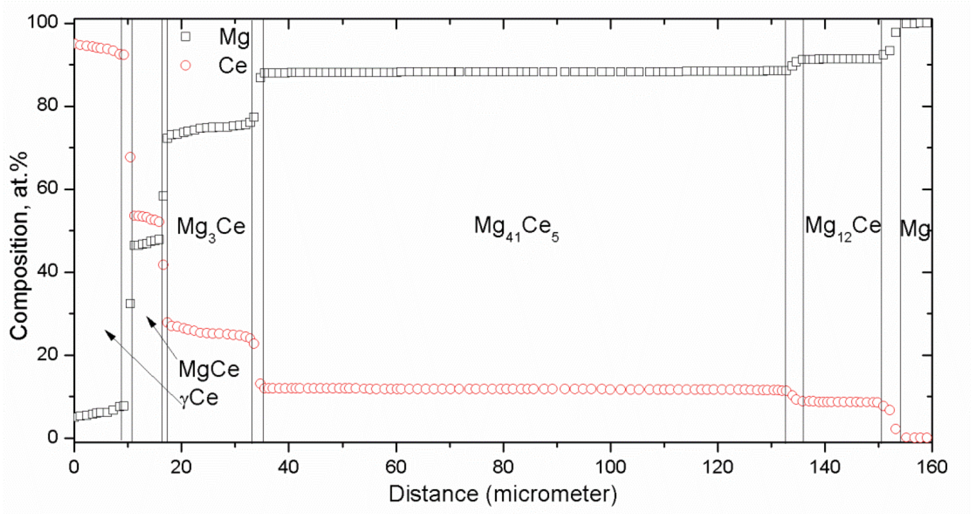

Figure 5-2: Composition profiles of the Mg-Ce diffusion couples annealed at 490°C and 48hr

Backscattered electron images of Mg-Nd diffusion couples, annealed at 400, 450 and 490°C for 120, 96 and 4hr, respectively, are shown in Figure 5-3 (a-c). Three diffusion layers appeared in all diffusion couples. These three layers are MgNd, Mg_3Nd and $Mg_{41}Nd_5$. This agrees with the Mg-Nd phase diagram [93] shown in Figure 5-3 (d). WDS line-scans were used to determine the homogeneity ranges of the terminal members and intermediate compounds. The terminal solubility of Mg in Nd was determined from the three diffusion couples as 6.3, 7.6 and 8.2 at.% Mg, at 400, 450 and 490°C, respectively.

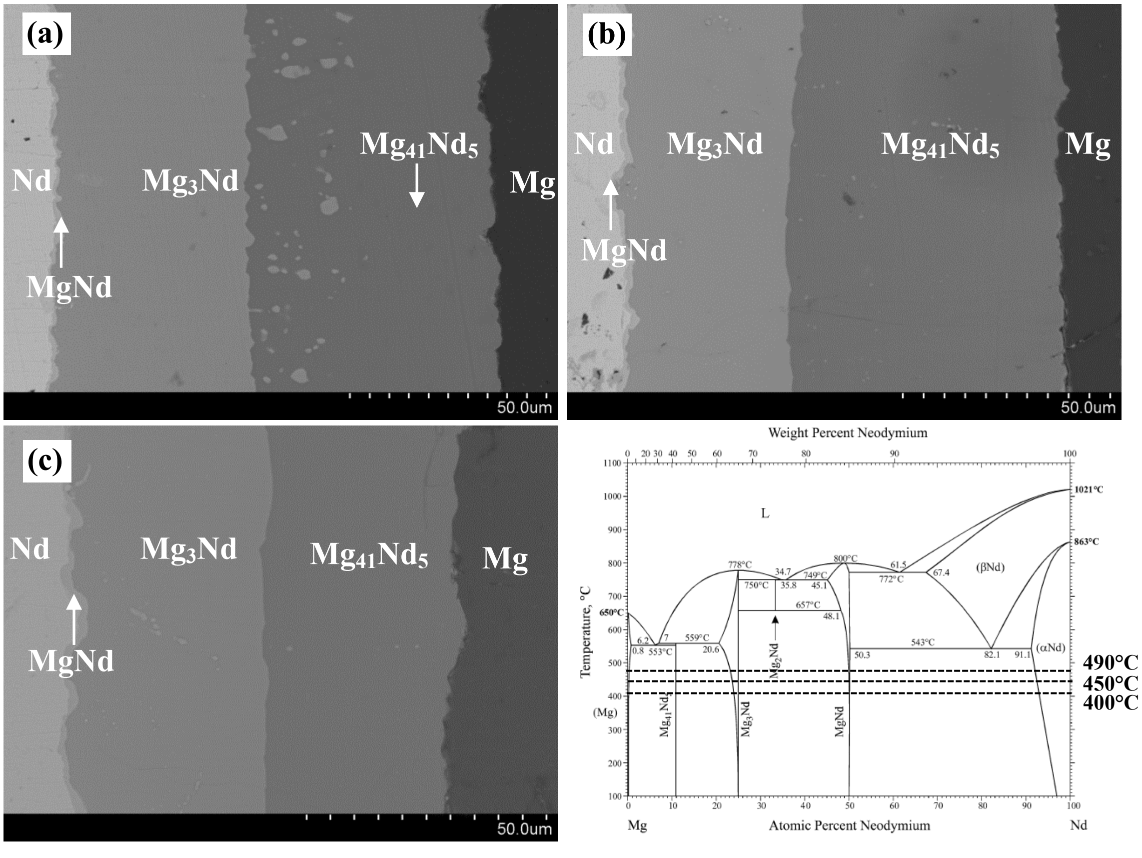

Figure 5-3: Backscattered electron images of Mg-Nd diffusion couples annealed at (a) 400°C for 120hr; (b) 450°C for 96hr; (c) 490°C for 48hr; (d) The Mg-Nd phase diagram [93] with the annealing temperatures marked as dashed lines

The plot of composition profile of the diffusion couple annealed at 490°C and 48hr is presented in Figure 5-4. The composition profiles within the $Mg_{41}Nd_5$ layer show constant composition of ~88.6 at.% Mg; whereas, the diffusion layers of Mg_3Nd appeared with a slope, which indicates the presence of a homogeneity range at 400, 450 and 490°C as 3.35, 3.61 and 3.85 at.% Mg, respectively. MgNd occurred in all diffusion couples with very low thicknesses of 1.5, 1.9 and 2.1µm at 400, 450 and 490°C, respectively. The spatial displacement of WDS line-scans was reduced to ~0.5µm across the MgNd diffusion layer to acquire more readings from its thin layer.

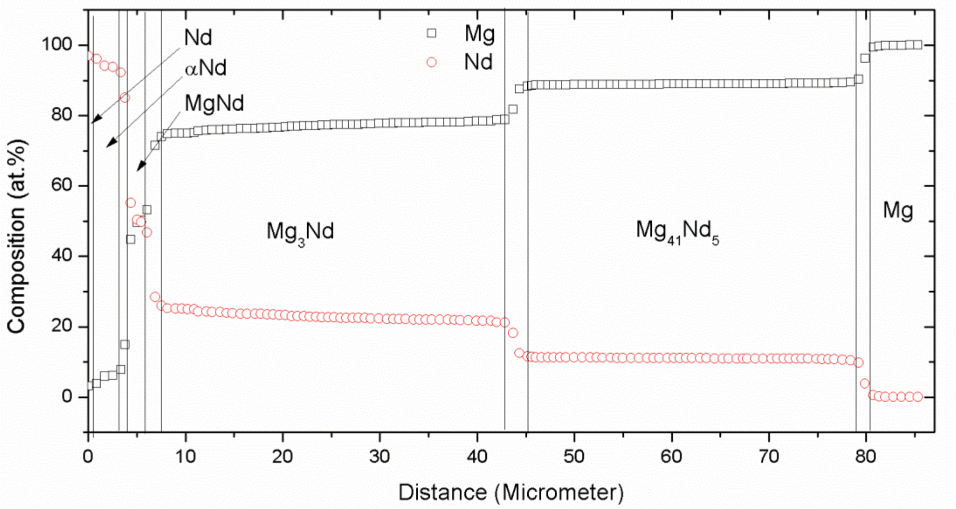

Figure 5-4: Composition profile of the Mg-Nd diffusion couple annealed at 490°C and 48 hr

The $Mg_{41}Nd_5$ diffusion layer, in the couple annealed at 400°C for 120hr, shown in Figure 5-3 (a), appeared with remaining traces of Mg_3Nd. Similar to this was observed in the Mg-Ce diffusion couple annealed under the same conditions, Figure 5-1 (a). It seems that the growth rate of the $Mg_{41}Ce_5$ and $Mg_{41}Nd_5$ compounds at the $Mg_3RE/Mg_{41}RE_5$ interface is relatively high at 400°C. This will be discussed in more details with experimental evidence in the interdiffusion coefficient calculations of this section.

Although, Mg-Ce and Mg-Nd diffusion couples were annealed at the same time and temperature, the total thickness of Mg-Ce diffusion layers, Table 5-7, was increasing with temperature. However, the total thickness of Mg-Nd diffusion layers was decreasing with temperature, as shown in Figure 5-5. This means that the diffusion in the Mg-Ce system is highly temperature dependent; whereas, it is highly time dependent reaction in the Mg-Nd system. This can also be related to the value of the activation energy and pre-exponential factor of Mg-Ce compounds; which appeared higher than those of Mg-Nd compounds, as can be concluded from Table 5-9. This means higher energy is required for the Ce-Mg compounds to grow at the same rate as those of Nd-Mg.

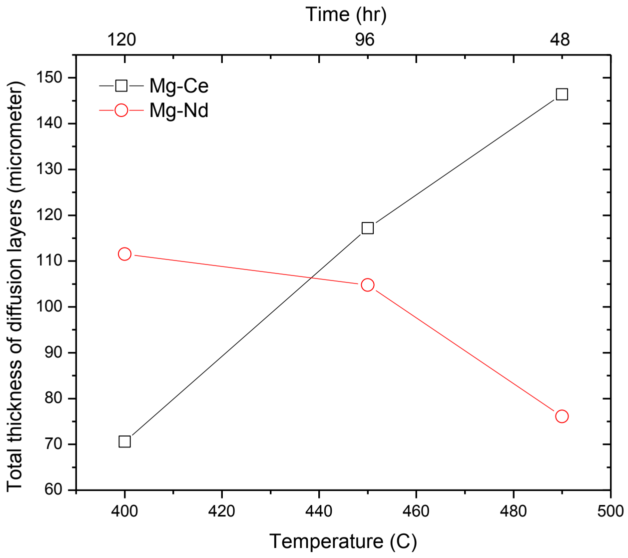

Figure 5-5: The total thickness of Mg-Ce and Mg-Nd diffusion zones with temperature regardless the annealing time

Backscattered electron images of Mg-Zn diffusion couples, annealed at 250, 275 and 300°C for 552, 408 and 504hr are shown in Figure 5-6 (a-c). The 300°C diffusion couple was firstly annealed for 350hr to follow the growth trend, i.e. higher temperature would require less annealing time. All the phases at 300°C were observed; nevertheless, the cracks in the Mg_2Zn_{11} diffusion layer did not allow for determining the interfaces on both sides clearly. This could be due to brittleness of this compound as well as the presence of the original diffusion interface. Thus, the same diffusion couple was annealed for 504hr to overcome the cracking problem by obtaining thicker Mg_2Zn_{11} layer. Four intermetallic compounds; namely, $Mg_{12}Zn_{13}$, Mg_2Zn_3, $MgZn_2$ and Mg_2Zn_{11}, were observed. Figure 5-6 (d) shows the $Mg_{12}Zn_{13}$ as a thin layer growing between Mg_2Zn_3 and pure Mg. The $Mg_{51}Zn_{20}$ was not observed in the Mg-Zn diffusion couples, because the annealing temperatures were intentionally selected below its stability temperature. This provides more practical diffusion data regarding the low temperature compounds that are present in Mg alloys at service temperature.

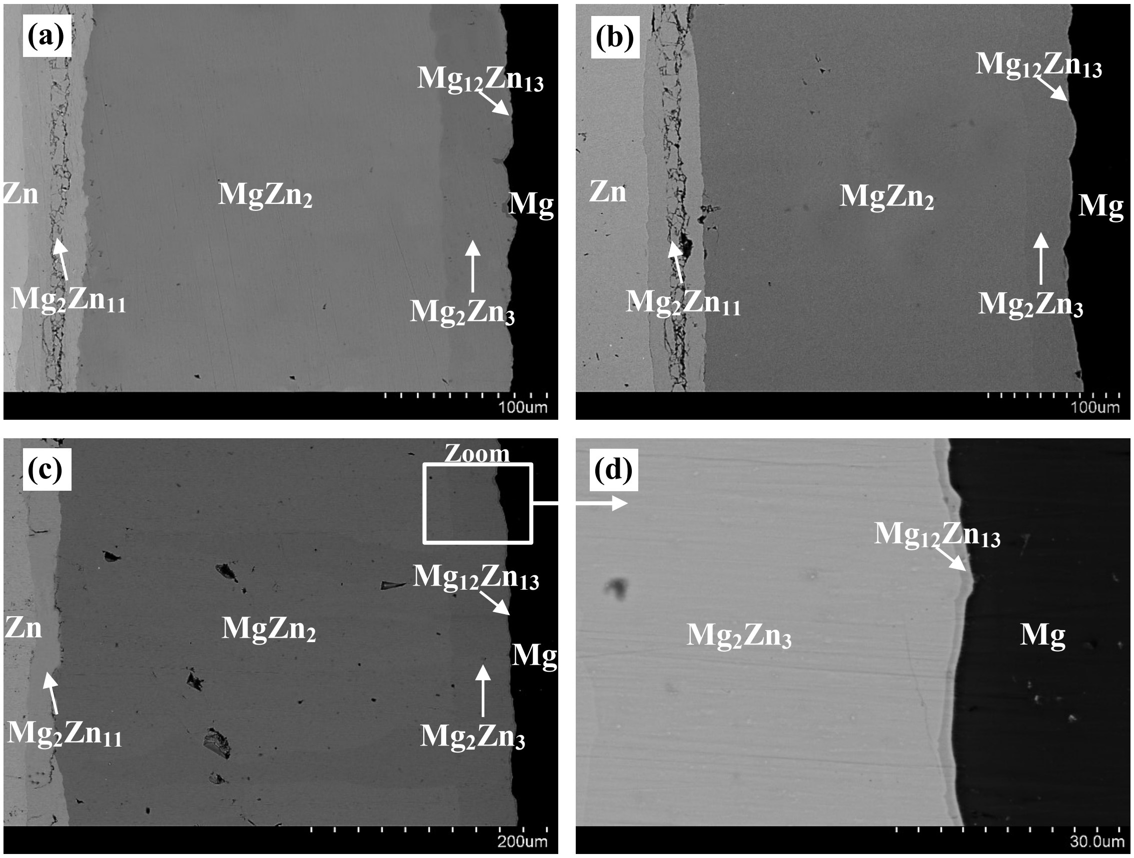

Figure 5-6: Backscattered electron images of Mg-Zn diffusion couples annealed at (a) 250°C for 552hr; (b) 275°C for 408hr; (c) 300°C for 504hr

The composition profile across Mg-Zn diffusion couple, annealed at 300°C for 504hr, is shown in Figure 5-7 (a) and (b). The composition profiles confirmed the existence of three stoichiometric compounds ($Mg_{12}Zn_{13}$, Mg_2Zn_3 and Mg_2Zn_{11}) and one intermediate solid solution, $MgZn_2$. The solubility range of $MgZn_2$ was determined at

250, 275 and 300°C as ~1, 1.3 and 2.1 at.%, respectively. Figure 5-7 (b) represents part of the composition profile shown in Figure 5-7 (a) to emphasis on the solubility of Zn in Mg. Accordingly, the solubility of Zn in Mg was determined as 1.5 at.% Zn at 300°C.

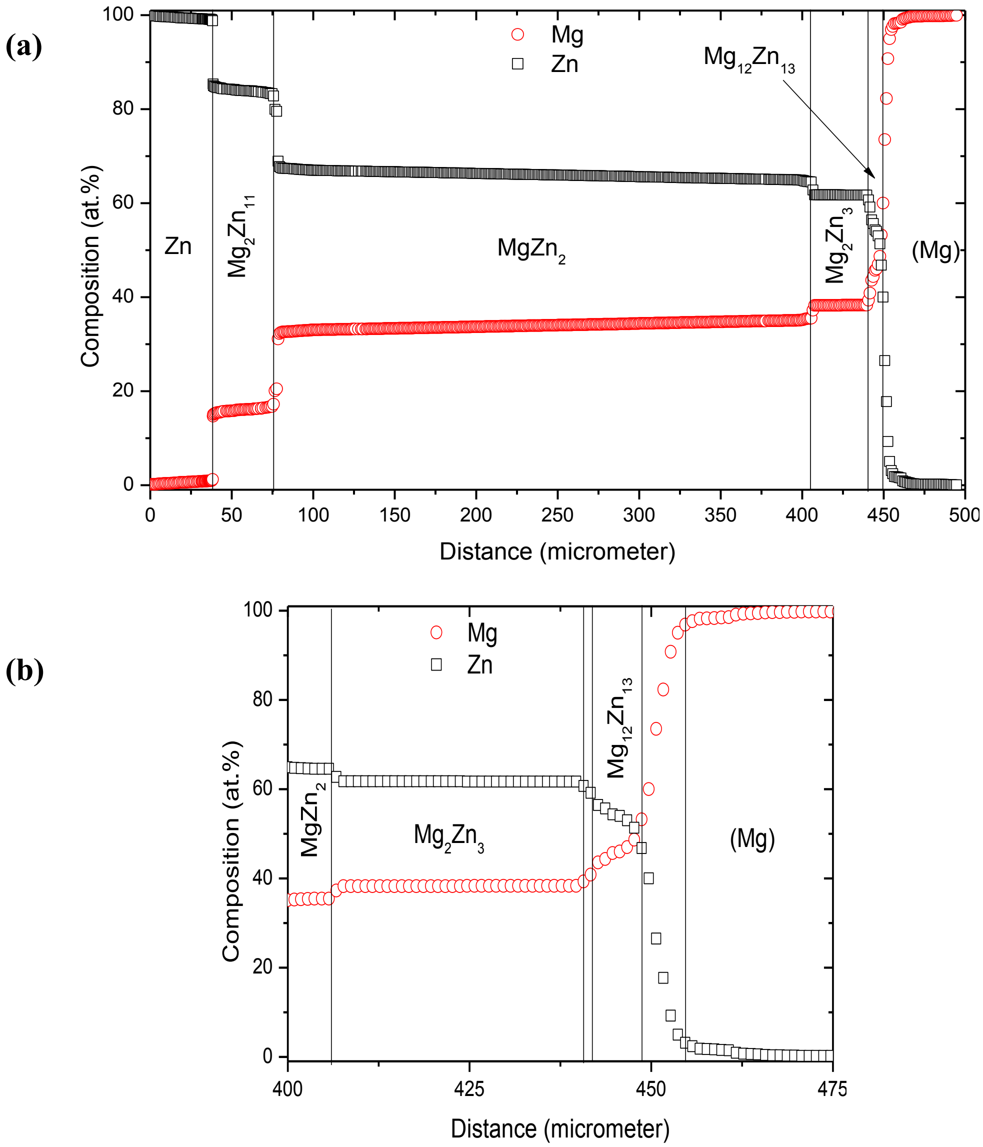

Figure 5-7: (a) and (b) The composition profile across Mg-Zn diffusion couple annealed at 300°C for 504hr

The experimental composition profiles determined by WDS line-scans for all diffusion couples were analyzed for interdiffusion coefficients using Boltzmann-Matano method [23, 24]; in which interdiffusion fluxes can be measured at any location of a diffusion couple [24]. In this work, the position of Boltzmann-Matano interface was determined from the composition profiles when the integrated areas above and under the curve are equal (Equation 5-2)). Using this method, Boltzmann-Matano plane position was determined at every intermetallic interface within the Mg-{Ce, Nd, Zn} and Zn-{Ce, Nd} diffusion couples. Once the plane position is known, the composition-dependent diffusion coefficient can be calculated for any given composition based on Equation 5-1. The following example illustrates the calculation of composition-dependent interdiffusion coefficient at the $Mg_3Nd/Mg_{41}Nd_5$ interface at 450°C. The composition of Nd falls across the interface from 25 at.% until it reaches 10.8 at.% as shown in Figure 5-8. Then, the integrated areas above and below the curve can be calculated while changing the location of the vertical line until the areas are equal. The point at which the areas are equal represents Boltzmann-Matano plane location. The same procedure is followed to determine Boltzmann-Matano plane at the other interfaces.

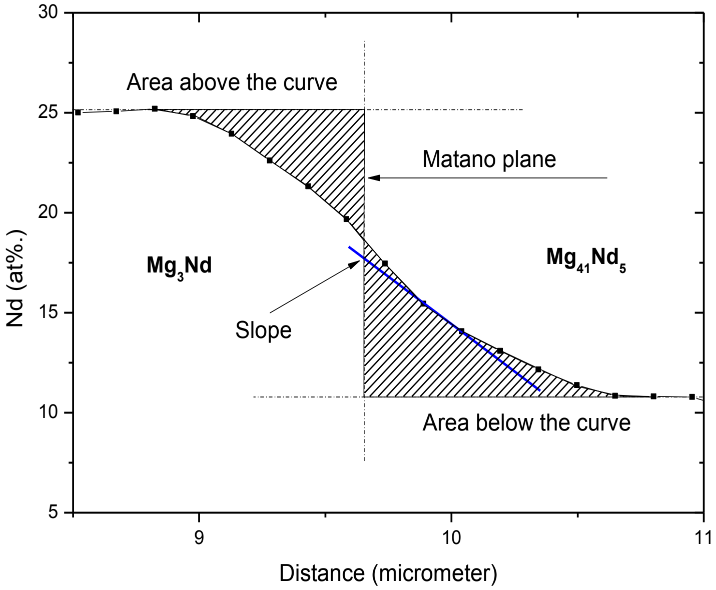

Figure 5-8: Demonstration of Boltzmann-Matano plane determination at the $Mg_3Nd/Mg_{41}Nd_5$ interface

The value of $\widetilde{D}$ can be calculated at any given composition C by measuring the area $\int_{C^o}^{C}(x - x_o)dC$ and the slope $\frac{dx}{dC}$. For $Mg_3Nd/Mg_{41}Nd_5$ interface, $\int_{C^o}^{C}(x - x_o)dC = 5.173 \times 10^{-4}$, $\frac{dx}{dC} = -19145$. Thus according to Equation 5-1, $\widetilde{D} = 3.0 \times 10^{-13}\ cm^2/s$. Similarly calculations at other interfaces in all the studied systems were performed. Table 5-9 summarizes the Boltzmann-Matano plane positions and the calculated interdiffusion coefficients at every interface and temperature of Mg-{Ce, Nd, Zn} diffusion couples.

Figures 5-1 and 5-3 (a) show that apparent two phase regions exist in the Mg-Ce and Mg-Nd diffusion couples annealed at 400°C for 120hr. The interdiffusion coefficients at $Mg_3Ce/Mg_{41}Ce_5$ and $Mg_3Nd/Mg_{41}Nd_5$ interfaces, at 400°C, show higher values than for the other adjacent interfaces, Table 5-9. This means that the interatomic diffusion of Mg atoms through $Mg_{41}\{Ce,Nd\}_5$ compound layers is faster than those of neighboring compounds at 400°C resulting in a very wavy interface that appears as two phase region. Also, this could be the reason of having traces of $Mg_3\{Ce,Nd\}$ compounds in the $Mg_{41}\{Ce,Nd\}_5$ diffusion layers.

Lal and Levy [99] measured the diffusion coefficient of Ce-Mg system considering a solid solution having a continuous composition profile assuming complete miscibility between the two components. However, the Ce-Mg should be treated as multiple-phase system, since four stable intermetallic compounds exist in the temperature range of 550-600°C.

Table 5-9: Interdiffusion coefficients at the interfaces of the Mg-{Ce, Nd, Zn} diffusion layers

System	Intermetallic interface	C^o Mg (at.%)	400°C		450°C		490°C	
			x_o (µm)	$\widetilde{D}$(C) (cm^2/s)	x_o (µm)	$\widetilde{D}$(C) (cm^2/s)	x_o (µm)	$\widetilde{D}$(C) (cm^2/s)
Mg-Ce	Ce/MgCe	25	9.7	1.8×10^{-13}	4.1	3.5×10^{-13}	9.8	6.0×10^{-13}
	MgCe/Mg_3Ce	62.5	12.6	8.7×10^{-14}	9.2	1.6×10^{-13}	16.2	3.2×10^{-13}
	Mg_3Ce/$Mg_{41}Ce_5$	82	22.0	1.6×10^{-13}	19.5	3.2×10^{-13}	33.5	5.6×10^{-13}
	$Mg_{41}Ce_5$/$Mg_{12}Ce$	90.7	60.8	1.1×10^{-13}	89.6	2.3×10^{-13}	133.3	4.2×10^{-13}
	$Mg_{12}Ce$/Mg	96	84.4	2.1×10^{-13}	118.0	4.8×10^{-13}	150.9	7.3×10^{-13}
Mg-Nd	Nd/MgNd	25	7.7	1.1×10^{-13}	8.9	1.5×10^{-13}	3.7	2.1×10^{-13}
	MgNd /Mg_3Nd	62.5	9.5	2.4×10^{-14}	10.5	3.7×10^{-14}	6.5	5.9×10^{-14}
	Mg_3Nd /$Mg_{41}Nd_5$	82	57.7	2.3×10^{-13}	47.0	3.0×10^{-13}	44.3	4.5×10^{-13}
	$Mg_{41}Nd_5$/Mg	94.5	122.5	7.5×10^{-14}	113.3	1.1×10^{-13}	79.5	1.8×10^{-13}
			250°C		275°C		300°C	
Mg-Zn	Mg/$Mg_{12}Zn_{13}$	96	301.5	4.2×10^{-14}	36.8	6.2×10^{-14}	423.5	8.8×10^{-14}
	$Mg_{12}Zn_{13}$/Mg_2Zn_3	66	299.7	9.1×10^{-15}	38.8	1.6×10^{-14}	421.0	2.9×10^{-14}
	Mg_2Zn_3/$MgZn_2$	36.5	263.9	2.5×10^{-14}	69.7	4.5×10^{-14}	370.1	6.8×10^{-14}
	$MgZn_2$/Mg_2Zn_{11}	24.3	31.5	8.5×10^{-14}	315.0	1.4×10^{-13}	42.9	2.1×10^{-13}
	Mg_2Zn_{11}/Zn	7.5	5.4	5.8×10^{-14}	354.8	9.4×10^{-14}	6.5	1.4×10^{-13}

Xu *et al.* [61] measured the diffusion coefficients of Mg-Nd system as a result of solid-liquid diffusion reaction. Therefore their measured coefficients were much higher than those obtained by Xu *et al.* [100], who used solid-solid diffusion reaction. Because Mg_3Nd/$Mg_{41}Nd_5$ and $Mg_{41}Nd_5$/Mg interfaces were missing in the work of Xu *et al.* [100], the diffusion coefficient at the Mg_3Nd/Mg interface could not be compared with their work. Comparing the binary interdiffusion coefficients of the Mg-Nd system calculated in this work, Table 5-9, with the values reported by Xu *et al.* [100], Table 5-3, the diffusion coefficients at the Nd/MgNd and MgNd/Mg_3Nd interfaces show the same order of magnitude. However, the magnitude of the current values are much higher than those calculated by Brennan *et al.* [101]. Same observation was noticed regarding the magnitude of the binary interdiffusion coefficients of the Mg-Zn system. There is an agreement between Sakakura and Sugino [103] and Brennan *et al.* [104], whereas the values provided in this work are much lower. This is due to that the interdiffusion coefficients were measured within each individual intermetallic layer [101, 104] using the parabolic growth constant formula [107] instead of the diffusion at the interface. Boltzmann-Matano interface is defined as being the plane across which an equal number of atoms have crossed in both directions [108]. The current work focuses on providing these coefficients at the interface of the intermetallic compounds. Thus, our results are in good agreement with Xu *et al.* [100] who also obtained the diffusion coefficients at the interfaces.

Matano [24] considered the value of $\widetilde{D}$ as a function of composition where the coefficient of diffusion decreases rapidly with composition; except at some point, where the values retained nearly the same even though the composition is changing. The point where the diffusion coefficient becomes almost constant represents the location of Matano plane. This implies that, once we move away from the interface, the diffusion coefficient value changes. This is illustrated in Figure 5-9, which represents the drop in the $\widetilde{D}$ value with composition and then the value remains almost constant where Matano plane exists. Thus, the calculated coefficients here could be more or less close to the values given by [101, 103, 104], if one considers the transient diffusion values and not those at the interface. The $\widetilde{D}$ value near Mg_3Nd diffusion layer at 450°C, in Figure 5-9, reads as 1.63×10^{-12} cm^2/s, which is still close to 1.7×10^{-11} cm^2/s which was reported by Brennan *et al.* [101] at the same temperature. This indicates that farther from the interface towards the center of the Mg_3Nd layer, the diffusion coefficient becomes closer to the values measured by Brennan *et al.* [101]. The same applies to other intermetallic compounds.

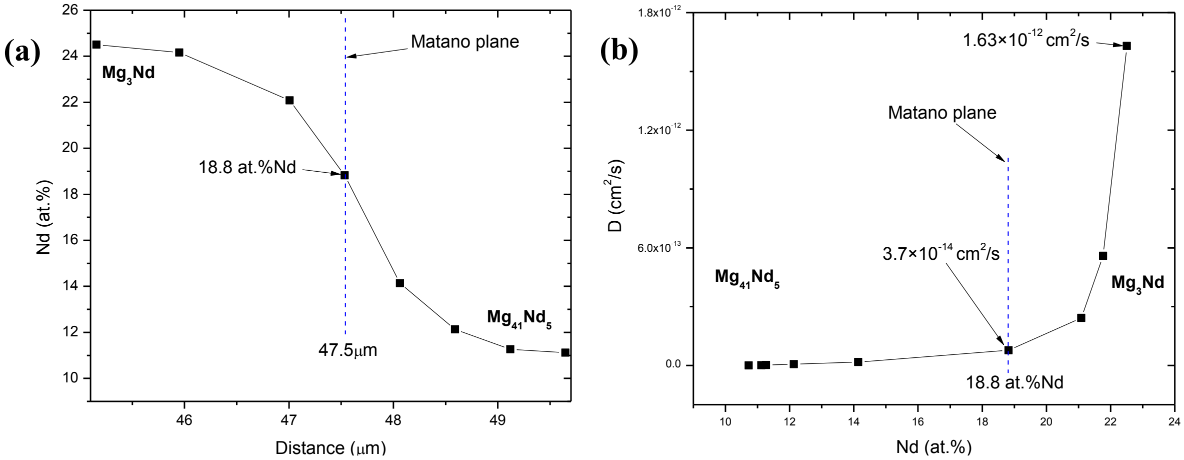

Figure 5-9: (a) The composition profile at the $Mg_3Nd/Mg_{41}Nd_5$ interface; (b) corresponding interdiffusion coefficient vs. at.% Nd composition at the $Mg_3Nd/Mg_{41}Nd_5$ interface

The composition-dependent interdiffusion coefficients were then used to calculate the activation energies and the pre-exponential factors at the interfaces of the Mg-{Ce, Nd, Zn} diffusion couples based on Equation 5-3. The plots of $log\widetilde{D}_o$ against *1/T* are presented in Figure 5-10 (a-c).

These plots were used to estimate the activation energy and pre-exponential factor, for the growth of the Mg-Ce, Mg-Nd and Mg-Zn diffusion layers at every interface, based on the data provided in Table 5-9 and Arrhenius equation. The activation energy and pre-exponential factor of the growth of the Mg-Ce, Mg-Nd and Mg-Zn layers are listed in Table 5-10.

The compound formation and growth take place at the interface where two substances of dissimilar chemical natures react with one another. So, the growth rate depends on the chemical composition of the initial phases. The layer of the same intermetallic compound may grow at the interface between pure elements, between another compound and pure element or between two other compounds [109]. Hence, it is concluded that the compound itself does not diffuse and the interdiffusion coefficient, activation energy and pre-exponential factor are characteristics of the diffusing atoms at certain location in the diffusion couple.

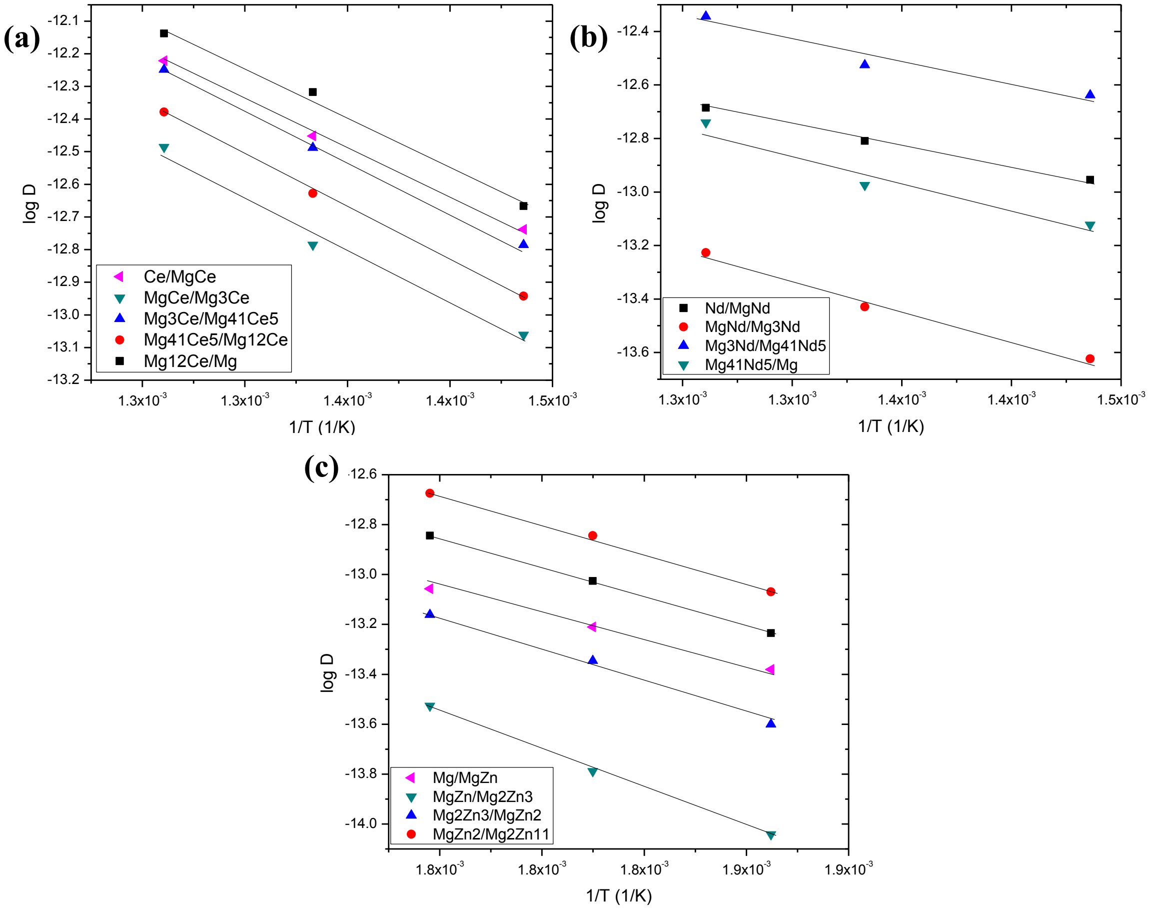

Figure 5-10: log$\widetilde{D}_0$ against 1/T plots at the intermetallic interfaces of (a) Mg-Ce; (b) Mg-Nd; (c) Mg-Zn diffusion layers

According to the results obtained from Table 5-10, the activation energy values of the growth of the Mg-Zn intermetallics, obtained from this work, were comparable to those calculated by Sakakura and Sugino [103]. On the other hand, the pre-exponential factor of the same compounds is much lower, because of the difference in the interdiffusion coefficients values. The activation energy of the growth of the Mg-Nd compounds obtained from this work were lower than the values reported by Brennan *et* *al.* [101]. This might be due to imposing a parabolic diffusion-controlled growth equation to calculate the interdiffusion coefficients in the corresponding phases without taking the diffusion reaction at the interfaces into account. Parabolic diffusion equations can only be used to examine whether the phases grow by a diffusion-controlled process, because the growth constant is calculated based on the total layer thickness. This may be correct for isomorphous systems but for systems that form intermediate compounds, such as the systems tackled in this paper, Boltzmann-Matano method is more appropriate.

Table 5-10: Activation energy and pre-exponential factor of the growth of the Mg-Ce, Mg-Nd and Mg-Zn diffusion layers

System	Intermetallic interface	Q_d (kJ/mole)	$\widetilde{D}_0$ (cm^2/s)
Mg-Ce	Ce/MgCe	56.1	4.2×10^{-9}
	MgCe/Mg$_3$Ce	61.9	5.4×10^{-9}
	Mg$_3$Ce/Mg$_{41}$Ce$_5$	58.9	5.6×10^{-9}
	Mg$_{41}$Ce$_5$/Mg$_{12}$Ce	61.3	6.6×10^{-9}
	Mg$_{12}$Ce/Mg	58.1	7.3×10^{-9}
Mg-Nd	Nd/MgNd	29.1	2.0×10^{-11}
	MgNd /Mg$_3$Nd	42.8	4.9×10^{-11}
	Mg$_3$Nd /Mg$_{41}$Nd$_5$	31.3	6.1×10^{-11}
	Mg$_{41}$Nd$_5$/Mg	40.7	1.0×10^{-10}
Mg-Zn	Mg/Mg$_{12}$Zn$_{13}$	37.0	2.1×10^{-10}
	Mg$_{12}$Zn$_{13}$/Mg$_2$Zn$_3$	58.8	5.8×10^{-10}
	Mg$_2$Zn$_3$/MgZn$_2$	50.3	2.7×10^{-9}
	MgZn$_2$/Mg$_2$Zn$_{11}$	45.3	2.9×10^{-9}
	Mg$_2$Zn$_{11}$/Zn	44.7	7.4×10^{-9}

5.5.2. Zn-{Ce-Nd} binary systems

Many attempts were carried out to obtain successful Zn-{Ce, Nd} diffusion couples by the current authors. Formation of all expected diffusion layers while preventing Zn evaporation is a real challenge. In the following two systems, pure Zn disappeared from the contacting interface of the two end-members after annealing at

400°C for 240hr. However, the diffusion reaction took place and all the expected compounds formed. It was observed that the diffusion reaction took place due to the migration of Zn atoms towards RE end-members. No diffusion reaction took place upon annealing at 300°C for up to 504hr. Annealing at 300°C for longer time might result in diffusion. However, this could lead to increasing the gap between the two end-members due to Zn volatility and Kirkendall effect [110].

A backscattered electron image of the Ce-Zn diffusion couple, annealed at 400°C for 240hr, is shown in Figure 5-11 (a). Figure 5-11 (b) represents the diffusion layers adjacent to Ce end-member. Seven diffusion layers, representing CeZn, $CeZn_2$, $CeZn_3$, Ce_3Zn_{11}, $Ce_{13}Zn_{58}$, Ce_2Zn_{17} and $CeZn_{11}$, were observed and determined using WDS spot analysis. Two sub-layers were also observed at the $Ce_{13}Zn_{58}/Ce_2Zn_{17}$ interface. WDS line-scan was performed to measure the composition profile across the diffusion layers as shown in Figure 5-11 (c). In order to show the composition of all the observed phases clearly, the data ranged from 60 to 300μm, located in the very wide layer of $Ce_{13}Zn_{58}$, was cut from the graph. Two intermetallic compounds were not detected by the WDS line-scan, because they formed in sub-layers with nonuniform interfaces. These compounds are: $CeZn_5$ and Ce_3Zn_{22}, which are located between $Ce_{13}Zn_{58}$ and Ce_2Zn_{17}. However, these compounds were observed in an other Ce-Zn diffusion couple annealed at 400°C for 48hr; which means that they are stable at this temperature. The couple annealed at 400°C for 48hr was not used for interdiffusion calculations, because the diffusion layers were very thin.

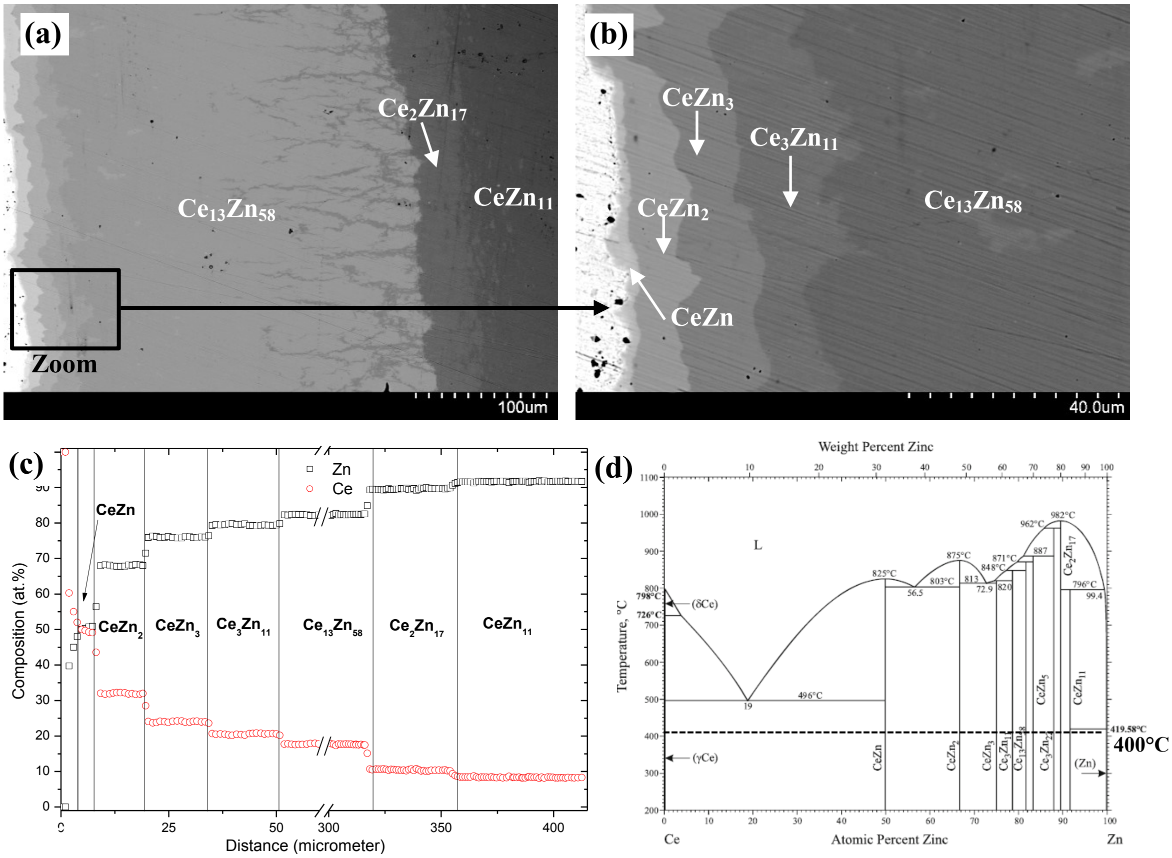

Figure 5-11: (a) and (b) backscattered electron images of Ce-Zn diffusion couples annealed at 400°C for 240hr; (c) WDS composition profile; (d) The Ce-Zn phase diagram [111] with the annealing temperature marked as dashed line

In a binary diffusion couple, the number of the intermetallic compounds in every diffusion layer cannot exceed one except at the interface. However, the diffusion layers of $Ce_{13}Zn_{58}$ and Ce_2Zn_{17} show the growth of sub-layers at the interface, as shown in Figure 5-11 (a). As a result, two intermetallic compounds, $CeZn_5$ and Ce_3Zn_{22}, were presumed missing. It is highly probable that all the intermetallic compounds of the Ce-Zn system were formed in the diffusion couple, because of the presence of the Ce-rich CeZn and the Zn-rich Ce_2Zn_{11} compounds in the sub-layers. This was based on the fact that the layer-growth kinetics in a diffusion couple is sequential and not simultaneous [112]. This means that the two far-end compound layers grow initially, at the interface with the pure elements, due to the participation of diffusing atoms of one of two components and surface atoms of the other component. Once these layers reach their maximum thickness, they are consumed partially to form the next layers [113]. From the Ce-Zn diffusion couple annealed at 400°C for 48hr, Figure 5-12 (a), it was noticed that the compounds $CeZn_5$ and Ce_3Zn_{22} were imbedded in the $Ce_{13}Zn_{58}$ and Ce_2Zn_{17} diffusion layers, representing $Ce_{13}Zn_{58}$+$CeZn_5$ and Ce_3Zn_{22}+Ce_2Zn_{17} sub-layers as shown in Figure 5-12 (b). In total, nine intermetallic compounds were found in this diffusion couple, which are equal to the number of the stable compounds at 400°C of the Ce-Zn binary phase diagram [111] shown in Figure 5-11 (d). Figure 5-12 (c) shows the wavy growth of Ce, $CeZn_2$, $CeZn_3$, Ce_3Zn_{11} and $Ce_{13}Zn_{58}$ diffusion layers. This is attributed to the anisotropic diffusion of Ce and Zn resulting in uneven growth of these layers as will be discussed in the Nd-Zn diffusion couple part of this work. Thus, $CeZn_5$ and Ce_3Zn_{22} compounds might have been consumed upon the formation of $Ce_{13}Zn_{58}$ and Ce_2Zn_{17} in the Ce-Zn diffusion couple annealed for 240hr. In addition, the fast formation kinetics of $Ce_{13}Zn_{58}$, which has obviously larger thickness (266.4μm) than other layers, led to the consumption of the diffusing Zn atoms contributing further to the consumption of the $CeZn_5$ and Ce_3Zn_{22} compounds. Similarly, Loo and Rieck [114] and Wöhlert and Bormann [115] reported the absence of phases other than $TiAl_3$ in the Al-Ti diffusion couples. Wöhlert and Bormann [115] made their diffusion couples using α_2-Ti_3Al and γ-TiAl sandwiched between Ti and Al layers. The results indicated that the phase absence in favor of Ti_3Al was caused by different growth velocities due to different diffusion fluxes. The kinetics of layers consumption were tackled thoroughly by Dybkov [112, 113].

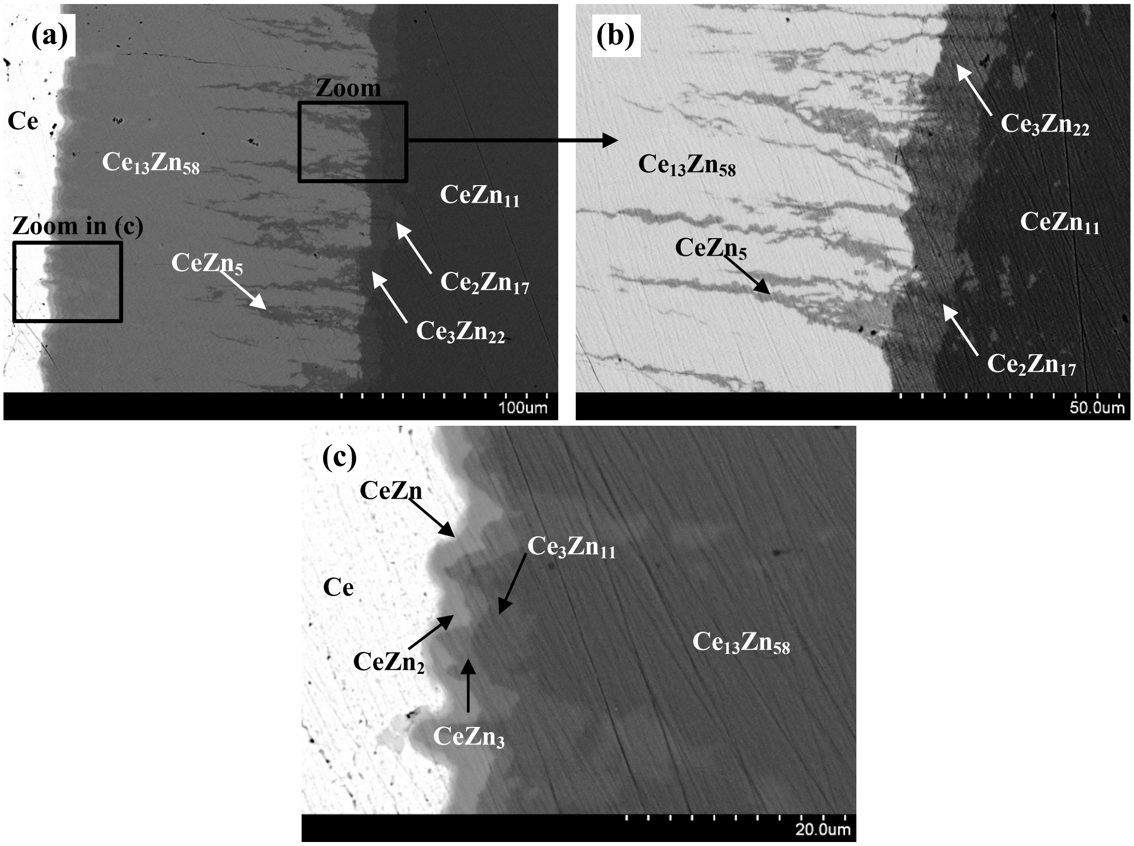

Figure 5-12: (a) Backscattered electron image of the Ce-Zn diffusion couple annealed at 400°C for 48hr; (b) diffusion sub-layer formation at the $Ce_{13}Zn_5$/Ce_3Zn_{22} interface; (c) anisotropic diffusion and irregular growth of the CeZn, $CeZn_2$, $CeZn_3$, Ce_3Zn_{11} and $Ce_{13}Zn_{58}$ diffusion layers

Backscattered electron image of Nd-Zn diffusion couple, annealed at 400°C for 240hr, is shown in Figure 5-13 (a). Figure 5-13 (b) represents an enlarged part near Nd end-member. Eight diffusion layers, representing NdZn, $NdZn_2$, $NdZn_3$, Nd_3Zn_{11}, $Nd_{13}Zn_{58}$, Nd_3Zn_{22}, Nd_2Zn_{17} and $NdZn_{11}$ intermetallic compounds, were observed and determined using WDS spot analysis. WDS line-scan was performed across these layers to measure the composition profile shown in Figure 5-13 (c).

Although the diffusion layer of NdZn could be observed in the micrograph (Figure 5-13 (b)), it could not be detected in the composition profile because it is very thin. Similar to Figure 5-11 (c), the data ranged from 140 to 500μm was cut from the graph for clarity. Based on the Nd-Zn phase diagram [116], shown in Figure 5-13 (d), all the expected sable phases at 400°C were detected.

The composition profile in Figure 5-13 (c) shows that a few values deviated from the stoichiometric composition of $Nd_{13}Zn_{58}$ (18.3 at.% Nd and 81.6 at.% Zn) near the interface with Nd_3Zn_{11}. This can be explained from the backscattered electron image in Figure 5-13 (b), which shows a sub-layer containing $Mg_{13}Zn_{58}$ dendrites extending in Nd_3Zn_{11} layer. Therefore, the WDS line-scan provided the composition of Nd_3Zn_{11} for some points and an average composition of the two phases for other points.

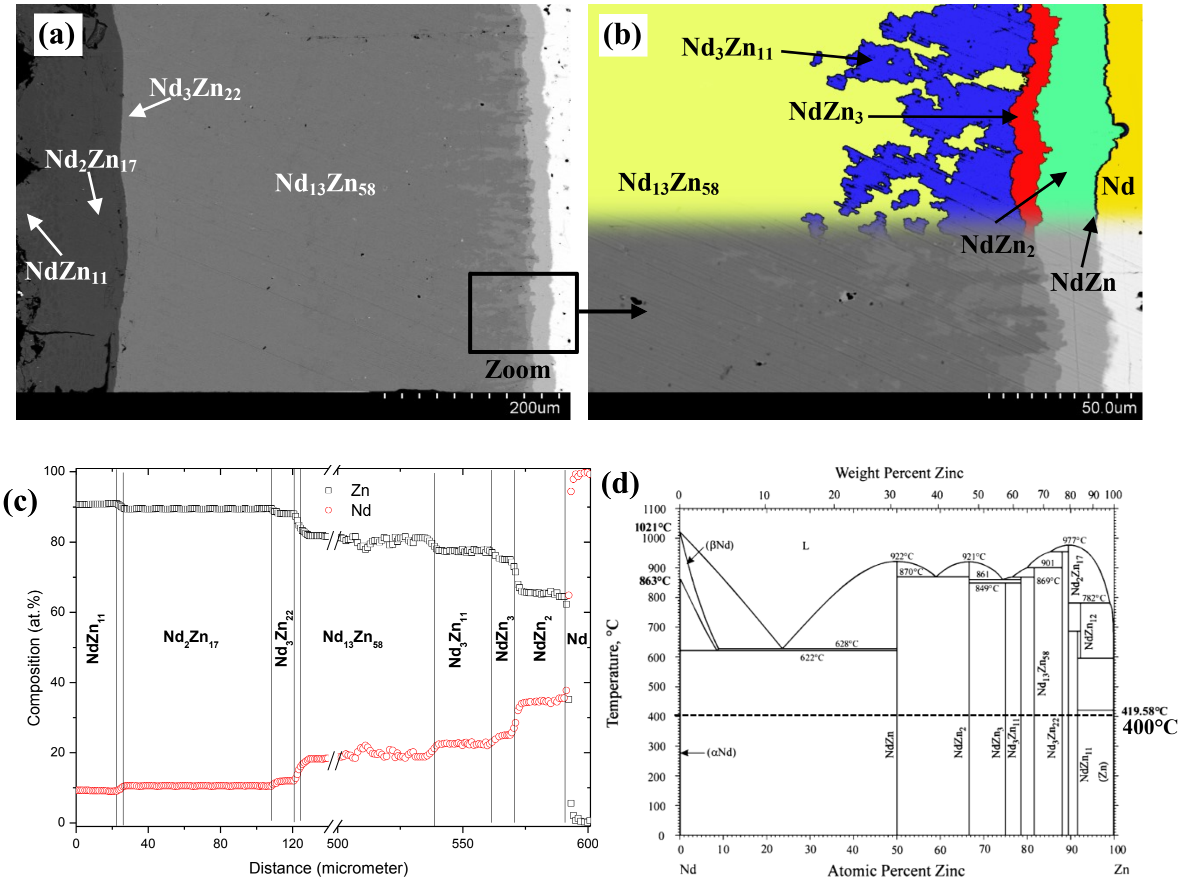

Figure 5-13: (a) and (b) backscattered electron images of Nd-Zn diffusion couples annealed at 400°C and 240hr; (c) WDS composition profile; (d) the Nd-Zn phase diagram [116] with the annealing temperature marked as dashed line

Initially, it was difficult to explain the existence of the sub-layers near the $Nd_{13}Zn_{58}/Nd_3Zn_{11}$ interface without experimental proof. Also, the interfaces between the layers are wavy indicating an isotropic diffusion between Mg and Nd. The same applies to Mg and Ce diffusion. In this work, an explanation is provided based on extensive experimental studies of the Nd-Zn diffusion couple annealed at 300°C for 576hr. The evolution of the diffusion process is discussed in Figure 5-14. Backscattered electron images of this diffusion couple are shown in Figure 5-14 (a-c). These micrographs were taken along the diffusion interface, where the diffusion process has just started at one location at the interface but progressed in another location. The contrast of these micrographs was modified to show details of the diffusion layers. The colored-schematic, shown in Figure 5-14 (d), was developed from Figure 5-14 (c) using image processing software to show the dendritic growth mechanism of $Nd_{13}Zn_{58}$.

Figure 5-14 (a) is an initial diffusion stage showing that the thickness of $NdZn_2$ layer is the largest among other layers. At this stage, $Nd_{13}Zn_{58}$ dendrites were initially growing in the $NdZn_3$ layer. According to the Nd-Zn phase diagram, Figure 5-13 (d), $NdZn_3$ cannot be in equilibrium with $Nd_{13}Zn_{58}$. There must be an intermediate layer representing Nd_3Zn_{11} compound, equilibrating with both $NdZn_3$ and $Nd_{13}Zn_{58}$ compounds. Also, if the diffusion process is interrupted at this stage, a two-compound layer, $NdZn_3$+$Nd_{13}Zn_{58}$, can appear. Figure 5-14 (b) shows an advanced diffusion stage, where $Nd_{13}Zn_{58}$ dendrites are continuously growing, displacing both interfaces, $NdZn_3/Nd_{13}Zn_{58}$ and $NdZn_3/NdZn_2$, forward at the expense of $NdZn_2$ layer. In other words, part of $NdZn_2$ is consumed to form $NdZn_3$ and part of $NdZn_3$ is consumed to form $Nd_{13}Zn_{58}$. The consumption means that more Zn atoms are transferred within $NdZn_3$

layer towards $NdZn_2$. This was demonstrated with dotted arrows in Figure 5-14 (c). At the bottom of Figure 5-14 (b), Nd_3Zn_{11} started to form, which means that $Nd_{13}Zn_{58}$ reached its maximum thickness.

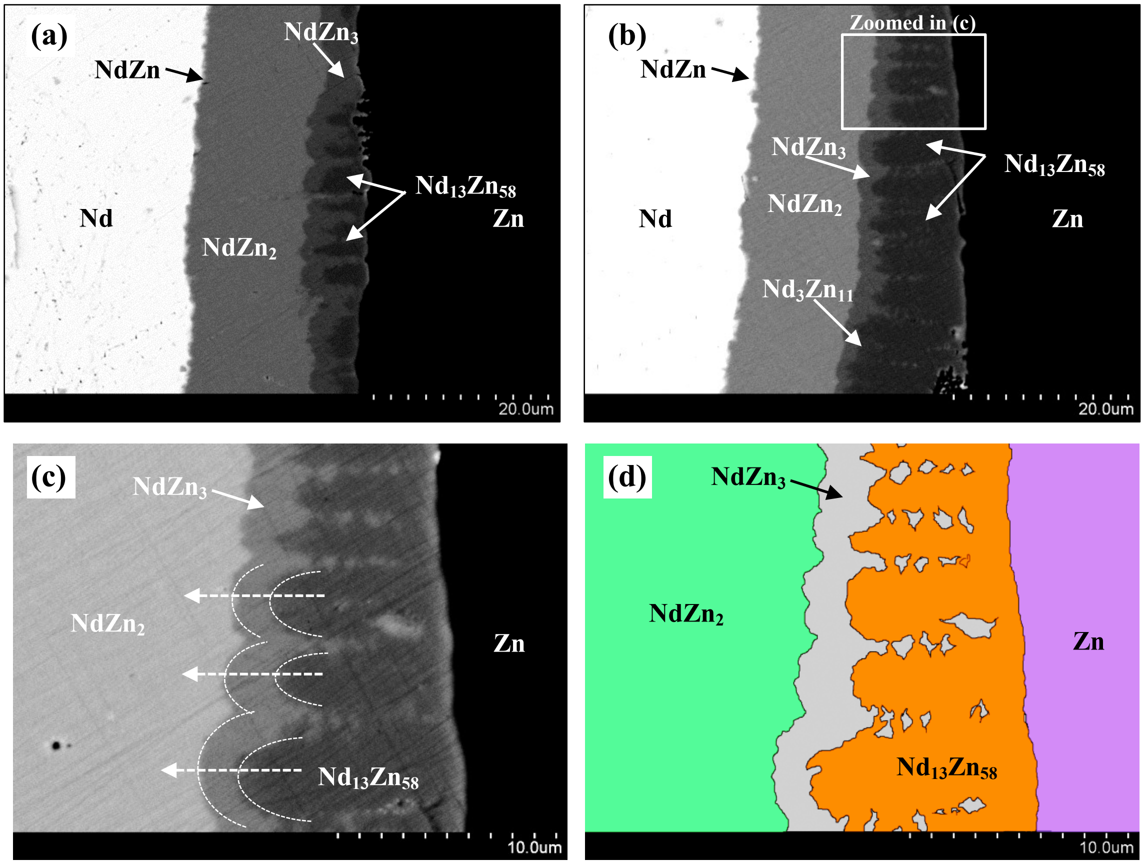

Figure 5-14: Evolution of phase growth in the Nd-Zn diffusion couple annealed at 300°C for 576hr. (a) initial diffusion stage (b) advanced diffusion stage; (c) dendritic growth representation; (d) colored-schematic showing the dendritic growth of $Nd_{13}Zn_{58}$. Reader is encouraged to refer to the online version for colored image.

In Figure 5-14 (c), the $NdZn_2/NdZn_3$ interface seems not to be straight; dotted curves were drawn to show that the wavy interface was due to the growth of $Nd_{13}Zn_{58}$ dendrites. With the aid of Figure 5-14 (d), it is concluded that the $Nd_{13}Zn_{58}$ dendrites were growing longitudinally across the $NdZn_3$ layer. The dendrites, then, became wider due to the side expansion resulted from the formation of secondary dendrites branched from the primary ones. The expansion continues with time, and the gaps between these branches, representing $NdZn_3$, become smaller until they disappear. This explanation might give an approach to understand that the growth mechanism of every diffusion layer is unique.

The location of Boltzmann-Matano plane and the composition-dependent interdiffusion coefficients of the Zn-{Ce, Nd} systems are listed in Table 5-11. Zn-{Ce, Nd} systems are considered among the difficult systems to be studied by diffusion couple experiments, because they contain large number of intermetallic compounds and the compositions of the Zn-rich compounds are very close to each other. In this work, two successful diffusion couples; i.e.: Ce-Zn and Nd-Zn, were obtained and the diffusion data of the 15 observed compounds are provided. The binary interdiffusion coefficients of the Ce-Zn system were not calculated at six metallic interfaces, because three phases; namely, $CeZn_5$, Ce_3Zn_{22} and Zn, were formed in the sub-layers which were not parallel to the original interface. These compounds might be partially consumed during the diffusion process, as discussed earlier in the Zn-{Ce, Nd} diffusion couples section. These interfaces were marked with single asterisk (*). Also, the experimentally observed interfaces, determined despite the missing compounds, were marked with bold font and double asterisks (**), as indicated in Table 5-11. The same procedure was applied to the interfaces in the Nd-Zn diffusion couple. Although NdZn diffusion layer was discovered by WDS spot analysis to be very thin, the interdiffusion calculations were not performed at the corresponding interfaces for the accuracy.

Table 5-11: Boltzmann-Matano plane locations and composition-dependent interdiffusion coefficients at the interface of the Zn-{Ce, Nd} diffusion layers

System	Intermetallic interface	C^o Zn (at.%)	x_o (μm)	$\widetilde{D}(C)$ (cm^2/s)	System	Intermetallic interface	C^o Zn (at.%)	x_o (μm)	$\widetilde{D}(C)$ (cm^2/s)
Ce-Zn	Ce/CeZn	25	1.8	5.7×10^{-15}	Nd-Zn	Nd/NdZn*	25	-	-
	CeZn/$CeZn_2$	58.3	8.1	1.9×10^{-14}		NdZn/$NdZn_2$*	58.3	-	-
	$CeZn_2$/$CeZn_3$	70.8	19.6	7.5×10^{-15}		**Nd/$NdZn_2$****	**33.3**	**592.3**	-
	$CeZn_3$/Ce_3Zn_{11}	76.7	34.7	3.3×10^{-14}		$NdZn_2$/$NdZn_3$	70.8	571.5	2.4×10^{-14}
	Ce_3Zn_{11}/$Ce_{13}Zn_{58}$	80.1	51.3	3.3×10^{-14}		$NdZn_3$/Nd_3Zn_{11}	76.7	562.3	4.1×10^{-14}
	$Ce_{13}Zn_{58}$/$CeZn_5$*	82.5	-	-		Nd_3Zn_{11}/$Nd_{13}Zn_{58}$	80.1	537.6	4.8×10^{-14}
	$CeZn_5$/Ce_3Zn_{22}*	85.6	-	-		$Nd_{13}Zn_{58}$/Nd_3Zn_{22}	84.8	124.0	4.5×10^{-14}
	Ce_3Zn_{22}/Ce_2Zn_{17}*	88.7	-	-		Nd_3Zn_{22}/Nd_2Zn_{17}	88.7	110.0	2.8×10^{-14}
	$Ce_{13}Zn_{58}$/Ce_2Zn_{17}**	**85.5**	**317.2**	-		Nd_2Zn_{17}/$NdZn_{11}$	90.5	24.7	3.8×10^{-14}
	Ce_2Zn_{17}/$CeZn_{11}$	90.5	355.6	1.7×10^{-14}		$NdZn_{11}$/Zn*	95.8	-	-
	$CeZn_{11}$/Zn*	95.8	-	-					

*** Indicates the missing interfaces based on the WDS composition profiles**
**** Indicates the location of the experimentally available interfaces**

5.6. Summary

Diffusion couple experiments were used to measure the interdiffusion coefficients at the intermetallic interfaces of the Mg-{Ce, Nd, Zn} and Zn-{Ce, Nd} systems. Mg-{Ce, Nd} diffusion couples were annealed at 400, 450 and 490°C for 120, 96 and 4hr, respectively. Mg-Zn diffusion couples were annealed at 250, 275 and 300°C for 552, 408 and 504hr, respectively. Zn-{Ce, Nd} diffusion couples were annealed at 400°C for 240hr. WDS line-scans were performed across diffusion layers of every diffusion couple to obtain the composition profiles. The obtained profiles were, then, analyzed using Boltzmann-Matano method to calculate the composition-dependent interdiffusion coefficients at every intermetallic interface. Arrhenius equation was also applied to calculate the activation energy and pre-exponential factor of the growth of the intermetallic compounds.

This work resolved the problem encountered in the literature of the missing phases in the Mg-{Ce, Nd, Zn} systems. The composition-dependent interdiffusion coefficient, activation energy and pre-exponential factor at the interfaces of the Mg-{Ce, Nd, Zn} intermetallic compounds were calculated.

Although Zn-{Ce, Nd} systems are considered among the difficult systems to be studied via diffusion couple experiments, two successful diffusion couples, annealed at 400°C for 240hr, were obtained. The difficulty stems from the presence of large number of intermetallic compounds in a narrow range of composition. In addition, some of these compounds appeared as very thin layers. Nine intermetallic compounds were detected in the Ce-Zn diffusion couple and eight compounds were detected in the Nd-Zn diffusion couple. The diffusion couples were analyzed thoroughly and their results were discussed and supported using the established phase diagrams. Explanation of the evolution of phases in the Nd-Zn system and the anisotropic diffusion behavior, resulting in wavy interfaces, were provided. Sequential instead of spontaneous layer formation was observed and the layer consumption of Ce-Zn compounds was also discussed. The composition-dependent interdiffusion coefficients at the intermetallic interfaces of these systems are also provided in this work.

5.7. Acknowledgement

The authors would like to acknowledge National Sciences and Engineering Research Council (NSERC) for the financial support of the project through Magnesium Network (MagNET) for excellence. More information on the Network can be found at www.magnet.ubc.ca.

5.7. Author's notes and significance of paper to thesis

In this chapter, the diffusion couple technique was used to measure the activation energy and pre-exponential factor of the growth of the Mg-{Ce, Nd, Zn} binary compounds. To obtain these values, for each system, diffusion couple experiments were performed at three different temperatures. The activation energy and pre-exponential factor values were obtained using Boltzmann-Matano analysis and Arrhenius equation. The binary interdiffusion coefficients of the Zn-{Ce, Nd} systems were also calculated at 400°C. Section 5.3 provided detailed analytical procedure on how to calculate interdiffusion coefficient, activation energy and pre-exponential factor of the growth of the compound layers.

Total thickness of the Mg-Ce diffusion layers was larger than the total thickness of the Mg-Nd diffusion layers when annealed under the same conditions. This means that the diffusion reaction in the Mg-Ce system is highly temperature dependent, while it is highly time dependent reaction in the Mg-Nd system. No diffusion data about the Zn-{Ce, Nd} systems could be found in the literature, also the available data of the Mg-{Ce, Nd, Zn} was considered incomplete, because many compounds did not form in the diffusion couples reported in the literature. This can be attributed to sequential growth of diffusion layers in multi-compound forming systems. In this chapter, all the stable phases, of the studied systems, were observed in all diffusion couples. The obtained diffusion data are essential for the ternary diffusivity measurements, since these values are important to verify the ternary diffusion coefficients at the early stages of diffusion. Also, the work provides essential information necessary to understand solidification, thermochemical processing, joining and other processes of Mg alloys containing Ce, Nd or Zn.

In the next chapter, conclusions, contributions and suggestions for future work are presented.

Chapter 6 : Conclusions, Contributions and Suggestions for Future Work

6.1. Conclusions

An extensive experimental investigation was performed on three ternary systems; Ce-Mg-Mn, Mg-Mn-Nd and Ce-Mg-Zn and five binary systems; Mg-{Ce, Nd, Zn} and Zn-{Ce, Nd} using solid-solid diffusion couples as the main experimental tool. Selected equilibrated key alloys were used to provide precise location of the phase boundaries in the ternary systems. The isothermal sections of Mg-Mn-{Ce, Nd} systems at 450°C and the Ce-Mg-Zn ternary system at 300°C were established in the full composition range based on the current experimental investigation. In addition, the binary interdiffusion coefficients of the Mg-{Ce, Nd, Zn} and Zn-{Ce, Nd} systems were calculated and provided in this thesis.

The diffusion couple method is an efficient tool for phase diagram determination, because it can provide myriad phase equilibrium information, which would normally require a large number of key alloys. It also eliminates the problems associated with alloy preparation especially for systems with components having high melting temperatures. However, the possibility of missing phases must be considered while using diffusion couples for phase diagram studies. This may occur because of the phase boundary migration due to the change in the driving force of the growing layers. In order to obtain more accurate and reliable information, diffusion couples are combined with equilibrated key alloys to obtain precise location of the phase boundaries. For this purpose, combination of diffusion couples and key alloys is used in the present work.

The isothermal section of the Ce-Mg-Mn phase diagram at 450°C was constructed for the full composition range. The phase relationships were determined using 6 solid-solid diffusion couples and 12 key alloys. No ternary compound was detected in this system at 450°C. Based on the accepted Ce-Mg binary phase diagram, the thermal stability range of $CeMg_2$ phase is between 615°C and 711°C, while the annealing temperature in this work was performed at 450°C. Thus, $CeMg_2$ is not a stable phase in the Ce-Mg-Mn isothermal section at 450°C. This was confirmed by SEM/EDS, XRD and metallographic studies. Many two-phase regions, composed mainly of Mn and other phase, were observed in the microstructure of each zone. However, a continuous thin layer of Mn was detected in two diffusion couples of this system indicating that Mn was diffusing. On the other hand, the ternary solid solubility extending from $(\gamma\text{-Ce})^{Mg,Mn}$, (CeMg), ($CeMg_3$) and ($CeMg_{12}$) compounds were measured at 450°C as 3.0, 5.1, 3.2 and 1.8 at.% Mn, respectively.

The Mg-Mn-Nd isothermal section at 450°C was constructed over the full composition range using diffusion couples and key alloys, analyzed by XRD, SEM/EDS/WDS and metallography. No ternary compound was found in the system at 450°C. Key alloys were used to confirm the phase relations obtained from diffusion couples and to determine the solid solubility limits. Diffusion couples revealed that Mn has relatively lower diffusivity than that of Mg and Nd. Thus, pure Mn was observed stationary in some diffusion zones forming Mn+(MgNd), Mn+(Mg_3Nd) and Mn+$Mg_{41}Nd_5$ two-phase regions. However, relatively small amount of Mn diffused towards the interface with Mg end-member forming a continuous thin layer of pure Mn. The reminder of Mn was dissolved in Mg-Nd binary compounds forming ternary extended solid solutions. $(\alpha\text{-Nd})^{\mathrm{Mg,Mn}}$, (MgNd) and ($Mg_3Nd$) were found to have ternary extended solid solubility of 3.0, 13.0, and 3.7 at.% Mn, respectively.

The Ce-Mg-Zn isothermal section at 300°C was constructed for the whole composition range using diffusion couples and key alloys experiments. Most of the ternary compounds and extended binary compounds have wide homogeneity ranges. The solid solutions in the system seem to occur due to the mutual substitution between Mg and Zn. Diffusion couples of this system showed complex relationships due to the dispersed morphologies. The high affinity of Mg to Zn atoms led to consumption of Mg from the $CeMg_{12}$ end-member by diffusion to form a series of Mg-Zn compounds. As a result, pure Mg was freed from the $CeMg_{12}$ solid solution, and ternary compounds with constant Ce concentration were observed. The ternary solubility of Zn in the Ce-Mg compounds was found to increase when the Mg concentration is decreasing. Accordingly, the ternary solid solubility of Zn in $CeMg_{12}$ and $CeMg_3$ was measured as 5.6 and 28.4 at.% Zn, respectively. Furthermore, a complete solid solubility was observed between CeMg and CeZn. The complete solubility was confirmed using a diffusion couple made from CeMg and CeZn end-members.

Diffusion couple experiments were used to measure the binary interdiffusion coefficients of the Mg-{Ce, Nd, Zn} and Zn-{Ce, Nd} systems. Mg-{Ce, Nd} diffusion couples were annealed at 400, 450 and 490°C for 120, 96 and 4hr, respectively. Mg-Zn diffusion couples were annealed at 250, 275 and 300°C for 552, 408 and 504hr, respectively. Zn-{Ce, Nd} diffusion couples were annealed at 400°C for 240hr. This work resolved the problem encountered in the literature of the missing phases in the Mg-{Ce, Nd, Zn} systems. Thus, the composition-dependent interdiffusion coefficient, activation energy and pre-exponential factor at the interfaces of the Mg-{Ce, Nd, Zn} intermetallic compounds were calculated.

Although Zn-{Ce, Nd} systems are considered among the more difficult systems to be studied via diffusion couple experiments, two successful diffusion couples, annealed at 400°C for 240hr, were obtained. The difficulty stems from the presence of large number of intermetallic compounds in a narrow range of composition. In addition, some of these compounds appeared as very thin layers. Nine intermetallic compounds were detected in the Ce-Zn diffusion couple and eight compounds were detected in the Nd-Zn diffusion couple. The diffusion couples were analyzed thoroughly and their results were discussed and supported using the established phase diagrams. Explanation of the evolution of phases in the Nd-Zn system and the anisotropic diffusion behavior, resulting in wavy interfaces, were provided. Sequential instead of spontaneous layer formation was observed and the layer consumption of Ce-Zn compounds was also discussed. The composition-dependent interdiffusion coefficients at the intermetallic interfaces of these systems are also provided. For the available literature data for some of the compounds in the Mg-{Ce, Nd, Zn} systems, the calculated interdiffusion coefficients are in good agreement. No diffusion data regarding Zn-{Ce, Nd} systems could be found in the literature compare with. The activation energies for the growth of the Mg-Ce compounds showed relatively higher values than those of Mg-Nd and Mg-Zn compounds.

6.2. Contributions

In this work, three promising Mg-based ternary systems, Ce-Mg-Mn, Mg-Mn-Nd and Ce-Mg-Zn, have been studied experimentally to provide accurate description of the phase equilibria. Also, the binary interdiffusion coefficients of the Mg-{Ce, Nd, Zn} and Mg-{Ce, Nd} systems were calculated. Some of the main contributions of this work are given below:

- Comprehensive binary and ternary diffusion couple analysis is provided for different systems.
- The isothermal section of the Ce-Mg-Mn system at 450°C was established for the full composition range based on the results of diffusion couples and key alloys. The solubility of Mn in the $(\gamma\text{-Ce})^{Mg,Mn}$, (CeMg), ($CeMg_3$) and ($CeMg_{12}$) solid solutions is determined as 3.0, 5.1, 3.2 and 1.8 at.% Mn, respectively, using XRD and EDS analysis. No ternary compound is found in the system at 450°C.
- The isothermal section of the Mg-Mn-Nd system at 450°C was established for the whole composition range by means of diffusion couples and key alloys. The solubility of Mn in $(\alpha\text{-Nd})^{Mg,Mn}$, (MgNd) and ($Mg_3Nd$) was measured at 450°C as 3.0, 13 and 3.7 at.% Mn, respectively.
- The diffusion behavior of Mn in the Mg-Mn-{Ce, Nd} systems is described based on microstructures of the diffusion couples and key alloys. Because Mn is found in equilibrium with most of the phases, the phase boundary lines in both systems are pointing towards the Mn-rich corner.
- The isothermal section of the Ce-Mg-Zn system at 300°C was established for the full composition range. Eight ternary compounds τ_1 ($Ce_6Mg_3Zn_{19}$), τ_2 ($CeMg_{29}Zn_{25}$), τ_3 ($Ce_2Mg_3Zn_3$), τ_4 ($CeMg_3Zn_5$), τ_5 ($CeMg_7Zn_{12}$), τ_6 ($CeMg_{2.3-x}Zn_{12.8+x}$; $0 \leq x \leq 1.1$), τ_7 ($CeMgZn_4$) and τ_8 ($Ce(Mg_{1-y}Zn_y)_{11}$; $0.096 \leq y \leq 0.43$) are

observed. The ternary solid solubility of Zn in $CeMg_{12}$ and $CeMg_3$ was measured at 300°C as 5.6 and 28.4 at.% Zn, respectively.

- The complete solid solubility between CeMg and CeZn compounds is confirmed using a diffusion couple containing these compounds as end-members.
- The complex morphologies observed in the Ce-Mg-Zn ternary diffusion couples are described based on the volumetric mismatch at the interface between two dissimilar phases, which occurs due to the lattice distortion.
- Interpolation of tie-lines in a ternary diagram is described based on the preliminary experimental tie-lines. This can retrieve the scientific meaning of the mass balance principle along these lines.
- The binary interdiffusion coefficients of the Mg-{Ce, Nd, Zn} and Zn-{Ce, Nd} systems are calculated. The activation energy and pre-exponential values of the growth of the Mg-{Ce, Nd, Zn} compounds are also calculated. The obtained results are in good agreement with the available data from literature.
- Diffusion couple studies confirmed the phase diagram data of the Mg-{Ce, Nd, Zn} and Zn-{Ce, Nd} binary systems.
- Evolution of the phase growth in the Zn-{Ce, Nd} systems is explained based on the sequential growth of the compound layers. The wavy interface phenomenon is presented based on the anisotropic growth of diffusion layers.

Four journal publications were used in the body of the entire thesis. In addition, the following publications have been accomplished during the course of the current work:

Journal publications

1. **Ahmad Mostafa** and Mamoun Medraj “Phase equilibria of the Mg-Nd-Zn ternary system at 300°C by means of diffusion couples and key alloys techniques” (In preparation).
2. Tian Wang, Dmytro Kevorkov, **Ahmad Mostafa**, and Mamoun Medraj, “Experimental investigation of the phase equilibria in the Al-Mn-Zn system at 400°C”, Journal of Materials, submitted on April 2014.
3. Mohammad Mezbahul-Islam, **Ahmad Mostafa**, and Mamoun Medraj, "Essential Magnesium Alloys Binary Phase Diagrams and their Thermochemical Data", Journal of Materials, Volume 2014, Article ID 704283.
4. Md. Imran Khan, **Aahmad Mostafa**, Mohammad Aljarrah, Elhachmi Essadiqi and Mamoun Medraj, "Influence of cooling rate on microsegregation behavior of magnesium alloys", Journal of Materials, Volume 2014, Article ID 657647, 18 pages.
5. **A. O. Mostafa**, A. E. Gheribi, D. Kevorkov, M. Mezbahul-Islam, and M. Medraj, “Experimental Investigation and Thermodynamic Modeling of Mn-Nd Phase Diagram”, CALPHAD, 2013, Vol. 42, pp. 27-37.

Conference publications:

1. **A. Mostafa**, D. Kevorkov, A. Gheribi, M. Medraj, “The Mg-Mn-Nd System: Experimental Investigation Coupled with Thermodynamic Modeling”, ICMAA2012, Vancouver, pp. 245-250.

6.3. Suggestions for future work

The present work provides the importance of the diffusion couple studies in the Ce-Mg-Mn, Mg-Mn-Nd and Ce-Mg-Zn ternaries and Mg-{Ce, Nd, Zn} and Zn-{Ce, Nd} binaries. However, it can be improved by further suggestions as following:

- The solubility limits of Mn in Ce-Mg compounds were measured using EDS analysis. However, EDS cannot determine the small solubilities accurately due to the high error limits. It is recommended to re-assess these values using WDS analysis.
- Crystallographic studies of the newly discovered intermetallic compounds in the Ce-Mg-Zn at 300°C are essential. This can be achieved by preparing alloys containing these compounds and examine them using single crystal XRD analysis and Transmission Electron Microscopy (TEM) with specimen preparation using Focused Ion Beam (FIB).
- The ternary interdiffusion coefficients of the Ce-Mg-Mn, Mg-Mn-Nd and Ce-Mg-Zn systems need to be determined. This can be achieved by using diffusion couples and Boltzmann-Matano analysis. The ternary diffusivities can be measured at specific composition where two diffusion paths are intersecting.
- Thermodynamic description is essential for establishing a self-consistent database of all ternary systems. This can be achieved using CALPHAD approach relying on the experimental results obtained from the current work.
- Liquidus projections are also essential for the thermodynamic description of the studied ternary systems. This can be achieved by thermal analysis of the ternary alloys using DSC.

- Hydrogen sorption properties of the Mg-Mn-{Ce, Nd} alloys can be tested using pressure-composition-temperature (PCT) instrument.

References

[1] D. Eliezer, E. Aghion, F. Froes, Magnesium science, technology and applications, Advanced Performance Materials, 5 (1998) 201-212.

[2] M. Bamberger, G. Dehm, Trends in the Development of New Mg Alloys, Annu. Rev. Mater. Res., 38 (2008) 505-533.

[3] C. Blawert, N. Hort, K.U. Kainer, Automotive applications of magnesium and its alloys, Transactions- Indian Institute of Metals, 57 (2004) 397-408.

[4] B. Mordike, T. Ebert, Magnesium: Properties - Applications - Potential, Materials Science and Engineering 302 (2001) 37-45.

[5] H. Friedrich, B. Mordike, Magnesium Technology, Springer-Verlag, Berlin, 2006.

[6] J.J. Kim, D.S. Han, Recent development and applications of magnesium alloys in the Hyundai and Kia Motors Corporation, Materials Transactions, 49 (2008) 894 to 897.

[7] M. Mezbahul-Islam, A. Mostafa, M. Medraj, Essential magnesium alloys binary phase diagrams and their thermochemical data, Journal of Materials, (2014) Article ID: 704283, (In press).

[8] J. Bohlen, S. Yi, D. Letzig, K.U. Kainer, Effect of rare earth elements on the microstructure and texture development in magnesium–manganese alloys during extrusion, Materials Science and Engineering: A, 527 (2010) 7092-7098.

[9] H.-Y. Qi, G.-X. Huang, H. Bo, G.-L. Xu, L.-B. Liu, Z.-P. Jin, Thermodynamic description of the Mg–Nd–Zn ternary system, Journal of Alloys and Compounds, (2011) 3274–3281.

[10] A. K. Meshinchi, Improving the properties of magnesium alloys for high temperature applications, in: F. Czerwinski (Ed.) Magnesium Alloys – Design, Processing and Properties, InTech, 2011.

[11] B. Mordike, K. Kainer, Magnesium alloys and their applications, Willey-VCH, Weinheim, 2000.

[12] J. Cai, G. Ma, Z. Liu, H. Zhang, A. Wang, Z. Hu, Influence of rapid solidification on the mechanical properties of Mg-Zn-Ce-Ag magnesium alloy, Materials Science and Engineering: A, 456 (2007) 364-367.

[13] J.S. Kirkaldy, Diffusion in multi component metallic systems: II. Solutions for two-phase systems with applications to transformations in steel, Canadian Journal of Physics, 36 (1958) 907-916.

[14] J.S. Kirkaldy, L.C. Brown, Diffusion behaviour in ternary, multiphase systems, Canadian Metallurgical Qarterly, 2 (1963) 89-115.

[15] J.-C. Zhao, Methods for phase diagram determination, Elsevier Science, Amsterdam, 2007.

[16] M. Mezbahul-Islam, M. Medraj, Experimental study of the Cu–Ni–Y system at 700°C using diffusion couples and key alloys, Journal of Alloys and Compounds, 561 (2013) 161-173.

[17] H. Xu, Y. Du, Z. Zhou, Z. Jin, Determination of phase diagrams using the diffusion couple technique, Rare Metals, 25 (2006) 427-430.

[18] J.C. Zhao, M.R. Jackson, L.A. Peluso, Mapping of the Nb–Ti–Si phase diagram using diffusion multiples, Materials Science and Engineering: A, 372 (2004) 21-27.

[19] B. Predel, Si-Ti (Silicon-Titanium), in: O. Madelung (Ed.) Pu-Re – Zn-Zr, Springer Berlin Heidelberg, 1998, pp. 1-3.

[20] A. Kodentsov, G. Bastin, F. Loo, The diffusion couple technique in phase diagram determination, Journal of Alloys and Compounds, 320 (2001) 207-217.

[21] F.C. Campbell, Phase diagrams: Understanding the basics, in, ASM International, Ohio, 2012.

[22] H. Mehrer, Diffusion in solids (Fundamentals, methods, materials, diffusion-controlled processes), Springer-Verlag Berlin Heidelberg, Heidelberg, 2007.

[23] P. Shewmon, Diffusion in solids, Second ed., McGraw-Hill, New york, 1963.

[24] C. Matano, On the relation between the diffusion-coefficients and concentrations of solid Metals, Japanese Journal of Physics, 8 (1933) 109-113.

[25] W. Callister, D. Rethwisch, Materials science and engineering: An introduction, 7th ed., John Wiley & Sons, Inc., United States, 2007.

[26] P. Echlin, Handbook of Sample Preparation for Scanning Electron Microscopy and X-Ray Microanalysis, Springer Science and Business Media, LLC, Cambridge, 2009.

[27] J.I. Goldstein, D. Newbury, D. Joy, C. Lyman, P. Echlin, E. Lifshin, L. Sawyer, J.R. Michael, Scanning electron microscopy and X-ray microanalysis, 3 ed., 2003 Kluwer Academic/Plenum Publishers, New York, 2003.

[28] R. Egerton, Physical Principles of Electron Microscopy: An Introduction to TEM, SEM, and AEM, Springer Science and Business Media, Inc, New York, USA, 2005.

[29] Y. Leng, Materials Characterization: Introduction to Microscopic and Spectroscopic Methods, JohnWiley & Sons (Asia) Ltd., Hong Kong 2008.

[30] T. Takenaka, Y. Narazaki, N. Uesaka, M. Kawakami, Improvement of corrosion resistance of magnesium alloys by surface film with rare earth element, Materials Transactions, 49 (2008) 1071-1076.

[31] D. Petrov, M. Mirgalovskaya, I. Strelnikova, E. Komova, The state diagram for magnesium corner of the Mg-Mn-Ce system, Baikov Institute of Metallurgy and Materials Science, 1 (1957) 144-147.

[32] L. Rolla, A. Iandelli, Contributions to the Knowledge of Rare Earth Metals and Their Alloys. The Alloys of Lanthanum with Manganese, Berichte der deutschen chemischen Gesellschaft (A and B Series), 75 (1942) 2091-2095.

[33] A. Iandelli, The Ce-Mn alloys, Proceedings of the National Academy of Sciences, 13 (1952) 265-268.

[34] B. Thamer, The system cerium-manganese in the range of 0-20 atomic percent manganese, Journal of the Less Common Metals, 7 (1964) 341-346.

[35] A. Palenzona, S. Cirafici, The Ce-Mn (Cerium-Manganese) system, Journal of Phase Equilibria, 17 (1996) 53-56.

[36] C. Tang, Y. Du, H. Xu, S. Hao, L. Zhang, Study on the nonexistence of liquid miscibility gap in the Ce-Mn system Journal of Mining and Metallurgy, 43 (2007) 21-28.

[37] C. Tang, Y. Du, L. Zhang, H. Xu, Z. Zhu, Thermodynamic assessment of the Ce-Mn system, Journal of Alloys and Compounds, 437 (2007) 102-106.

[38] Y. Kang, A. Pelton, P. Chartrand, P. Spencer, C. Fuerst, Critical evaluation and thermodynamic optimization of the binary systems in the Mg-Ce-Mn-Y system, Journal of Phase Equilibria and Diffusion, 28 (2007) 342-354.

[39] D. Petrov, M. Mirgalovskaya, I. Strelnikova, E. Komova, The Constitution Diagram for the Magnesium-Manganese System, Institute of Materials Science, Academy of Sciences of the Ukrainian SSR, 1 (1958) 142-143.

[40] N. Tiner, The Solubility of Manganese in Liquid Magnesium, Metals Technology, (1945) 1-7.

[41] A. Nayeb-Hashemi, J. Clark, The Mg−Mn (Magnesium-Manganese) system, Journal of Phase Equilibria, 6 (1985) 160-164.

[42] J. Gröbner, D. Mirkovic, M. Ohno, R. Schmid-Fetzer, Experimental investigation and thermodynamic calculation of binary Mg-Mn phase equilibria, Journal of Phase Equilibria and Diffusion, 26 (2005) 234-239.

[43] M. Asgar-Khan, M. Medraj, Thermodynamic description of the Mg-Mn, Al-Mn and Mg-Al-Mn systems using the modified quasichemical model for the liquid phases, Materials Transactions, 50 (2009) 1113-1122.

[44] X. Zhang, D. Kevorkov, I.-H. Jung, M. Pekguleryuz, Phase equilibria on the ternary Mg-Mn-Ce system at the Mg-rich corner, Journal of Alloys and Compounds, 482 (2009) 420-428.

[45] D. Wood, E. Cramer, Phase relations in the magnesium-rich portion of the cerium-magnesium system, Journal of the Less Common Metals, 9 (1965) 321-337.

[46] Q. Johnson, G. Smith, The crystal structure of Ce_5Mg_{42}, Acta Crystallographica, 22 (1967) 360-365.

[47] J. Pahlman, J. Smith, Thermodynamics of formation of compounds in the Ce-Mg, Nd-Mg, Gd-Mg, Dy-Mg, Er-Mg, and Lu-Mg binary systems in the temperature range 650to 930K, Metallurgical and Materials Transactions B, 3 (1972) 2423-2432.

[48] A. Nayeb-Hashemi, J. Clark, The Ce-Mg (Cerium-Magnesium) system, Journal of Phase Equilibria, 9 (1988) 162-172.

[49] A. Saccone, D. Macciò, S. Delfino, F. Hayes, F. Ferro, Mg-Ce alloys. Experimental investigation by Smith thermal analysis, Journal of Thermal Analysis and Calorimetry, 66 (2001) 47-57.

[50] ASM Handbook, Volume 03 - Alloy Phase Diagrams, ASM International, Ohio, 1992.

[51] X. Zhang, D. Kevorkov, M. Pekguleryuz, Stoichiometry Study on the Binary Compounds in the Mg-Ce System: Part I, Journal of Alloys and Compounds, 475 (2009) 361-367.

[52] H. Okamoto, Ce-Mg (Cerium-Magnesium), Journal of Phase Equilibria and Diffusion, 32 (2011) 265–266.

[53] X. Zhang, D. Kevorkov, M. Pekguleryuz, Study on the binary Intermetallic compounds in the Mg-Ce system, Intermetallics, 17 (2009) 496-503.

[54] X. Zhang, D. Kevorkov, M. Pekguleryuz, Study on the intermetallic phases in the Mg-Ce system: Part II. Diffusion couple investigation, Journal of Alloys and Compounds, 501 (2010) 366-370.

[55] P. Villars, L. Calvert, Pearson's Crystal Data, Crystal Structure Database for Inorganic Compounds, CD-ROM software version 1.3, (2009).

[56] G. Raynor, Constitution of Ternary and Some Complex Alloys of Magnesium, International metals reviews, 22 (1977) 65-96.

[57] M. Pezat, A. Hbika, B. Darriet, Study of alloy composition $CeMg_{11}M$ (M = V, Cr, Mn, Fe, Co) and their application in hydrogen storage, Materials Research Bulletin, 15 (1980) 139-146.

[58] PANalytical, Ver2.2b (2.2.2), in, Almelo, The Netherlands, 01-11-2006.

[59] Y.-N. Zhang, D. Kevorkov, F. Bridier, M. Medraj, Experimental study of the Ca–Mg–Zn system using diffusion couples and key alloys, Science and Technology of Advanced Materials, 12 (2011) 1-13.

[60] J.A. Gann, A.W. Winston, Magnesium and its alloys, Industrial and Engineering Chemistry, 19 (1927) 1193-1201.

[61] Y. Xu, L.S. Chumbley, F.C. Laabs Liquid metal extraction of Nd from NdFeB magnet scrap, Journal of Materials Research, 15 (2000) 2296-2304.

[62] D. Wellbeloved, P. Craven, J. Waudby, Manganese and Manganese Alloys, in: Ullmann's Encyclopedia of Industrial Chemistry, Wiley-VCH Verlag GmbH & Co., 2000.

[63] V.T. Witusiewicz, F. Sommer, E.J. Mittemeijer, Reevaluation of the Fe-Mn phase diagram, Journal of Phase Equilibria and Diffusion, 25 (2004) 346-354.

[64] A. Saccone, S. Delfino, R. Ferro, Systematics of rare earth-manganese alloys: Nd-Mn phase diagram, International Journal of Materials Research, 84 (1993) 563-568.

[65] Y. Kang, A. Pelton, P. Chartrand, P. Spencer, C. Fuerst, Thermodynamic database development of the Mg-Ce-Mn-Y system for Mg alloy design, Metallurgical and Materials Transactions A, 38 (2007) 1231-1243.

[66] A. Nayeb-Hashemi, J. Clark, The Mg−Nd system (Magnesium-Neodymium), Bulletin of Alloy Phase Diagrams, 9 (1988) 618-623.

[67] S. Delfino, A. Saccone, F. Ferro, Phase relationships in the neodymium-magnesium alloy system, Metallurgical and Materials Transactions A, 21 (1990) 2109-2114.

[68] R. Joseph, K. Gschneidner, Solid solubility of magnesium in some lanthanide metals, Transactions of the American Institute of Mining and Metallurgical Engineers, 233 (1965) 2063-2069.

[69] J.J. Park, L.L. Wyman, Phase Relationships in Magnesium Alloys., in, WADC Technical report: Astia Document No. AD142110, 1957, pp. 1-27.

[70] M. Drits, E. Padezhnova, N. Miklina, The combined solubility of noedymium and zinc in solid magnesium, Russian Metallurgy (Metally), 3 (1974) 143-146.

[71] L.L. Rokhlin, Magnesium alloyscontaining rare earth metals: Structure and properties, Taylor and Francis, New York, 2003.

[72] H. Kirchmayr, W. Lugscheider, Die Zustandsbilder Neodym-Samarium- und Terbium-Mangan, Zeitschrift für Metallkunde, 61 (1970) 22-23.

[73] S. Makhalenko, Y. Kuz'ma, X-ray diffraction investigations of the Nd-Mn system, Izvestiya Akademii Nauk SSSR, Neorganicheskie Materialy (Inorganic Materials (USSR)), 26 (1990) 2432-2433.

[74] A.O. Mostafa, A.E. Gheribi, D. Kevorkov, M. Mezbahul-Islam, M. Medraj, Experimental investigation and first-principle calculations coupled with thermodynamic modeling of the Mn–Nd phase diagram, Calphad, 42 (2013) 27-37.

[75] M. Drits, Z. Sviderskaya, L. Rokhlin, Alloys of the Mg-Mn-Nd system adjacent to the magnesium corner, Zhurnal neorganjoheskoi Khimii (Journal of Inorganic Chemistry), 7 (1963) 2771-2777.

[76] M. Drits, N. Bochvar, Phase equilibria in the Mg-Nd-Mn-Ni system, Doklady Akademii Nauk SSSR 178, No. 2 (1968) 403-405.

[77] V.I. Dybkov, Growth Kinetics of Chemical Compound Layers, Cambridge Int Science Publishing, Cambridge, UK, 2004.

[78] A.A. Kodentsov, G.F. Bastin, F.J.J. Van Loo, The diffusion couple technique in phase diagram determination, Journal of Alloys and Compounds, 320 (2001) 207-217.

[79] S. Gorsse, C. Hutchinson, B. Chevalier, J. Nie, A thermodynamic assessment of the Mg-Nd binary system using random solution and associate models for the liquid phase, Journal of Alloys and Compounds, 392 (2005) 253-262.

[80] M. Huang, H. Li, H. Ding, Y. Ren, G. Qin, S. Hao, Partial phase relationships of Mg-Zn-Ce system at 350°C, Transactions of Nonferrous Metals Society of China, 19 (2009) 681-685.

[81] P. Ghosh, M. Mezbahul-Islam, M. Medraj, Critical assessment and thermodynamic modeling of Mg–Zn, Mg–Sn, Sn–Zn and Mg–Sn–Zn systems, Calphad, 36 (2012) 28-43.

[82] Y.M. Zhu, A.J. Morton, J.F. Nie, Improvement in the age-hardening response of Mg–Y–Zn alloys by Ag additions, Scripta Materialia, 58 (2008) 525-528.

[83] G. Omori, S. Matsuo, H. Asada, Precipitation process in a Mg-Ce alloy, Transactions of the Japan Institute of Metals, 16 (1975) 247-256.

[84] M.-l. Huang, H.-x. Li, H. Ding, L. Bao, X.-b. Ma, S.-m. Hao, Intermetallics and phase relations of Mg-Zn-Ce alloys at 400 °C, Transactions of Nonferrous Metals Society of China, 22 (2012) 539-545.

[85] A.M. Korolkov, Y.P. Saldau, Solubility of Zn and Ce in Mg in the Solid State, Izvestiia Sektora fiziko-khimicheskogo analiza, 16 (1946) 295-306.

[86] E.V. Melnik, M.F. Kostina, Ya.P. Yarmlyuk, O.F. Zmii, Study of the Magnesium-Zinc-Cerium and Magnesium-Zinc-Calcium Ternary Systems, Magnievye Splavy, Mater.Vses. Soveshch. Issled., Razrab. Primen. Magnievyhk Splavov, (1978) 95-99.

[87] M.E. Drits, E.I. Drozdova, I.G. Korolkova, V.V. Kinzhibalo, A.T. Tyvanchuk, Investigation of Polythermal Sections of the Mg-Zn-Ce System in the Mg-Rich Region, Russian Metallurgy (Metally), 2 (1989) 195-197.

[88] U. Kolitsch, P. Bellen, S. Kaesche, D. Maccio, N. Bochvar, Y. Liberov, P. Rogl, Cerium-Magnesium-Zinc, in: G. Effenberg, G. Petzow (Eds.) Ternary Alloys –A Comprehensive Compendium of Evaluated Constitutional Data and Phase Diagrams, VCH Verlagsgesellscahft, MSI GmbH,Weinheim, Stuttgart, Germany, 2000, pp. 168–176.

[89] R. Agarwal, S. G. Fries, H. L. Lukas, G. Petzow, F. Sommer, T. G. Chart, G. Effenberg, Assessment of the Mg-Zn system, Zeitschrift für Metallkunde, 83 (1992) 216-223.

[90] D. Kevorkov, M. Pekguleryuz, Experimental study of the Ce-Mg-Zn phase diagram at 350°C via diffusion couple techniques, Journal of Alloys and Compounds, 478 (2009) 427-436.

[91] C.-n. Chiu, J. Gröbner, A. Kozlov, R. Schmid-Fetzer, Experimental study and thermodynamic assessment of ternary Mg–Zn–Ce phase relations focused on Mg-rich alloys, Intermetallics, 18 (2010) 399-405.

[92] V. Pavlyuk, B. Marciniak, E. Różycka-Sokołowska, The isothermal section of the phase diagram of Ce–Mg–Zn ternary system at 470 K, Intermetallics, 20 (2012) 8-15.

[93] H. Okamoto, Supplemental literature review of binary phase diagrams: Cs-In, Cs-K, Cs-Rb, Eu-In, Ho-Mn, K-Rb, Li-Mg, Mg-Nd, Mg-Zn, Mn-Sm, O-Sb, and Si-Sr, Journal of Phase Equilibria and Diffusion, 34 (2013) 251-263.

[94] Available online: www.MagNET.ubc.ca, (accessed on May 22, 2014).

[95] R. Ferro, A. Saccone, G. Borzone, Rare earth metals in light alloys, Journal of Rare Earths, 15 (1997) 45-61.

[96] X. Tao, Y. Ouyang, H. Liu, Y. Feng, Y. Du, Y. He, Z. Jin, Phase Stability of Magnesium-Rare Earth Binary Systems From First-Principles Calculations, Journal of Alloys and Compounds, 509 (2011) 6899-6907.

[97] X.K. Zhu, R.K. O'Nions, Monazite chemical composition: some implications for monazite geochronology, Contrib Mineral Petrol, 137 (1999) 351-363.

[98] N. Stanford, D. Phelan, The formation of randomly textured magnesium alloy sheet through rapid solidification, Acta Materialia, 58 (2010) 3642-3654.

[99] K. Lal, V. Levy, Study of the diffusion of cerium and lanthanum in magnesium, Comptes rendus hebdomadaires des séances. Série C: Sciences chimiques, 262 (1966) 107-109.

[100] Y. Xu, L. Chumbley, G. Weigelt, F. Laabs Analysis of interdiffusion of Dy, Nd, and Pr in Mg, Journal of Materials Research, 16 (2001) 3287-3292

[101] S. Brennan, K. Bermudez, Y. Sohn, Intermetallic growth and interdiffusion in the Mg-Nd system, in: W. Pool, K. Kainer (Eds.) 9th International Conference on Magnesium Alloys and their Applicatiions, Vancouver, Canada, 2012, pp. 417-421.

[102] K. Kulkarni, A. Luo, Interdiffusion and phase growth kinetics in magnesium-aluminum binary system, Journal of Phase Equilibria and Diffusion, (2013) 1-12.

[103] T. Sakakura, S. Sugino, Fundamental study on interdiffusion in h.c.p. alloys. Part 2. Magnesium-Zinc system, Memories Suzuka Coll. Technol., 10 (1977) 141-153.

[104] S. Brennan, K. Bermudez, N. Kulkarni, Y. Sohn, Diffusion couple investigation of the Mg-Zn system, in: Magnesium Technology 2012, John Wiley & Sons, Inc., 2012, pp. 323-327.

[105] Y. Du, L.-J. Zhang, S.-L. Cui, D. Zhao, D. Liu, W.-B. Zhang, W.-H. Sun, W.-Q. Jie, Atomic mobilities and diffusivities in Al alloys, Science China Technological Sciences, 55 (2012) 1-23.

[106] E.R. Wallach, Interdiffusion coeffiecients and the calculation of phase widths in bi-metallic diffusion couples, Scripta Metallurgica, 11 (1977) 361-366.

[107] J. Philibert, Atom movements: Diffusion and mass transport in solids, Les Editions de Phusique, France, 1991.

[108] A. Green, J. Humphreys, R. Mackenzie, I.G. Jones, Materials Science on CD-ROM, in: Atomic Diffusion in Metals and Alloys, The University of Liverpool, 2000.

[109] V.I. Dybkov, Solid state growth kinetics of the same chemical compound layer in various diffusion couples, Journal of Physics and Chemistry of Solids, 47 (1986) 735-740.

[110] E.O. Kirkendall, Diffusion of zinc in alpha brass, Transactions of the American Institute of Mining, Metallurgical and Petroleum Engineers, 147 (1942) 104-110.

[111] H. Okamoto, Ce-Zn (Cerium-Zinc), Journal of Phase Equilibria and Diffusion, 34 (2013) 170-170.

[112] V.I. Dybkov, Phase formation and diffusion in binary systems: Real facts and misleading views, in: Proceedings of Materials Science and Technology MS&T, Detroit, USA, 16-20 September 2007, pp. 525-536.

[113] V.I. Dybkov, Interfacial interaction and diffusion in binary systems, Defect and Diffusion Forum, 263 (2007) 75-80.

[114] F. Van Loo, G. Rieck, Diffusion in the titanium-aluminium system—I. Interdiffusion between solid Al and Ti or Ti-Al alloys, Acta Metallurgica, 21 (1973) 61-71.

[115] S. Wöhlert, R. Bormann, Phase selection governed by different growth velocities in the early stages of the Ti/Al phase reaction, Journal of Applied Physics, 85 (1999) 825-832.

[116] H. Okamoto, Nd-Zn (Neodymium-Zinc), Journal of Phase Equilibria and Diffusion, 33 (2012) 81-81.